Numerical Modelling of Sooting Laminar Diffusion Flames at Elevated Pressures and Microgravity

by

Marc Robert Joseph Charest

A thesis submitted in conformity with the requirements
for the degree of Doctor of Philosophy
Graduate Department of Aerospace Science and Engineering
University of Toronto

ABSTRACT

Numerical Modelling of Sooting Laminar Diffusion Flames at Elevated Pressures and Microgravity

Marc Robert Joseph Charest

Doctor of Philosophy

Graduate Department of Aerospace Science and Engineering

University of Toronto

2011

Fully understanding soot formation in flames is critical to the development of practical combustion devices, which typically operate at high pressures, and fire suppression systems in space. Flames display significant changes under microgravity and high-pressure conditions as compared to normal-gravity flames at atmospheric pressure, but the exact causes of these changes are not well-characterized. As such, the effects of gravity and pressure on the stability characteristics and sooting behavior of laminar coflow diffusion flames were investigated.

To study these effects, a new highly-scalable combustion modelling tool was developed specifically for use on large multi-processor computer architectures. The tool is capable of capturing complex processes such as detailed chemistry, molecular transport, radiation, and soot formation/destruction in laminar diffusion flames. The proposed algorithm represents the current state of the art in combustion modelling, making use of a second-order accurate finite-volume scheme and a parallel adaptive mesh refinement algorithm on body-fitted, multi-block meshes. An acetylene-based, semi-empirical model was used to predict the nucleation, growth, and oxidation of soot particles. Reasonable agreement with experimental measurements for different fuels and pressures was obtained for predictions of flame height, temperature and soot volume fraction. Overall, the algorithm displayed excellent strong scaling performance by achieving a parallel efficiency of 70% on 384 processors.

The effects of pressure and gravity were studied for flames of two different fuels: ethylene-air flames between pressures of 0.5–5 atm and methane-air flames between 1–60 atm. Based on the numerical predictions, zero-gravity flames had lower temperatures, broader soot-containing zones, and higher soot concentrations than normal-gravity flames at the same pressure. Buoyant forces caused the normal-gravity flames to narrow with increasing pressure while the increased soot concentrations and radiation at high pressures lengthened the zero-gravity flames. Low-pressure flames at both gravity levels exhibited a similar power-law dependence of the maximum carbon conversion on pressure which weakened as pressure was increased. This dependence decayed at a faster rate in zero gravity when pressure was increased beyond 1–10 atm.

ACKNOWLEDGEMENTS

I owe my deepest gratitude to my supervisors, Profs. Clinton Groth and Ömer Gülder. It is an honor to work with them and this thesis would not have been possible without their guidance. I would also like to thank Profs. James Gottlieb and Jean Sislian. My research benefited immensely from their questions and comments.

I am indebted to Dr. Fengshan Liu at the National Research Council Canada (NRC) for his advice and discussions on this research. I gratefully acknowledge Profs. Mitchell Smooke and Murray Thomson for their involvement in my final oral examination.

I would like to show my gratitude to my colleagues at UTIAS for their help and discussions over the years. Many thanks to Scott Northrup, Dr. James McDonald, Dr. Wen Lin, Dr. Jason Hicken, Dr. Jai Sachdev, Dr. Stephen Guzik and Pradeep Jha.

I would like to thank all my friends and family for their support and inspiration over the years. Most of all, I would like to express my deepest appreciation to my parents for their encouragement, love and continued support.

Operational funds for this work have been provided by the Natural Sciences and Engineering Research Council (NSERC) and the Canadian Space Agency (CSA). Computational resources for performing all of the calculations reported herein were provided by the SciNet High Performance Computing Consortium at the University of Toronto and Compute/Calcul Canada through funding from the Canada Foundation for Innovation (CFI) and the Province of Ontario, Canada.

Marc Robert Joseph Charest
University of Toronto Institute for Aerospace Studies
December 14, 2010

CONTENTS

LIST OF TABLES

LIST OF FIGURES

NOMENCLATURE

Variables

A_s	soot particle surface area per unit volume aerosol
$\hat{\mathbf{A}}$	linearized flux Jacobian evaluated at reference state $\hat{\mathbf{W}}$
$\mathbf{A}_\Gamma$	linearized flux Jacobian for preconditioned system
A	Arrhenius factor or area of two-dimensional computational cell
a	sound speed
a'	preconditioned sound speed
a_e	equilibrium sound speed
$\mathbf{B}$	Schwarz gather matrix
$\mathbf{b}$	system residual vector
B	effective line half-width
C_a	agglomeration constant
C_{min}	number of carbon atoms in an incipient soot particle
c_p	mixture constant-pressure specific heat
c_v	mixture constant-volume specific heat
CFL	time step constant
C	slip correction factor or empirical constant for soot spectral absorption coefficient
c	specific heat or speed of light
C_2	second Planck function constant (1.4388 cm K)
d_p	soot particle diameter
D_s	Brownian diffusion coefficient
$\mathcal{D}$	binary diffusion coefficient
D	diffusion coefficient
e	total energy
E_a	activation energy
$\mathcal{F}$	inviscid flux function
$\mathbf{F}$	solution flux vector in x- or r-direction
$\vec{\mathbf{F}}$	solution flux diad
f	friction factor or distribution function
ΔG°	change in standard-state Gibbs free energy
$\mathcal{G}$	viscous flux function
$\mathbf{G}$	solution flux vector in y- or z-direction
g	gravitational acceleration vector or cumulative distribution function
Δh_f^o	heat of formation
h	total enthalpy

$\bar{I}$	spectrum-averaged intensity
I_b	blackbody intensity
$\overline{I_{\Delta\nu}}$	narrow-band-averaged intensity
I	soot particle current or radiative intensity
$\mathbf{J}$	system Jacobian matrix
J	particle flux (particles/m^2/s)
k_b	backward reaction rate constant
k_B	Boltzmann constant (1.38×10^{-23} m^2 kg s^{-2} K^{-1})
K_c	equilibrium constant
k_f	forward reaction rate constant
Kn	Knudsen number
k	thermal conductivity, Arrhenius reaction rate constant or reordered absorption coefficient
Δl	edge-length of a two-dimensional computational cell
$\mathbf{M}$	global preconditioning matrix
$\dot{m}_\mathrm{c}$	carbon mass flow rate
$\dot{m}_\mathrm{s}$	soot mass flow rate
M_ref	reference Mach number
M	molar mass
L	number of directions in azimuthal direction
M	number of directions in polar direction
N_A	Avogadro's number (6.022×10^{26} kmol^{-1})
N_s	number of particles per mass of mixture
N_s	soot particle number density
$\hat{n}$	surface normal vector
N	number of gas species in mixture
n	particle size distribution
N_∞	total number concentration
N_B	number of solution blocks
N_b	number of narrow bands
N_q	number of Gauss quadrature points used for SNBCK
N_R	number of reactions
p_0	reference pressure
p	pressure
p'	pressure fluctuation
$\vec{q}_\mathrm{rad}$	radiation heat flux
$\vec{q}$	heat flux
q_i	rate of progress for ith reaction
$\mathcal{R}$	Riemann problem
$\hat{\mathbf{R}}$	matrix of primitive variable right eigenvectors evaluated at reference state $\hat{\mathbf{W}}$
$\mathbf{R}_\mathbf{\Gamma}$	matrix of primitive variable right eigenvectors for preconditioned system
$\mathbf{R}$	solution residual vector
$\bar{R}$	perfect gas constant (8.314 kJ kmol^{-1} K^{-1})
R	reaction rate or individual gas constant
$\mathbf{S}$	source term vector

S_{ml} source term in DOM equations
S_N source term related to soot particle number density
S_Y source term related to soot particle mass fraction
$\hat{s}$ photon direction or direction cosine unit vector
S soot particle nucleation rate or
s entropy
$\vec{\tau}$ fluid stress tensor
T temperature
t time
$\mathbf{U}$ conserved solution vector
u velocity in r-direction
u' preconditioned velocity in r-direction
$\widetilde{V}$ uncorrected diffusion velocity
$\vec{V}_c$ diffusion velocity
$\vec{V}$ diffusion velocity
$\vec{v}$ mixture bulk velocity
V_{inv} inviscid velocity scale
$\vec{V}_N$ diffusion velocity related to soot particle number density
V_p preconditioned velocity scale
V_{pgr} pressure gradient velocity scale
$\vec{V}_p$ soot particle velocity
$\vec{V}_T$ thermophoretic velocity of soot
V_{vis} viscous velocity scale
$\vec{V}_Y$ diffusion velocity related to soot mass fraction
V molar volume
v particle volume
v velocity in z-direction
v' preconditioned velocity in z-direction
v_i'' stoichiometric coefficients of ith product
v_i' stoichiometric coefficients of ith reactant
$\hat{\mathbf{W}}$ Roe-averaged solution vector
$\mathbf{W}$ primitive solution vector
[X] molar concentration of species X
$\mathbf{x}$ system solution vector
w quadrature weight
X mole fraction
Y mass fraction
Z compressibility factor or mixture fraction

Greek Symbols

α preconditioning parameter, accommodation coefficient or angular redistribution coefficient
β extinction coefficient
β preconditioning parameter, particle collision kernel, blending function or Arrhenius temperature exponent

χ	Nagle-Strickland-Constable model parameter
δ	$c_{\mathrm{s}}/c_{p_{\mathrm{g}}}$
ϵ	solution error or emissivity
ε	smallness parameter or Newton tolerance
Φ	scattering phase function
ϕ	particle volume fraction or slope limiter
φ	collision efficiency
Γ	effective specific heat ratio for a gas-particle mixture
γ	gas-phase specific heat ratio
γ_{a}	angular differencing parameter for the DOM
γ_{s}	spatial differencing parameter for the DOM
$\mathbf{\Gamma}$	preconditioning matrix for the primitive variables
η_{s}	carbon conversion factor
η	direction cosine for y-coordinate
κ	thermal conductivity or absorption coefficient
$\boldsymbol{\lambda}$	vector of eigenvalues
λ	mean-free-path of gas molecules
$\hat{\mathbf{\Lambda}}$	eigenvalue matrix evaluated at reference state $\hat{\mathbf{W}}$
$\mathbf{\Lambda}_{\mathbf{\Gamma}}$	eigenvalue matrix for preconditioned system
μ	mixture viscosity, direction cosine for x- or r-coordinate
$\Delta\nu$	wavenumber interval size
ν	wavenumber
$\dot{\omega}_k$	mass rate of production of species k
Ω	solid angle
ψ	azimuthal angle
ρ	mixture density
ρ_{s}	soot particle material density
σ_{s}	scattering coefficient
Θ	preconditioning parameter
θ	polar angle
ξ	direction cosine for z-coordinate
ζ	GMRES tolerance

Superscripts

n	iteration index

Subscripts

$\Delta\nu$	narrow band quantity
ν	spectral quantity
c	property at the critical point
g	property of gas phase
k	species index
L	left solution state
l	polar direction index
m	azimuthal direction index

mix	property of the mixture
p	property of particle material
R	right solution state
s	property of soot particle phase
st	stoichiometric quantity
v	viscous quantity
w	property at the wall surface

Abbreviations

AMR	adaptive mesh refinement
CFD	computational fluid dynamics
CFL	Courant-Friedrichs-Lewy
CK	correlated-k
DOM	discrete ordinates method
EOS	equation of state
FAS	full-approximation storage
FVM	finite volume method for radiation heat transfer
GDE	general dynamic equation
HACA	hydrogen-abstraction/acetylene-addition
LTE	local thermodynamic equilibrium
MOL	method of lines
ODE	ordinary differential equation
OTA	optically-thin approximation
PAH	polycyclic aromatic hydrocarbon
PDE	partial differential equation
PSD	particle size distribution
RHS	right-hand-side
RTE	radiative transfer equation
SNB	statistical narrow-band
SNBCK	statistical narrow-band correlated-k
SSE	spectral soot emission
TVD	total-variation-diminishing

Chapter 1

INTRODUCTION

Incomplete combustion of hydrocarbon fuels in practical combustion devices such as industrial furnaces, gas turbine combustors and diesel engines generates nanometer-sized carbon particulates called soot. The structure of these particles primarily consists of organic and elemental carbon with a multitude of absorbed and deposited compounds. Soot is considered a major pollutant and about 70% of fine airborne particles in the atmosphere are generated from combustion processes [1]. It poses significant risks to human health as there are many epidemiological studies that have demonstrated a link between exposure to airborne particulates and increased mortality/morbidity rates (see, for example, [2] and references therein). Such studies associate low-level ambient exposure with acute and long term adverse health effects. For example, exposure to particulate matter can cause respiratory problems [3, 4], eye, nose, and airway irritations, and even lung diseases [5]. Some of the major absorbed organic components in soot, polycyclic aromatic hydrocarbon (PAHs), are known mutagens and carcinogens [5, 6]. Soot also has a negative impact on the environment and the performance of combustion devices, and it is an important factor in the spread of fires in space [7].

Due to the complex nature of hydrocarbon combustion, the physics and chemistry related to soot formation are not well characterized. Soot formation and oxidation strongly affects the structure and stability of laminar diffusion flames by enhancing radiation transport and altering local temperatures. Reaction rates are highly dependant upon temperature and therefore local gaseous species concentrations are strongly influenced by the presence of soot. Since the total soot yield is drastically enhanced under high-pressure [8, 9] and zero-gravity conditions [10], better understanding the soot formation process in laminar diffusion flames is essential for the design of soot-free, high-pressure combustors and fire-suppression systems in space. However, our current understanding of the effects of pressure and gravity on soot formation/oxidation is limited since previous experimental and numerical studies generally focused on normal-gravity atmospheric flames [11–21].

Numerical modelling is an attractive tool to study the effect of pressure and gravity on soot formation. Measurements in high-pressure laminar diffusion flames are complicated by small flame diameters and limited optical access [22] while it is difficult and costly to conduct zero-gravity experiments [7]. There are only a few numerical studies on the effects of gravity [23–27] and pressure [22, 28] on soot formation in gaseous laminar diffusion flames. However, none of these studies have looked at the effects of pressure in

the absence of gravity.

Numerical modelling also permits cost effective development of new low-emission designs for practical combustion devices. Unfortunately, mathematical models representing realistic combusting flows must rely heavily on approximations to ensure that computations remain tractable. Hydrocarbon combustion is inherently complex and these approximate models are not accurate enough to capture interactions between gas-phase chemistry, turbulence, radiation transport, soot formation/oxidation, and multiphase transport. As such, there is an immediate need for more efficient numerical algorithms for solving reacting flows. These algorithms would enable the use of more realistic models to represent the underlying physics and provide quantitative soot predictions. They should be flexible enough to easily incorporate state-of-the-art numerical methods, such as adaptive mesh refinement (AMR), high-order discretization schemes and implicit non-linear relaxation/time-evolution schemes, while simultaneously taking advantage of today's trend towards large-scale parallel computing.

This thesis presents a new highly scalable finite-volume scheme for solving laminar reacting flows with detailed chemistry, radiation, and soot formation/destruction. The scheme was applied to several laminar coflow diffusion flames to study the effects of gravity and pressure on soot formation and flame structure.

1.1 Soot Formation and Oxidation

Soot formation and oxidation in hydrocarbon combustion involves many different physical processes that occur over a wide range of temporal and spatial scales. Fuel is rapidly pyrolyzed to form smaller hydrocarbons, such as acetylene, which react and produce small aromatic compounds. These small aromatic species combine with other aromatics and smaller alkyl species to form larger PAHs. Continued growth eventually leads to the appearance of small identifiable soot particles that typically have diameters on the order of 1 nm and masses of 1000 amu [29]. This whole conversion processes from gas to solid carbon is mainly chemistry controlled and occurs in only several milliseconds [30]. The newly formed particles are convected with the gas and continue to grow in size through further chemical reactions on the particle surface. They can also collide with each other to coalesce into new larger particles or form large chain-like agglomerates. Throughout this entire process, the soot particles are constantly undergoing oxidation.

1.2 Soot Modelling

The rapid transition between gas and solid phases, ongoing competition between growth and oxidation, and complex aerosol dynamics hinder our ability to identify key pathways that lead to the formation of soot. As a result, simple models for soot formation that are accurate and applicable to a wide range of operating conditions and fuels do not exist. Simpler semi-empiric models treat soot formation and oxidation as a chemically controlled process that is dependent on some precursor species such as acetylene [29]. They rely heavily on approximation, describing the overall process with only a few global reactions and one or two transport equations. Alternative detailed models attempt to improve predictive accuracy by incorporating more physical features and formation pathways [17, 31, 32]. Such detailed models typically combine gas-phase chemical kinetics describing the formation of heavy molecular weight PAH species with

complex descriptions for aerosol dynamics and gas-particle interactions. Although these models provide good quantitative predictions of minor gaseous species molar fractions, soot particle concentrations and particle size distributions, they are too complex for practical use in realistic combustor geometries. More efficient numerical techniques are therefore required to allow their application to practical devices.

1.3 Laminar Diffusion Flames

The previously described inability to fully characterize the soot formation process is largely due to experimental limitations related to optical accessibility, complex flame geometries, and the vast range of time and length scales. It is difficult to relate minute changes in flame structure or pollutant emissions to small scale processes such as chemistry or fluid interactions. As such, laminar flames with simple configurations are commonly studied even though most practical combustion devices use turbulent flames [33]. Laminar flames are more easily controlled in laboratory experiments yet still share many similar features with turbulent flames. Their detailed study is essential to advancing combustion science [34].

Growing evidence suggests that, under gravity or forced convection conditions, laminar non-premixed flames are stabilized by a small premixed flame base fed by a premixed mixture [35]. This fresh mixture is created when O_2 diffuses inwards toward the flame base and mixes with fuel. Several researchers proposed that this premixed flame is actually a triple flame with a stoichiometric flame base and two branches — a fuel-rich branch and a fuel-lean branch [36, 37]. However, recent numerical studies revealed that the premixed flame stabilization concept was flawed with insufficient time for O_2 to diffuse and mix with unburnt fuel [38, 39]. Thomson et al. [40] inadvertently confirmed this experimentally when studying the formation of soot in laminar flames at elevated pressures. They initially observed a blue zone indicating a premixed flame at the base of the flame that vanished as the pressure was increased beyond a few atmospheres. At sufficiently large pressures, the flame resided at or below the burner exit plane where no premixed mixture exists. This study by Thomson et al. highlights the need for more detailed numerical studies of high pressure laminar flames to help identify key stabilization mechanisms.

1.4 Effects of Pressure

Both pressure and gravity profoundly influence the structure and sooting characteristics of laminar diffusion flames [7, 41]. This influence occurs through the effects of pressure and gravity on buoyant forces which rapidly accelerate the expanding hot gases. Since the effective gravitational acceleration scales with pressure-squared, increasing pressure drastically alters the shapes of normal-gravity flames. For example, increasing pressure in laminar diffusion flames causes flow streamlines to contract towards the centerline and the flame diameter to decrease [8, 9, 40, 42]. Miller and Maahs [8] suggested that this change in flame diameter with pressure is likely due to changes in reaction mechanism. Experimental measurements [40, 42–44] and numerical predictions [22] for soot volume fraction indicate that the flame diameter is proportional to $p^{-1/2}$. These findings imply that residence time is independent of pressure for constant fuel mass flow rates since the cross-sectional area of the flame varies inversely with pressure. This was confirmed numerically by Liu et al. [22] who showed that the axial velocity along the flame centerline was roughly independent of

pressure. If residence time does not change with pressure, flame height should also remain constant. Roper's correlations for buoyancy-dominated laminar jet diffusion flames [45, 46] state that the visible flame height, to a first-order approximation, is independent of pressure and depends on mass flow rate only. However, Miller and Maahs [8], Flower and Bowman [9], McCrain and Roberts [42], and Thomson et al. [40] have all observed pressure-dependent flame heights during experiments involving high-pressure laminar diffusion flames. These experiments reported that the visible flame height initially increased with pressure at low pressures, remained constant over a range of pressures, and then decreased with further increase in pressure. Recently, Bento et al. [43] and Joo and Gülder [44] observed pressure-independent visible flame heights over a wide range of pressures. Constant flame heights were also predicted numerically by Liu et al. [22].

As pressure is increased in normal-gravity flames, measured soot volume fractions increase since the flame narrows and soot must flow through a smaller cross-section. This narrowing of the flame causes local temperatures near the centerline to increase and fuel pyrolysis rates in the central core to intensify. Enhanced air entrainment into the flame near the burner is also expected to increase pyrolysis rates [22]. Miller and Maahs [8] estimated total soot concentrations in high-pressure axisymmetric methane-air diffusion flames between 1–50 atm from measurements of the flame emissive power. The data indicates that soot yield is proportional to p^n, where n is approximately 1.7±0.7 up to 10 atm. Above 10 atm, the dependence of soot yield on pressure decreased significantly. Flower and Bowman [9] studied laminar diffusion flames of ethylene at pressures between 1–10 atm by measuring line-of-sight integrated soot volume fractions and temperatures along the flame centerline. They reported maximum diameter-integrated soot volume fractions proportional to $p^{1.2}$. Measurements made by Lee and Na [47] in laminar ethylene diffusion flames from 1 to 4 atm indicated a $p^{1.26}$ dependence of the maximum diameter-integrated soot volume fraction on pressure. McCrain and Roberts [42] obtained similar pressure exponents in methane flames from 1 to 25 atm and ethylene flames from 1 to 16 atm based on path-integrated and local soot volume fraction measurements. Radially-resolved soot concentration and temperature measurements were reported by Thomson et al. [40] for methane diffusion flames from 5 to 40 atm. These measurements were later extended to 60 atm by Joo and Gülder [44]. Both concluded that the maximum amount of fuel carbon converted to soot, which is most suitable for assessing the sensitivity of soot formation to pressure [9], varied proportional to p between 5 to 20 atm. Between 30 and 60 atm, Joo and Gülder measured a pressure exponent equal to 0.33. Similar soot and temperature measurements were made by Bento et al. [43] for propane flames from 1 to 7.2 atm.

There are many numerical studies on soot formation in laminar diffusion flames at atmospheric pressure [17–21, 48–72], but only a few at elevated pressures [22, 28]. The detailed numerical study by Liu et al. [22] on methane-air diffusion flames between 5–40 atm concluded that the increase in soot production with increasing pressure was due to larger mixture densities and higher species concentrations. The study showed large discrepancies between measurements and predictions which were attributed to the inability of simplified soot formation/destruction models to accurately predict soot concentrations. However, the fuel preheating effect, which is known to significantly affect numerical predictions [64], was neglected in the study.

1.5 Effects of Microgravity

Like buoyant flames, non-buoyant laminar diffusion flames also exhibit pressure-independent flame lengths [73]. Although, non-buoyant flames are both longer and wider than their buoyant counterparts [23, 73, 74]. Non-buoyant flames are wider because there is no upward acceleration to induce an inward radial motion that would cause the flame to contract. However, the reason for the lengthening of flames when buoyancy is eliminated is not clear. Investigators have cited causes such as the increased importance of axial diffusion [75, 76], the lack of radial convection [77], reduced mass diffusivities associated with lower flame temperatures [73], and reduced flame temperatures in general [78]. Roper's model for circular port burners, which includes radial convection and neglects axial diffusion, states that flame length should be independent of gravity [45].

Soot particles are too large to diffuse like gas molecules and are instead primarily convected by the gas flow. Temperature gradients also influence the motion of particles, causing them to deviate from the fluid streamlines [79]. Therefore, the path and residence time of soot particles in laminar diffusion flames are strongly affected by buoyancy since buoyant forces drastically alter the flow field [80]. For example, the dividing streamline, the locus of points where the radial velocity component is zero, diverges radially-outward in non-buoyant jet diffusion flames and converges towards the centerline in buoyant ones. Residence times for particles in non-buoyant flames are much longer than for particles in buoyant flames since local gas flow velocities are lower. These effects of buoyancy on the gas flow field and particle path cause non-buoyant diffusion flames to exhibit broader soot-containing regions and larger soot oxidation regions [23]. Higher soot concentrations and bigger particles are also generally observed in non-buoyant flames [10, 81, 82].

Although there are many experimental studies on the sooting characteristics of non-buoyant diffusion flames, none specifically address the combined effects of pressure and gravity on flame structure. Smoke-point measurements reported by Sunderland et al. [80] and Urban et al. [83] for flames between 0.3–2 atm with various gaseous hydrocarbon fuels indicated that the laminar smoke-point flame lengths of non-buoyant flames were much shorter than equivalent buoyant flames. Ku et al. [81] measured soot particle sizes in laminar diffusion flames of propane and ethylene under normal- and micro-gravity conditions. They found that primary particle sizes were larger in non-buoyant flames due to the longer residence times. Soot volume fractions were measured and soot particles sampled in weakly-buoyant gaseous laminar diffusion flames at sub-atmospheric pressures by Sunderland et al. [84–86]. These authors exploited the fact that the buoyancy-induced acceleration scales with $p^2 g$ where g is the gravitational acceleration. Others have obtained quantitative two-dimensional measurements for soot volume fraction in either reduced-gravity [10, 82, 87–89] or normal-gravity [90–92] environments. Generally, measured peak soot concentrations in micro-gravity flames are approximately a factor of two larger than those measured in normal-gravity flames. None of these studies considered pressures beyond one atmosphere.

Numerical modeling is an attractive tool to study the effect of gravity on soot formation in gaseous laminar diffusion flames as it is difficult and costly to simulate zero-gravity environments [7]. Drop-towers do not provide sufficient time to reach steady-states and experiments on parabolic flights are subjected to

small fluctuations in gravity, called g-jitter. Experiments aboard spacecraft in orbit can provide long, zero-gravity environments, but such experiments are limited by high costs and payload size/weight. Alternatively, buoyancy can be minimized by reducing pressure below atmospheric. However, low-pressure experiments are not representative of true, zero-gravity flames as flames are not completely isolated from the effects of gravity and reactions rates are slow [93]. Measured soot volume fractions instead follow trends similar to those observed in high-pressure flames.

There are only two detailed numerical studies of soot formation in zero-gravity gaseous laminar diffusion flames [26, 27]. These particular studies investigated the effects of gravity and coflow velocity on the structure and soot yield of a methane-air laminar diffusion flames. In some cases, reducing gravity was observed to cause local extinction and suppress soot formation when coflow velocities were below a critical level. Walsh et al. [89] studied the effect of buoyancy on the temperature and species concentrations in lifted laminar diffusion flames, but these flames were weakly-sooting and soot was not accounted for in their model.

1.6 Objectives

The objective of this doctoral research project is to study the effects of buoyancy and pressure on soot formation and flame structure through numerical analysis. One of the primary motivations for this work is the identification of key flame stabilization mechanisms in gaseous laminar diffusion flames. This research involves the following tasks:

- the development of a new, highly-scalable numerical solution algorithm to study soot formation in laminar reacting flows over a wide range of conditions.
- the investigation of the characteristics of existing soot formation/oxidation models and their accuracy at elevated pressures.
- the identification of the errors associated with common simplifying assumptions applied to high-pressure laminar flames.
- the study of the effects of pressure/gravity on flame stability and sooting characteristics.

1.7 Outline

Chapter 2 focuses on modelling soot produced during hydrocarbon combustion. It begins with a brief introduction on the physical processes involved and the equations governing the dynamics of soot aerosols suspended in gaseous flows. The various modelling efforts for soot in diffusion flames are reviewed and a detailed description of the soot model used herein is provided.

In Chapter 3, the techniques for modelling reactive gas mixtures is discussed. The first half provides a short introduction with an emphasis on the effects of pressure on the equation of state, heat and mass transport, and chemistry. In the second half, the employed mathematical representation for the reacting gas-particle mixture is described and analyzed.

Chapter 4 focuses on modelling radiation transport in participating media. The chapter first describes the conservation law governing radiation and outlines the techniques for its solution in non-gray media.

The remainder of this chapter describes the specific technique used to solve the governing equation and the models used to compute the spectroscopic properties of gas and soot.

The algorithm used to solve the system of governing equations, which were derived in Chapters 2–4, is described in Chapter 5. Chapter 5 includes descriptions of the solver used for the gas-particle equations and the solver used for the equations governing radiation. The coupling of these two solvers is also outlined.

In Chapter 6, the proposed computational framework is verified against published experimental measurements and numerical predictions for two different laminar coflow diffusion flames at atmospheric pressure. The predictive capability of the framework and the parallel efficiency of the algorithm is discussed.

To study the effects of pressure and gravity, the computational framework was applied to two sooting laminar coflow diffusion flames that were previously studied experimentally: a methane-air flame at pressures between 10–60 atm [44], and an ethylene-air flame between 0.5–5 atm [93]. Chapters 7 and 8 describe these laminar flames and compares predictions with measurements to assess the applicability of the employed soot model to high-pressure flames. Both flames are studied in detail with respect to the effects of pressure and gravity on flame structure and sooting behavior.

Chapter 9 summarizes the conclusions and contributions of the thesis and provides recommendations for future research.

Chapter 2

SOOT FORMATION AND OXIDATION

The complex and rapid nature of hydrocarbon combusting flows, along with current experimental and computational limitations, hinders our ability to fully understand the soot formation process [94]. In diffusion flames, soot is formed in only about ten milliseconds [95]. This time is much shorter, about one millisecond, in premixed flames. Within this time frame, the fuel molecule breaks down into smaller hydrocarbon species and forms small soot particles through a series of chemical reactions. These particles are on the order of a nanometer and consist of cyclic hydrocarbon structures with considerable amounts hydrogen and oxygen [95]. The least understood aspects of soot formation are the intermediate steps leading up to the appearance of the first soot particles. Despite this, the main steps involved in the formation and destruction of soot are well defined. Primary soot particles first appear after the formation of soot precursors. These particles react with the gas at the particle surface, increasing in size, and collide with each other, forming new larger particles or complex three-dimensional fractal structures called agglomerates. Soot is constantly oxidized by various oxygen-containing species, beginning at the early precursor stage and continuing until soot particles have been completely oxidized or eventually leave the high-temperature flame environment. As such, modelling soot formation in combusting flows requires mathematical descriptions for all of these processes and their effect on the size and distribution of particles over time.

The many different physical processes which occur over a wide range of temporal and spatial scales pose significant challenges for modelling soot in gaseous reacting flows. Soot models must capture all these processes to provide accurate predictions but also remain computationally tractable. Fortunately, models of varying complexity exist [29]. Detailed models are the most complex and make use of three main components: a gas phase kinetic mechanism, a soot chemistry sub-model, and an aerosol dynamics model. The gas-phase kinetic model is used to describe the formation of soot precursors and large cyclic hydrocarbon molecules while the soot sub-model describes gas-particle conversion. Gas-particle conversion includes both the nucleation of primary soot particles and any reactions which occur between the gas and particle surface. The third model, the aerosol dynamics model, is used to describe inter-particle collision as well as any transfer of heat and mass between the two phases. Alternative empirical soot models formulate the presence and growth of soot based on a precursor species, drastically simplifying the problem [96, 97]. This latter approach has been adopted here.

This chapter first provides an overview of soot formation in gaseous hydrocarbon combustion and outlines the different modelling techniques used for soot. Following this brief overview, the mathematical model employed in the thesis to describe soot formation and oxidation is presented.

2.1 Background

2.1.1 Chemistry

Various species are hypothesized to be key gaseous soot precursors such as polyacetylenes or polyynes [98–100], ionic species [101, 102], and PAHs [31, 32, 103, 104]. Of these different hypotheses, PAHs are the most widely accepted soot precursors. In the PAH model, aliphatic fuels are first broken down through pyrolysis into smaller hydrocarbon molecules and free radicals [105]. Following this process, single or double ring aromatic species such as benzene, phenyl, or naphthalene are formed which serve as nuclei for the growth of larger PAHs. The formation mechanisms for these first aromatic ring species are not known, but the most important reactions in aliphatic flames include the recombination of propargyl, the addition of allyl to propargyl, and cyclopentadienyl recombination [106]. Further growth of one- and two-ring aromatics into larger multi-ring structures is believed to follow the hydrogen-abstraction/acetylene-addition (HACA) pathway proposed by Frenklach and Wang [103, 107]. This pathway is a repetitive two-step sequence involving the abstraction of a hydrogen atom from an aromatic molecule and subsequent acetylene addition to the newly formed radical site. Other species have also been suggested responsible for aromatic ring growth such as methyl, propargyl, and cyclopentadienyl [54, 108–112]. Frenklach and coworkers suggested that hydrogen atom migration reactions may also be important [113–116].

At some point in the growth of larger and larger cyclic hydrocarbon structures, solid carbonaceous particles appear. These particles are believed to form as a result of condensation or combination reactions between larger aromatic structures [103, 117–119] and are roughly 500 to 2000 amu in size [120]. Molecules around this size are large enough to be held together by Van der Waals forces. Once nucleated, these particles grow via surface reactions either through acetylene addition [121, 122], PAH addition [123], or a combination of both [124]. Surface growth accounts for most or almost all of the total soot mass produced [120].

Soot is constantly oxidized by gaseous species such as O, O_2, and OH into carbon monoxide and water vapour. This process is in direct competition with the reactions that produce soot mass and is a key factor in determining the overall soot yield in a particular flame. Studies have indicated that soot particle oxidation occurs primarily by OH radicals under most conditions [30, 125] and by O_2 in lean or OH-deficient environments. Carbon dioxide does not appear to directly oxidize soot, rather it suppresses soot formation by reducing H-radial concentrations [126, 127]. Studies show that the overall soot yield is strongly affected by the oxidation of important precursor species, such as aromatics, prior to the formation of the soot particles themselves [128–131]. Unlike for soot, the oxidation of precursors via reactions with O_2 is significantly more important than those with OH [130].

2.1.2 Aerosol Dynamics

Accurate models for soot formation and oxidation in gaseous combusting flows must correctly predict the particle size distribution (PSD) and track its evolution over time. The PSD, which is governed by the general dynamic equation (GDE), defines the specific amount of particles present in a system according to their sizes [132]. It is required because many of the steps involved in the production of soot, such as aggregate formation, nucleation, and surface reactions, are dependant upon properties of the soot aerosol. Unfortunately, analytic solutions for the GDE do not exist [133, 134] and direct numerical solution can be computationally impractical [135]. Numerical difficulties arise primarily because aerosol dynamics involve a wide range of scales from a few nanometers to at least 10 micrometers [134]. Additionally, processes that affect the size and chemical structure of aerosols are highly nonlinear while the GDE itself involves many degrees of freedom.

Several approximate treatments exist to overcome these difficulties. Among the popular choices are the method of moments [135–137] and the sectional approach [133, 138–140] which both attempt to simplify the representation of the particle size distribution in some manner. Sectional methods divide the particle size distribution into a discrete number of sections or bins for which conservation of the integral form of the GDE is solved. They have proved successful for the study of soot in several areas including the structure of soot particles and aggregates [141–144], one-dimensional flames [32, 108, 145, 146], two-dimensional flames [17–19, 49, 50, 58, 70, 71, 147–149], and turbulent diffusion jet flames [150]. Moment methods require much less computational effort since only the time dependence of moments of the PSD are tracked. The moment method has been applied to study soot formation in perfectly stirred reactors [151], one-dimensional laminar premixed flames [31, 103, 107, 124, 152, 153], opposed-jet ethylene diffusion flames [154], two-dimensional laminar diffusion flames [57, 68], and turbulent flames [155–162].

A simpler approach, which is applied in this work and described in more detail in the following sections, assumes a uniform particle size distribution and solves the GDE for one or two moments of the PSD: soot volume fraction and number density, for instance. This approach is commonly used in large multi-dimensional simulations with complex geometry since it requires less computational effort than a full sectional or moment representation. Successful applications include opposed jet diffusion flames [163–165], laminar jet diffusion flames [22–24, 28, 48, 60, 60, 63–67, 166–172], and turbulent flames [173–179].

2.1.3 Computational Modelling

One of the first detailed kinetic modelling efforts was performed by Frenklach et al. [180], who developed a quantitative chemical kinetic model for soot formation based on the PAH hypothesis. Frenklach and Wang [107] later added a solid phase sub-model using the method of moments to describe particle nucleation, coagulation, and surface growth/oxidation. This particular model has been updated several times over the years and successfully applied to various premixed hydrocarbon flames operating at pressures up to 10 bar [31, 124, 152, 153]. D'Anna and Violi [110] developed a detailed gas-phase kinetic mechanism describing the formation of two- and three-ring PAHs via the various pathways discussed in Section 2.1.1. This mechanism was later modified to include the growth of larger PAH structures [56, 119] and a sub-

mechanism for particle inception, coagulation, growth, and oxidation [57]. D'Anna and Kent [58] extended this work to predict particle size distributions with a sectional model while D'Anna and Kent [17] included formation pathways for nano-sized particles and their coagulation to larger soot particles. Another important detailed modelling effort is the kinetic scheme of Richter and Howard [104] describing the formation of heavy hydrocarbons up to $C_{30}H_{10}$ and the extension of this scheme by Richter et al. [32] to include particle formation.

Detailed schemes such as those previously discussed are computationally prohibitive when applied to complex multi-dimensional geometries and large systematic studies. They require hundreds of intermediate species and thousands of elementary reactions to describe the gas-phase kinetics alone. In multiple dimensions, transport equations must be solved for each gaseous species as well as for each aerosol section or moment. The large number of unknowns and wide range of physical scales results in a large, stiff system that requires substantial computational resources to solve. Empirical and semi-empirical methods are much easier to solve numerically. These methods apply reduced mechanisms for soot formation and oxidation with simplified aerosol representations (see, for example, [29] and references therein). One of the first popular semi-empirical models was the simple two-step kinetic model of Tesner et al. [181, 182]. Others have made improvements over Tesner's original treatment by incorporating more physical and chemical features [183–186].

More realistic semi-empirical models use rate equations to account for chemistry and solve a small number of conservation laws for quantities such as soot volume fraction and number density. They include specific rates for soot inception, surface growth, coagulation, and oxidation. One particularly early example is the flamelet approach proposed by Moss et al. [187] for modelling soot formation in diffusion flames. In their work, the authors solved balance equations for both soot particle number density and volume fraction with rates computed based on the local mixture fraction. A similar approach was applied to turbulent flames by Syed et al. [188]. Young and Moss [189] extended these previous flamelet formulations by fully coupling soot formation and radiation to the flame calculations, eliminating prior post-processing strategies. Honnery and Kent [190–192] attempted to improve the mixture fraction approach by mapping soot growth rates in diffusion flames as functions of both mixture fraction and temperature. This was motivated by the fact that previous correlations based only on the mixture fraction provided poor agreement with measurements.

Kennedy et al. [167] took a slightly different approach than those described above. They assumed a constant number density and only added one equation for volume fraction to the standard governing equations for gaseous combustion. This assumption worked well for flames with high soot loading but provided poor results when applied to lightly sooting flames. Several researchers made improvements to this model, such as extending it to predict the growth of PAHs in laminar diffusion flames [193] and adding a soot intermediate to widen the range of applicable fuels [194].

Lindstedt and co-workers developed a more realistic set of soot models applicable for both laminar and turbulent flames [96, 97, 195, 196]. These models use a simple kinetic mechanism based on acetylene as the sole precursor responsible for the nucleation and growth of soot particles. Surface growth was assumed first order in acetylene concentration and dependent upon some function of the aerosol surface area. Two trans-

port equations are solved in their model: one for the soot mass fraction, and one for the soot particle number density. Lindstedt [197] later added benzene as a possible precursor species with a kinetic mechanism for the production of C_3 and C_4 species. Other improvements to the original formulation described by Fairweather et al. [97] include, for example, those proposed by Kennedy et al. [48]. These authors added soot particle thermophoresis and replaced the oxidation mechanism with the more realistic Nagle-Strickland-Constable model [198]. OH oxidation was also added because it was found to be particularly important when modelling ethylene diffusion flames. Despite these and many other enhancements, the original models of Leung et al. [96] and Fairweather et al. [97] have been widely used over the years due to their excellent balance between accuracy and computational efficiency.

With the recent improvements in computer hardware and numerical methods, it is possible to apply detailed soot models such as those discussed previously to fundamental laminar flame studies [18, 53, 70]. Researchers have therefore begun focusing on creating more complex models with many pathways and physical aspects. Despite this, semi-empirical models still have an important use; they are applied extensively in large multi-dimensional computations of turbulent laboratory flames [161, 199–202]. These mathematical models for turbulent flames cannot, however, be confidently applied to practical devices. Gas turbines and diesel engines operate at pressures beyond which any soot model has been fully validated. Therefore, a simple semi-empirical model was chosen in the present work to fully assess its predictive capability at high pressures and identify areas for further improvement.

2.2 Mathematical Model

The remainder of this chapter focuses on the description of a semi-empirical model for the formation and destruction of soot. This particular implementation follows the approaches presented by Leung et al. [96] and Fairweather et al. [97], and includes the modifications made by Liu et al. [60]. The aerosol representation is first presented and followed by the kinetic sub-model. The integration of the soot model into the equations governing the gas-phase is discussed later in Chapter 3.

2.2.1 Aerosol Description

The mathematical representation employed to describe the suspended soot particles and their interactions with the gas is simplified to help reduce the overall complexity of the problem. It assumes that soot particles are perfectly spherical and coalesce instantaneously upon collision to form a new spherical particle with the same equivalent mass. Particles are also assumed to have a constant composition and material density which implies that either a mass- or volume-based representation for the PSD may be used interchangeably. As a result of these assumptions, the PSD is completely described by a single quantity $n(v)$. It is defined by

$$\mathrm{d}N = n(v)\,\mathrm{d}v \tag{2.1}$$

where v is the particle volume, and $\mathrm{d}N$ is the concentration of particles in the size range v to $v + \mathrm{d}v$. The evolution of $n(v)$ is governed by [132]

$$\frac{\partial n}{\partial t} + \nabla \cdot n\vec{V}_\mathrm{p} + \frac{\partial I}{\partial v} = \frac{1}{2}\int_0^v \beta(\widetilde{v}, v - \widetilde{v})n(\widetilde{v})n(v - \widetilde{v})\,\mathrm{d}\widetilde{v} - \int_0^\infty \beta(v, \widetilde{v})n(v)n(\widetilde{v})\,\mathrm{d}\widetilde{v} + S(v) \tag{2.2}$$

where $\vec{V}_\mathrm{p}$ is the soot particle velocity, $I = n \cdot \frac{\mathrm{d}v}{\mathrm{d}t}$ is the particle current, $\frac{\mathrm{d}v}{\mathrm{d}t}$ is the migration velocity through v space (surface growth rate), $\beta(v, \widetilde{v})$ is the collision kernel for two particles of volume v and $\widetilde{v}$, and $S(v)$ is the nucleation rate. The first term on the left-hand-side of Eq. (2.2) describes the time rate of change of number density and the second accounts for the advection of particles. Change in number density via surface growth is represented by the third term. On the right-hand-side, the first two terms account for particle coagulation and the last term accounts for changes in number density through nucleation. Equation (2.2) represents a continuous particle size distribution and is valid when the particle size v is much larger than the molecular volume. It is most suitable for populations with constant composition particles that can take on any size [203].

Both the total number concentration, N_∞, and the volume fraction, ϕ, are moments of particular interest. They are the zeroth and first volume moments of the particle size distribution, defined by

$$N_\infty = \int_0^\infty n(v)\,\mathrm{d}v \tag{2.3}$$

$$\phi = \int_0^\infty n(v)v\,\mathrm{d}v \tag{2.4}$$

The dynamic equation for N_∞ is obtained by integrating Eq. (2.2) with respect to v over all values of v. A similar approach is performed for the volume fraction except that Eq. (2.2) is multiplied by v before integration. Since most multi-component combustion formulations of the compressible gas equations are designed to conserve mass, it is desirable to formulate the dynamic equation for N_∞ and ϕ in terms of the number of soot particles per unit mass, N_s, and soot mass fraction, Y_s, respectively. For a dilute particle phase [204]

$$N_\infty = \rho N_\mathrm{s} \qquad \text{and} \qquad \phi = \frac{\rho}{\rho_\mathrm{s}} Y_\mathrm{s}$$

where ρ is the gas-particle mixture density and ρ_s is the density of the soot particle material. The resulting two transport equations for N_s and Y_s are

$$\frac{\partial}{\partial t}(\rho Y_\mathrm{s}) + \nabla \cdot \left[\rho Y_\mathrm{s}(\vec{v} + \vec{V}_Y)\right] = S_Y \tag{2.5a}$$

$$\frac{\partial}{\partial t}(\rho N_\mathrm{s}) + \nabla \cdot \left[\rho N_\mathrm{s}(\vec{v} + \vec{V}_N)\right] = S_N \tag{2.5b}$$

where $\vec{v}$ is the mixture velocity, $\vec{V}_Y$ and $\vec{V}_N$ are soot diffusion velocities which include contributions from both thermophoresis and Brownian motion. The variables S_Y and S_N are the source terms for Y_s and N_s, respectively, due to nucleation, growth, oxidation, and coagulation. They are defined in the section to follow.

One of the major shortcomings of this formulation is the assumption of instantaneous coalescence and

its effect on particle surface area. Soot particle growth and oxidation rates are highly dependant upon the availability of reactive surface sites and the particle surface area [24, 152]. As a consequence, the correct treatment of soot particle agglomeration is necessary to accurately predict the chemical interactions between the gas and soot [52]. When two particles collide and stick together, they form some type of agglomerate structure. At one extreme, they coalesce instantaneously to form a new spherical particle. At the other extreme, which is called perfect agglomeration, particles are essentially rigid spheres that collide and attach at the point of contact between the two. The main difference is that surface area is conserved during perfect agglomeration while it is destroyed when two particles coalesce. Actual agglomerates formed in sooting flames lie somewhere in between these two limiting cases [205].

2.2.1.1 Brownian Motion

Aerosol transport processes take place at both small and large scales. The particle-scale (small) processes involve the transfer of mass, momentum, and heat between the particle and surrounding fluid. Processes such as the movement of particle clouds under the influence of temperature or concentration gradients occur at the larger scales. These two scales are strongly coupled since particle flux is proportional to the product of a large-scale gradient and a coefficient depending on particle-scale (small-scale) transport processes.

Analysis of particle-scale transport is simplified in two limiting regimes which are determined by the particle Knudsen number, Kn. The Knudsen number is defined as $\mathrm{Kn} = 2\lambda/d_\mathrm{p}$ where λ is the mean-free-path of the gas molecules and d_p is particle diameter. When particles are large compared to the mean-free-path of the gas, $\mathrm{Kn} \ll 1$, transport processes from the gas to the particle surface are well described by the equations of fluid mechanics for continuous media. This limit is referred to as the continuum limit. The other limit, called the free-molecular limit, occurs when the particles are small and $\mathrm{Kn} \gg 1$. Here the presence of the particle does not affect the motion of the molecules near the particle surface and kinetic theory applies. For all intermediate Knudsen numbers between the two limits, semi-empirical interpolation formulas are typically applied [132].

When small particles suspended in a fluid are subjected to concentration gradients, diffusion or Brownian motion drives them from regions of high to low concentrations. These particles exhibit a random motion caused by fluctuating forces that are exerted on them by the surrounding molecules. The resulting diffusive flux of particles is given by [132]

$$J_x = -D\frac{\partial n}{\partial x} \tag{2.6}$$

where D is the diffusion coefficient and J_x is in units of particles/m^2/s. In multiple dimensions, the rate of change of the PSD due solely to diffusion is

$$\frac{\partial n}{\partial t} = -\nabla \cdot \vec{J} = \nabla \cdot (D\nabla n) \tag{2.7}$$

An expression for the diffusion coefficient based on the size of the particle and local gas properties can be derived from the one-dimensional form of Eq. (2.7). Small particles share the molecular-thermal motion of the fluid and therefore Brownian motion is directly related to the motion of gas molecules. Assuming

that the principle of equipartition of energy applies to the translational energy of the particles, the diffusion coefficient is obtained from Eq. (2.7) as

$$D = \frac{k_B T}{f} \tag{2.8}$$

where $k_B = 1.38 \times 10^{-23}\ \mathrm{m^2\,kg\,s^{-2}\,K^{-1}}$ is the Boltzmann constant and f is the friction coefficient. Based on Stokes law for a rigid sphere moving through a fluid at a Reynolds number less than unity, the friction coefficient f is equal to [132]

$$f = 3\pi\mu d_p \tag{2.9}$$

where μ is the viscosity of the surrounding fluid. Equation (2.9) is only valid in the continuum regime when $\mathrm{Kn} \ll 1$ and begins to overpredict particle drag as particle size becomes much smaller than the mean-free-path of the gas. In the free-molecular regime ($\mathrm{Kn} \gg 1$), f can be derived from kinetic theory as [132]

$$f = \frac{2}{3} d_p^2 \rho \left(\frac{2\pi k_B T}{M}\right)^{1/2} \left[1 + \frac{\pi\alpha}{8}\right] \tag{2.10}$$

where M is the molecular mass for the gas molecules, and α is an accommodation coefficient. The accommodation coefficient represents the fraction of the gas molecules leaving the particle surface in equilibrium with the surface. The remaining fraction of molecules are specularly reflected. A value of 0.9 is generally used for the momentum transfer accommodation coefficient [132]. The main difference between Eq. (2.9) and Eq. (2.10) is that $f \propto d_p^2$ in the free-molecular regime and $f \propto d_p$ in the continuum. An interpolation formula in the form of a correction factor applied to Stokes-law is typically used to cover the entire Kn range [132]. It has the following form:

$$f = \frac{3\pi\mu d}{C} \tag{2.11}$$

where C is the slip correction factor defined by

$$C = 1 + \mathrm{Kn}\left[A_1 + A_2 \exp\left(-\frac{2A_3}{\mathrm{Kn}}\right)\right] \tag{2.12}$$

The constants $A_1 = 1.257$, $A_2 = 0.400$, and $A_3 = 0.55$ were determined based on experimental data by Davies [206]. Li and Wang [207, 208] performed a more rigorous derivation for free-molecular drag on a spherical particle and extended it over the entire range of Knudsen numbers. However, issues related to numerical stability were encountered when this advanced formulation was tested in multi-dimensional flame calculations as part of this thesis.

Preliminary calculations were performed to estimate typical values of Kn that occur over the lifetime of a particle in laminar diffusion flames. These predictions for Kn were carried out by approximating the hot combustion gases as N_2 at 2000 K and assuming that particles vary in size from 1 to 100 nm. This representative size range was chosen as soot particles are typically a few nanometers in diameter upon inception and grow into large agglomerates consisting of primary particles with diameters up to 50 nm [29, 209–211]. The effects of pressure and diameter on Knudsen number are provided in Table 2.1. Knudsen numbers at atmospheric pressure are well above unity for small young soot particles and approach the

Table 2.1: Effect of pressure and diameter on the Knudsen number of a spherical particle suspended in N_2 at 2000 K.

Pressure (atm)	Diameter (nm)		
	1	40	100
1	117	2.92	1.17
100	1.17	0.03	0.01

transition regime (Kn $\approx$ 1) with increasing diameter. Particle Knudsen numbers are much lower at elevated pressures, beginning at approximately unity for young particles and decreasing well into the continuum regime as particles grow. These estimates indicate that formulations for soot particle diffusion coefficients must remain valid over the entire range of Kn.

Most researchers modelling soot formation in multi-dimensional laminar flames either neglect Brownian motion [22, 65, 70] or include it under the assumption that particles remain in the free-molecular regime [18, 50, 127, 146]. Kennedy et al. [167] neglected Brownian motion but included an artificially small soot diffusivity to help smooth out numerical oscillations. More recently, Zhang et al. [19, 71] included the effects of Brownian motion over the entire Knudsen number regime in their detailed sectional model using the interpolation formula proposed by Sorensen and Wang [212]. Brownian motion was neglected in this work because of numerical issues encountered resulting from the fact that $D \propto d_{\mathrm{p}}^{n}$ where $n < 0$ ($n = -1$ in the continuum and $n = -2$ in the free-molecular regime). Rather, the same approach as Kennedy et al. was employed; a small Fickian diffusive flux was included in the soot particle transport equations. This was required to enhance numerical stability even though the transport of soot via Brownian motion is generally negligible. The resulting diffusion velocities for soot are

$$\vec{V}_Y = -\frac{D_{\mathrm{s}}}{Y_{\mathrm{s}}}\nabla Y_{\mathrm{s}} + \vec{V}_{\mathrm{T}} \tag{2.13}$$

$$\vec{V}_N = -\frac{D_{\mathrm{s}}}{N_{\mathrm{s}}}\nabla N_{\mathrm{s}} + \vec{V}_{\mathrm{T}} \tag{2.14}$$

where $D_{\mathrm{s}} = 10^{-8}$ m^2/s is the soot diffusion coefficient. The thermophoretic velocity of soot, $\vec{V}_{\mathrm{T}}$, appearing in the two expressions above, is defined in the next section.

2.2.1.2 Thermophoresis

Temperature gradients can also induce the motion of small particles and drive them from regions of high to low temperature. This phenomenon is called thermophoresis and is closely related to the thermal diffusion processes in multi-component gases. Subjected to a temperature gradient, particles much smaller than the mean-free-path (Kn $\gg$ 1) are bombarded by high-energy molecules on the hot side which induces a velocity that can be computed using gas kinetic theory as [213]

$$\vec{V}_{\mathrm{T}} = -\frac{3}{4(1+\pi\alpha/8)}\frac{\mu}{\rho T}\nabla T \tag{2.15}$$

where the thermal accommodation coefficient, α, which represents the fraction of heat transferred between the particle surface and the colliding molecules, is usually about 0.9 [132, 146]. Thus, Eq. (2.15) can be approximated by

$$\vec{V}_{\mathrm{T}} \approx -0.55 \frac{\mu}{\rho T} \nabla T \tag{2.16}$$

When particles subjected to temperature gradients are much larger than the mean-free-path ($Kn \ll 1$), Eqs. (2.15) and (2.16) no longer apply [214]. Brock [215] derived an expression for the resulting thermophoretic velocity in the limit that $Kn \ll 1$ based on the continuum equations for fluid mechanics with slip-corrected boundary conditions. It is derived by equating the drag force to the thermophoretic force and equal to

$$\vec{V}_{\mathrm{T}} = -\frac{2C_s\left(\frac{k_{\mathrm{g}}}{k_{\mathrm{p}}} + C_t \mathrm{Kn}\right)}{(1 + 2C_m \mathrm{Kn})\left(1 + 2\frac{k_{\mathrm{g}}}{k_{\mathrm{p}}} + 2C_t \mathrm{Kn}\right)} \frac{\mu}{\rho T} \nabla T \tag{2.17}$$

where C_s, C_t, and C_m are dimensionless constants related to kinetic theory, k_{g} and k_{p} are the gas and particle thermal conductivities. Since this relation is only valid in the continuum regime, Talbot et al. [216] proposed a fitting formula valid for all Kn that approaches Eq. (2.15) in the free molecular limit and Eq. (2.17) in the continuum limit. It is given by

$$\vec{V}_{\mathrm{T}} = -\frac{2C_s\left(\frac{k_{\mathrm{g}}}{k_p} + C_t \mathrm{Kn}\right)C}{(1 + 3C_m \mathrm{Kn})\left(1 + 2\frac{k_g}{k_p} + 2C_t \mathrm{Kn}\right)} \frac{\mu}{\rho T} \nabla T \tag{2.18}$$

where C is defined in Eq. (2.12). Suggested values for the constants are $C_s = 1.17$, $C_t = 2.18$, and $C_m = 1.14$ for perfectly diffuse reflection and complete thermal accommodation. Li and Wang [217] also proposed an expression for the thermophoretic velocity, but it is only valid for particles in the free-molecular limit.

Multi-dimensional soot models for laminar flames generally compute soot particle thermophoretic velocities based on Eq. (2.15) or (2.16) [18, 19, 22, 50, 70, 71, 127, 146]. However, preliminary calculations using Eq. (2.18) revealed numerical stability and convergence issues similar to those discussed in Section 2.2.1.1. These issues are attributed to the inverse dependence of $\vec{V}_{\mathrm{T}}$ on d_{p}. For these reasons, the free-molecular thermophoretic velocity defined by Eq. (2.16) was used for all of the flames considered herein.

2.2.2 Soot Chemistry

Soot formation and destruction was modelled using the simplified soot kinetics described by Liu et al. [22, 60]. This model is based on the reduced soot mechanisms of Leung et al. [96] and Fairweather et al. [97] which describe the evolution of soot through four basic steps — nucleation, surface growth, coagulation, and oxidation. Acetylene is assumed to be the only precursor responsible for the presence of soot. The

resulting mechanism is

$$C_2H_2 \longrightarrow 2\,C(s) + H_2 \tag{R2.1}$$

$$C_2H_2 + n{\cdot}C(s) \longrightarrow (n+2)\,{\cdot}C(s) + H_2 \tag{R2.2}$$

$$C(s) + \tfrac{1}{2}O_2 \longrightarrow CO \tag{R2.3}$$

$$C(s) + OH \longrightarrow CO + H \tag{R2.4}$$

$$C(s) + O \longrightarrow CO \tag{R2.5}$$

$$n{\cdot}C(s) \longrightarrow C_n(s) \tag{R2.6}$$

It follows from the mechanism above that the source term in Eq. (2.5a) can be written as

$$S_Y = 2M_s(R_1 + R_2) - (R_3 + R_4 + R_5)A_s \tag{2.19}$$

where M_s is the molar mass of soot (assumed equal to the molar mass of carbon, 12 kmol/kg) and A_s is the surface area of soot per unit volume of aerosol. The terms R_3, R_4, and R_5 are the soot oxidation rates for reactions involving O_2, OH, and O, respectively. The terms R_1 and R_2 are the soot nucleation and surface growth rates defined by

$$R_1 = k_1[C_2H_2] \tag{2.20}$$

$$R_2 = k_2 f(A_s)[C_2H_2] \tag{2.21}$$

The function $f(A_s)$ incorporates the dependence of soot surface growth on the soot surface area per unit volume, A_s. Proposed forms of $f(A_s)$ include: $f(A_s) = A_s^{0.5}$ [96] and $f(A_s) = A_s$ [97]. Here we have used the first relationship. The corresponding rate constants k_1 and k_2 are given by [60]

$$k_1 = 1000\exp(-16\,103/T) \tag{2.22}$$

$$k_2 = 1750\exp(-10\,064/T) \tag{2.23}$$

Surface area is related to the soot mass and number density by

$$A_s = \pi\left(\frac{6}{\pi}\frac{1}{\rho_s}\frac{Y_s}{N_s}\right)^{2/3}(\rho N_s) \tag{2.24}$$

where ρ_s is the density of soot, taken to be 1900 kg/m^3. The oxidation reaction rates per unit surface area are modelled by [22]

$$R_3 = 120\left\{\frac{k_a p_{O_2}\chi}{1+k_z p_{O_2}} + k_b p_{O_2}(1-\chi)\right\} \tag{2.25}$$

$$R_4 = \varphi_{OH} k_4 T^{-1/2} p_{OH} \tag{2.26}$$

$$R_5 = \varphi_O k_5 T^{-1/2} p_O \tag{2.27}$$

where

$$\chi = \left\{1 + \frac{k_T}{k_b p_{O_2}}\right\}^{-1} \tag{2.28}$$

The symbols p_{O_2}, p_{OH}, and p_O denote the partial pressures of O_2, OH and O in atm, respectively. The collision efficiencies for OH, φ_{OH}, and O, φ_O, were both assumed equal to 0.2. The rate of soot oxidation by O_2 was based on the Nagle-Strickland-Constable model [198] with the rate constants k_a, k_b, k_z, k_T, and k_4 taken from Moss et al. [218]. The rate constant k_5 was taken to be equal to the value used by Bradley et al. [219].

The source term in Eq. (2.5b) represents the production and destruction of the soot particle number density with nucleation and agglomeration. It is modelled herein as follows:

$$S_N = \frac{2}{C_{min}} N_A R_1 - 2C_a \left(\frac{6M_s}{\pi\rho_s}\right)^{1/6} \left(\frac{6k_B T}{\rho_s}\right) [C(s)]^{1/6} (\rho N_s)^{11/6} \tag{2.29}$$

where N_A is Avogadro's number (6.022×10^{26} kmol^{-1}), C_{min} is the number of carbon atoms in the incipient soot particle, C_a is the agglomeration rate constant, and $[C(s)] = \rho Y_s / M_s$ is the molar concentration of soot. Leung et al. [96] set the number of carbon atoms to 100 which corresponds to a particle size of 1.24 nm. The authors suggested that the results are not strongly dependant on the initial size provided that nucleated particle sizes are between 1 to 10 nm. A minimum size of 6 nm ($C_{min} = 9 \times 10^4$) was used by Fairweather et al. [97] while Liu et al. [60] specified a particle size of 2.4 nm ($C_{min} = 700$). Values for C_a of 3 [24, 97] and 9 [96, 155] have been used.

Based on the recommendations of Liu et al. [22, 60], coalescence was neglected by setting C_a to zero. In fact, Ezekoye and Zhang [24] achieved better agreement with experimental measurements for surface area when coalescence was neglected. The minimum number of incipient carbon atoms was taken to be $C_{min} = 700$.

2.2.2.1 Numerical Stability

Several issues related to numerical stability and convergence were encountered using the previously described soot model. First, both S_Y and S_N are functions of Y_s and N_s raised to sub-unity powers. For example,

$$S_Y \propto Y_s^{1/3} N_s^{1/6} \quad \text{and} \quad S_N \propto Y_s^{1/6} \tag{2.30}$$

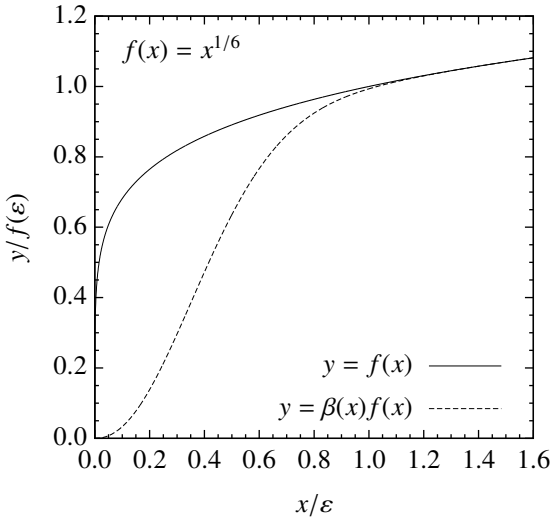

Figure 2.1: Blending function applied to soot source terms.

As a result, derivatives of S_Y and S_N with respect to Y_s or N_s become infinite as $Y_s \to 0$ or $N_s \to 0$. Additionally, oscillations in Y_s or N_s caused by round-off and numerical diffusion errors can produce large fluctuations in the source terms when Y_s and N_s are small. Both of these issues caused the Newton-Krylov time-marching algorithm employed in this work to solve the governing PDEs to stall (see Section 5.1.6 for a complete description of the proposed numerical solution algorithm). To overcome this stall, A_s was modified by applying a blending function to eliminate any on/off switching experienced by S_Y and smooth its derivative with respect to Y_s and N_s. The modified surface area is given by

$$A_s^* = \beta(Y_s)\beta(N_s)A_s \tag{2.31}$$

where the blending function, $\beta(x)$, is defined as

$$\beta(x) = 1.0 - \exp\left[-5\left(\frac{x}{\varepsilon}\right)^2\right] \tag{2.32}$$

with $\varepsilon = 10^{-6}$. The modification was applied by replacing A_s with A_s^* in Eqs. (2.19) and (2.21).

The effect of the blending function is illustrated in Fig. 2.1. Applied to a function $f(x) = x^{1/6}$ representing the relationship between S_Y and Y_s, $\beta(x)$ activates for $x < \varepsilon$ and ensures that $\frac{\partial f}{\partial x}|_{x=0}$ remains finite. The net result is a system of governing equations that are much easier to solve numerically without any spurious oscillations in the resulting solutions.

Chapter 3

MATHEMATICAL MODELLING OF REACTING GASES

Describing the physical processes that govern reacting gaseous flows is a challenging task complicated by interactions between chemistry and fluid transport processes. Hydrocarbons undergo thousands of reactions during combustion that generate intermediate molecules or radicals in times as short as several milliseconds. Soot particle formation occurs on a similar timescale [220] with the inception process lasting a few milliseconds [221]. In contrast, transport processes such as convection and molecular diffusion occur at a much slower rate. Laminar diffusion flames are therefore considered a specific class of combusting flows with a wide range of temporal and spacial scales. This disparity between scales poses significant challenges to the design of efficient computational fluid dynamics (CFD) solvers because stability characteristics are governed by the fastest moving timescales while convergence characteristics are governed by the slowest ones.

Laminar reacting flows are generally described mathematically using the conservation equations for compressible, thermally-perfect, gaseous mixtures and the ideal gas equation of state (EOS) [222]. Many have modified these equations to deal with two-phase flows in sooting flames by adding transport equations for quantities related to soot and modifying the EOS [50, 53, 60, 65, 70, 223]. Such an approach works well at atmospheric pressure, but fails at elevated pressures near the critical point where deviations from the ideal gas law and non-equilibrium effects are large. As a result, many of the simplifying assumptions commonly employed are invalid at elevated pressures and researchers are required to use more realistic and costly models. For instance, including real gas effects with a cubic EOS and corresponding thermodynamic functions for enthalpy, heat capacity, and sound speed adds significant iteration and solution time [224]. Sophisticated models such as these are generally restricted to simple problems since current computational resources are not sufficient to simultaneously model real gas effects, soot formation, complex chemistry, and radiation transport in multi-dimensional laminar flames. For this reason, the more standard modelling techniques that can only be applied to flames under atmospheric conditions are applied herein. Nonetheless, it is very instructive to review the implications of using these standard models for treating flames at high pressures.

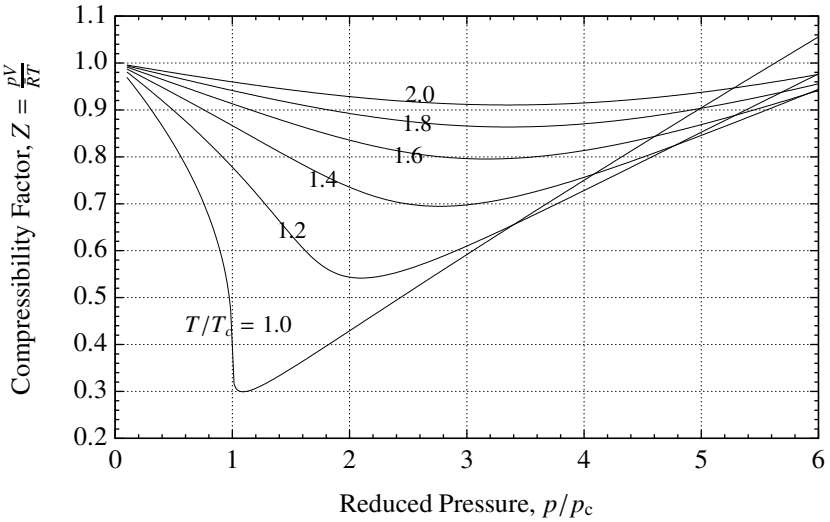

Figure 3.1: Generalized compressibility chart computed using the Van der Waals equation of state.

This chapter first provides a brief overview of modelling laminar flames and the challenges that are faced at elevated pressures. This overview is proceeded by a detailed description of the governing equations used to characterize the reacting, sooting flow. The techniques used to model radiation heat transfer and the numerical algorithm used to solve the overall system are discussed in Chapters 4 and 5.

3.1 Background

3.1.1 Real-Gas Effects

Most practical combustion devices such as diesel engines or gas turbines operate at pressures well in excess of atmospheric conditions. Gas turbines combustors operate anywhere from several to 40 atm while pressures inside diesel engines can exceed 100 atm. At these pressures, the use of the ideal gas law is questionable [225].

Most gases of practical interest can be treated as ideal gases with little or no error at low pressures and high temperatures. However, deviations from ideal gas behavior occur at or near the critical point where pressures are high and temperatures relatively low. These deviations result from the fact that as gases become more dense, molecules move closer together and become more tightly packed. Repulsive Van der Waals forces become larger as molecules move closer together and the volume occupied by the molecules themselves becomes significant. Increasing pressure further cannot move molecules any closer together and, as a result, the volume occupied by the gas becomes larger than if it were an ideal gas.

Deviations from ideal gas behavior are measured by the compressibility factor, Z, which is the ratio of the actual volume per unit mole gas to that for an ideal gas. It is defined as

$$Z = \frac{pV}{\bar{R}T} \tag{3.1}$$

where V is the molar volume of the gas and $\bar{R} = 8.314\ \mathrm{kJ\,kmol^{-1}\,K^{-1}}$ is the perfect gas constant. This factor is unity for an ideal gas. The effects of temperature and pressure on Z are illustrated in Fig. 3.1 using the

Table 3.1: Critical temperatures and pressures of several gases [226].

Species	Temperature (K)	Pressure (MPa)
Air	132.5	3.77
N_2	126.2	3.39
O_2	154.6	5.04
CO	132.9	3.50
CO_2	304.1	7.38
H_2	33.2	1.30
H_2O	647.3	22.12
CH_4	190.4	4.60
C_2H_2	308.3	6.14
C_2H_4	282.4	5.04

Van der Waals EOS to compute Z for a given reduced temperature, T/T_c, and pressure, p/p_c. The variables T_c and p_c correspond to the temperature and pressure at the critical point, respectively. As shown in the figure, non-ideal gas effects are the most significant at the critical point where the gas and liquid phases can not coexist in equilibrium. Above the critical point, fluids exhibit characteristics of both gases and liquids such as liquid-like densities and gas-like properties [226].

The critical temperature and pressure of several gases relevant to hydrocarbon combustion are tabulated in Table 3.1. Many of these gases have critical pressures between 20 to 60 atm, which is within the operating range of most practical combustion devices. For example, consider methane at 60 atm and 300 K. This state corresponds to a compressibility factor of approximately 0.88. At the same conditions, ethylene has a compressibility factor of 0.5 while N_2 and O_2 are both roughly 0.95. The compressibility of all these gases quickly approaches unity as temperatures are increased. As such, errors related to the ideal gas law are expected to be larger in the cold fuel stream, especially for high-pressure ethylene flames.

Reid et al. [226] provide a large compilation of the different methods for modelling non-ideal equations of state. Common methods usually make use of multi-parameter correlations based on functions of T_c, p_c, and some other parameter [227, 228]. Popular forms of cubic EOSs include those of Redlich and Kwong [229], Soave [230], and Peng and Robinson [231]. Higher-order virial expansions also exist, e.g. see Lee and Kesler [227].

Despite the large errors encountered when applying ideal gas models at high pressures, more accurate real gas models are too computationally demanding for large problems. Such models make use of complicated relations between pressure, temperature and volume that generally require iterative methods to solve. They are accompanied by complex relations for thermodynamic quantities such as enthalpy, heat capacity, and acoustic speed which correspond to the specific EOS. These thermodynamic relations are generally formulated in terms of departure functions that estimate the deviation from ideal gas behavior. As a result of the added complexities, including real gas effects with a more detailed EOS is generally limited to simplified systems. Example applications include binary and tertiary mixing layers [225, 232–234], zero-dimensional reactors [235], and one-dimensional counter-flow diffusion flames [236–238]. Some of the more relevant

results include those of Sohn et al. [236] and Ribert et al. [238] who both studied high-pressure counter-flow diffusion flames using a numerical approach. Sohn et al. found that real-gas effects significantly affected the flame structure and extinction characteristics of these types of flames. Ribert et al. reported large variations in the compressibility factor across the flame and also observed large changes in thermodynamic and transport properties. The resultant influence on the flame properties was less dramatic, however, since the fluid behaviour approximates that of an ideal gas in the high temperature flame region.

3.1.2 Heat and Mass Flux

The Navier-Stokes equations extend the Euler equations by allowing small deviations from local thermodynamic equilibrium (LTE) through the viscous and heat conduction terms. These deviations include the flux of heat resulting from temperature gradients, called Fourier conduction, and the flux of mass resulting from concentration gradients, known as Fickian diffusion. There are also other non-equilibrium or irreversible effects which can become important as pressure increases such as the Soret and the Dufour effects [239]. The Soret effect, also called thermal diffusion, is molecular transport induced by a temperature or pressure gradient while the Dufour effect is the flux of energy produced by concentration or pressure gradients. The two are generally referred to as "cross-diffusion" effects and there is significant evidence that they can be important at both atmospheric pressures [65, 240–243] and high pressures [225, 233, 237, 238, 244]. In some cases the effects of cross-diffusion were found to increase with pressure [237, 245]. Bellan [246] demonstrated that Soret mass diffusion becomes more prominent as pressure is increased while Fickian mass diffusion is greatly reduced. Dufour effects were generally found to be minor [238, 240, 241] while Soret diffusion was particularly important when large differences in molecular masses existed [65, 225, 244]. This forms the basis for a commonly applied simplifying assumption that Dufour effects are negligible and that Soret effects can also be neglected unless there are species with largely differing molecular weights [242]. Typically, only the Soret transport for light species such as H and H_2 in H_2-air flames are modelled. Rosner et al. [242] argued that Soret transport is also important for heavy fuel vapor species and heavy intermediates such as soot precursors and PAHs. In more recent studies, Soret diffusion was shown to significantly affect soot production in diffusion flames through its impact on the pyrolysis zone [18, 65, 247].

Soot predictions in diffusion flames do not appear to be significantly affected by the choice of molecular diffusion model, i.e., mixture-averaged versus full multi-component [18]. However, the chosen molecular diffusion model can have a large influence on numerical results in some cases [248].

3.1.3 Chemistry

Hydrocarbon oxidation is a highly nonlinear process that depends strongly on pressure. As a result, pressure has a significant influence on key chemistry-related combustion phenomena such as flame propagation rate, extinction and flammability limits, flame front instabilities, and the formation of pollutants [236, 249–253]. This influence of pressure on chemistry manifests through the dependence of the reaction rates on density and, as a result, pressure variations alter the reaction orders (the pressure exponents of Arrhenius reactions) and reaction rates. The two main phenomena that play a prominent role in this pressure-chemistry dependence are the fall-off behavior and chain mechanisms [253]. Fall-off behavior refers to the strong asymptotic

pressure dependency that uni-molecular or recombination reactions display due to the involvement of a collision partner molecule [254, 255]. Chain mechanisms are altered by pressure through the change in emphasis on key rate controlling steps. For example, increasing pressure increases radical concentrations, which subsequently increases the rates of their involved reactions. Kinetic models for hydrocarbon combustion must therefore incorporate all of these complex effects of pressure and provide reliable predictions over a wide range of operating conditions.

Full mechanisms that describe all elementary reactions and intermediates do not exist even for simple systems such as hydrogen and methane fuels. Nonetheless, there has been a large amount of work on methane and natural gas combustion which has led to popular mechanisms such as GRI-Mech [256–258]. The latest version, GRI-Mech 3.0, consists of 325 reactions and 53 species. It was validated against experimental measurements for induction time and flame speed, as well as time- and space-resolved concentration profiles for several important species. The mechanism is optimized for a range of parameters including temperatures from 1000 to 2500 K, pressures from 10 torr to 10 atm, and equivalence ratios between 0.1 to 5. Tan et al. [259, 260] have also proposed a detailed mechanism for natural gas based on experimental data collected in a jet-stirred reactor. It was validated against measurements for temperature, ignition delay and species concentrations over a wide range of residence times and operating conditions (1–10 atm, equivalence ratios between 0.1–1.5, and 800–1400 K). This mechanism has been expanded over the years to include 99 species and 743 reversible reactions [261, 262].

There have been many modifications made over the years to improve GRI-Mech and extend its valid range. For example, Petersen et al. [263] made several improvements to GRI-Mech 1.2 in order to model shock tube ignition delay times for CH_4/O_2 mixtures at elevated pressures between 40 to 260 atm. Further modifications to the work of Petersen et al. were made by Huang et al. [264–266] to improve predictions of ignition delay in various enriched methane-air mixtures. Zhukov et al. [267] found that GRI-Mech 3.0 adequately predicted ignition delay times all the way up to 500 atm yet produced noticeable discrepancies at low temperatures. The recommendations that were put forth in this particular study were later incorporated in a new model for the oxidation of alkanes from methane to n-heptane at high pressures [268]. The new model provided improved predictions for the ignition delay times in methane-air mixtures over a wide range of operating conditions. Despite these advances, none of the studies previously discussed incorporate real gas effects in their numerical analysis and none of these mechanisms for methane are validated up to 60 atm against detailed data for quantities such as species concentration or flame temperature.

There is also considerable interest in ethylene oxidation kinetics due to its importance in the oxidation of higher hydrocarbons [269]. Ethylene is highly reactive, found in significant concentrations in some practical fuels, and an important product of pyrolysis for many liquid fuels [270]. A large number of mechanisms for ethylene oxidation are available in the literature [270–276] although none are validated at the high pressures encountered in practical combustion devices (i.e., 40 atm and above). Simple ethylene kinetics are included in GRI-Mech 3.0 but the mechanism was shown to greatly over-predict laminar flame speeds at atmospheric pressures [277]. Of the available mechanisms for ethylene combustion, some of the more recent works specifically address high pressure combustion. For example, the mechanism of Varatharajan and Williams

[270] was based on a review of available experimental data for laminar flame speeds and ignition data. While they could only validate their mechanism for temperatures between 1000 to 2500 K and pressures of 0.5 to 10 bar, fall-off reactions were added to hypothetically provide reasonable results up to 100 bar. Recent experimental/numerical studies of ignition delay in different ethylene/O_2/N_2/Ar mixtures at pressures from 15 to 50 bar [278] and 5.9 to 16.5 atm [279] illustrate the inability of current detailed mechanisms to capture high pressure ethylene kinetics.

3.2 Mathematical Description

The preceding review has highlighted key issues in the mathematical modelling of high-pressure combustion. The remainder of this chapter presents the mathematical model used to describe the reacting flow and its integration with the soot model described in Chapter 2. The EOS, viscous transport models, fluid properties, and finite-rate chemical kinetics are also presented.

3.2.1 Governing Equations

Gaseous combusting flow is described herein mathematically using the conservation equations for continuous, multi-component, compressible, thermally-perfect, gaseous mixtures [222]. The equations consist of the conservation of total mass, individual species mass, momentum, and energy. In addition, modelling soot formation and destruction in gaseous mixtures requires tracking a solid phase and capturing the interactions that occur between phases. Interactions between the particle and gas phases — some of which where already discussed in Chapter 2 — can include mass transfer, momentum transfer via drag, and heat transfer via particle heating. Particles also interact with each other through collisional processes such as coagulation and agglomeration.

Particle transport in this work is treated using an Eulerian formulation assuming that the particle phase is dilute (see Section 2.2.1) and volume affects are negligible [204]. As a result, the particle phase may be formulated as an additional gas species, which is valid since peak soot volume fractions are not expected to exceed about 100 ppm for the flames of interest. Furthermore, soot particles generally follow the streamlines [30] and do not deviate significantly from the gas temperature [280]. Non-equilibrium momentum and heat transfer between the solid and gas phases may therefore be neglected since their associated relaxation times are small in comparison to the fluid time-scales. This means that the velocities and temperatures of the two phases can be taken to be equal. With the above assumptions, conservation equations for particle momentum and energy are no longer required; only the change in particle size distribution must be tracked using Eqs. (2.5a) and (2.5b). This modelling approach for the soot transport is the same as those taken by Leung et al. [96] and Fairweather et al. [97].

Assuming Newtonian flow, the conservation of global mass, momentum, energy, individual species

mass, soot mass, and particle number can be summarized as

$$\frac{\partial \rho}{\partial t} + \nabla \cdot (\rho \vec{v}) = 0 \tag{3.2a}$$

$$\frac{\partial}{\partial t}(\rho \vec{v}) + \nabla \cdot (\rho \vec{v}\vec{v} + p\vec{\mathbf{I}}) = \nabla \cdot \vec{\boldsymbol{\tau}} + \rho \vec{g} \tag{3.2b}$$

$$\frac{\partial}{\partial t}(\rho e) + \nabla \cdot \left[\rho \vec{v}\left(e + \frac{p}{\rho}\right)\right] = \nabla \cdot (\vec{v} \cdot \vec{\boldsymbol{\tau}}) - \nabla \cdot \vec{q} + \rho \vec{g} \cdot \vec{v} \tag{3.2c}$$

$$\frac{\partial}{\partial t}(\rho Y_k) + \nabla \cdot \left[\rho Y_k (\vec{v} + \vec{V}_k)\right] = \dot{\omega}_k, \quad k = 1, \ldots, N \tag{3.2d}$$

$$\frac{\partial}{\partial t}(\rho Y_\mathrm{s}) + \nabla \cdot \left[\rho Y_\mathrm{s} (\vec{v} + \vec{V}_Y)\right] = S_Y \tag{3.2e}$$

$$\frac{\partial}{\partial t}(\rho N_\mathrm{s}) + \nabla \cdot \left[\rho N_\mathrm{s} (\vec{v} + \vec{V}_N)\right] = S_N \tag{3.2f}$$

where t is the time, p is the total mixture pressure, e is the total mixture energy, Y_k is the mass fraction of species k, $\vec{V}_k$ is the diffusion velocity of gas species k, $\dot{\omega}_k$ is the time rate of change of the kth species mass, $\vec{\boldsymbol{\tau}}$ is the fluid stress tensor, $\vec{g}$ is the acceleration vector due to gravity, N is the number of gaseous species in the mixture, and $\vec{q}$ is the heat flux vector. The time rate of change of gaseous species includes contributions from both gas-phase chemistry and soot surface reactions. Axisymmetric forms of Eqs. (3.2a)–(3.2f) are provided in Appendix A.

In order to recover global continuity, Eq. (3.2a), from the sum of Eq. (3.2d) over all N species, consistency requires that the following conditions must be satisfied:

$$\sum_{k=1}^{N+1} Y_k = 1 \qquad \sum_{k=1}^{N+1} Y_k \vec{V}_k = \vec{0} \qquad \sum_{k=1}^{N+1} \dot{\omega}_k = 0 \tag{3.3}$$

where the $(N+1)$th species here refers to the solid soot particles. The first property in Eq. (3.3) produces an over-constrained system of equations. This problem is easily eliminated by removing the mass conservation equation for the Nth gaseous species and making Y_N a dependent variable, $Y_N = 1 - \sum_{i \neq N} Y_i$. The second property states that the net momentum associated with species diffusion is zero and the third states that chemical reactions do not create or destroy mass. While the third property is easily enforced, satisfaction of the second requires special attention and is addressed in Section 3.2.3.

3.2.2 Thermodynamics and Equation of State

Despite deviations from ideal behavior that occur when pressures are sufficiently high and temperatures low, the ideal gas model is used in this work. As already discussed in Section 3.1.1, current computational resources are generally not sufficient enough to incorporate real gas effects with detailed chemistry, radiation transport, and soot formation. It is therefore important to estimate the errors introduced by the ideal gas model and many of the other assumptions made in this thesis.

As a first step, the effects of the particles on the thermodynamic properties of the mixture and the validity of the dilute phase approximation are investigated. The relationship between the volume fraction, ϕ, and the

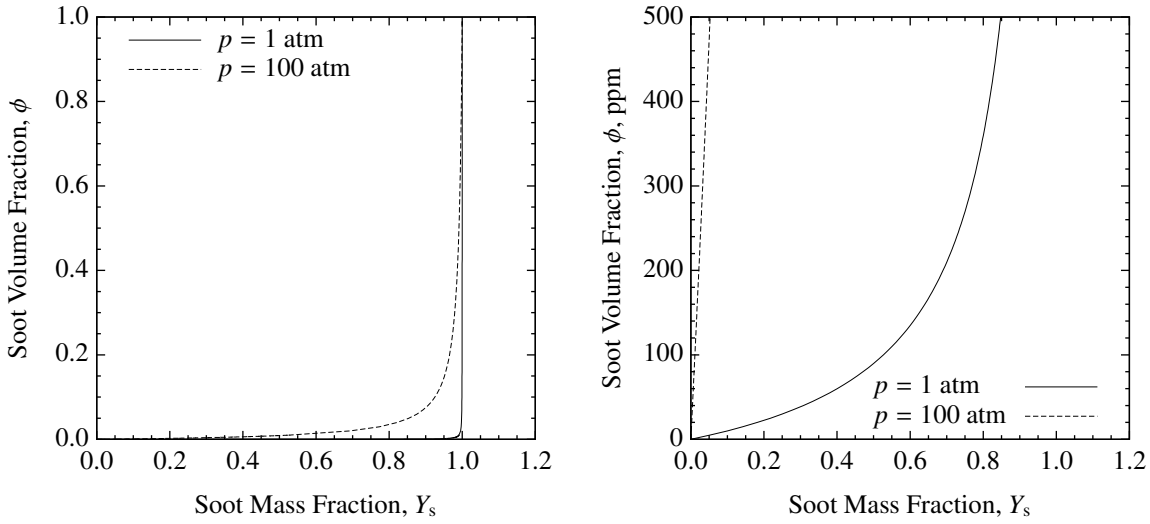

Figure 3.2: Relationship between soot mass fraction and volume fraction.

mass fraction, Y_s, of soot particles is [204]

$$\frac{\phi}{1-\phi} = \frac{Y_s}{1-Y_s}\frac{\rho_g}{\rho_s} \tag{3.4}$$

where ρ_g is the density of the gas. This relationship is plotted in Fig. 3.2 assuming that soot particles are suspended in N_2 at 2000 K and pressures of 1 and 100 atm. The soot volume fraction is relatively small at 1 atm for mass fractions up to 0.8, so one can safely assume that soot occupies a negligible volume compared to the gas at this pressure. However, this assumption becomes less valid as pressure is increased to 100 atm since a mass fraction of only 0.05 corresponds to a relatively large soot volume fraction of 500 ppm. As a result, the dilute phase assumption becomes invalid for highly sooting flames at high pressures. Peak soot volume fractions no larger than several hundred ppm are expected in this work, so a dilute phase approximation is still valid.

Using the dilute particle-phase simplifying assumption, the density of the gas-particle mixture can be related to the gas density by [204]

$$\rho = \frac{\rho_g}{1-Y_s} \tag{3.5}$$

Equation (3.5) is not a complete EOS since it does not relate the mixture density to the mixture pressure.

The EOS is derived by considering the effect of the particles on the pressure. Here, the particles are treated as though they were molecules of an additional gaseous species. If the particles are small enough, their random motion will be significant relative to the other gas molecules and therefore contribute to the overall pressure. Following the analysis outlined by Rudinger [204], the ratio of the partial pressure of the gas, p_g, to the overall pressure of the mixture p is written as

$$\frac{p_g}{p} = \frac{(1-Y_s)/M_g}{Y_s/M_s + (1-Y_s)/M_g} \tag{3.6}$$

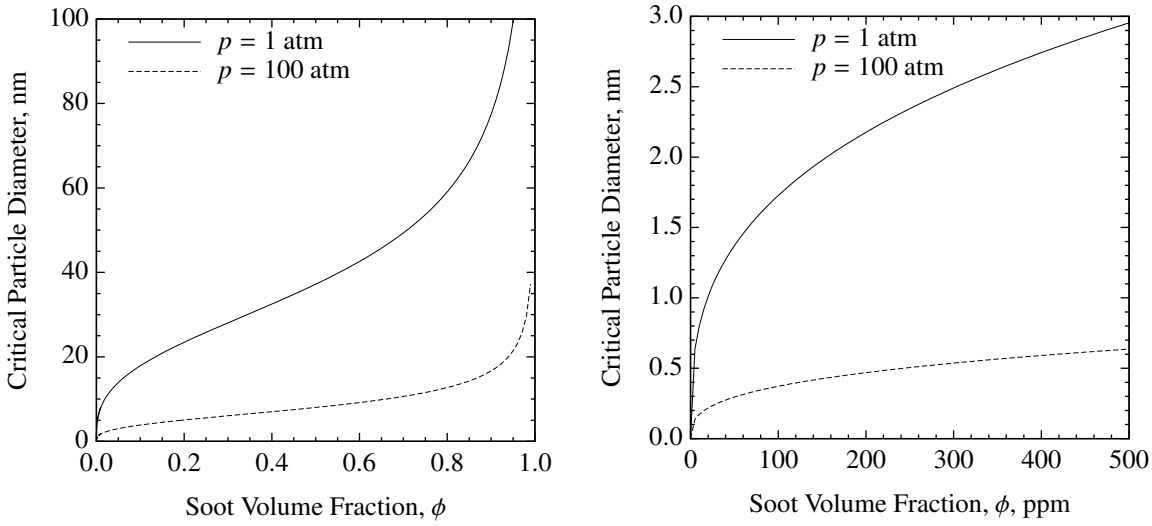

Figure 3.3: Particle diameter below which the particle contribution to the pressure exceeds one percent.

where M_g is the molecular weight of the gas phase. The molecular weight of the fictitious gaseous soot phase is

$$M_s = \frac{1}{6}\pi d_p^3 \rho_s N_A \tag{3.7}$$

Substituting Eq. (3.7) into (3.6) and solving for d_p in the limit that $p_g/p \geq 0.99$, we obtain the minimum particle diameter below which the contribution of the soot particles to the mixture pressure exceeds one percent. The result, plotted in Fig. 3.3, indicates that soot does not contribute to the mixture pressure as long as d_p remains above several nanometers.

Assuming that the random motion associated with the soot particles is negligible, as is done in the present study, the pressure of a gas-soot mixture is given by the gas pressure alone

$$p = \rho_g R_g T \tag{3.8}$$

where R_g is the individual gas constant. While Eq. (3.8) provides the pressure of the mixture, it only relates the pressure to the gas phase and cannot represent the EOS for the mixture. Substituting Eq. (3.5) into (3.8) gives the final mixture EOS as

$$p = \rho(1 - Y_s)R_g T \tag{3.9}$$

where the mixture behaves like a perfect gas with a gas constant $R = (1 - Y_s)R_g$. For a mixture of N perfect gases and soot, Eq. (3.9) can be written as

$$p = \rho \bar{R} T \left(\sum_{k=1}^{N} Y_k / M_k \right), \qquad \rho = \sum_{k=1}^{N} \rho_k \tag{3.10}$$

where $\bar{R} = 8.314$ kiloJ/kmol/K is the perfect gas constant and $\rho_k = \rho Y_k$. The mixture molecular weight, M,

is given by

$$\frac{1}{M} = \sum_{k=1}^{N} \frac{Y_k}{M_k} \tag{3.11}$$

The internal energy and the enthalpy of the mixture is given by the weighted mean of the constituents as

$$e = (1 - Y_\mathrm{s})e_\mathrm{g} + Y_\mathrm{s}e_\mathrm{s} \tag{3.12}$$

$$h = e + p/\rho \tag{3.13}$$

The constant-pressure and constant-volume specific heats of the mixture, c_p and c_v, follow from the simple mixing rule given by

$$c_p = (1 - Y_\mathrm{s})c_{p_\mathrm{g}} + Y_\mathrm{s}c_\mathrm{s} \tag{3.14}$$

$$c_v = (1 - Y_\mathrm{s})c_{v\mathrm{g}} + Y_\mathrm{s}c_\mathrm{s} \tag{3.15}$$

where c_s is the specific heat of the soot particle material, assumed equal to the value for graphite ($c_\mathrm{s} = 715\ \mathrm{J\,kg^{-1}\,K^{-1}}$). The corresponding ratio of specific heats is

$$\Gamma = \gamma \frac{1 + \delta Y_\mathrm{s}/(1 - Y_\mathrm{s})}{1 + \gamma\delta Y_\mathrm{s}/(1 - Y_\mathrm{s})} \tag{3.16}$$

where $\gamma = c_{p_\mathrm{g}}/c_{v\mathrm{g}}$ and $\delta = c_\mathrm{s}/c_{p_\mathrm{g}}$. The change in Γ with ϕ is illustrated in Fig. 3.4. As the particle loading becomes high, Γ approaches unity and the mixture behaves similar to isothermal flow. This behavior occurs because the contribution to the mixture specific heat by the particles increases with particle loading. As such, temperature changes in the gas caused by expansion or compression are compensated by heat transfer from the particles without significantly affecting their temperature. As Fig. 3.4 illustrates, soot has a significant effect on Γ at low pressures which diminishes as pressure is increased. This effect of the soot particles on the mixture specific heat ratio is therefore included in the present research.

Lastly, the effect of the particles on the local sound speed in the mixture is investigated. If the particles remain in equilibrium with the gas at all times, the mixture behaves like a perfect gas with [204]

$$a_\mathrm{e}^2 = \frac{\Gamma RT}{(1 - \phi)^2} = \gamma R_\mathrm{g} T \frac{1 - Y_\mathrm{s}}{(1 - \phi)^2} \frac{1 + \delta Y_\mathrm{s}/(1 - Y_\mathrm{s})}{1 + \gamma\delta Y_\mathrm{s}/(1 - Y_\mathrm{s})} \tag{3.17}$$

where a_e is the equilibrium speed of sound. It assumes that the particle velocity and temperature quickly catch-up to the gas across any disturbances. Following our previous assumption that the particle volume fraction is negligible, Eq. (3.17) becomes

$$a_\mathrm{e}^2 = \gamma R_\mathrm{g} T (1 - Y_\mathrm{s}) \frac{1 + \delta Y_\mathrm{s}/(1 - Y_\mathrm{s})}{1 + \gamma\delta Y_\mathrm{s}/(1 - Y_\mathrm{s})} \tag{3.18}$$

The effect of particle loading on the ratio between the equilibrium sound speed and the gas sound speed a_g is illustrated in Fig. 3.5 for pressures of both 1 and 100 atm. Using the negligible volume fraction assumption,

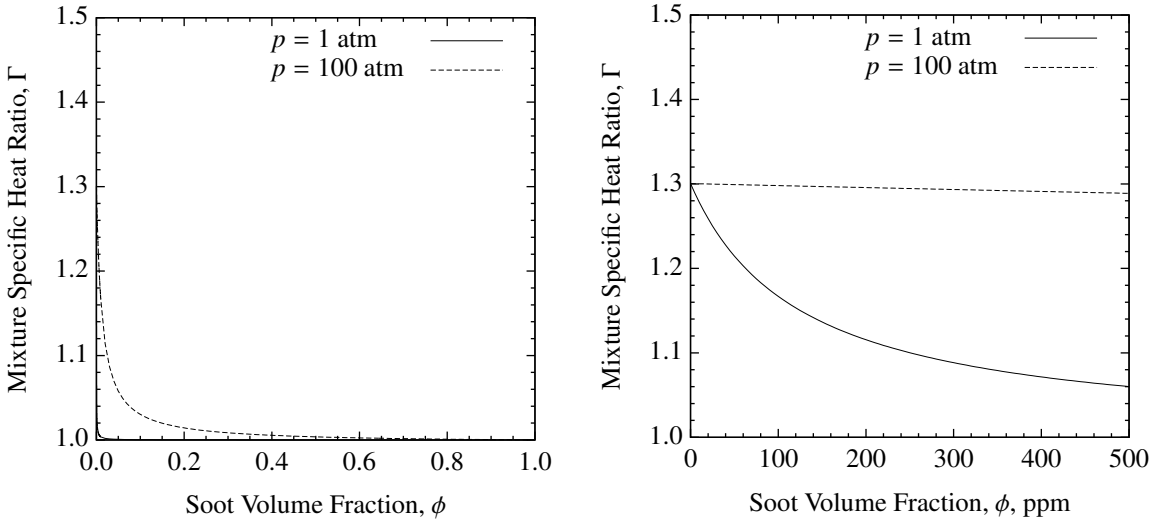

Figure 3.4: Effect of soot particle volume fraction on mixture specific heat ratio.

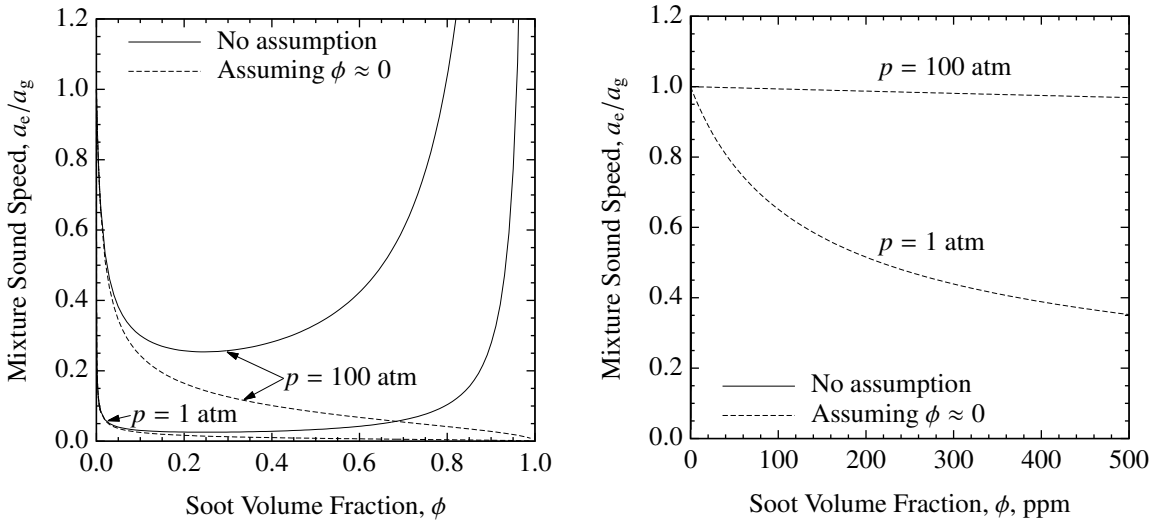

Figure 3.5: Effect of soot volume fraction on the equilibrium sound speed for the gas-particle mixture.

the mixture sound speed rapidly approaches zero as ϕ approaches unity. Volume effects become important as ϕ increases beyond 0.1 and the two curves computed with and without the $\phi = 0$ assumption deviate. This occurs as a result of the increasing volume displaced by the soot particles which causes sound waves to accelerate. The value of a_e computed including volume effects becomes infinite at $\phi = 1$ since the sound speed of the incompressible particle material is effectively infinite. While volume effects are insignificant below 500 ppm, there is a considerable influence of the soot particles on the mixture sound speed, a_e. This influence is strongest at low pressures and weakens as pressure is increased. The speed of sound for the mixture was computed herein using Eq. (3.18).

3.2.3 Heat and Mass Flux

The vector $\vec{q}$ in Eq. (3.2c) accounts for the transport of energy through multiple pathways including Fourier conduction, species inter-diffusion, Soret and Dufour effects, and radiation. Heat flux resulting from species inter-diffusion refers to the net flux of enthalpy carried by the individual species molecules. This occurs when there is a mass flux of component k relative to the bulk mass flux. Soret and Dufour effects have been neglected in this work as their contribution to the overall heat flux is low in most situations [222]. The heat flux vector is therefore defined as

$$\vec{q} = -\kappa \nabla T + \rho \sum_{k=1}^{N+1} h_k Y_k \vec{V}_k - \vec{q}_{\text{rad}} \tag{3.19}$$

where h_k is the absolute enthalpy (chemical and sensible) of species k and $\vec{q}_{\text{rad}}$ is the radiation heat flux.

In general, the determination of individual species diffusion velocities, $\vec{V}_k$, requires the inversion of a $N \times N$ matrix where N is number of gas species [281, 282]. This inversion is costly when using detailed mechanisms with hundreds of species, so simplifying assumptions such as constant Schmidt or Lewis number are usually made to reduce the cost of evaluating $\vec{V}_k$. A more accurate treatment is the use of mixture-averaged diffusion coefficients [283]. This is essentially a first-order approximation to $\vec{V}_k$ which assumes that the diffusive flux of one species into the mixture is independent of the flux of the other species. More accurate algorithms exist that solve the full system and retain the multi-component nature, but they require significantly more computational effort than a mixture-averaged formulation. Examples of these algorithms include the work of Oran and Boris [284], Ern and Giovangigli [285] and Pope and Gogos [286].

The diffusive velocity for each individual species is evaluated in this work using the mixture-averaged approach. Here, $\vec{V}_k$ is defined as

$$\vec{V}_k Y_k = -D_k \nabla Y_k \qquad \text{with} \qquad D_K = \frac{1 - Y_k}{\sum_{j \neq k} X_j / \mathcal{D}_{j,k}} \tag{3.20}$$

where D_k is the equivalent diffusion coefficient of species k into the rest of the mixture, X_j is the mole fraction of species j, and $\mathcal{D}_{j,k}$ is the binary diffusion coefficient of species j into species k. Substituting Eq. (3.20) into (3.2d) and summing over all the species does not fully recover the global continuity equation, Eq. (3.2a), because

$$\frac{\partial}{\partial x_i} \left(\rho \sum_{k=1}^{N} D_k \frac{\partial Y_k}{\partial x_i} \right) \neq 0 \tag{3.21}$$

To ensure the global conservation of mass, it is usual to introduce a correction velocity,$\vec{V}_{\text{c}}$, such that [282]

$$\vec{V}'_k = \vec{V}_k + \vec{V}_{\text{c}} \tag{3.22}$$

where

$$\vec{V}_{\text{c}} = -\sum_{k=1}^{N+1} Y_k \vec{V}_k \tag{3.23}$$

and $\vec{V}_k'$ is the corrected diffusion velocity for a gaseous species or soot.

3.2.4 Thermodynamic and Transport Properties

The total internal energy for the mixture, e, and the total mixture enthalpy, h, are computed as follows:

$$e = \sum_{k=1}^{N+1} Y_k e_k + \frac{1}{2}|\vec{v}|^2 \tag{3.24}$$

$$h = \sum_{k=1}^{N+1} Y_k h_k + \frac{1}{2}|\vec{v}|^2 \tag{3.25}$$

where c_{p_k} and c_{v_k} are taken to be functions of temperature only, $e_k = \int_0^T c_{v_k}(T')dT'$ and $h_k = \int_0^T c_{p_k}(T')dT'$.

Thermodynamic properties, transport properties and species net production rates were evaluated using CANTERA [287], an open-source, object-oriented software package for chemically-reacting flows. CANTERA evaluates species standard-state properties using NASA polynomials [288–290] which provide species specific heat, c_{p_k}, enthalpy, h_k, and entropy, s_k, as functions of temperature only. To estimate the mixture averaged values, CANTERA makes use of Wilke's formula for viscosity [291] and a combination-averaging formula for thermal conductivity [292]. Soot is assumed to have no effect on the mixture viscosity or thermal conductivity.

3.2.5 Gas-Phase Chemical Kinetics

For a set of N_R elementary reactions involving N species, the rate equations can be written in the following general form [222]:

$$\sum_{j=1}^{N} \nu_{ij}'[X_j] \rightleftharpoons \sum_{j=1}^{N} \nu_{ij}''[X_j] \tag{3.26}$$

where $[X_j] = \frac{\rho Y_j}{M_j}$ is the molar concentration for species j, and ν_{ij}' and ν_{ij}'' are the stoichiometric coefficients for species j appearing as a reactant in the ith forward and backward reactions, respectively. The forward and backward reaction rate constants for the ith reaction step, $k_{\mathrm{f}i}$ and $k_{\mathrm{b}i}$, respectively, are given by

$$k_i = A_i T_i^{\beta} \exp\left(-\frac{E_\mathrm{a}}{\bar{R}T}\right) \tag{3.27}$$

where E_a represents the activation energy whereas A_i and β_i are constants. The forward and reverse rate constants are related by the equilibrium constant, K_c, as

$$K_\mathrm{c} \equiv \frac{k_{\mathrm{f}i}}{k_{\mathrm{b}i}} = \prod_{j=1}^{N} \left[X_j\right]^{\nu_{ij}''-\nu_{ij}'} = \left(\frac{p}{\bar{R}T}\right)^{\sum_{k=1}^{N}(\nu_{ki}''-\nu_{ki}')} \times \exp\left(\frac{\Delta G_i^\circ}{\bar{R}T}\right) \tag{3.28}$$

where ΔG_i° is the change in standard-state Gibbs free energy for reaction i. The rate of progress variable, q_i, for the ith elementary reaction is

$$q_i = k_{\mathrm{f}i} \prod_{j=1}^{N} \left(\frac{\rho Y_j}{M_j}\right)^{\nu_{ij}'} - k_{\mathrm{b}i} \prod_{j=1}^{N} \left(\frac{\rho Y_j}{M_j}\right)^{\nu_{ij}''} \tag{3.29}$$

which is related to the total rate of change of mass fraction of species j by

$$\dot{\omega}_j = \frac{M_j}{\rho} \sum_{i=1}^{N_R} \left(\nu''_{ij} - \nu'_{ij} \right) q_i \tag{3.30}$$

In some reactions, such as dissociation or recombination, a third-body collision partner is required for the reaction to proceed. For example,

$$\mathrm{H} + \mathrm{O}_2 + \mathrm{M} \rightleftharpoons \mathrm{HO}_2 + \mathrm{M}$$

The concentration of this effective third body, M, is accounted for by modifying the net rate of progress, Eq. (3.29), to be

$$q_i = \left\{ \sum_{j=1}^{N} \alpha_{ij} \left(\frac{\rho Y_j}{M_j} \right) \right\} \left\{ k_{\mathrm{f}i} \prod_{j=1}^{N} \left(\frac{\rho Y_j}{M_j} \right)^{\nu'_{ij}} - k_{\mathrm{b}i} \prod_{j=1}^{N} \left(\frac{\rho Y_j}{M_j} \right)^{\nu''_{ij}} \right\} \tag{3.31}$$

where α_{ij} is the efficiency factor for the jth species contributing to reaction i. Species which contribute to the reaction as third-bodies have non-zero values for α_{ij}. As previously mentioned in Section 3.2.4, CANTERA was used to compute the net rates of progress and evaluate Eq. (3.30).

Even though pressure does not appear explicitly in the expression for $\dot{\omega}_j$, there is a strong influence of pressure on reaction rate through its effect on density and species concentration. As previously mentioned in Section 3.1.3, this pressure effect manifests itself by affecting chain mechanisms and fall-off behavior. Chain mechanism effects are incorporated directly into the mechanism and do not require any special treatment. Fall-off behavior, however, must be treated separately.

3.2.5.1 Fall-Off Behavior

The temperature dependent rate expressions, Eq. (3.27), still apply in the high and low pressure limits. These expressions must be modified for cases where the pressure lies between these limits in the fall-off region. With Lindemann theory [254], a blending function, which is based on the rate constants given in both the low- and high-pressure limits, is used to describe the Arrhenius reactions in the fall-off regime. This blending function is given by

$$k = k_\infty \left(\frac{p_\mathrm{r}}{1 + p_\mathrm{r}} \right) F \tag{3.32}$$

where $p_\mathrm{r} = \frac{k_0[\mathrm{M}]}{k_\infty}$ is the reduced pressure, k_0 is the reaction rate constant in the low pressure limit, and k_∞ is the rate constant in the high pressure limit. For the Lindemann form, $F = 1$. An extension to this is Troe's fall-off formula [255], which is given by

$$\log F = \left\{ 1 + \left[\frac{\log p_\mathrm{r} + c}{n - d\left(\log p_\mathrm{r} + c\right)} \right] \right\} \log F_{cent} \tag{3.33}$$

where

$$c = -0.4 - 0.67 \log F_{cent}$$

$$n = 0.75 - 1.27 \log F_{cent}$$

$$d = 0.14$$

$$F_{cent} = (1 - a) \exp\left(-T/T^{***}\right) + a \exp\left(-T/T^{*}\right) + \exp\left(-T^{**}/T\right)$$

and a, T^{***}, T^{*}, and T^{**} are fitting parameters. The mechanisms employed in this study all make use of Eq. (3.33) to describe pressure-dependent fall-off behaviour.

Chapter 4

MATHEMATICAL DESCRIPTION OF RADIATION TRANSPORT

Radiation is the emission and absorption of electromagnetic waves or photons which occurs when materials undergo translational, rotational and vibrational motions that lower or raise their molecular energy level. The strength and wavelength at which these photons are emitted depends strongly on the temperature of the emitting material. Since photons at different frequencies carry vastly different amounts of energy, their behavior changes drastically throughout the electromagnetic spectrum. For heat transfer analysis, we are only concerned with the portion of the spectrum where the emissive power or emitted energy is large. This is called thermal radiation and generally occurs at wavelengths between 10^{-7} μm (ultraviolet) to 10^{-3} μm (infrared) [293]. Emission by a medium is dictated solely due to its temperature within this range.

As photons travel through a medium, they are either attenuated or augmented as the two interact with each other. A medium which interacts with passing photons is called a participating medium while one which does not interact with photons is said to be transparent. In hydrocarbon combustion, participating media include gases such as H_2O, CO, CO_2 and unburned hydrocarbons as well as clouds of small particles such as soot. Concentrated regions of these participating gases and soot reach high temperatures in flames which results in a significant heat loss to the cold surroundings via radiation. In sooting flames, soot radiation dominates and the degree of radiative loss depends strongly on the number density and size of soot particles [294, 295].

Detailed treatment of thermal radiation is necessary for accurate prediction of the flame structure, species concentrations, and formation of soot [296]. The net production rates of both soot and the intermediate gaseous species are highly temperature-dependent [52]. However, modelling radiation is an arduous task that involves the solution of complex integro-differential equations with many degrees of freedom and widely varying properties. Numerical solution is usually required as exact solutions only exist for idealized cases that do not realistically describe typical combusting flows. Two effective numerical techniques for solving the radiation transfer equation (RTE) are the discrete ordinates method (DOM) [297] and the finite-volume method (FVM) [298, 299]. Although both methods were evaluated as part of this thesis, the DOM was used exclusively for the detailed flame calculations in Chapters 6–8. The statistical narrow-band correlated-*k*

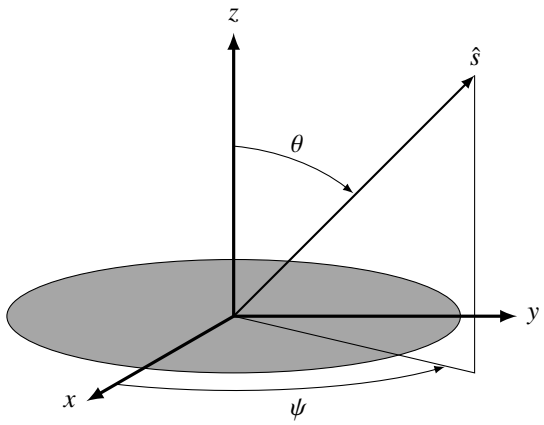

Figure 4.1: Cylindrical coordinate system used for radiative heat transfer analysis.

(SNBCK) method [300] was used to model the spectral absorption coefficient of the gas mixture while the absorption properties of soot were estimated using the Rayleigh scattering approximation.

This chapter gives a brief background on modelling radiation in soot-laden combusting flows and describes the DOM method used to solve the RTE. It also details the models employed for the non-gray spectral properties of the gas mixture and soot.

4.1 Background

4.1.1 The Radiation Transfer Equation

The RTE is the conservation law for the spectral intensity applied to a monochromatic beam of light [293]. It is derived by applying an energy balance to a beam of photons which are confined to a infinitesimal solid angle element and passing through an infinitesimal volume of participating media. In a direction defined by the unit vector $\hat{s}$, the RTE is

$$\frac{1}{c}\frac{\partial I_\nu}{\partial t} + \hat{s}\cdot\nabla I_\nu = \kappa_\nu I_{b\nu} - \kappa_\nu I_\nu - \sigma_{s\nu} I_\nu + \frac{\sigma_{s\nu}}{4\pi}\int_{4\pi} I_\nu(\hat{s}')\Phi_\nu(\hat{s}',\hat{s})\,\mathrm{d}\Omega' \tag{4.1}$$

where c is the speed of light in a vacuum, ν is the wavenumber, I_ν is the spectral intensity, $I_{b\nu}$ is the blackbody radiative intensity, κ_ν is the absorption coefficient, $\sigma_{s\nu}$ is the scattering coefficient, and Φ_ν is the scattering phase function. All quantities of Eq. (4.1) may vary with location in space, time and wavenumber while the intensity and the phase function also depend on direction. Since the speed of light is much faster than the local velocities in most reacting flows, solutions for the steady-state form of Eq. (4.1) are usually sought [296].

In cylindrical coordinates, shown in Fig. 4.1, the steady form of the RTE is a function of two dimensions (r, z) and two angular coordinates (θ,ψ). For this coordinate frame, Eq. (4.1) can be re-cast as

$$\frac{\mu}{r}\frac{\partial(rI_\nu)}{\partial r} - \frac{1}{r}\frac{\partial(\eta I_\nu)}{\partial\psi} + \xi\frac{\partial I_\nu}{\partial z} = -\beta_\nu I_\nu + \kappa_\nu I_{b\nu} + \frac{\sigma_{s\nu}}{4\pi}\int_{4\pi} I_\nu(\hat{s}')\Phi_\nu(\hat{s}',\hat{s})\,\mathrm{d}\Omega' \tag{4.2}$$

where $\beta_\eta = \kappa_\nu + \sigma_{s\nu}$ is the extinction coefficient, θ and ψ are the polar and azimuthal angles, and μ, η and ξ

are the direction cosines. These values are related to the polar and azimuthal angles by

$$\mu = \sin\theta\cos\psi, \quad \eta = \sin\theta\sin\psi, \quad \xi = \cos\theta \tag{4.3}$$

and define the unit vector, $\hat{s}$, in the Cartesian coordinate system given by

$$\hat{s} = \mu\hat{i} + \eta\hat{j} + \xi\hat{k} \tag{4.4}$$

Equations (4.1) and (4.2) are both multidimensional hyperbolic integro-differential equations which reduce to first-order linear-hyperbolic differential equations in the absence of scattering.

The spectral radiation flux vector is defined as the net flow of radiant energy due to radiation from all directions per unit area, time and wavenumber interval. It is defined by an integral of I_ν over the full range of solid angles, Ω, given by

$$\vec{q}_\nu = \int_0^{4\pi} \hat{s} I_\nu \, \mathrm{d}\Omega \tag{4.5}$$

The total incident radiation G_ν is given by

$$G_\nu = \int_0^{4\pi} I_\nu \, \mathrm{d}\Omega \tag{4.6}$$

Rearranging the RTE and integrating over all solid angles, we obtain the divergence of the heat flux vector as

$$\nabla \cdot \vec{q}_\nu = \kappa_\nu \left(4\pi I_{\mathrm{b}\nu} - \int_0^{4\pi} I_\nu \, \mathrm{d}\Omega \right) = \kappa_\nu \left(4\pi I_{\mathrm{b}\nu} - G_\nu \right) \tag{4.7}$$

When the radiative properties vary with the wavenumber, Eq. (4.7) must be integrated over the entire spectrum to give the divergence of the *total* radiation heat flux, $\nabla \cdot \vec{q}_{\mathrm{rad}}$, which is needed in the energy equation, Eq. (3.2c).

4.1.2 Solution of the RTE

The nature of radiation is inherently complex and, as a result, analytical solutions exist only for relatively simple problems. Therefore, solutions for more realistic cases are sought using one of the many numerical techniques that have been developed over the years [296]. The most physically-accurate and computationally intensive of them are statistical or Monte Carlo methods [301]. Hotel's Zonal method [302, 303] divides the domain into zones and performs energy balances of the radiative exchange between the zones. The method of moments is another technique for solving the RTE whereby a series in products of angular and spatial functions are used to express the variation of the radiation intensity. Series expansions using spherical harmonics have also been applied to approximate the angular dependence of the intensity [304]. Flux methods take a different approach and divide the solid angle into intervals over which the intensity is assumed constant. A particularly popular technique, primarily due to its excellent balance between computational efficiency and accuracy, is the discrete ordinates method (DOM) [297]. This method divides the solid angle into a number of directions and solves the RTE in each individual direction. A variation of this

technique is the finite-volume method (FVM) [298, 299] where finite-sized control angles are used instead to subdivide the solid angle. Another popular method that has been used extensively is the discrete transfer method (DTM) of Lockwood and Shah [305].

Researchers investigating soot formation in laminar flames have mainly used either the DOM or DTM for highly sooting flames [17, 19, 22, 52, 54, 56, 57, 60, 61, 63–68, 70, 71, 166] and the optically-thin approximation for lightly- to non-sooting flames [18, 50–52, 306]. The optically-thin approximation, described in Appendix B, requires much less computational effort and is sometimes employed when available resources are limited. It assumes that every point within the medium has the same incident radiation and attenuation rate, so the intensity field is known and $\nabla \cdot \vec{q}_{\text{rad}}$ can be directly evaluated without solving the RTE. However, Liu et al. [60, 166] observed significant differences between predictions of sooting laminar diffusion flames obtained using the optically-thin approximation and the DOM.

4.1.3 Real-Gas Absorption Models

Most of the numerical techniques discussed in the previous section are designed to solve the RTE for a single wavelength. However, radiative properties of gases, specifically the absorption coefficient, vary rather chaotically with wavenumber. Scattering is usually assumed to be small in comparison to absorption and neglected in the numerical analysis of combusting flows. Since spectrum integrated quantities such as the total radiant heat flux or its divergence are usually desired, some means of estimating the absorption coefficient and integrating the RTE over the spectrum is required.

For numerical computation of radiant heat transfer in gases, there exists several classes of spectral models of varying degrees of complexity [293]. They will be discussed here briefly in decreasing order of accuracy. In line-by-line computations, the problem is solved for hundreds of thousands of wavenumbers and the results are integrated over the spectrum. Narrow band models replace the actual absorption coefficient and intensity with values averaged over narrow spectral ranges. These models can be simplified by integrating narrow band results over larger ranges to form wide band correlations. Lastly, global models evaluate quantities of interest such as the radiant heat flux or its divergence directly using spectrally integrated radiation properties.

Narrow band methods offer the ability to efficiently compute low-resolution spectral intensities nearly as accurate as more expensive line-by-line calculations [307, 308]. They divide the wavenumber spectrum into small intervals across which the Planck function varies little and integrate the RTE over each of these narrow bands. Two of the more popular models that have been used extensively are the statistical narrow band (SNB) and correlated-k (CK) distribution methods [309]. SNB methods can be difficult to apply with many of the RTE solution techniques as they require approximations when applied to non-isothermal or inhomogeneous media [310, 311] and are incompatible for cases involving scattering [312]. Alternative CK methods are more versatile but require expensive numerical computation of the distribution function from large line-by-line databases [300, 313]. This distribution function can be computed much easier, however, if accurate narrow band data is available. A hybrid approach called the statistical narrow band correlated-k (SNBCK) method attempts to combine the advantages of both the SNB and CK. This approach is adopted

in this work.

4.2 The Spectral Absorption Coefficient

As previously discussed in Section 4.1.3, radiative heat transfer in combustion systems occurs over a range of wavenumbers. Radiation models must therefore incorporate non-gray effects through the use of real-gas spectral properties and accurate approximations for the optical properties of soot. Absorption and emission from the gas mixture and soot is accounted for using the SNBCK method and Raleigh theory for small spherical particles, respectively. Scattering was neglected for the reasons mentioned in Section 4.1.3 and because of the added computational costs associated with scattering. The evaluation of the mixture spectral absorption coefficient and its integration into the solution of Eq. (4.2) is discussed in the following sections.

4.2.1 Statistical Narrow Band Correlated-k Model

The SNBCK divides the wavenumber spectrum into small intervals, $\Delta\nu$, across which the Planck function varies little and solves the RTE for the average intensity over each interval [300]. It is similar to the CK approach as they both use a cumulative distribution function to describe the absorption coefficient except that the SNBCK model builds this function analytically using SNB parameters. This distribution function reorders the absorption coefficient field into a smooth monotonically-increasing function of a dimensionless wavenumber which is easily integrated [300, 313].

The CK method defines a distribution function $f(k)$ such that $f(k)\mathrm{d}k$ represents the fraction of the spectrum between ν and $\nu + \Delta\nu$ where the absorption coefficient lies between k and $k + \mathrm{d}k$. The function $f(k)$ is directly computed from the absorption coefficient spectrum as a weighted sum of the number of points where $\kappa_\nu = k$ [293]. Integrating $f(k)$ we obtain a cumulative distribution function:

$$g(k) = \int_0^k f(k')\mathrm{d}k' \tag{4.8}$$

where $g(k)$ is a monotonically increasing function from 0 to 1 that represents the fraction of the spectrum where the $\kappa_\nu \leq k$. Essentially, g is a dimensionless wavenumber normalized by $\Delta\nu$ that replaces the independent variable ν. Integrating the steady-form of Eq. (4.1) in the absence of scattering ($\sigma_\mathrm{s} = 0$) over an interval $\Delta\nu$, we obtain

$$\int_{\Delta\nu} \frac{\partial I_\nu}{\partial s}\,\mathrm{d}\nu = \int_{\Delta\nu} \kappa_\nu \left(I_{\mathrm{b}\nu} - I_\nu\right)\,\mathrm{d}\nu \tag{4.9}$$

The wavenumber in Eq. (4.9) is replaced with the new dimensionless parameter g to give

$$\int_0^1 \frac{\partial I_{\Delta\nu}}{\partial s}\,\mathrm{d}g = \int_0^1 k_{\Delta\nu}(g)\left(I_{\mathrm{b}\Delta\nu} - I_{\Delta\nu}\right)\mathrm{d}g \tag{4.10}$$

where the function $k_{\Delta\nu}(g)$ is the inverse function of $g(k)$ and the subscript $\Delta\nu$ refers to the specific interval for which a quantity is defined. The blackbody intensity within each range, $I_{\mathrm{b}\Delta\nu}$, is evaluated at the band center. In the CK approach, the integrals over g in Eq. (4.10) are evaluated using numerical quadrature. For

a particular quadrature point, g_i, the RTE can be written as

$$\frac{\partial I_{\Delta\nu,i}}{\partial s} = k_{\Delta\nu}(g_i)\left(I_{\mathrm{b}\Delta\nu} - I_{\Delta\nu,i}\right) \tag{4.11}$$

where $I_{\Delta\nu,i}$ is the solution at the ith quadrature point of band $\Delta\nu$. Once all $I_{\Delta\nu,i}$ are obtained, the band-averaged intensity, $\overline{I_{\Delta\nu}}$, and the total intensity, $\bar{I}$, are computed as

$$\overline{I_{\Delta\nu_j}} = \sum_{i=1}^{N_\mathrm{q}} w_i I_{\Delta\nu_j,i} \tag{4.12a}$$

$$\bar{I} = \sum_{j=1}^{N_\mathrm{b}} \overline{I_{\Delta\nu_j}} \tag{4.12b}$$

where N_q and N_b are the number of quadrature points and bands, respectively, w_i are the quadrature weights associated with g_i, and j is the narrow band index. The solution of Eq. (4.11) is discussed in detail in Section 4.3.

The CK method uses line-by-line data for the absorption coefficient from databases like HITRAN [314] to numerically compute $f(k)$. However, if the gas is assumed to follow the Malkmus model [315], an exact analytical expression for the k-distribution can be written as [300]

$$f(k) = \mathcal{L}^{-1}\{\overline{\tau_{\Delta\nu}}\} = \frac{1}{2}k^{-3/2}(BS)^{1/2}\exp\left[\frac{\pi B}{4}\left(2 - \frac{S}{k} - \frac{k}{S}\right)\right] \tag{4.13}$$

where $\mathcal{L}^{-1}$ is the inverse Laplace transform, $\overline{\tau_{\Delta\nu}}$ is the narrow-band averaged transmissivity, B is the effective line half-width, and S the effective line strength. Similarly, the cumulative distribution function is

$$g(k) = \frac{1}{2}\,\mathrm{erfc}\left(\frac{a}{\sqrt{k}} - b\sqrt{k}\right) + \frac{1}{2}\,\mathrm{erfc}\left(\frac{a}{\sqrt{k}} + b\sqrt{k}\right)\exp(\pi B) \tag{4.14}$$

where $\mathrm{erfc}(x)$ is the complementary error function, $a = \frac{1}{2}\sqrt{\pi BS}$ and $b = \frac{1}{2}\sqrt{\pi B/S}$. Taine and coworkers [316–318] generated data for the band model parameters, B and S, from the HITRAN spectroscopic database [319]. More complete narrow band properties were derived by Soufiani and Taine [307] for H_2O, CO_2 and CO using all the lines in the HITRAN database plus additional lines which significantly contribute to absorption and emission at high temperatures (up to 2500 K). This dataset consists of 367 uniformly-spaced bands between 150 to 9300 cm^{-1} with a bandwidth of 25 cm^{-1}. More recently, Perrin and Soufiani [320] generated band model parameters for high-temperature methane up to 2000 K. The dataset of Soufiani and Taine was used in this work to account for gas-band radiation from H_2O, CO_2, and CO only.

Both $f(k)$ and $g(k)$ vary with position in non-homogeneous gases, so there is no way to uniquely invert $g(k)$ and obtain $k(g)$. This problem is solved by assuming that the k-distribution remains correlated everywhere in the domain, which is the basis of the CK procedure. As a result, the cumulative distribution function can be used to map the absorption coefficient from one location to another; a value of k and g at one location maps to the same value of g, but different k, at a different location. While this is not strictly true in any

sense, Goody et al. [313] showed that the CK method is correct in the weak- and strong-line limits. Errors resulting from the correlated approximation are only several percent for atmospheric conditions with small temperature changes, but can become significant when there are large changes in pressure [300, 313, 321].

Following the procedure outlined by Lacis and Oinas [300], the RTE defined in Eq. (4.11) is solved for each quadrature point, g_i, of each band, $\Delta\nu_j$. A Newton-Raphson procedure is used to invert Eq. (4.14) and calculate the absorption coefficient for each quadrature point, k_i, everywhere in the domain. Good accuracy is achieved with only 5–10 quadrature points [300, 313], but Liu et al. [166, 322] determined that four Gauss-Legendre quadrature points are sufficient for detailed flame calculations. As such, the four-point Gauss-Legendre quadrature rule is used here.

4.2.1.1 Treatment of Overlapping Bands

The described treatment of gas-band absorption and emission is applicable to pure gases or mixtures of gases with no overlapping bands only. Overlapping bands occur when two or more gases actively absorb and emit within the same wavelength ranges. For example, CO_2 and H_2O are both active between 2150–2400 cm^{-1} and 3400–3700 cm^{-1}. At bands which two gases overlap, the SNB transmissivity in Eq. (4.13) is no longer valid because the product of two Malkmus bands is not a Malkmus band [313]. It is generally assumed that the transmissivity of the mixture is the scalar product of the two individual gas transmissivities, which adds significant complexity to the SNBCK formulation [300]. Considerable computational savings are achieved by treating the absorption of several overlapping gases with equivalent band model parameters for the mixture that describe an average Malkmus band.

Liu et al. [323] studied several approximate treatments and found that an approximate Malkmus band based on the optically-thin limit offered the best balance between accuracy and cost. As such, this approach was adopted here. In the optically-thin limit, the mixture band model parameters are [300]

$$S_{\text{mix}} = S_1 + S_2 \tag{4.15a}$$

$$\frac{S_{\text{mix}}^2}{B_{\text{mix}}} = \frac{S_1^2}{B_1} + \frac{S_2^2}{B_2} \tag{4.15b}$$

where the subscripts 1 and 2 denote the two overlapping gases.

4.2.1.2 Band-Lumping Procedure

Additional computational savings are achieved by combining bands to form several wide bands using the lumping procedure described by Liu et al. [324, 325]. Five to ten successive narrow bands are typically grouped together and the RTE is integrated over each new wide band. Errors are incurred that grow with the size of the newly grouped bands since the Planck function is no longer constant across each wide band [326]. The cumulative distribution function for a wide band is

$$g_{\text{lumped}} = \frac{1}{K} \sum_{i=1}^{K} g_i(k) \tag{4.16}$$

where K is the number of narrow bands lumped together to form a single wide band. Optimized lumping can be performed whereby the number of narrow bands grouped together varies throughout the spectrum [326]. The optimized 9-band scheme of Goutiere et al. [326] was employed here based on several recommendations [166, 326].

4.2.1.3 Tabulation

The inversion process to obtain the absorption coefficient from Eq. (4.14) composes a large portion of the overall solution time in radiative heat transfer calculations [325]. Liu and Smallwood [327] developed a more efficient approach to implement the SNBCK method that pre-calculates and stores the absorption coefficients. This tabulated approach was also employed in this work.

4.2.2 Soot-Band Radiation

Particles can generally be approximated as spherical since deviations tend to be smoothed out when averaged over millions of irregular shapes [293]. The light scattering and extinction characteristics of spherical particles are well described by Mie theory [328] which is valid for all size ranges. For spherical particles that are small in comparison to the wavelength of the incident radiation, Mie Theory reduces to the Rayleigh scattering approximation. Soot particles in most combustion applications can generally be treated using Rayleigh scattering since they typically have diameters smaller than 50 nm and are irradiated by light with a wavelength of approximately 3 μm [293].

Radiation extinction by particle clouds occurs from both absorption and scattering, but scattering becomes negligible as particles approach the zero-size limit. This approximation was made here since soot particles are typically fairly small. Assuming that the complex index of refraction does not vary significantly across the spectrum, the spectral absorption coefficient for a cloud of spherical particles of varying size can be written as

$$\kappa_{\nu s} = C\phi\nu \tag{4.17}$$

where C is an empirical constants. Values of C ranges from 3–7 depending up the fuel used [329]. A value of 5.5 was used based on the work of Liu et al. [60].

With this definition for $\kappa_{\nu s}$, the mean absorption coefficients in the optically-thin and optically-thick limits differ by only about 6%. As such, Felske and Tien [330] suggest the following average value for all optical regimes:

$$\kappa_s = 3.72\ C\phi T/C_2 \tag{4.18}$$

where $C_2 = 1.4388$ cm K is the second Planck function constant. It is important to remember that the above derivation only applies for very small soot particles. The extinction coefficient increases for aggregates or if primary particles exceed the Rayleigh scattering limits.

4.2.3 The Mixture Spectral Absorption Coefficient

Soot is treated as a gray absober while the gas absorption coefficient is allowed to vary over the whole spectrum. The spectral absorption coefficient for the gas-soot mixture is given by

$$\kappa_{\nu\mathrm{mix}} = \kappa_{\mathrm{s}} + \kappa_{\nu\mathrm{g}} \tag{4.19}$$

where $\kappa_{\nu\mathrm{g}}$ and $\kappa_{\nu\mathrm{mix}}$ are the spectral absorption coefficients for the gas and mixture, respectively.

4.3 The Discrete Ordinates Method

The DOM transforms the equation of transfer into a coupled set of partial differential equations with only spatial position coordinates as independent variables [297]. This is accomplished by dividing the solid angle into discrete directions and assigning weights to each of these directions. The RTE is solved in each direction and any integrals over the solid angle are evaluated using numerical quadrature. This method proves advantageous because it works well for radiation propagating through optically thin as well as thick media and it can be extended to include the effects of multiple wavelength lines of radiation. Accuracy is easily varied by extending the order of the solution and considering more directions while the basic grid structure used by this method easily integrates with CFD solution methods.

In the DOM, Eq. (4.2) is solved for a set of M different directions in the polar and L different directions in the azimuthal coordinates. The DOM approximation to Eq. (4.11) in cylindrical coordinates for a specific direction $\hat{s}_{ml}$ is given by

$$\frac{\mu_{ml}}{r}\frac{\partial(rI_{\Delta\nu,iml})}{\partial r} - \frac{1}{r}\frac{\partial(\eta_{ml}I_{\Delta\nu,iml})}{\partial\psi} + \xi_{ml}\frac{\partial I_{\Delta\nu,iml}}{\partial z} = k_{\Delta\nu}(g_i)\left(I_{\mathrm{b}\Delta\nu} - I_{\Delta\nu,iml}\right) \tag{4.20}$$

where m and l are the polar and azimuthal direction indices, respectively.

Equation (4.20) can be solved in each direction using any finite-volume or finite-difference technique to evaluate the spatial derivatives. Special consideration is required when discretizing the second partial derivative in Eq. (4.20) to avoid any unphysical coupling between the intensity in different directions [297]. This is required because the propagating direction of a neutron in a curvilinear coordinate system is constantly varying even though the neutron does not physically change its direction. As a result, a redistribution of radiative intensity among the different discrete directions occurs. Carlson and Lathrop [297] proposed a means of discretizing this term that permits minimal directional coupling while maintaining neutron conservation. Their approach assumes

$$\frac{1}{r}\frac{\partial(\eta_{ml}I_{ml})}{\partial\psi} = \frac{1}{r}\left(\frac{\alpha_{m,l+1/2}I_{m,l+1/2} - \alpha_{m,l-1/2}I_{m,l-1/2}}{\omega_{ml}}\right) \tag{4.21}$$

where ω_{ml} are the ordinate weights associated with $\hat{s}_{ml}$, and $\alpha_{m,l+1/2}$ and $\alpha_{m,l-1/2}$ are the angular redistribu-

tion coefficients. They are determined from the divergenceless flow condition by

$$\begin{aligned} \alpha_{m,l+1/2} &= \alpha_{m,l-1/2} + \omega_{ml}\mu_{ml} \\ \alpha_{m,1/2} &= 0 \end{aligned} \tag{4.22}$$

The intensities $I_{m,l+1/2}$ and $I_{m,l-1/2}$ are those centered on the faces of the control angles. Equation (4.22) requires that the directions cosines are ordered such that neutrons flow out of the first control angle ($\alpha_{m,1/2} = 0$) and into the last control angle ($\alpha_{m,L+1/2} = 0$). In other words, μ_{ml} must be monotonically increasing with index l for each polar angle m when η_{ml} is positive and decreasing when η_{ml} is negative. Improper ordering of the direction cosines would result in an unrealistic coupling between directional intensities.

Direction-integrated quantities are readily calculated once all the intensities in each direction are determined. The spectrum-integrated radiative heat flux, total incident radiation, and divergence of the radiative heat flux are

$$\vec{q} \approx \sum_{m}\sum_{l} \omega_{ml}\bar{I}_{ml}\hat{s}_{ml} \tag{4.23a}$$

$$G \approx \sum_{m}\sum_{l} \omega_{ml}\bar{I}_{ml} \tag{4.23b}$$

$$\nabla \cdot \vec{q}_{\text{rad}} \approx \sum_{j=1}^{N_\text{b}}\sum_{i=1}^{N_\text{g}} w_i k_{\Delta\nu_j}(g_i)\left(4\pi I_{\text{b}\Delta\nu_j} - \sum_{m=1}^{M}\sum_{l=1}^{L}\omega_{ml}I_{\Delta\nu_j,ml}(g_i)\right)\Delta\eta_j \tag{4.23c}$$

Ordinate directions and weights are chosen arbitrarily, however, they are usually derived using moment matching techniques [331] or geometric principles [332]. The T_3 angular quadrature scheme of Thurgood et al. [332] was selected for this work.

CHAPTER 5

NUMERCIAL SOLUTION METHOD

Mathematical models representing realistic combusting flows must rely heavily on engineering approximations to ensure that computations remain tractable. Hydrocarbon combustion is inherently complex and these approximate models are not accurate enough to capture the interactions between gas-phase chemistry, turbulence, radiation transport, soot formation/oxidation, and multi-phase transport. As such, efficient numerical algorithms for reacting flows are needed so that the most realistic physics models can be used to provide quantitative soot predictions. These algorithms should exploit state-of-the-art numerical methods such as adaptive mesh refinement (AMR), high-order discretization schemes, and implicit nonlinear relaxation/time-evolution schemes. They should also take advantage of the availability of today's large-scale, high-performance, parallel computing facilities.

Several numerical frameworks exist for solving reacting flows with soot. A numerical framework was developed by Ern et al. [333] and later applied to the study of soot formation by Smooke and coworkers [18, 50, 52, 306]. The framework uses a damped Newton method [334], a Krylov-based linear matrix solver, and an implicit Euler time-marching scheme for startup. Moderate scaling was achieved with a parallel efficiency of 64% on 16 processors (relative to four). Liu and Guo [60, 64] have also developed a mathematical model for studying soot formation in laminar coflow diffusion flames. This model was updated to include an advanced fixed-sectional aerosol description and parallelized via domain decomposition to deal with the stiff nature of the soot transport equations [70]. The predictions of the updated scheme agree well with experimental measurements and modest parallel efficiencies of 82% were achieved on 12 processors. Although not specifically designed for the study of soot formation, Day and Bell [335] developed a highly efficient parallel solution algorithm with AMR. Excellent parallel performance up to 4096 processors was observed when the scheme was applied to turbulent flames [336]. A drawback of this particular framework is the restriction to low-Mach-number flows as the equation of state is only satisfied to the order of the Mach number squared.

In this chapter, a new framework for the study of soot formation in complex reacting laminar flows is presented. It solves the unmodified equations governing compressible flows, which are applicable for all flow speeds, with a Newton-Krylov-based implicit solver. Discretization is performed using a high-order upwind-reconstructed finite-volume scheme on multi-block, body-fitted meshes with AMR. To cope

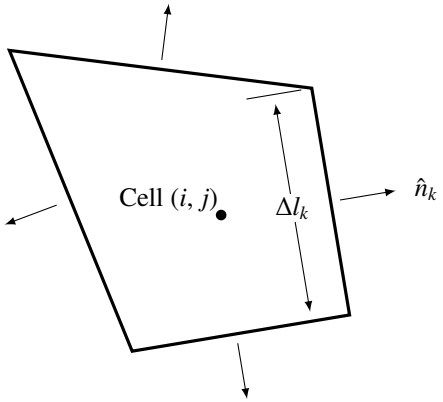

Figure 5.1: Two-dimensional quadrilateral computational cell.

with excessive dissipation and convergence stall commonly encountered when applying the compressible gas equations to low-Mach-number flows, the temporal derivative and the inviscid fluxes are modified via local preconditioning. This framework extends the previous work of Groth et al. [337–340] and is a robust, highly-scalable solution method for sooting laminar flames. The finite-volume scheme applied to the gas and soot equations is presented in this chapter, followed by the DOM scheme applied to solve the RTE and an outline of the overall solution algorithm.

5.1 Gas/Soot Equations

Numerical solutions of the two-dimensional, axisymmetric form of Eqs. (3.2a)–(3.2f) are obtained using the parallel, implicit, finite-volume scheme with block-based AMR previously developed by Groth and co-workers [339, 341]. The scheme solves conservation equations on body-fitted, multi-block, quadrilateral meshes. In this finite-volume approach, the physical domain is discretized into finite-sized computational cells and the integral forms of conservation laws are applied to each individual cell. For cell (i, j), as shown in Fig. 5.1, the approach results in the following coupled system of nonlinear ordinary differential equations (ODEs) for cell-averaged solution quantities:

$$\frac{\mathrm{d}\mathbf{W}_{ij}}{\mathrm{d}t} = \left.\frac{\partial \mathbf{W}}{\partial \mathbf{U}}\right|_{ij} \cdot \left\{ -\frac{1}{A_{ij}} \sum_{\text{faces},\, k} \left(\vec{\mathbf{F}}_k \cdot \hat{n}_k \Delta l_k \right)_{ij} + \mathbf{S}_{ij} \right\} \tag{5.1}$$

where

$$\mathbf{U}_{ij} = \left[\rho, \quad \rho u, \quad \rho v, \quad \rho e, \quad \rho Y_1, \quad \ldots, \quad \rho Y_N, \quad \rho Y_\mathrm{s}, \quad \rho N_\mathrm{s} \right]^\mathrm{T}$$
$$\mathbf{W}_{ij} = \left[p, \quad u, \quad v, \quad T, \quad Y_1, \quad \ldots, \quad Y_N, \quad Y_\mathrm{s}, \quad N_\mathrm{s} \right]^\mathrm{T}$$

are the cell-averaged conserved and primitive solution vectors, respectively, A_{ij} is the cell area, $\hat{n}_k$ and Δl_k are the normal vector and edge length for the kth face, and $\mathbf{S}_{ij}$ is the source term which includes contributions from axisymmetric terms, gravitational forces, finite rate-chemistry, and radiation. Here, it has been assumed that $\mathbf{S}_{ij} = \int_{A_{ij}} \mathbf{S}(\mathbf{U})\, \mathrm{d}A \approx \mathbf{S}(\mathbf{U}_{ij})$. The numerical flux $\vec{\mathbf{F}}_k = (\mathbf{F}, \mathbf{F}_\mathbf{v})$ comprises both inviscid, $\mathbf{F}$, and viscous,

$\mathbf{F_v}$, components which must be evaluated separately. The evaluation of these terms and the solution of Eq. (5.1) are described in the following sections.

5.1.1 Low-Mach-Number Preconditioning

Solution of the nonlinear ODEs given by Eq. (5.1) can be somewhat challenging as large differences between spatial and temporal scales can make the ODEs stiff. The stiffness of the ODEs is also significantly enhanced at very low flow speeds, which is a feature of the laminar flames of interest here, when the disparities between the convective and acoustic velocities become large [342]. Additionally, the nature of upwind discretizations for the inviscid fluxes can produce excessive dissipation at low speeds, corrupting overall solution accuracy [343].

One approach to dealing with low flow speeds is offered by low-Mach-number preconditioning. Preconditioning replaces physical time derivatives with artificial ones in order to alter the speeds at which waves propagate. Successful applications of preconditioning include viscous non-reacting flows [344–346], reacting flows [342, 347–350], multiphase flows [351–353], and zero-dimensional chemical reactors [354]. As per Weiss and Smith [348], application of the preconditioning to Eqs. (3.2a)–(3.2f) leads to the following system for axisymmetric coordinates:

$$\mathbf{\Gamma}\frac{\partial \mathbf{W}}{\partial t} + \frac{\partial}{\partial r}\mathbf{F} + \frac{\partial}{\partial z}\mathbf{G} = \frac{\partial}{\partial r}\mathbf{F_v} + \frac{\partial}{\partial z}\mathbf{G_v} + \mathbf{S} \tag{5.2}$$

where $\mathbf{\Gamma}$ is the preconditioning matrix for the primitive variables, $\mathbf{F}$ and $\mathbf{G}$ are the inviscid fluxes in the r- and z-directions, respectively, and $\mathbf{F_v}$ and $\mathbf{G_v}$ are the corresponding viscous fluxes. The Weiss and Smith preconditioning matrix, modified to include the equations for soot mass fraction and number density, is given by

$$\mathbf{\Gamma} = \begin{bmatrix} \Theta & 0 & 0 & \rho_T & \rho_{Y_1} & \cdots & \rho_{Y_{N+1}} & 0 \\ u\Theta & \rho & 0 & u\rho_T & u\rho_{Y_1} & \cdots & u\rho_{Y_{N+1}} & 0 \\ v\Theta & 0 & \rho & v\rho_T & v\rho_{Y_1} & \cdots & v\rho_{Y_{N+1}} & 0 \\ h\Theta - (1-\rho h_p) & \rho u & \rho v & h\rho_T + \rho h_T & h\rho_{Y_1} + \rho h_{Y_1} & \cdots & h\rho_{Y_{N+1}} + \rho h_{Y_{N+1}} & 0 \\ Y_1\Theta & 0 & 0 & Y_1\rho_T & Y_1\rho_{Y_1} + \rho & \cdots & Y_1\rho_{Y_{N+1}} & 0 \\ \vdots & \vdots & \vdots & \vdots & \vdots & \ddots & \vdots & \vdots \\ Y_{N+1}\Theta & 0 & 0 & Y_{N+1}\rho_T & Y_{N+1}\rho_{Y_1} & \cdots & Y_{N+1}\rho_{Y_{N+1}} + \rho & 0 \\ N_s\Theta & 0 & 0 & N_s\rho_T & N_s\rho_{Y_1} & \cdots & N_s\rho_{Y_{N+1}} & \rho \end{bmatrix} \tag{5.3}$$

where u and v are the r- and z-components of velocity, respectively, h is the total mixture enthalpy, and Θ is given by

$$\Theta = \frac{1}{V_p^2} - \frac{\rho_T(1-h_p)}{\rho h_T} \tag{5.4}$$

The variables ρ_p, ρ_T, h_p, h_T, ρ_{Y_k}, and h_{Y_k} are thermodynamic quantities that describe the properties of the fluid. The subscripts denote partial derivatives. For a perfect gas, $\rho_p = 1/(RT)$, $\rho_T = -\rho/T$, $h_T = c_p$, $h_p = 0$, $\rho_{Y_k} = -\rho M/M_k$, and $h_{Y_k} = h_k$. The eigenvalues for the preconditioned Jacobian matrix in the r-direction,

$\boldsymbol{\Gamma}^{-1}\frac{\partial \mathbf{F}}{\partial \mathbf{W}}$, become

$$\boldsymbol{\lambda} = \left[u' - a', \quad u, \quad u, \quad u' + a', \quad u, \quad \ldots, \quad u\right]^{\mathrm{T}} \tag{5.5}$$

where

$$u' = u\,(1-\alpha) \qquad a' = \sqrt{\alpha^2 u^2 + V_{\mathrm{p}}^2}$$
$$\alpha = \frac{1}{2}\left(1 - \beta V_{\mathrm{p}}^2\right) \qquad \beta = \rho_p + \frac{\rho_T(1-h_p)}{\rho h_T}$$

The preconditioned velocity scale, V_{p}, is an artificial sound speed defined as

$$V_{\mathrm{p}} = \min\left[\max\left(V_{\mathrm{inv}},\, V_{\mathrm{pgr}},\, V_{\mathrm{vis}},\, M_{\mathrm{ref}}\cdot a\right),\, a\right] \tag{5.6}$$

where a is the speed of sound defined by Eq. (3.18). The inviscid, pressure-gradient-induced, and viscous velocity scales, V_{inv}, V_{pgr}, and V_{vis}, respectively, are given by [348, 355]

$$V_{\mathrm{inv}} = \sqrt{u^2 + v^2} \tag{5.7a}$$

$$V_{\mathrm{pgr}} = \sqrt{\frac{|\Delta p|}{\rho}} \tag{5.7b}$$

$$V_{\mathrm{vis}} = \frac{\mu/\rho}{\Delta x} \tag{5.7c}$$

where Δp is the cell pressure gradient and Δx is the length of the computational cell. The term M_{ref} in Eq. (5.6) is a reference Mach number included to prevent singularities at stagnation points. Typical values for M_{ref} range from $0.5M_\infty$ to $10^{-5}M_\infty$ where M_∞ is the Mach number in the surrounding free-stream [343, 344, 348]. A value for M_{ref} of 10^{-4} was used throughout this work.

5.1.2 Round-Off Error Control

Another difficulty for flame computations with low flow velocities is the increasing significance of machine round-off errors that begin to denominate at Mach numbers below 10^{-3}. Following the procedure described by Choi and Merkle [344], a reference pressure, p_0, is introduced to minimize the influence of round-off errors at low Mach numbers. As a result, the pressure, p, is given by

$$p = p_0 + p' \tag{5.8}$$

where p_0 is a constant equal to the ambient pressure and p' represents the deviation of the local pressure from p_0. The reference pressure is subtracted from Eq. (3.2b) and p' replaces p in $\mathbf{W}$ when numerical solutions are sought.

5.1.3 Inviscid Flux Evaluation

To determine the numerical flux at the cell face, a high-order upwind Godunov scheme is used. Godunov's method [356] begins by assuming that the solution in each cell is piecewise-constant and that the inter-

mediate solution state at the cell interface is approximated by upwinding. It is this upwinding that ensures monotonicity and prevents any unwanted oscillations near solution discontinuities. In two-dimensions, given the left and right solution states, $\mathbf{W_L}$ and $\mathbf{W_R}$, the numerical flux at the cell interface is defined as

$$\vec{\mathbf{F}} \cdot \hat{n} = \mathcal{F}\left(\mathbf{W_L}, \mathbf{W_R}, \hat{n}\right) \tag{5.9}$$

where $\mathcal{F}$ is a flux function which solves a Riemann problem, $\mathcal{R}$, in a direction aligned along the face normal, $\hat{n}$.

Roe's approximate Riemann solver was used throughout this work to evaluate the inviscid fluxes [357, 358]. Additionally, the correction proposed by Harten [359] was added to ensure that the entropy condition is never violated at the sonic point. The numerical flux in one direction is given by

$$\mathbf{F}\left(\mathcal{R}\left(\mathbf{W_L}, \mathbf{W_R}\right)\right) = \frac{1}{2}\left(\mathbf{F_R} + \mathbf{F_L}\right) - \frac{1}{2}|\hat{\mathbf{A}}|\Delta\mathbf{W} \tag{5.10}$$

where $\mathbf{F_L}$ and $\mathbf{F_R}$ are the inviscid fluxes evaluated based on $\mathbf{W_L}$ and $\mathbf{W_R}$, $\Delta\mathbf{W} = \mathbf{W_R} - \mathbf{W_L}$, $|\hat{\mathbf{A}}| = \hat{\mathbf{R}}|\hat{\mathbf{\Lambda}}|\hat{\mathbf{R}}^{-1}$, $\hat{\mathbf{R}}$ is the matrix of primitive variable right eigenvectors and $\hat{\mathbf{\Lambda}}$ is the eigenvalue matrix. The matrix $\hat{\mathbf{A}}$ is the linearized flux Jacobian evaluated at a reference state, $\hat{\mathbf{W}}$. For simplicity, a reference state which relaxes Roe's conditions is used when dealing with multi-species, reacting flows [360, 361]. As such, the Roe-averaged flow variables, $\hat{f}$, are defined in terms of a mass weighting of the left and right flow variables, f_L and f_R, as given by

$$\hat{f} = \frac{\rho_\mathrm{R} f_\mathrm{R} + \rho_\mathrm{L} f_\mathrm{L}}{\rho_\mathrm{R} + \rho_\mathrm{L}} \tag{5.11}$$

where f_L and f_R can be any of the variables u, v, h, Y_k, Y_s, and N_s. The Roe-average density is given by $\hat{\rho} = \sqrt{\rho_\mathrm{R}\rho_\mathrm{L}}$.

The dissipation associated with the upwind discretization procedure can be controlled in the low-Mach-number limit by re-deriving Eq. (5.10) based on the preconditioned wave speeds. Following the procedure outlined by Weiss and Smith [348], $|\hat{\mathbf{A}}|\Delta\mathbf{W}$ in Eq. (5.10) is modified as follows:

$$|\hat{\mathbf{A}}|\Delta\mathbf{W} = \left|\mathbf{\Gamma}\left(\mathbf{\Gamma}^{-1}\frac{\partial\mathbf{F}}{\partial\mathbf{W}}\right)\right|\Delta\mathbf{W} \approx \mathbf{\Gamma}|\mathbf{A_\Gamma}|\Delta\mathbf{W} \tag{5.12}$$

where $|\mathbf{A_\Gamma}| = \mathbf{R_\Gamma}|\mathbf{\Lambda_\Gamma}|\mathbf{R_\Gamma}^{-1}$. The subscript $\mathbf{\Gamma}$ denotes that the matrix of eigenvectors and eigenvalues were derived based on the preconditioned system. The resulting numerical flux function has the form

$$\mathbf{F}\left(\mathcal{R}\left(\mathbf{W_L}, \mathbf{W_R}\right)\right) = \frac{1}{2}\left(\mathbf{F_R} + \mathbf{F_L}\right) - \frac{1}{2}\mathbf{\Gamma}|\mathbf{A_\Gamma}|\Delta\mathbf{W} \tag{5.13}$$

and ensures the correct scaling of the numerical dissipation in the low-Mach-number limit.

5.1.4 High-Order Spatial Accuracy

The extension of Godunov's scheme to second-order can prove challenging as second-order schemes always generate oscillations [362]. Godunov's scheme is first-order because the projection of the cell-averaged

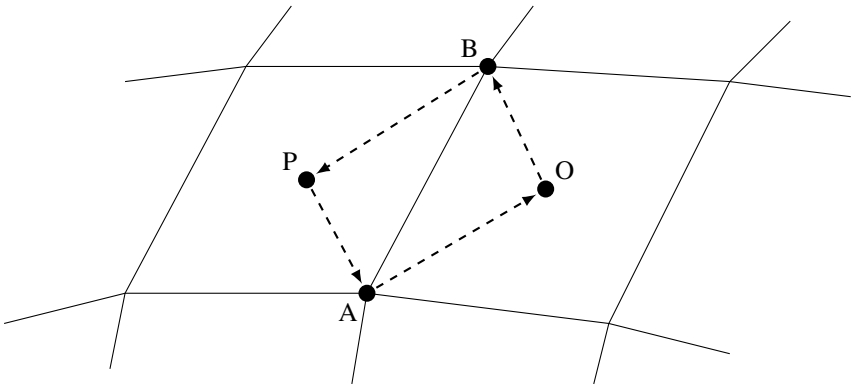

Figure 5.2: Diamond path viscous flux reconstruction for a quadrilateral cell.

solution in each cell occurs on piecewise-constant states. This projection is completely decoupled from the upwinding process and thus one can easily modify the spatial approximation. For this work, second-order spatial accuracy is achieved by interpolating the solution state at the cell interface between two adjacent cells. We ensure monotonicity using limiters to control gradients and damp any over- and under-shoots [363]. The reconstructed left and right states for interface $(i + \frac{1}{2}, j)$ in two-dimensions

$$\mathbf{W_L} = \mathbf{W}_{ij} + \phi_{ij}\left[\left.\frac{\partial \mathbf{W}}{\partial r}\right|_{ij}(r_{i+\frac{1}{2},j} - r_{ij}) + \left.\frac{\partial \mathbf{W}}{\partial z}\right|_{ij}(z_{i+\frac{1}{2},j} - z_{ij})\right] \tag{5.14a}$$

$$\mathbf{W_R} = \mathbf{W}_{i+1,j} + \phi_{i+1,j}\left[\left.\frac{\partial \mathbf{W}}{\partial r}\right|_{i+1,j}(r_{i+\frac{1}{2},j} - r_{i+1,j}) + \left.\frac{\partial \mathbf{W}}{\partial z}\right|_{i+1,j}(z_{i+\frac{1}{2},j} - z_{i+1,j})\right] \tag{5.14b}$$

where ϕ is a slope limiter. Slope limiting is performed with a limiter specifically designed for use in multiple dimensions [364]. The cell gradients are computed using linear reconstruction based on Green-Gauss theory [365].

5.1.5 Viscous Flux Evaluation

The centrally-weighted diamond-path method described by Coirier and Powell [366, 367] was employed to evaluate the viscous component of the numerical flux at the cell faces. The viscous component is given by

$$\vec{\mathbf{F}_\mathbf{v}} \cdot \hat{n} = \mathcal{G}(\mathbf{W}, \nabla\mathbf{W}, \hat{n}) \tag{5.15}$$

where $\mathcal{G}$ is the viscous flux function.

In the diamond-path method, the gradients at each face are found by applying the divergence theorem to a four-sided polygon, or diamond path, whose vertices are defined as shown in Fig. 5.2. The four vertices correspond to the two neighboring cell centers and the nodes of the interface separating the two cells. While the solution data at the cell centers is easily interpreted from the cell averages, the solution state at the vertices must be interpolated. A linearity-preserving weighting scheme that linearly constructs the nodal data from the cell-centered solution states of the neighboring cells was used [368]. This diamond path technique avoids instabilities due to even/odd decoupling that occur in standard cell-centered formulations [366] and reduces to standard centered differences on Cartesian grids with uniform mesh spacing.

5.1.6 Steady-State Relaxation Method

Newton's method is applied to obtain steady-state solutions for the coupled set of nonlinear ODEs, given by Eqs. (3.2a)–(3.2f). It is used to relax the semi-discrete form of the governing equations to a steady-state such that

$$\mathbf{R}(\mathbf{W}) = \frac{\mathrm{d}\mathbf{W}}{\mathrm{d}t} = \mathbf{0} \tag{5.16}$$

The Newton algorithm developed by Groth and Northrup [369] specifically for use on large multi-processor computer architectures is used here. The implementation makes use of a Jacobian-free inexact Newton method coupled with an iterative Krylov subspace linear solver. In Newton's method, a solution to Eq. (5.16) is sought by iteratively solving a sequence of linear systems given an initial estimate, $\mathbf{W}^0$. Successively improved estimates are obtained by solving the linear system

$$\left(\frac{\partial \mathbf{R}}{\partial \mathbf{W}}\right)^n \Delta\mathbf{W}^n = \mathbf{J}(\mathbf{W}^n)\Delta\mathbf{W}^n = -\mathbf{R}(\mathbf{W}^n) \tag{5.17}$$

where $\mathbf{J} = \frac{\partial \mathbf{R}}{\partial \mathbf{W}}$ is the residual Jacobian. The improved solution at step n is then determined from

$$\mathbf{W}^{n+1} = \mathbf{W}^n + \Delta\mathbf{W}^n \tag{5.18}$$

The Newton iteration proceeds until some desired reduction in the norm of the residual is achieved and the condition

$$\|\mathbf{R}(\mathbf{W}^n)\| < \varepsilon\|\mathbf{R}(\mathbf{W}^0)\| \tag{5.19}$$

is met. The tolerance, ε, used in this work was 10^{-7}.

As mentioned, each step of Newton's method requires the solution of the linear problem

$$\mathbf{J}\mathbf{x} = \mathbf{b} \tag{5.20}$$

where $\mathbf{x} = \Delta\mathbf{W}$ and $\mathbf{b} = -\mathbf{R}(\mathbf{W})$. This system is relatively large, sparse, and non-symmetric. It is solved using the generalized minimal residual (GMRES) technique developed by Saad and co-workers [370–373], which is widely used for solving systems of this type. GMRES is an Arnoldi-based solution technique which generates orthogonal bases of the Krylov subspace to construct the solution. The technique is particularly attractive because the matrix $\mathbf{J}$ is not explicitly formed and instead only matrix-vector products are required at each iteration to create new trial vectors. This greatly reduces the required storage. Termination also generally only requires solving the linear system to some specified tolerance, $\|\mathbf{R}^n + \mathbf{J}^n\Delta\mathbf{W}^n\| < \zeta\|\mathbf{R}(\mathbf{W}^n)\|$, where ζ is typically in the range 0.1–0.5 [374]. Lastly, a restarted version of the GMRES algorithm, GMRES(m), was used that minimizes storage by restarting every m iterations.

GMRES requires preconditioning to be effective. Right preconditioning the matrix $\mathbf{J}$ is performed to help facilitate the solution of Eq. (5.20) without affecting the solution residual vector, $\mathbf{b}$. The preconditioning

takes the form

$$\left(\mathbf{J}\mathbf{M}^{-1}\right)(\mathbf{M}\mathbf{x}) = \mathbf{b} \tag{5.21}$$

where $\mathbf{M}$ is the preconditioning matrix. A combination of an additive Schwarz global preconditioner and a block incomplete lower-upper (BILU) local preconditioner is used which is easily implemented in the block-based AMR scheme. In additive Schwarz preconditioning, the solution in each block is updated simultaneously and shared boundary data is not updated until a full cycle of updates has been performed on all domains. The preconditioner is defined as follows

$$\mathbf{M}^{-1} = \sum_{k=1}^{N_\mathrm{B}} \mathbf{B}_k^T \mathbf{M}_k^{-1} \mathbf{B}_k \tag{5.22}$$

where N_B is the number of blocks and $\mathbf{B}_k$ is the gather matrix for the kth domain. The local preconditioner, $\mathbf{M}_k^{-1}$, in Eq. (5.22) is based on block ILU(p) factorization [373] of the Jacobian for the first-order approximation of each domain. In the present research, the level of fill, p, was maintained at four in order to minimize storage requirements.

Newton's method can fail when initial solution estimates fall outside the radius of convergence. To ensure global convergence of the algorithm, the implicit Euler startup procedure with switched evolution/relaxation (SER) that was proposed by Mulder and Van Leer [375] was used. Application of this startup procedure to the semi-discrete form of the governing equations gives

$$\left[-\frac{\mathbf{\Gamma}}{\Delta t^n} + \left(\frac{\partial \mathbf{R}}{\partial \mathbf{W}}\right)^n\right] \Delta \mathbf{W}^n = -\mathbf{R}^n \tag{5.23}$$

where Δt^n is the time step. In the SER approach, the time step is varied from some small finite value and gradually increased as the steady state solution is approached. As $\Delta t^n \to \infty$, Newton's method is recovered.

In the quasi-Newton and SER methods, the time step size was determined by considering the inviscid Courant-Friedrichs-Lewy (CFL) and viscous Von Neumann stability criteria only. Time scales associated with gas-phase and soot chemistry were not incorporated into the time step size estimates. The time step size is determined by

$$\Delta t^n = \mathrm{CFL} \cdot \min\left[\frac{\Delta x}{u + a}, \frac{\rho \Delta x^2}{\mu}\right] \tag{5.24}$$

where CFL is a constant greater than zero which determines the time step size. During the startup phase of the Newton calculation, a value for CFL between 10–100 is typically used.

5.1.7 Parallel Adaptive Mesh Refinement Scheme

Modelling practical combustion devices with complex chemistry, turbulence and radiation transport can quickly tax computational resources even on relatively coarse meshes. Unfortunately, high mesh densities are required in areas with steep gradients and small length scales to accurately capture these processes. These locations can change over time and would normally require the use of large, fine uniform meshes. A flexible block-based AMR scheme is adopted here to limit the number of necessary computational cells by

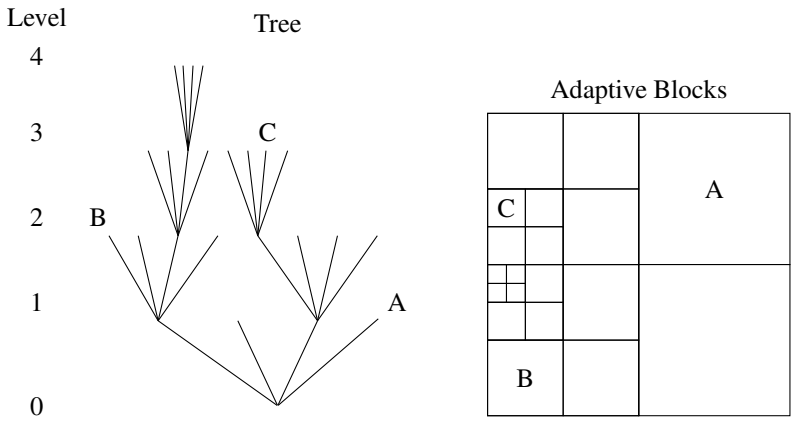

Figure 5.3: Adaptive mesh refinement quad-tree data structure and associated solution blocks for a quadrilateral mesh.

dynamically adapting the mesh to meet solution requirements. Details of the scheme and its implementation in parallel are described by Sachdev et al. [376, 377]. The extension of the scheme to three dimensions is described by Gao and Groth [340]. In this approach, block-based domain decomposition is applied to a body-fitted quadrilateral mesh. The grid blocks are organized in a hierarchical quad-tree data structure to facilitate automatic solution-directed mesh adaptation with physics-based criteria. The scheme borrows aspects from previous work by Berger and co-workers [378–381], Quirk [382], and De Zeeuw and Powell [383] for Cartesian grids and has similarities with the block-based approaches described by Quirk and Hanebutte [384] and Berger and Saltzman [380].

Relaxation of Eq. (5.1) with AMR proceeds as follows. The equations are first integrated forward in time on an initial structured, multi-block mesh to obtain updated volume-averaged solution quantities. The mesh is then adapted by coarsening or refining the blocks designated by the refinement criteria. A hierarchical tree-like data structure, shown in Fig. 5.3, is used to retain connectivity between solution blocks and track their refinement history. The blocks requiring refinement are termed "parents" and are divided into four new blocks called "children". Each child is a new block with the same number of cells as its parent, doubling the mesh resolution in the region. Coarsening flagged blocks is carried out by reversing this process and combining four children into one single parent.

For reacting flows, refinement is based on the gradients of both species mass fractions and temperature. The refinement criteria employed here are defined by

$$\epsilon_1 \propto \frac{|\nabla T|}{T} \tag{5.25}$$

$$\epsilon_2 \propto |\nabla Y_k| \tag{5.26}$$

Based on either of these criteria, the mesh is refined and blocks are added wherever ϵ_1 or ϵ_2 are large. In the present work, grids were refined based on temperature in addition to fuel, acetylene, and soot mass fractions.

To further decrease the overall computational time, integration of the governing equations is performed in parallel. This is carried out by distributing the computational blocks among the available processors and

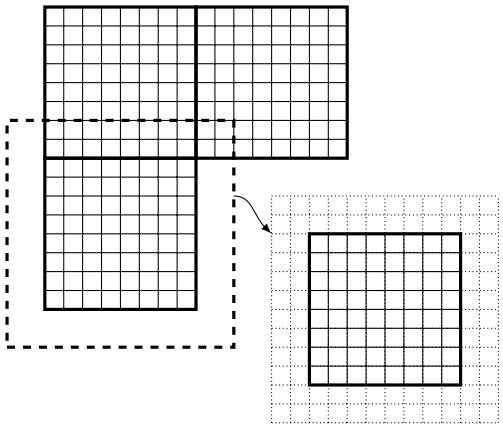

Figure 5.4: Sample multi-block grid and solution blocks depicting ghost cells.

simultaneously computing the solutions for each block on each processor. An even distribution of solution blocks is generally sought on homogeneous architectures while a weighted distribution is permissible for computations performed on heterogeneous systems such as networked workstations or computational grids. To ensure efficient load balancing, blocks are organized using a Morton ordering space filling curve which co-locates nearest neighbors on the same processor [381]. This minimizes the amount of necessary communication and improves the overall parallel efficiency of the implementation. The proposed AMR scheme was implemented using the message passing interface (MPI) library and the C++ programming language [385].

As shown by Fig. 5.4, ghost cells which surround the solution block and overlap cells on neighboring blocks are used to share solution content through inter-block communication. The conservation properties of the finite-volume discretization are retained across blocks with resolution changes by using the fine-grid interface flux to correct the flux computed on neighboring coarse blocks [378, 379]. Passing these flux corrections and the overlapping cell solution content between processors at each stage of the integration scheme accounts for the main source of inter-processor communication.

5.2 Radiation Transfer Equation

The contribution from radiation to $\vec{q}$ in Eq. (3.2c) was either computed using the optically-thin approximation (see Appendix B) or by solving the RTE with the DOM (Section 4.3). When using the optically-thin approximation, $\nabla \cdot \vec{q}_{\text{rad}}$ is evaluated along with the other sources terms in Eq. (5.1) at each right-hand-side (RHS) evaluation. GMRES requires one RHS per inner iteration, yet the additional cost of including non-gray radiation via the optically-thin approximation is relatively low. This is because the Planck-mean absorption coefficient is easily tabulated prior to starting each computation and quickly evaluated when needed using polynomial curve-fits. Evaluating $\nabla \cdot \vec{q}_{\text{rad}}$ using the DOM is much more costly due to the large number of unknowns associated with non-gray radiation. As a result, solution of the RTE is decoupled from the gas-particle flow equations and solved sequentially in a loosely-coupled fashion at each iteration or time step.

The set of ODEs resulting from the DOM (Eq. (4.20)), which consists of $N_{\text{b}} \times N_{\text{q}} \times M \times L$ equations, were solved using a space-marching procedure [297]. However, the serial nature of space-marching techniques

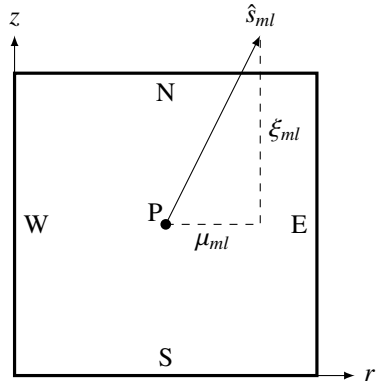

Figure 5.5: Axisymmetric control volume.

applied to the DOM are problematic for large-scale parallel CFD solution algorithms. Additionally, complications arise when applying standard space-marching techniques to complex geometry and non-orthogonal meshes. Several authors have developed optimized sweeping procedures that simultaneously solve the DOM equations in different directions [386, 387], but these approaches generally do not scale well to a large number of processors and do not address the issues related to complex geometry. To remedy these problems, a new highly-scalable time-marching algorithm for solving the DOM discretization of the RTE was developed in this work and is described in Appendix C. However, the large number of unknowns in Eq. (4.20) and the large memory requirements of implicit methods prohibited the new method's use in the multi-dimensional flame calculations considered here. No attempt was made here to improve the parallel performance of the standard DOM solution algorithm.

5.2.1 DOM

Equation (4.20) is solved using the space-marching finite-volume approach outlined by Carlson and Lathrop [297]. Substituting Eq. (4.21) into (4.20) and integrating over a general volume element, illustrated in Fig. 5.5, yields

$$\begin{aligned}\mu_{ml}\left(A_{\mathrm{E}}I_{\mathrm{E},ml}-A_{\mathrm{W}}I_{\mathrm{W},ml}\right)+\xi_{ml}\left(A_{\mathrm{N}}I_{\mathrm{N},ml}-A_{\mathrm{S}}I_{\mathrm{S},ml}\right)&\\ -\left(A_{\mathrm{E}}-A_{\mathrm{W}}\right)\left(\alpha_{m,l+1/2}I_{\mathrm{P},m,l+1/2}-\alpha_{m,l-1/2}I_{\mathrm{P},m,l-1/2}\right)/\omega_{ml}&\\ =\Delta V\kappa_{\mathrm{P}}\left(I_{\mathrm{bP}}-I_{\mathrm{P},ml}\right)&\quad(5.27)\end{aligned}$$

where the subscript P denotes quantities at the cell center, and the subscripts E, W, N and S refer to quantities evaluated at the respective cell faces. Note that the band and quadrature indices have been dropped in Eq. (5.27) for clarity.

The cell volume, ΔV, and face areas, A, are given by

$$A_{\mathrm{N}} = A_S = \pi(r_{\mathrm{E}}^2 - r_{\mathrm{W}}^2) \tag{5.28a}$$

$$A_{\mathrm{E}} = 2\pi\Delta z r_{\mathrm{E}} \tag{5.28b}$$

$$A_{\mathrm{W}} = 2\pi\Delta z r_{\mathrm{W}} \tag{5.28c}$$

$$\Delta V = \pi(r_{\mathrm{E}}^2 - r_{\mathrm{W}}^2)\Delta z \tag{5.28d}$$

where Δr and Δz are the cell-sizes in the r- and z-directions, respectively. To reduce the number of unknowns, the cell-edge intensities are related to the volume-averaged intensity by

$$I_{\mathrm{P},ml} = \gamma_s I_{\mathrm{N},ml} + (1-\gamma_s) I_{\mathrm{S},ml} = \gamma_{\mathrm{s}} I_{\mathrm{E},ml} + (1-\gamma_{\mathrm{s}}) I_{\mathrm{W},ml} \tag{5.29a}$$

$$I_{\mathrm{P},ml} = \gamma_{\mathrm{a}} I_{\mathrm{P},m,l+1/2} + (1-\gamma_{\mathrm{a}}) I_{\mathrm{P},m,l-1/2} \tag{5.29b}$$

where γ_{s} and γ_{a} are the spatial and angular differencing parameters, respectively. For both parameters, a value of 1 corresponds to upwind differences and 0.5 corresponds to central differences. Central differences were used for both the spatial and angular discretization in all computations.

Substituting Eqs. (5.29a) and (5.29b) into Eq. (5.27) and rearranging for the nodal intensity gives

$$\begin{aligned}\left\{\Delta V\kappa_{\mathrm{P}} + \mu_{ml}A_{\mathrm{E}}/\gamma_{\mathrm{s}} + \xi_{ml}A_{\mathrm{N}}/\gamma_{\mathrm{s}} - \frac{(A_{\mathrm{E}} - A_{\mathrm{W}})\alpha_{m,l+1/2}}{\omega_{ml}\gamma_{\mathrm{a}}}\right\} I_{\mathrm{P},ml} = \\ \Delta V\kappa_{\mathrm{P}} I_{\mathrm{bP}} + \mu_{ml}A_{\mathrm{EW}} I_{\mathrm{W},ml}/\gamma_{\mathrm{s}} + \xi^{ml}A_{\mathrm{NS}} I_{\mathrm{S},ml}/\gamma_{\mathrm{s}} \\ - (A_{\mathrm{E}} - A_{\mathrm{W}})\left[\alpha_{m,l-1/2} + (1-\gamma_{\mathrm{a}})\alpha_{m,l+1/2}/\gamma_{\mathrm{a}}\right] I_{\mathrm{P},m,l-1/2}/\omega_{ml}\end{aligned} \tag{5.30}$$

where

$$A_{\mathrm{EW}} = (1-\gamma_{\mathrm{s}})A_{\mathrm{E}} + \gamma_{\mathrm{s}}A_{\mathrm{W}} \tag{5.31a}$$

$$A_{\mathrm{NS}} = (1-\gamma_{\mathrm{s}})A_{\mathrm{N}} + \gamma_{\mathrm{s}}A_{\mathrm{S}} \tag{5.31b}$$

Numerical solution of Eq. (5.27) proceeds as follows. First, the surface intensities and internal source terms are estimated everywhere in the domain. The lower left corner of the domain is chosen as a starting point so that all outgoing directions lie in the first quadrant (i.e. $\mu_{ml} > 0$ and $\xi_{ml} > 0$). Since the west and south faces of the control volume in this corner are part of the enclosure surface, their intensities are specified by the boundary conditions. From these known face values, $I_{\mathrm{P},ml}$ is computed using Eq. (5.30) and the downstream intensities $I_{\mathrm{E},ml}$ and $I_{\mathrm{N},ml}$ are determined from Eq. (5.29a). One by one, the first-quadrant intensities are calculated for all volumes in the enclosure. This procedure is repeated three more times starting from the remaining corners of the enclosure and covering the other three quadrants of directions. After sweeping all directions for $I_{\mathrm{P},ml}$, the boundary values and radiative source terms are updated. This procedure is repeated until convergence is met.

Solutions were deemed converged when the maximum change in the cell-averaged intensity everywhere

in the domain from one iteration to the next was less than a specified tolerance. Throughout this thesis, the following convergence criterion was used:

$$\left|I_{\mathrm{P}}^{n+1} - I_{\mathrm{P}}^{n}\right| \leq 10^{-12} \qquad \text{for all P, } m, l \tag{5.32}$$

where the superscripts n and $n+1$ denote the iteration number.

5.2.1.1 Parallel Block-Based Solution Scheme

The DOM was solved in a parallel fashion at each time-step on the multi-block mesh along with Eqs. (3.2a)–(3.2f) by simultaneously sweeping all directions on the domain local to each processor. Solution content was shared among the processors by exchanging the state at the face-center of cells aligned with the block boundaries. Changes in mesh resolution were handled by linearly interpolating the coarse-mesh solution onto the fine-mesh and averaging the fine-mesh solution onto the coarse-mesh. Since the radiation solver employs a point-implicit space-marching technique, iteration is required to propagate information from upstream boundaries to downstream blocks. As a result, a penalty in terms of parallel efficiency was incurred because the number of iterations required to solve the radiation field increased with the number of blocks.

5.3 Overall Solution Algorithm

The overall algorithm is summarized as follows:

1. Set initial conditions for $\mathbf{W}$ and I everywhere in domain.
2. Compute $\kappa_{\nu\mathrm{mix}}$ for the gas/soot mixture using Eq. (4.19).
3. Solve the RTE using the DOM described in Section 5.2.1.
4. Update $\nabla \cdot \vec{q}_{\mathrm{rad}}$.
5. Solve Eq. (5.1) for the gas/soot mixture, performing n Newton iterations.
6. Update primitive solution state $\mathbf{W}$.
7. If not converged, return to step 2. The convergence criteria is defined in Eq. (5.19).

Throughout this work, only one Newton iteration ($n = 1$) for Eq. (5.1) was performed before updating the radiation intensity field. Larger values of n up to five were tested but found to deteriorate the performance of the overall solver. As n is increased, the CPU time required to advance the solution a fixed interval Δt in the computational domain decreases. However, increasing n also increases the number of iterations required to obtain a converged, coupled solution.

Chapter 6

VERIFICATION AND VALIDATION

In an effort to validate the proposed computational framework before applying it to high-pressure and low-gravity flames, two different laminar coflow diffusion flames were modelled under atmospheric conditions: the weakly-sooting methane-air flame studied extensively by Smooke et al. [50] and the heavily-sooting ethylene-air flame examined by Snelling et al. [388]. These flames were investigated specifically to address the predictive capability of the models used as well as the parallel efficiency of the algorithm. The effects of grid resolution and gas-phase reaction mechanism on the overall flame solutions were also assessed. Reasonable agreement with experimental measurements was obtained for both flames for predictions of flame height, temperature and soot volume fraction. Overall, the algorithm displayed excellent strong scaling performance by achieving a parallel efficiency of 70% on 384 processors. The proposed algorithm proved to be a robust, highly-scalable solution method for sooting laminar flames.

6.1 Laminar Coflow Diffusion Flames

A schematic illustrating the two-dimensional computational domain and applied boundary conditions for both coflow flames is provided in Fig. 6.1. Reflection boundary conditions are applied along the centerline and in the far-field. At the outlet, temperature, velocity, species mass fractions and soot number density are extrapolated while pressure is held fixed. The gas/soot mixture is specified at the inlet (i.e., pure fuel with no soot) along with velocity and temperature while pressure is extrapolated. These boundary conditions where found to closely mimic boundary schemes based on a characteristic analysis [346]. For the radiation solver, all boundaries except for the axis of symmetry are assumed to be cold and black.

6.1.1 Methane-Air Flame

For the methane-air flame, the burner configuration consisted of a central fuel tube with a 5.556 mm inner radius and a 0.794 mm wall thickness. Coflow air was supplied by a concentric tube of inner radius 47.625 mm. Both fuel and air were assumed to have uniform inlet velocity and temperature profiles with a fuel velocity of 5.5 cm/s, an air velocity of 12.54 cm/s, and an inlet temperature of 298 K. The original investigators [50] found that an inlet temperature of 420 K was required to obtain better agreement with the predicted flame height and local temperatures. This was later verified by Liu et al. [166] who also investigated this particular flame configuration numerically. In the current study, the axisymmetric computational

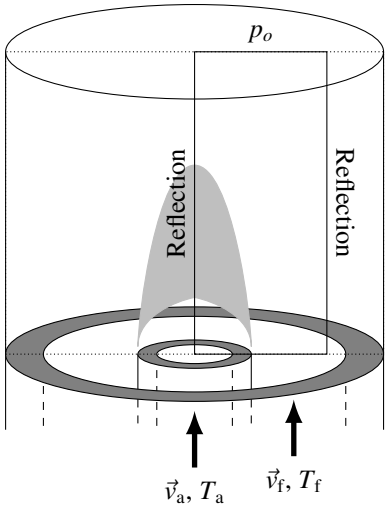

Figure 6.1: Schematic of laminar coflow diffusion flame.

domain was rectangular with $0 \leq r \leq 47.625$ mm and $0 \leq z \leq 85$ mm and the initial mesh consisted of 72 cells in the r- and 112 in the z-direction for a total of 8064 cells. The initial mesh was divided amongst 96 blocks of 14 by 6 cells. The cells were clustered towards the centerline in the radial direction and towards the burner exit plane in the axial direction. Finite-rate chemistry was modelled using a modified version of the GRI-Mech 3.0 mechanism for CH_4 combustion [258]. In this modified version, N_2 was assumed inert and all reactions and species related to NO_x formation were removed. The final reduced mechanism consisted of 36 species and 219 reactions.

6.1.2 Ethylene-Air Flame

The heavily-sooting ethylene-air flame studied experimentally by Snelling et al. [388] and numerically by Liu et al. [60] used a configuration similar to the one described in the previous section. The burner fuel tube inner radius, wall thickness, and coflow-air tube inner radius are 4.45, 0.95, and 50 mm, respectively. Fuel and air are delivered at room temperature (294 K) with specified volume flow rates of 194 ml/min and 284 l/min. Unlike the methane flame, a parabolic laminar pipe flow velocity profile was assumed for the fuel inlet while a uniform velocity profile with a boundary layer along the outer fuel tube wall was assumed for the coflow air inlet. For this flame, the rectangular computational domain was defined here in the range $0 \leq r \leq 30$ mm and $0 \leq z \leq 97.3$ mm with a similar initial grid to that used for the methane-air flame: 72 by 112 non-uniformly spaced cells divided into 96 blocks of 14 by 6 cells. The simulations were performed using the skeletal mechanism of Law [389] for ethylene-air combustion which consisted of 33 species and 205 elementary reactions. This mechanism was derived from the detailed mechanism proposed by Qin et al. [274] using a skeletal reduction technique which eliminates un-important species and reactions based on a sensitivity analysis.

6.1.3 Solution Procedure

All computations were performed on a high performance parallel cluster consisting of 104 IBM P6-575 nodes with 128 GB RAM per node and a high-speed interconnect. The nodes each have 32 IBM POWER6

Table 6.1: Mesh statistics for both flames.

	Methane-Air				Ethylene-Air			
Level	Blocks	Cells	$T_{\max}$ (K)	$f_{v,\max} \times 10^7$	Blocks	Cells	$T_{\max}$ (K)	$f_{v,\max} \times 10^6$
0	96	8 064	2010.43	8.50	96	8 064	2102.01	8.46
1	144	12 096	2012.53	8.77	159	13 356	2103.53	8.55
2	294	24 696	2013.33	8.86	282	23 688	2103.06	8.58
3	462	38 808	2013.69	8.92	402	33 768	2104.30	8.63
4	765	64 260	2013.68	8.92	822	69 048	2104.09	8.60
5					1167	98 028	2104.07	8.61

cores (4.7GHz) and are inter-connected via a non-blocking switch with four 4x-DDR InfiniBand links.

For both flames, a converged solution was obtained on the initial 96 block mesh, the mesh was adapted, and then a new solution was obtained. This procedure was repeated and the meshes were adapted several more times to yield a final computational grid roughly 8–12 times the original size. Solutions were terminated when the L^2-norms of the mass, momentum, and energy residuals were all reduced by approximately seven orders of magnitude. In the sections to follow, the grid convergence is discussed, the numerical predictions are verified, and the performance of the proposed algorithm is assessed.

6.2 Adaptive Mesh Refinement

The mesh statistics for each flame and level of refinement are given in Table 6.1. The table also provides the maximum predicted values for temperature and soot volume fraction in each calculation. For both flames, the maximum values converge asymptotically towards a final value. The minimum grid spacing for the finest mesh in the r- and z-directions are 0.017 and 0.009 mm for the methane flame and 0.017 and 0.01 mm for the ethylene flame, respectively.

The mesh adaption process is illustrated in Figs. 6.2(a) and 6.2(b) for the methane- and ethylene-air flames, respectively. These figures depict the mesh solution blocks at each level of refinement superimposed upon contours of predicted soot volume fraction. In both cases, the AMR algorithm correctly identified the locations with high gradients and locally refined the mesh in the corresponding areas. This resulted in substantial reductions in computational cost and storage since equivalent uniform meshes with the same resolution as the finest meshes would require approximately 535 500 and 515 937 cells for the methane and ethylene flames, respectively. This corresponds to a factor of 5 and 8 reduction in mesh size.

In both cases, refinement occurred primarily in regions with high soot mass fraction gradients. Additional blocks were identified for refinement in the ethylene-air case. These blocks were outside the high-soot region and near the outer radius of the flame where temperature gradients were steep. Temperature gradients in the ethylene-air flame were much larger compared to the methane-air flame due to increased radiative heat losses to the surroundings. This increased radiative heat loss in the ethylene-air flame was confirmed by comparing the predicted $\nabla \cdot \vec{q}_{\text{rad}}$ for the two flames. It was approximately four times larger in the ethylene flame as compared to the methane flame.

Although the AMR procedure for mesh refinement appears to be quite efficient, further investigation

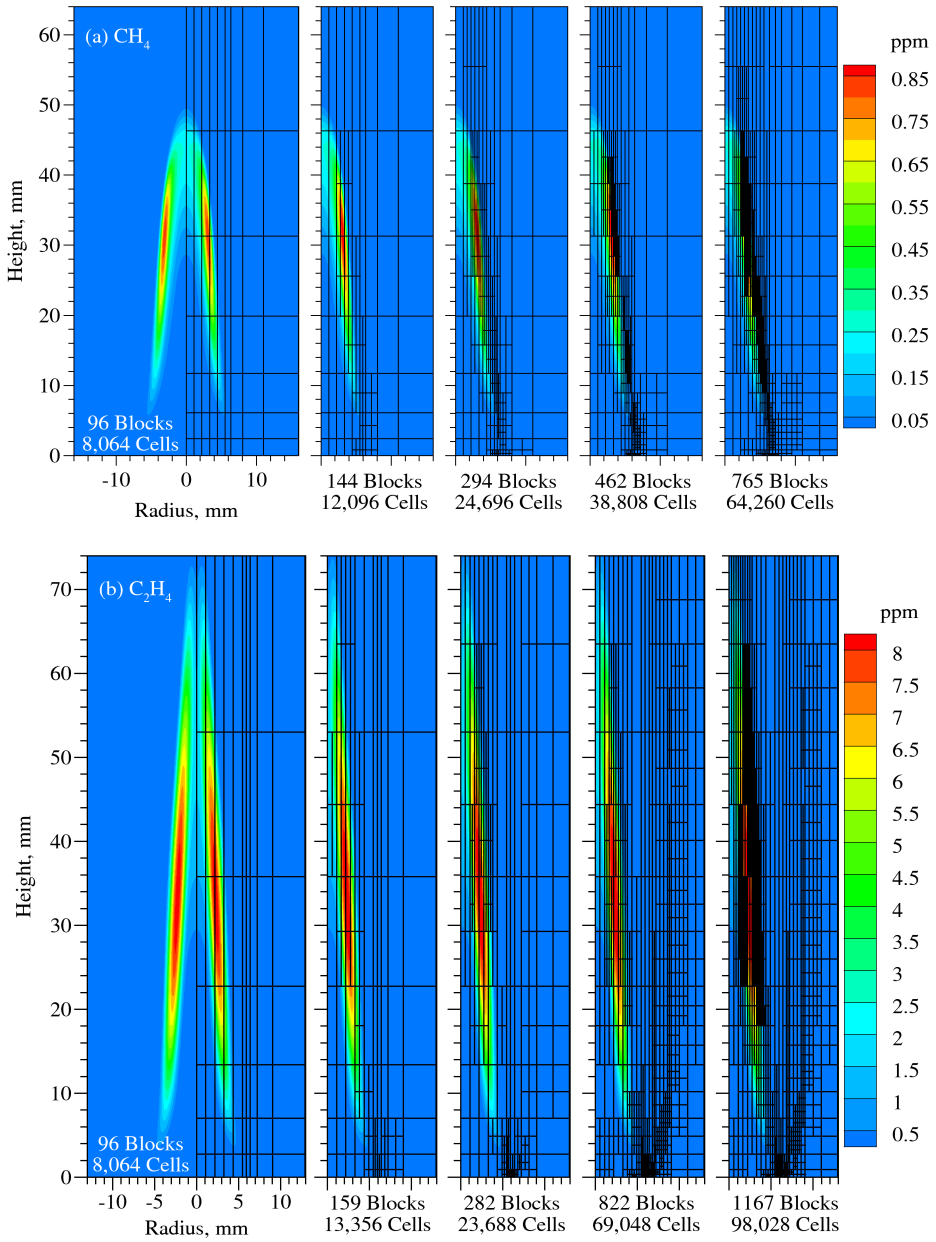

Figure 6.2: Refined multi-block computational mesh showing the solution blocks after each level of refinement superimposed on contours of soot volume fraction for (a) the CH_4 and (b) the C_2H_4 flame.

reveals that the finest mesh used in the ethylene-air case was possibly over-refined in the high-temperature-gradient areas. Cells were added along the flame sheet (defined by the peak temperature) where temperature gradients are high. However, temperature varies almost linearly with radius on both sides of the peak, Fig. 6.5(a). As such, fewer cells are required to resolve these gradients near the peak since the second-order scheme is capable of accurately resolving them with few cells. While the ϵ_1 refinement criteria (Eq. (5.25)) may be easily adjusted to reduce the amount of refinement with respect to temperature gradients, such an adjustment is case-specific and therefore not performed here. These results emphasize the importance of improved error-based mesh adaptation techniques that do not rely on gradient- or physics-based refinement criteria [390, 391]. This is especially relevant for reacting flows which have a large numbers of chemical

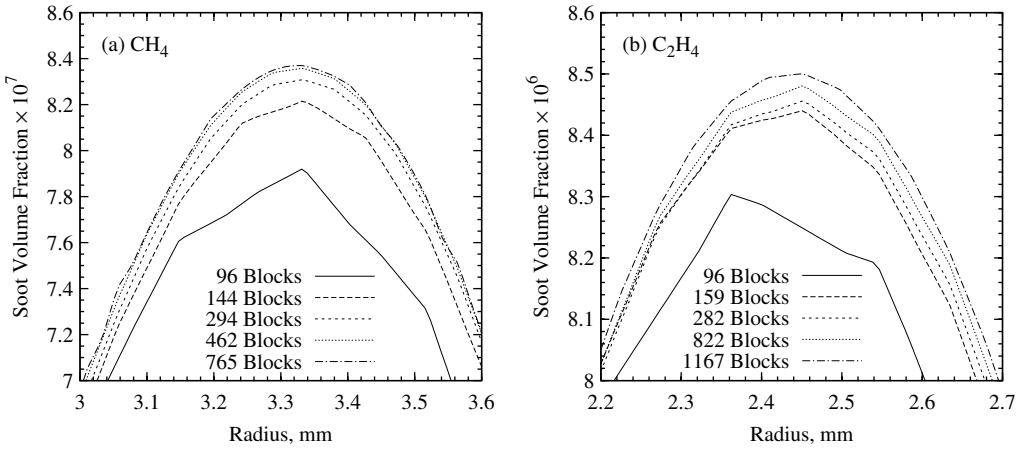

Figure 6.3: Effect of grid resolution on radial profiles of soot volume fraction for (a) the CH_4 flame at z=27.5 mm and (b) the C_2H_4 flame at z=30 mm.

species and where the most effective refinement criterion is not readily apparent.

To further investigate the effect of grid resolution, predicted radial profiles of soot volume fraction as a function of mesh refinement level are compared in Fig. 6.3. For the methane-air flame, illustrated in Fig. 6.3(a), the profile along z=27.5 mm clearly converges asymptotically after three levels of refinement. It is also evident that the minimum mesh spacing of 0.2 mm in the radial direction used by Liu et al. [166] for the same flame is not sufficient to fully describe the soot volume fraction peaks. Grid convergence is not strictly obtained for the ethylene-air flame, illustrated in Fig. 6.3(b), as slight changes in the profile along z=30 mm are still observed after the final refinement operation. The differences in the grid convergence characteristics between the two sets of flame calculations are explained by comparing the contours for soot volume fraction depicted in Figs. 6.2(a) and 6.2(b). The figures indicate that the number of mesh points in areas of high soot concentration is significantly lower in the ethylene flame and suggest that further refinement in these areas may be required.

6.3 Experimental Comparison

6.3.1 Methane Flame

The results for the methane flame are compared with the numerical and experimental results obtained by Smooke et al. [50] to verify and validate the models used. Overall, the flame structure is predicted reasonably well and the results are similar to those obtained by Smooke et al. Experimental measurements indicated that the flame height based on the location where the centerline temperature reached a maximum was 40 mm. The proposed framework slightly over-predicted this flame height. A value of 55 mm is obtained here, which is similar to the predicted value of approximately 50 mm obtained by the previous investigators.

Predicted radial profiles for temperature, methane mole fraction, acetylene mole fraction, and soot volume fraction at various axial locations are compared with the previously published experimental measurements in Fig. 6.4. The temperature profiles, Fig. 6.4(a), are under-predicted by about 100 to 200 K along the centerline and over-predicted at the outer edges of the flame. The agreement between numerical and exper-

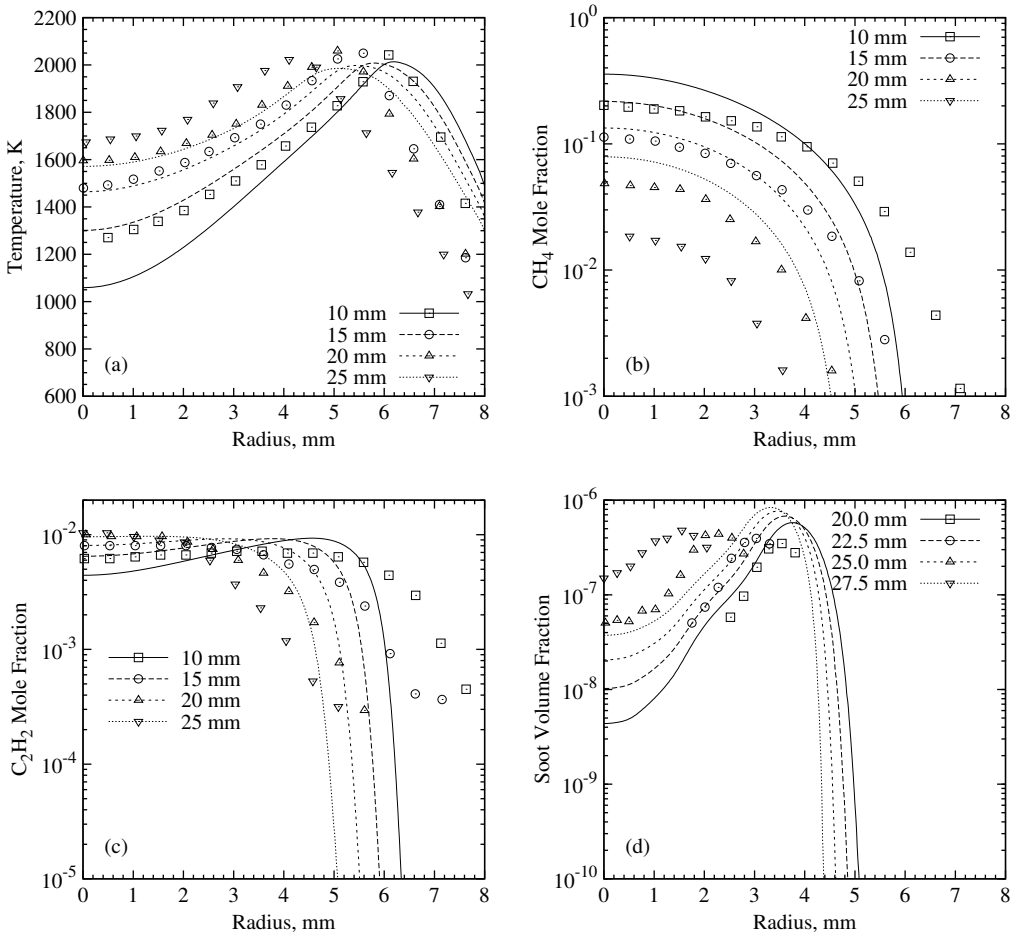

Figure 6.4: Comparison between the experimental measurements of Smooke et al. [50] (dots) and numerical predictions (lines) for (a) temperature, (b) CH_4 mole fraction, (c) C_2H_2 mole fraction, and (d) soot volume fraction for the methane-air laminar diffusion flame.

imental results along the centerline is worse lower in the flame, at z=10 mm, and improves with increasing axial distance from the burner exit plane. Similar agreement between numerical and experimental results are reported by Smooke et al. [50].

Comparisons between the predicted and measured radial profiles for methane and acetylene mole fraction are depicted in Figs. 6.4(b) and 6.4(c), respectively. Although the general trends are captured, the quantitative agreement between experimental and numerical results is somewhat poor. Methane is over-predicted on average by a factor of two along the centerline and a factor of four at an axial height of 25 mm above the burner. Smooke et al. [50] obtained similar results and attributed this poor agreement to low computed flame temperatures, despite having increased inlet temperatures to improve predictions. As a result, methane is consumed at a slower rate and penetrates further downstream in the calculations. This poor agreement for the methane concentrations may also be a result of uncertainties at the fuel inlet boundary. Large gradients in methane concentration exist at the mouth of the burner which suggest that combustion may actually begin slightly upstream of the fuel tube exit plane. The predictions of acetylene concentration agree well with the measurements although the predicted profiles are narrower and the values along the centerline are slightly

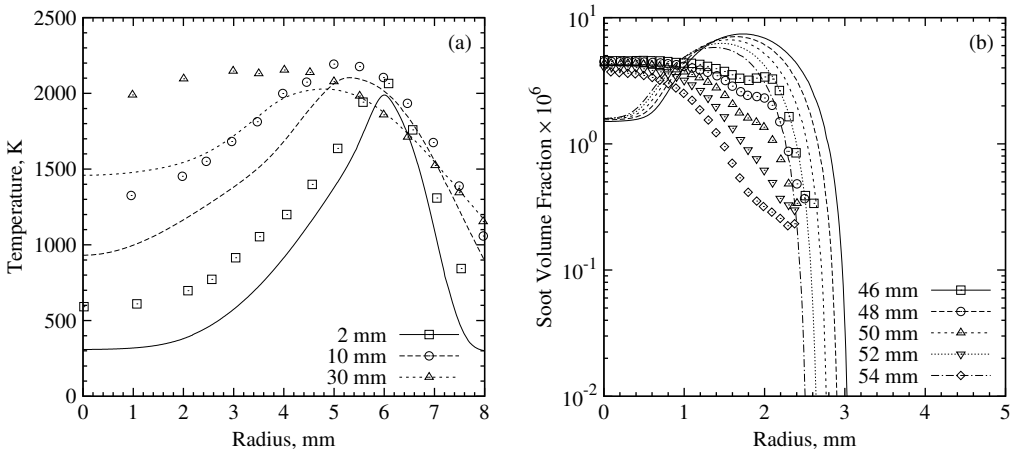

Figure 6.5: Comparison between the experimental measurements of Snelling et al. [388] (dots) and numerical predictions (lines) for (a) temperature, and (b) soot volume fraction for the ethylene-air laminar diffusion flame.

under-predicted. Acetylene concentrations rapidly vanish near the edges of the flame in the numerical results but measurements indicate that they slowly decrease. The under-prediction along the centerline may be a direct result of the delayed methane decomposition and under-predicted flame temperatures.

The predictions for soot volume fraction are compared with the measurements in Fig. 6.4(d). A large improvement over the numerical results obtained by Smooke et al. [50] is observed which may be due to differences in the gas-phase and soot kinetics employed. The overall structure of soot is properly captured and the predicted values agree with experimental measurements. Smooke et al. [50] predicted a peak soot volume fraction three times larger than the measured value while the proposed framework only over-predicted by a factor of 1.7. These predicted peaks occurred in an annular region approximately 28 mm above the burner for Smooke et al. [50] and 33 mm here. Both numerical studies obtained values along the centerline that were a full order-of-magnitude lower than the experimentally measured values.

The predictions for the methane-air flame described in this section also agree with other numerical predictions obtained by Liu et al. [166] for the same flame. As with the original investigators, these authors used the artificially-increased fuel and air inlet temperatures to reduce the discrepancies between the predicted and measured peak flame temperatures. Such an adjustment was not required here.

6.3.2 Ethylene Flame

The results obtained using the proposed algorithm are similar to those reported by Liu et al. [60]. Comparing the two sets of predictions, the computed temperature field in the present study is in slightly better quantitative agreement with the experimental measurements. The proposed framework calculated a peak temperature of 2104 K as compared to a measured peak of 2156 K and the prediction of 2010 K by Liu et al. [60]. The predicted radial profiles of temperature along selected axial heights are compared with the measurements in Fig. 6.5(a). While the predicted temperature profiles agree well with the measurements near the peaks, the values near the centerline and outer portion of the flame are significantly under-predicted. These low predicted flame temperatures are attributed to the neglect of fuel preheating and other uncertainties in

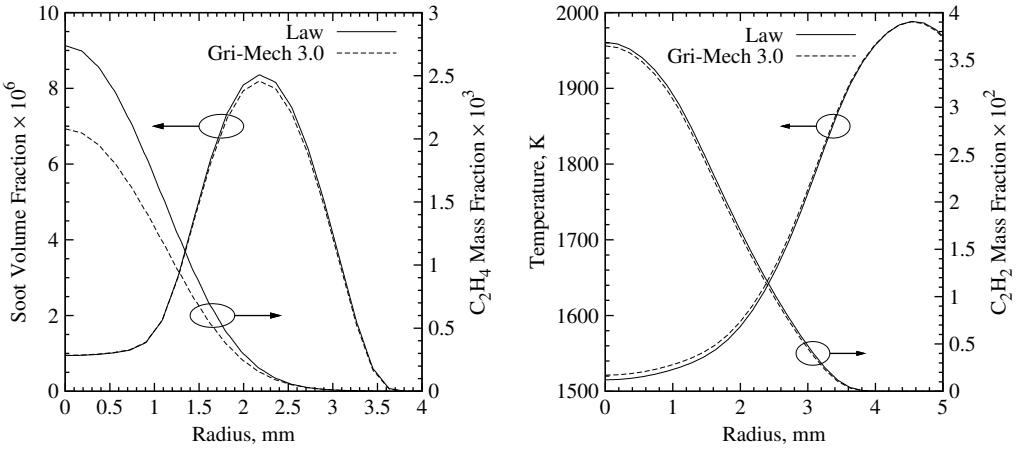

Figure 6.6: Predicted radial profiles of temperature, soot volume fraction, C_2H_2 and fuel mass fraction for the C_2H_4 flame at z=30 mm obtained using different gas-phase mechanisms.

the inlet boundary conditions.

As shown in Fig. 6.5(b), the predictions of soot volume fraction are also in reasonable quantitative agreement with the experimental measurements. A peak value of 8.6 ppm was predicted using the current implementation compared to the measured peak of 8.021 ppm. Liu et al. [60] obtained slightly better quantitative agreement, predicting a peak soot volume fraction of 8.0 ppm. The computed structure of the soot distributions differs significantly from the experimental results. This is observed in Fig. 6.5(b), which compares the predicted soot volume fraction along various radial profiles with the previously published experimental measurements. The calculations predict a more annular structure with lower soot concentrations along the centerline than the measurements. Similar results were obtained by Liu et al. [60].

6.4 Effect of Gas Phase Mechanism

Calculations of the ethylene-air flame with the initial coarse mesh were performed a second time using the modified form of GRI-Mech 3.0 to assess the sensitivity of soot formation to gas-phase kinetics. A comparison of the radial profiles along z=30 mm for ethylene and acetylene mass fraction, temperature, and soot volume fraction which were obtained using both mechanisms is illustrated in Fig. 6.6. Calculations using GRI-Mech 3.0 predicted a slightly lower peak soot volume fraction and a 25% lower centerline fuel mass fraction when compared to calculations using the skeletal mechanism of Law [389]. Negligible differences are observed between predictions for temperature and acetylene concentrations. The large differences in fuel mass fraction can be attributed to the higher laminar flame speeds predicted by GRI-Mech 3.0. Egolfopoulos and Dimotakis [277] found that this mechanism drastically over-predicted the laminar flame speeds in ethylene-air mixtures. In contrast, the skeletal mechanism of Law [389] was demonstrated to accurately reproduce laminar flame speeds under atmospheric conditions. Despite these large differences in the predicted ethylene concentrations, acetylene and soot concentrations are not greatly affected by the change in mechanism.

6.5 Parallel Performance

The parallel performance of the algorithm was assessed for both strong and weak scaling. These two properties are a measure of the ability to demonstrate a proportionate increase in parallel speedup with more processors. For the strong scaling test, the problem size is held fixed while the number of processors used to perform the computation is varied. Weak scaling is measured by holding the work load per processor fixed and varying the problem size with the number of processors. These two scaling properties are measured by the parallel speedup S_p and efficiency η_p which are defined as

$$S_p = \frac{t_1}{t_p} \tag{6.1}$$

$$\eta_p = \frac{S_p}{p} \tag{6.2}$$

where t_1 and t_p are the total wall times required to solve the problem with 1 and p processors, respectively.

In both the strong and weak scaling tests, solutions were also obtained using the OTA for radiative heat transfer [60]. The OTA assumes that radiation leaving a surface travels through the domain unattenuated. As a result, the radiative intensity field is known everywhere and $\nabla \cdot \vec{q}_{\text{rad}}$ can be evaluated directly without solving the radiative transfer equation. The parallel performance of the current DOM implementation is quantified by comparing the results using both the OTA and DOM.

6.5.1 Strong Scaling

Strong scaling of the algorithm applied to both coflow flames was measured using fixed-size meshes consisting of 384 equally-sized blocks of 14 by 6 cells (32 256 total cells). The work load per processor was varied without affecting the partitioning of the mesh by changing the number of blocks assigned to each processor. As a result, only the effect of inter-processor communication on parallel efficiency is taken into account. The negative effects of mesh partitioning on the effectiveness of Schwarz preconditioning and the parallel efficiency of the implemented DOM space-marching technique were not directly assessed for this study.

The resulting relationship between parallel speedup, efficiency, and number of processors is shown in Fig. 6.7(a) for the two flames. Excellent parallel performance is achieved with an efficiency greater than 70% up to 384 processors. Slight differences between the results for both flames exist which are caused by changes in governing equation stiffness with soot production and gas-phase kinetic mechanism. Comparing the results obtained using the two radiation models, the parallel performance of the overall algorithm improved when the OTA was used to evaluate $\nabla \cdot \vec{q}_{\text{rad}}$. Parallel efficiencies of 70 and 77% on 384 processors were obtained using the DOM and OTA, respectively. This improvement is attributed to the added communication required when solving the DOM equations. When using the DOM with the proposed algorithm, both the fluid solution for the surrounding ghost cells and the radiative intensities along the block boundaries are communicated. Only the fluid solution states are be passed when using the OTA.

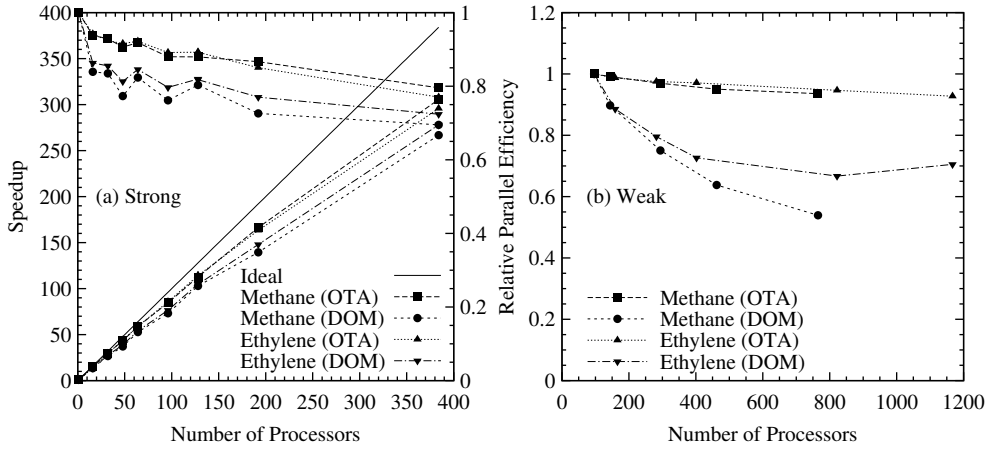

Figure 6.7: Parallel performance of the proposed solution algorithm showing the (a) strong and (b) weak scaling performance obtained for the methane- and ethylene-air laminar diffusion flame simulations.

6.5.2 Weak Scaling

The weak scaling performance of the proposed solution algorithm is observed in Fig. 6.7(b) for the two different flames and radiation models. It was obtained by assigning each processor a single block and iterating for a fixed number of Newton steps. When the OTA was used, excellent weak scaling performance is observed with a parallel efficiency of 92% achieved on 1167 processors. A significant reduction in parallel performance is observed when the DOM radiation model is used. Using the DOM, increasing the mesh size by a factor of eight produced a two-fold decrease in parallel efficiency for the methane flame. This large decrease in parallel performance is due to the serial nature of the space-marching technique used to solve the DOM equations. The lowest parallel efficiencies achieved using the DOM were 54% for the methane-air flame on 765 processors and 67% for the ethylene-air flame on 822 processors.

6.5.3 Computational cost for methane flame

The computational cost as measured in terms of the wall-clock time for the methane flame calculations on the 96-block mesh (8064 cells) is provided in Table 6.2 for several different gas-phase mechanisms with varying levels of complexity. All computations use the DOM for radiation and solve the full set of governing equations, Eqs. (3.2a)–(3.2f). They were each started from the same initial guess. The results show that although wall time increases as more species are introduced to describe the gaseous phase, the number of Newton iterations remains virtually unaffected. This demonstrates the effectiveness of the Newton-Krylov approach advocated here. The calculation with 101 species is completed in less than three hours when 96 processors are used.

The performance of the proposed algorithm was also compared to similar numerical frameworks for studying soot that were discussed at the beginning of Chapter 5. Zhang et al. [70] performed computations for the same methane flame that is studied here on a mesh with 16 512 cells using the modified version of GRI-Mech 3.0. They reported wall-clock times of 350 min to obtain converged flame solutions when soot was neglected using 12 processors with similar floating point performance as those used in the the

Table 6.2: Wall-clock times for methane flame on 96-block mesh using 96 processors and various gas-phase reaction mechanisms.

Gas-Phase Mechanism	Gaseous Species	Wall Time (min)	Newton Steps
Kazakov and Frenklach [392]	24	16.8	620
Gri-Mech 3.0	36	29.8	662
Appel et al. [31]	101	176.5	609

present work. Assuming a 50% parallel efficiency on 96 processors (this a valid assumption since parallel performance decays exponentially as more processors are used [393]) and that computation time varies linearly with the number of cells, their solution algorithm is expected to take 35 min using 96 processors on a mesh with 8064 cells. The new algorithm proposed here required only 29.8 min to solve the full governing equations, which included soot. This would seem to provide a substantial reduction in the computational time required to perform detailed simulations of laminar flames since the estimated computation time for the Zhang et al. solution method does not include the additional cost of solving the equations governing soot. Additionally, the computational framework described herein provides a much more general approach for laminar flames by solving the unmodified, fully-compressible, gas-phase equations on complex domains using multi-block, body-fitted mesh. The proposed framework would also seem to offer similar performance improvements over the methodology proposed by Ern et al. [333]. Although, the comparison is made difficult by uncertainties in the relative computational performance of the computer processors used and because Ern et al. only report wall-clock times for a portion of the overall solution.

CHAPTER 7

EFFECTS OF PRESSURE AND GRAVITY IN ETHYLENE DIFFUSION FLAMES

One of the main goals of this research is to study the influence of gravity and pressure on the sooting characteristics and structure of laminar diffusion flames. In this chapter, predictions for the ethylene-air diffusion flames studied by Panek and Gülder [93] at pressures between 0.5–5 atm are presented and discussed. Calculations were performed under both normal- and zero-gravity conditions to help separate the effects of pressure and buoyancy on soot formation. Similar results for methane-air diffusion flames between 1–60 atm follow in Chapter 8.

The burner configuration is first discussed and specific details of the calculations are described. Following this, the accuracy of the soot model and its ability to capture the effects of pressure are assessed against the available experimental data. The influence of gravity and pressure are then discussed in detail.

7.1 Coflow Burner Configuration

The experimental apparatus used by Panek and Gülder [93] consists of a coflow burner, Fig. 7.1(b), housed inside a cylindrical pressure vessel, Fig. 7.1(a). The burner has a central fuel tube of 3.06 mm exit diameter and a concentric coflow-air tube of 25.4 mm inner diameter. Both the inner and outer surfaces of the fuel tube are chamfered with a round edge at the nozzle exit plane, which introduces uncertainties in the fuel's outlet velocity profile. For all the flames, constant mass flow rates for ethylene and air of 0.482 mg/s and 0.11 g/s were maintained, respectively, corresponding to an equivalent carbon flow rate of 0.412 mg/s. Panek and Gülder obtained measurements for temperature and soot volume fraction in flames at pressures between 0.5 to 5 atm, so calculations were performed at 0.5, 0.7, 1, 2, and 5 atm. While experimental measurements were only obtained under normal-gravity conditions, the calculations were performed for both normal- and zero-gravity levels. The temperature of the fuel and air supplied to the burner was assumed to be equal to 300 K for all cases. All computations were obtained using the skeletal mechanism of Law [389] for ethylene-air combustion (see Section 6.1.2).

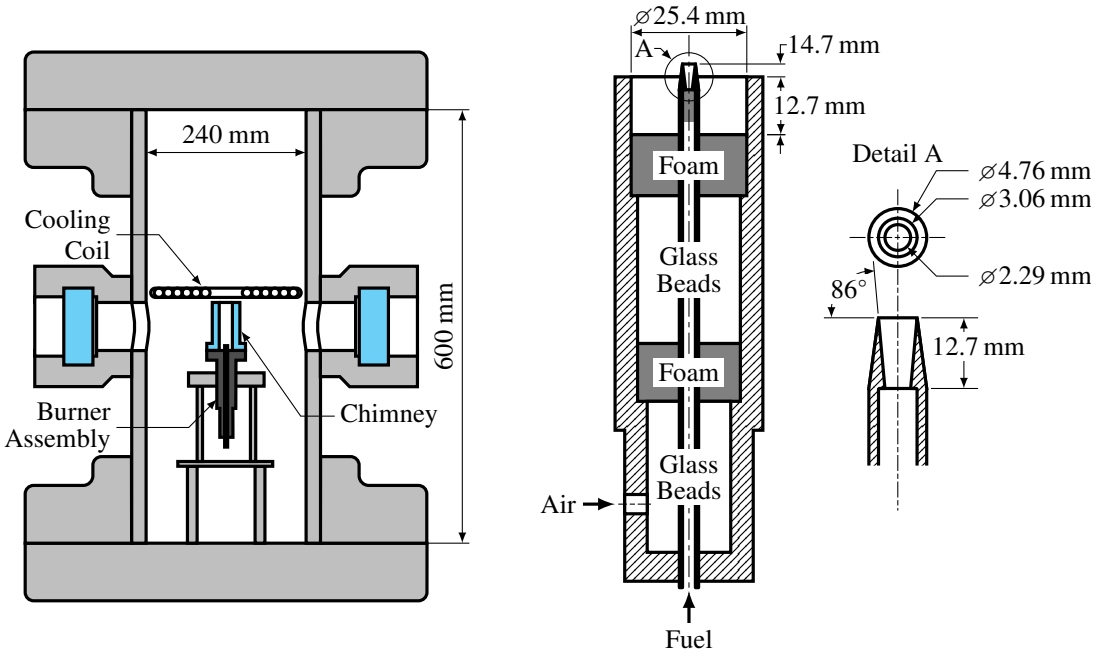

(a) Pressure vessel (b) Burner assembly

Figure 7.1: Schematic of the pressure vessel combustion apparatus used in the experiments conducted by Panek [394] and Joo and Gülder [44].

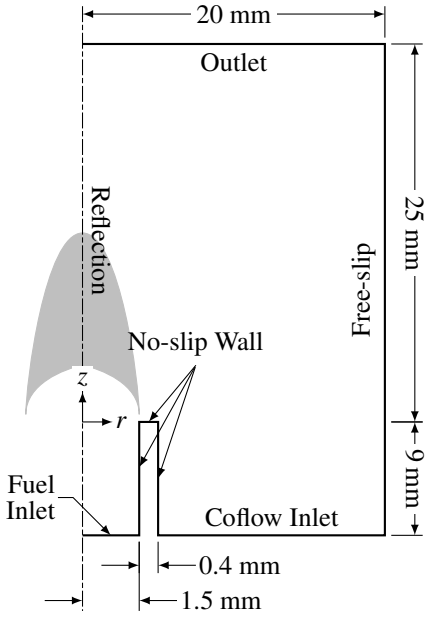

Figure 7.2: Computational domain and boundary conditions.

7.2 Numerical Model

7.2.1 Computational Domain and Boundary Conditions

The two-dimensional computational domain used for the coflow burner is shown schematically in Fig. 7.2 along with the applied boundary conditions. The domain extends radially outwards 20 mm and downstream

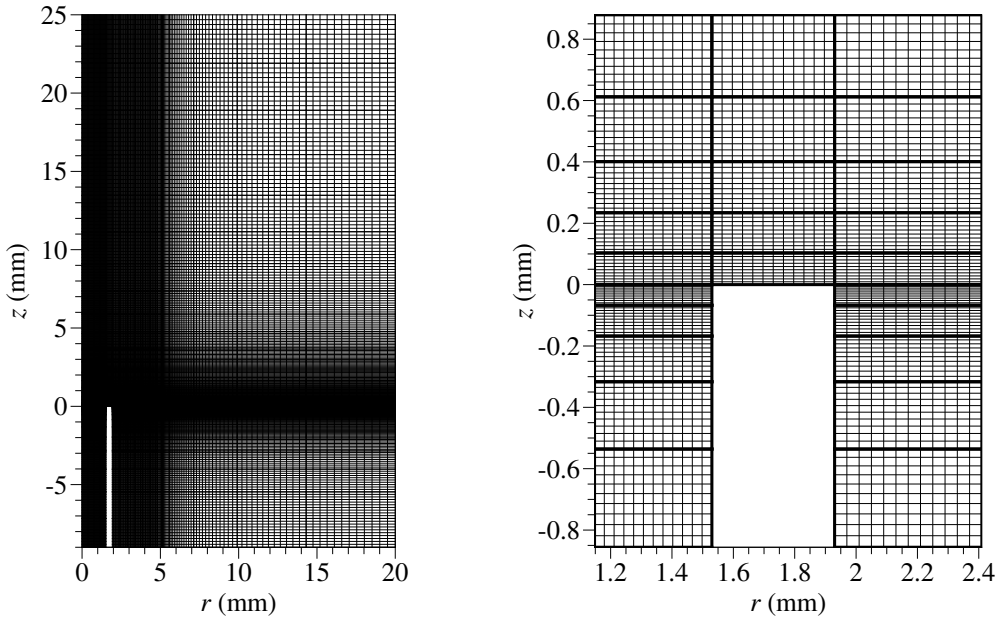

(a) Entire domain (b) Closeup of fuel tube region

Figure 7.3: Computational grid used for all flame calculations described in Chapters 7 and 8. Block boundaries are shown in (b) designated by bold lines.

25 mm. It also extends 9 mm upstream into the fuel and air tubes to account for the effects of fuel preheating [64] and better represent the inflow velocity distribution. As shown in Fig. 7.2, the chamfered edge of the fuel tube was approximated by a tube with 0.4 mm uniformly-thick walls. The three surfaces that lie along the tube wall were modelled as fixed-temperature walls at 300 K with zero-slip conditions on velocity. All other boundary conditions are exactly the same as those described in Section 6.1.

The computational domain in Fig. 7.2 was subdivided into 192 cells in the radial- and 320 in the axial-direction to form a structured, non-uniformly-spaced mesh of 60 000 cells. These cells were clustered towards the burner exit plane to capture interactions near the fuel tube walls and towards the centerline to capture the core flow of the flame. A fixed mesh spacing of approximately 35 μm was specified in the radial-direction between r=0 and r=4.8 mm. The vertical spacing approaches 5.6 μm near the fuel tube exit plane. The resulting mesh, Fig. 7.3, was employed for all calculations in this chapter, zero- and normal-gravity, to facilitate the comparison. While no AMR was used for this study and the one described in Chapter 8, manually refining the mesh did not significantly improve the numerical solution.

7.2.2 Solution Procedure

Solutions for each operating condition were obtained through the following steps:

Step 1. *Specify the initial conditions.* The domain is initialized with cold air and fuel and a small rectangular region above the burner exit plane is used as an igniter to initiate chemical reactions. This igniter region is either initialized with an unburt mixture of stoichiometric proportions at 1400–1800 K or a mixture of equilibrium combustion products.

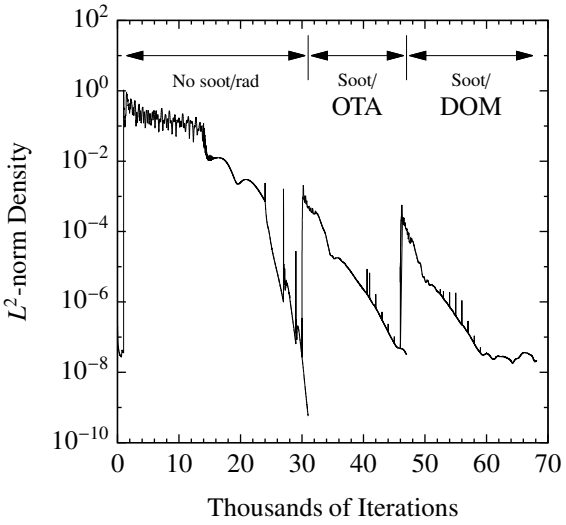

Figure 7.4: Typical convergence histories for the ethylene-air flames. The normalized L^2-norm of the continuity equation is plotted as a function of non-linear iteration number.

Step 2. *Compute the initial guess neglecting soot and radiation.* To overcome the somewhat chaotic transient period that accompanies ignition, a semi-implicit relaxation scheme [337] is used to partially-solve Eqs. (3.2a)–(3.2d) and compute an initial guess for Newton's method. The initial guess is obtained after about 10 000 iterations using a CFL between 0.1–0.5 and $M_{\text{ref}} = 0.1$.

Step 3. *Solve reacting flow neglecting soot and radiation.* Using the solution computed in step 2 as an initial guess, Eqs. (3.2a)–(3.2d) are solved with the implicit algorithm described in Section 5.1.6. As the solver converges towards the final solution, the CFL is slowly increased to between 10–100 and M_{ref} is decreased to 10^{-3}.

Step 4. *Turn on soot and optically-thin radiation models.* The fully converged solution obtained in step 3 is used as an initial guess. Due to the strong coupling between soot, radiation and temperature, another chaotic non-linear phase results as the solution adjusts. This phase is nursed by reducing the CFL to between 0.1–1 and then slowly increasing it back up to 4–10.

Step 5. *Solve for the final solution using the DOM.* Typically, no special treatment is required when the solution from step 4 is used as an initial guess. For cases involving soot concentrations exceeding 10 ppm, the CFL must be lowered slightly to maintain stability.

Convergence was achieved when the L^2-norms of the mass, momentum, and energy residuals were reduced by at least seven orders of magnitude. A sample convergence history for the density residual is illustrated in Fig. 7.4.

7.3 Comparison with Experiment

Panek and Gülder [93] constructed radial profiles for temperature and soot volume fraction from line-of-sight measurements obtained using the spectral soot emission diagnostic (SSE) technique [395]. This technique

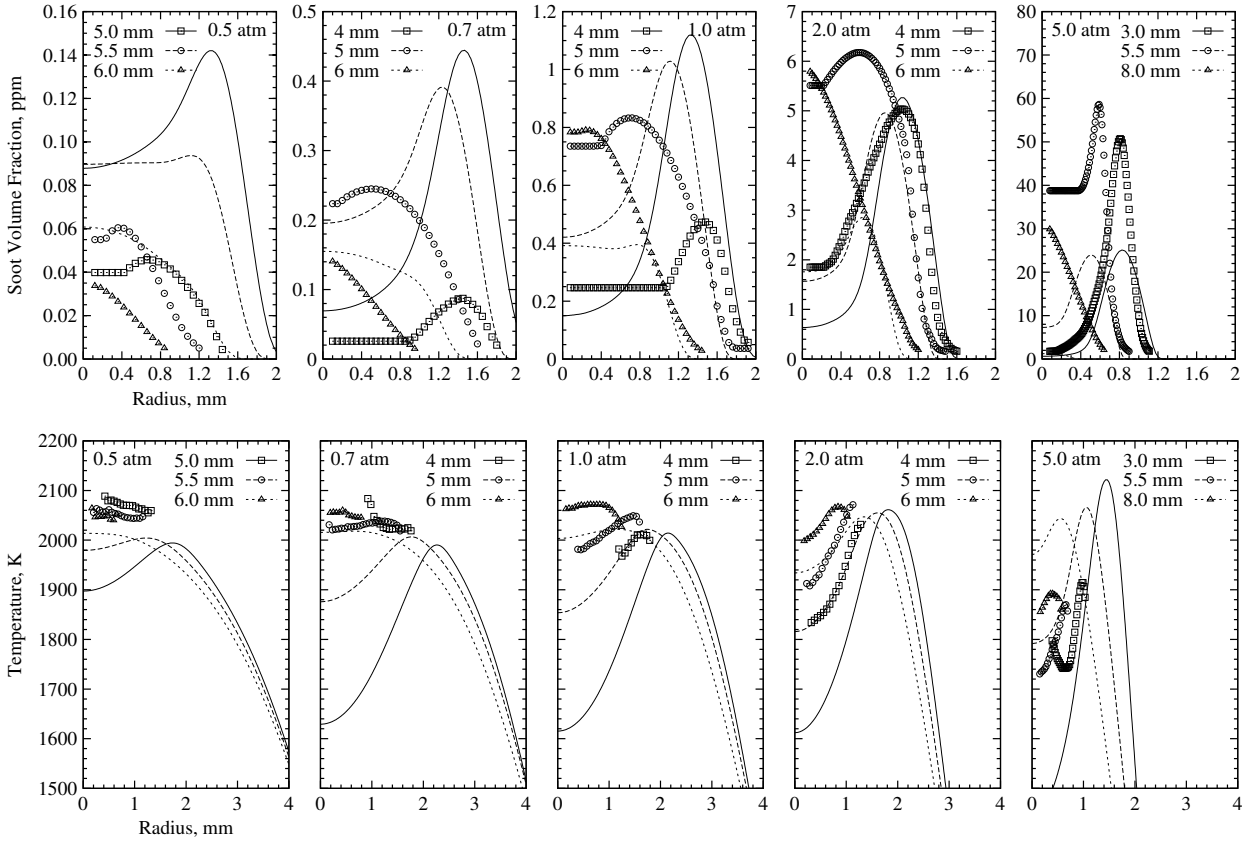

Figure 7.5: Measurements of Panek and Gülder [93] (symbols) and numerical predictions (lines) for radial profiles for soot volume fraction and temperature at various flame heights.

measures the line-of-sight radiation emitted by the soot particles along chords through the flame using a charge-coupled device (CCD) camera.

7.3.1 Radial Profiles

Predicted radial profiles for soot volume fraction and temperature are compared with the experimental measurements obtained by Panek and Gülder [93] in Fig. 7.5 for each operating pressure investigated. Only the numerical results obtained for the normal-gravity flames are presented in the figure. Three axial locations were chosen for this comparison: low in the flame where soot particles undergo nucleation and growth, the middle of the flame near the maximum soot volume fraction, and higher in the flame where soot is oxidized. The model predicts many of the experimentally-observed trends, but generally over-predicts soot volume fractions throughout the 0.5 to 1 atm flames and under-predicts soot in the 2 and 5 atm flames.

In both the experiments and calculations, soot is formed in an annulus downstream of the fuel tube rim. The measured soot volume fractions initially increase with height and then decrease as soot is oxidized higher up in the flame. This initial increase is not predicted between the three axial heights shown in Fig. 7.5 as soot volume fractions have already begun decreasing at the lowest height considered for each flame. This discrepancy suggests that the numerical model predicts the initial formation of soot lower in the flame than measured. As pressure is increased, the location of the peaks in the measured radial

profiles for soot volume fraction contract radially-inwards, the peaks become more pronounced, and soot concentrations increase. While these features are observed in the numerical results, the magnitudes of the computed soot volume fractions are greatly over-predicted in most cases, especially in the annular region with high soot concentrations. The degree of this over-prediction is largest at 0.5 atm and diminishes as pressure is increased. At 5 atm, the calculations under-predict the peak soot volume fractions by about a factor of two.

Despite the errors in the predicted soot volume fraction, the computed radial temperature profiles given in Fig. 7.5 agree quite well with the measurements. One exception occurs at 5 atm where peak temperatures are over-predicted by up to 200 K. Moreover, the observed discrepancies for temperature do not explain the errors in the computed soot volume fraction that were discussed previously. At low pressures, between 0.5 and 1 atm, temperatures are under-predicted while soot volume fraction is over-predicted. The opposite is observed at 5 atm. In all flames, the temperatures along the centerline are somewhat under-estimated.

Similar relationships between pressure, flame height, and temperature are observed in both the numerical predictions and experimental measurements. The experimental and numerical temperature profiles possess an annular structure similar to the radial profiles for soot volume fraction except that the radial location where temperature peaks occurs at a much larger radius. With increasing height in the flame, the location of the peak temperatures gradually shifts towards the centerline in both sets of results. A slight increase in temperature with increasing height is observed in the numerical results, except between 2 and 5 atm where peak temperatures steadily decrease with increasing height. While similar trends were also measured, the small number of valid temperature measurements makes a detailed comparison rather difficult. For example, the measured peak temperatures increase with height in the 0.7, 1, and 2 atm flames while they decrease with height in the 0.5 and 5 atm flames.

7.3.2 Soot Volume Fraction Contours

Two-dimensional contour plots of soot volume fraction were constructed from the experimental measurements and are compared with the numerical results for the normal-gravity flames in Fig. 7.6. Qualitatively, the predicted and measured flame geometries are similar and the narrowing of the flame with increasing pressure is clearly observed in both sets of results. The flame height based on soot volume fraction between 0.5 and 1 atm is also accurately predicted by the model. Within this range of pressures, a constant height of approximately 6.7 mm is predicted when the edge of the visible flame is approximated by the isocontour where the soot volume fraction is equal to 0.01 ppm. While the measured heights are comparable, it is difficult to clearly distinguish a visible flame height from the measured contours since the tip of the flame appears cut off. As pressure is increased from 1 to 5 atm, both the measured and predicted flame heights increase, but the model under-predicts this increase. A height of roughly 8.5 mm is predicted at a pressure of 5 atm compared to a measured height of 9.5 mm. The model also incorrectly predicts the location of the peak soot volume fraction and, in general, some significant differences between predicted and measured soot concentrations are observed at lower flame heights. Soot is predicted to reach a maximum in an annular region near the middle of the flame whereas the peak is experimentally-observed to occur along the centerline

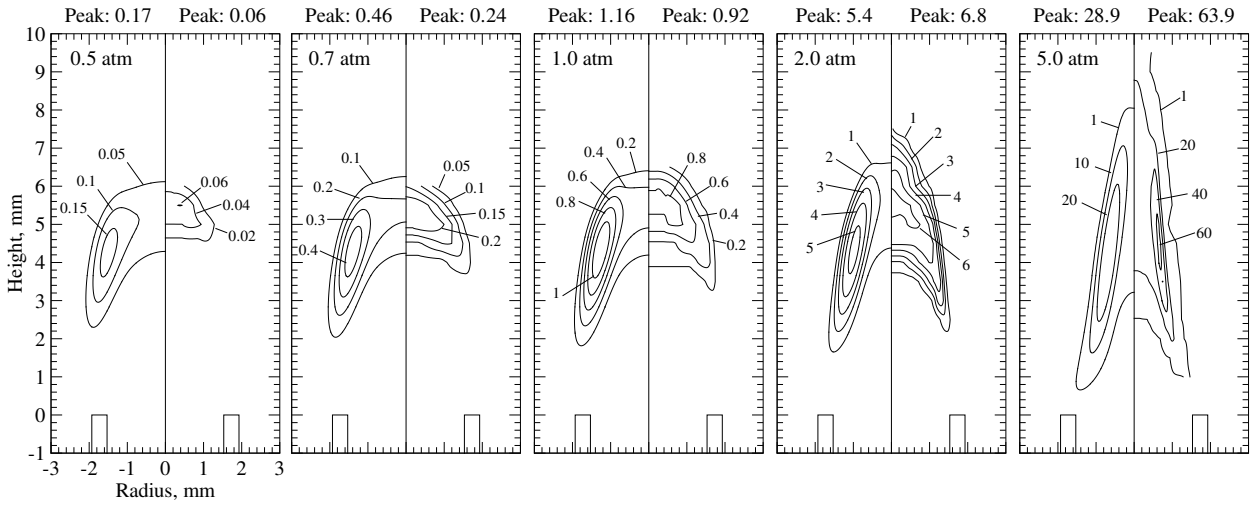

Figure 7.6: Predicted (left) and measured (right) contours for soot volume fraction in ppm. Experimental measurements are taken from Panek and Gülder [93].

near the flame tip, although the measurements display a pronounced annular structure at 5 atm. Additionally, the model always predicts that soot production begins further upstream than in the experiments. With increasing pressure, both experiments and predictions show that soot formation begins lower in the flame and that the annular structure becomes thinner. However, these observations are more pronounced in the experimental measurements.

7.3.3 Soot Yield

To assess the fuel's propensity to soot and its sensitivity to pressure, the variation in the carbon conversion factor with pressure was studied. This factor is defined as $\eta_s = \dot{m}_s/\dot{m}_c$ where $\dot{m}_c$ is the carbon mass flow rate at the nozzle exit [9]. The mass flux of soot through a horizontal cross-section is

$$\dot{m}_s = 2\pi\rho_s \int \phi v r \, \mathrm{d}r \tag{7.1}$$

where $\rho_s = 1.9$ g/cm^3 is the density of soot and v is the axial velocity. Since the velocity is not known in the experiments, it is estimated by $v = \sqrt{2az}$ where z is the height above the burner and a is an acceleration constant commonly assumed equal to 25 m/s^2 [46]. However, at sub-atmospheric pressure, assuming non-buoyant conditions, the acceleration varies proportional to the square of pressure, $a \propto p^2$ [7]. Therefore, $a = 12.25$ m/s^2 at 0.7 atm and $a = 6.25$ m/s^2 at 0.5 atm. The computed velocity was also used as an alternative to estimate $\dot{m}_s$ in Eq. (7.1) using the experimentally-measured soot volume fractions.

The effect of pressure on the predicted and measured maximum η_s for the normal-gravity flames is presented in Fig. 7.7. Numerical results obtained using a gravitational constant of 0 m/s^2 are also provided in the figure, but they are not discussed until the following section. As observed in the figure, the normal-gravity calculations greatly over-predict the experimental values at 0.5 atm. Nonetheless, the agreement between measurements and predictions improves as pressure is increased to 2 atm. At 5 atm, the predictions under-predict the maximum amount of fuel carbon that is converted to soot. It is believed that the larger

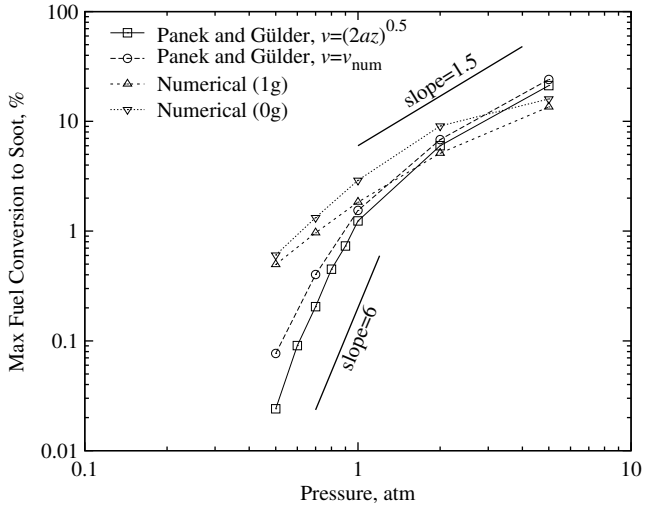

Figure 7.7: Maxium fuel carbon converted to soot as a function of pressure.

differences at low pressures (0.5 and 0.7 atm) are caused by systematic errors in the values for soot volume fraction derived using the SSE technique. SSE errors become large as soot volume fractions decrease below 0.5 to 1 ppm since measured intensities approach the background levels. This may also explain the extremely large measured dependence of η_s on pressure at low pressures. The measured relationship between η_s and pressure is approximately $\eta_s \propto p^{5.6}$ between 0.5 to 1 atm and $\eta_s \propto p^{1.8}$ between 1 and 5 atm (based on $v = \sqrt{2az}$). Using the calculated velocity to determine the experimental values for η_s instead of $v = \sqrt{2az}$ does not significantly affect these observed trends with pressure ($\eta_s \propto p^{4.3}$ between 0.5 to 1 atm and $\eta_s \propto p^{1.7}$ between 1 and 5 atm), but shifts the values for η_s upward slightly. Numerical predictions for the maximum η_s in the normal-gravity flames display a dependence proportional to $p^{1.7}$ between 0.5 to 2 atm and $p^{1.1}$ from 2 to 5 atm. While the model correctly predicts the decreasing sensitivity of the peak η_s with increasing pressure, the strength of this pressure dependence is always under-predicted and the magnitudes of the peak η_s are over-predicted. This under-estimated pressure-dependence is consistent with the over-predicted soot volume fractions at low pressures and under-predicted soot volume fractions at 5 atm that were observed in Figs. 7.5 and 7.6.

7.4 Effects of Gravity and Pressure

7.4.1 Soot Yield

As observed in Fig. 7.7, gravity has a large effect on the predicted maximum value for η_s. The maximum η_s at each pressure is larger in zero-gravity with the largest difference between the two, a factor of 1.7, occurring at a pressure of 2 atm. There is also a significant change in the relationship between η_s and pressure when gravity is eliminated. For example, the maximum η_s in the zero-gravity flames displays a dependence on pressure proportional to $p^{2.0}$ between 0.5 to 2 atm and $p^{0.6}$ from 2 to 5 atm. This observed zero-gravity relationship between η_s and pressure is stronger than predicted in normal-gravity at low pressures and weaker at high pressures.

The differences observed between the η_s-pressure relationships at the two levels of gravity are partially

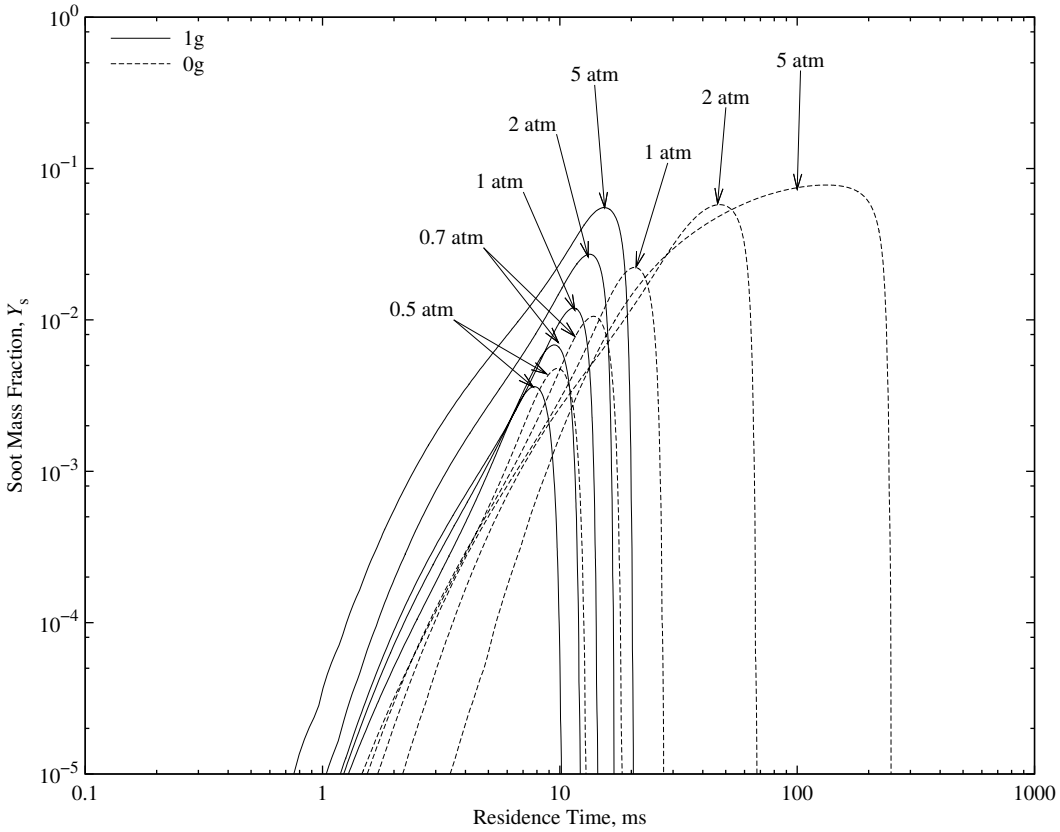

Figure 7.8: Soot mass fraction along a particle streamline originating from the reaction zone and passing through the maximum soot volume fraction.

explained by comparing the local variation of the soot mass fraction, Y_s, along a soot particle's path, shown in Fig. 7.8 for each flame. In the figure, the trajectory of the soot particle originates at the reaction zone and passes through the region of maximum soot volume fraction. The reaction zone was designated by the location where the mixture fraction is stoichiometric. A similar procedure was performed by Honnery and Kent [396, 397] to analyze experimental measurements in laminar diffusion flames of ethylene and ethane.

For this numerical study, the mixture fraction was computed using the following relation proposed by Bilger [398] for ethylene-air flames:

$$Z = \frac{\frac{1}{2}Y_C/M_C + \frac{1}{4}Y_H/M_H + \frac{1}{3}(Y_{O,2} - Y_O)/M_O}{\frac{1}{2}Y_{C,1}/M_C + \frac{1}{4}Y_{H,1}/M_H + \frac{1}{3}Y_{O,2}/M_O} \tag{7.2}$$

From Eq. (7.2), the stoichiometric value of Z is equal to

$$Z_{st} = \frac{Y_{O,2}/M_O}{\frac{1}{2}Y_{C,1}/M_C + \frac{1}{4}Y_{H,1}/M_H + \frac{1}{3}Y_{O,2}/M_O} \tag{7.3}$$

where Y_j and M_j are the mass fractions and atomic masses for the elements carbon, hydrogen, and oxygen. Subscripts 1 and 2 refer to values in the fuel and air streams, respectively.

As observed in Fig. 7.8, Y_s initially increases with residence time, peaks, and rapidly decreases. At 0.5 atm, the differences between the normal- and zero-gravity flames are small. Residences times are similar

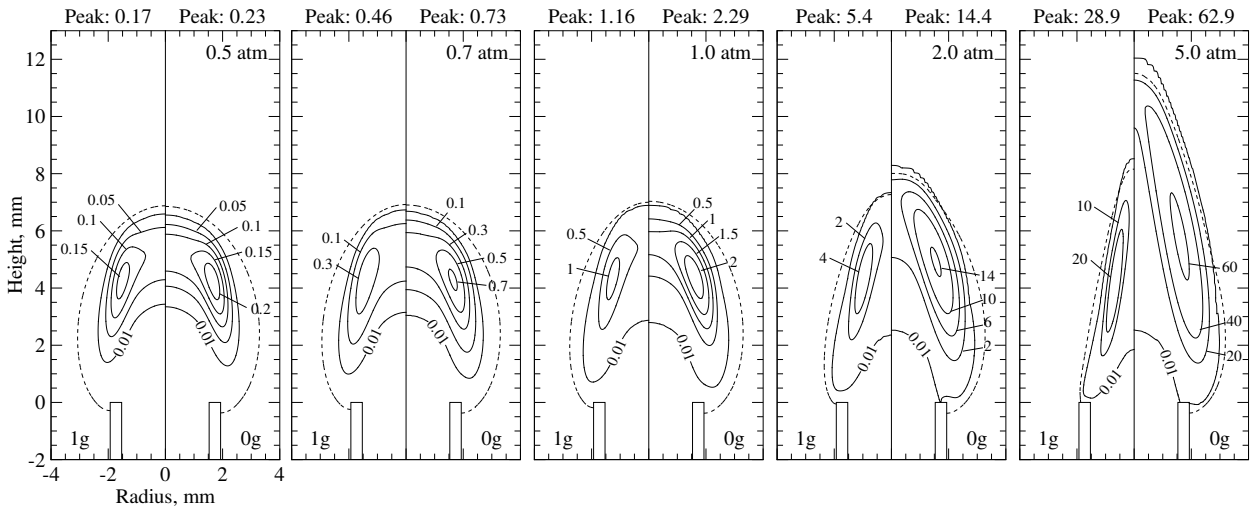

Figure 7.9: Predicted contours for soot volume fraction in the normal-gravity (left) and zero-gravity (right) flames. Units in ppm. Dashed black lines denote the location where the mixture fraction is equal to the stoichiometric value. Visible flame shape is denoted by the 0.01 ppm contour.

and the peak Y_s is only slightly enhanced at zero-gravity. Since soot levels are low and residence times do not increase much from normal to zero gravity at 0.5 atm, differences in predicted temperatures are expected to be small at this pressure. As such, the enhanced soot production which occurs in the 0.5 atm flame when gravity is neglected is attributed to longer residence times and reduced flow velocities. Reducing flow velocities slows the entrainment of fresh oxidizer into the flame, promoting pyrolysis and delaying soot oxidation.

For the normal-gravity cases, more soot is produced at elevated-pressures mainly because soot formation begins earlier and lasts longer. The soot formation rates, i.e., the slopes of the lines in Fig. 7.8, do not change much as pressure is increased. Soot formation takes more time to start when pressure is increased for the zero-gravity flames, but the soot yield still increases because the overall time from nucleation to complete destruction gets longer. This observed increase in residence time between 0.5–5 atm is significantly larger for the zero-gravity flames; a factor of 2 increase is observed at normal gravity while a factor of 20 increase occurs under zero-gravity conditions. This produces higher soot concentrations in zero gravity and results in the previously-mentioned enhanced dependence of η_s on pressure at low pressures. The lower zero-gravity dependence of η_s on pressure above 2 atm is attributed to a lack of available acetylene for further soot production and decreased temperatures. Radiative heat losses increase significantly above 1 atm in zero gravity since residence times increase with pressure-squared and soot levels are high.

The predicted contours of soot volume fraction for the flames at both levels of gravity are compared in Fig. 7.9. The location of the stoichiometric mixture fraction surface in each flame is also indicated in Fig. 7.9 to compare the effects of gravity and pressure on flame geometry. As observed in the figure, soot concentrations at each pressure are consistently higher for the zero-gravity flames. For example, the peak soot volume fraction in zero gravity is roughly 1.4, 1.6, 2.0, 2.7, and 2.2 times larger than the equivalent normal-gravity flame at 0.5, 0.7, 1, 2, and 5 atm, respectively. A similar factor-of-two enhancement of the peak soot volume fraction in micro-gravity was measured during drop-tower experiments [82, 87, 399]

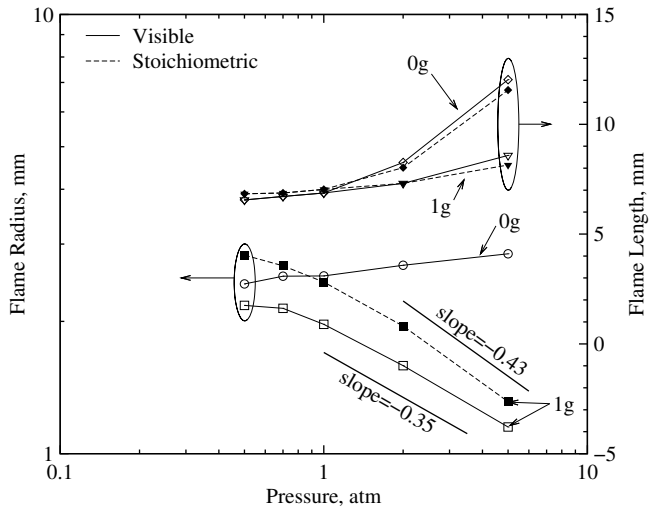

Figure 7.10: Effect of pressure and gravity on the computed flame shape. Flame radii correspond to an axial height of 4 mm.

and predicted by Kong and Liu [26, 27]. Kaplan et al. [23] predicted a much larger 11-fold increase in soot volume fraction for laminar ethylene-air jet diffusion flames in quiescent air. Between 0.5 and 1 atm, the predicted soot concentrations for each pressure have a similar structure under normal- and zero-gravity conditions except that soot is formed slightly lower in the zero-gravity flames. This earlier appearance of soot occurs primarily because velocities are slower and residence times longer for the zero-gravity cases. Above 1 atm, the heights of the zero-gravity flames become significantly longer than the normal-gravity flames since more soot is produced and oxidation rates are slower in zero-gravity.

There is a noticeable difference in the effect of pressure on flame structure at the two gravity levels. Under normal gravity, the annular soot-containing region becomes thinner and more pronounced as pressure is increased to 5 atm. However, thermophoretic forces become relatively more important in zero-gravity, especially at high pressures where flow velocities are low, which drive particles off flow streamlines and thicken the annular soot-containing region. The increased effects of molecular diffusion, which also become more important as pressures are increased in the absence of gravity, contribute to the thickening of the soot-containing region by widening the reaction zone.

7.4.2 Flame Geometry

The effect of pressure on flame shape, illustrated in Fig. 7.9, is different at normal- and zero-gravity. The shapes of the flames are similar when pressure is low, but deviate significantly as pressure is increased. For example, flame width decreases with increasing pressure at normal-gravity, in accordance with previous findings [22, 40, 42–44], while it increases with pressure at zero-gravity. The zero-gravity flames also become significantly longer than the normal-gravity ones above 1 atm. These observed differences are summarized in Fig. 7.10, which compares the computed flame lengths and radii for all flames. Two different methods were used to define the edge of the flame — based on the visible flame geometry and based on the stoichiometric mixture fraction. In this study, the visible edge of the flame is defined by the isocontour where soot volume fraction is equal to 0.01 ppm. At normal-gravity and high pressures, the visible and

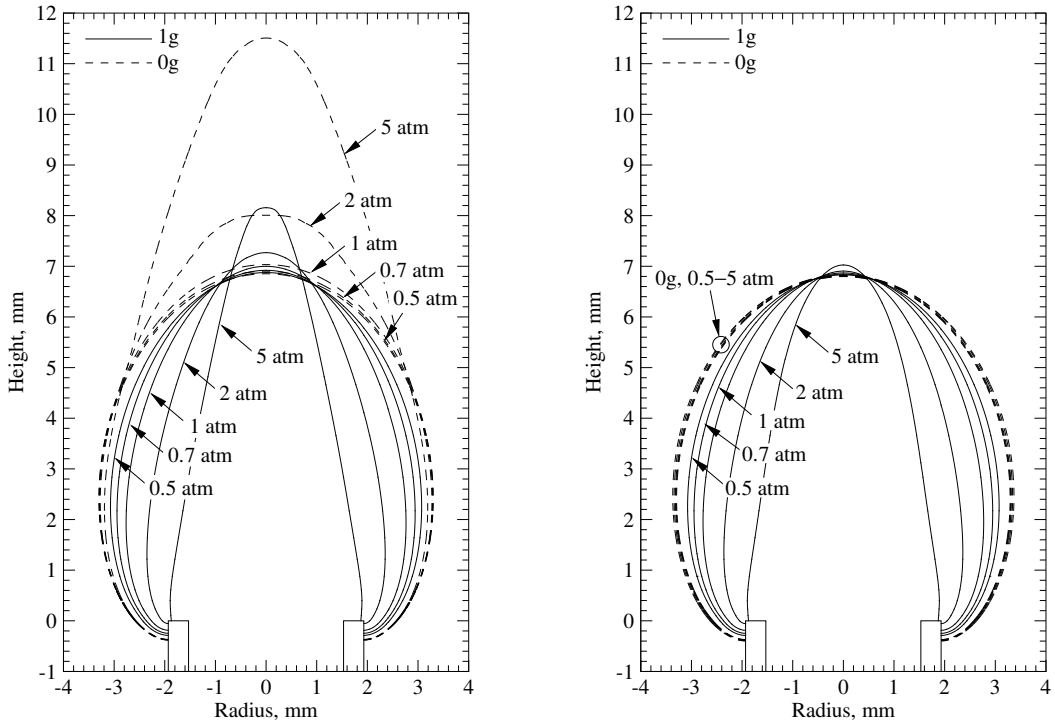

(a) soot and radiation included (b) soot and radiation neglected

Figure 7.11: The effect of pressure and gravity on the stoichiometric mixture fraction surface.

stoichiometric flame radii are proportional to $p^{-0.43}$ and $p^{-0.35}$, respectively. However, a much slower rate of decrease is observed between 0.5 to 2 atm since the effects of buoyancy weaken as pressure is decreased. Buoyant forces are not present in the zero-gravity cases and therefore soot transport via thermophoresis becomes increasingly important at high pressures where axial velocities are small. As a result, the visible widths of the zero-gravity flames increase proportional to $p^{0.07}$ over the entire range of pressures considered. The rapid increase in flame height between 1 and 5 atm at zero-gravity suggests that the 5 atm zero-gravity flame is close to the smoke point.

The strong effect of gravity and pressure on flame shape is illustrated in Fig. 7.11(a), which compares the predicted stoichiometric mixture fraction isocontours for each flame. Gravity has absolutely no effect on the flame height when soot and radiation are turned off, Fig. 7.11(b). This implies that the lengthening of the zero-gravity flames with pressures occurs solely because of the reduced flame temperatures and slower oxidation of soot.

7.4.3 Residence Time and Velocity

Under normal-gravity conditions, pressure should not affect the residence times in buoyancy-dominated laminar diffusion flames (see discussion in Section 1.4). However, as observed in Fig. 7.8, the particle residence time increases with pressure regardless of gravity level. While this change in residence time is expected for zero-gravity conditions because there are no buoyant forces to accelerate the flow, it is not clear why residence time increases at normal gravity. Under zero-gravity conditions, the axial velocity along the centerline, illustrated Fig. 7.12(a), decreases almost linearly with pressure. However, the centerline ve-

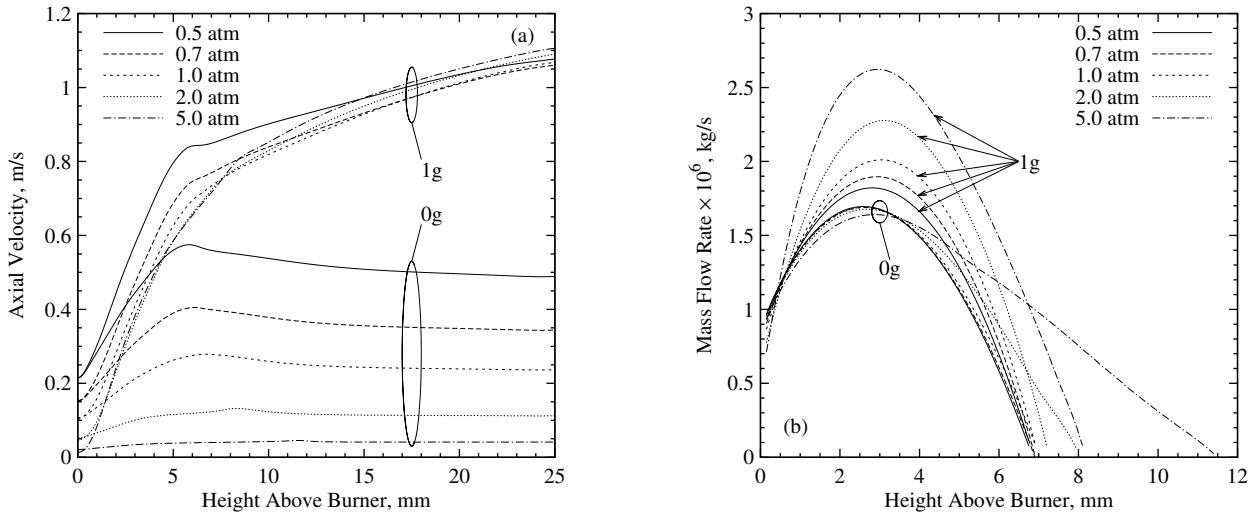

Figure 7.12: (a) Distributions of the predicted axial velocity along the flame centerline and (b) the mass flow rate through the stoichiometric flame envelope.

locities for the normal-gravity flames do not change much with pressure because buoyant forces quickly accelerate the flow. Thus, the change in residence time with increasing pressure at normal gravity occurs because the flame diameter is approximately proportional to $p^{-0.4}$ instead of $p^{-0.5}$ (the theoretical relationship). This leads to lower average velocities through the core of the flame and longer residence times under normal-gravity conditions. It suggests that the ethylene-flames studied here are still developing and not fully buoyancy dominated, even at 5 atm. This development is observed in Fig. 7.10 since the relationship between pressure and flame diameter appears to be changing asymptotically. These results would also explain the increase in flame height observed as pressure is increased under normal-gravity conditions.

Oddly, the mass flow rate through the flame envelope actually increases with pressure under normal-gravity conditions, illustrated in Fig. 7.12(b). For this study, the flame envelope is defined by the isocontour where the mixture fraction is stoichiometric. The mass flow decreases beyond about 3 mm since the flame begins to close. Under normal-gravity conditions, more of the surrounding coflow is entrained into the flame at higher pressures because the velocity of the surrounding air decreases while the velocity of the central core remains roughly constant. This creates an intense shear-layer between the two streams. The mass flow rate through the zero-gravity flames is unaffected by pressure, possibly because the flame diameter doesn't change and the velocities of the two streams both decrease at the same rate with pressure. The results shown in Fig. 7.12 indicate that residence time cannot always be assumed independent of pressure, at least at lower pressures.

7.4.4 Temperature and Radiation Heat Transfer

The predicted temperature contours for the normal- and zero-gravity flames are compared in Fig. 7.13(a). Temperature predictions were also computed neglecting soot and radiation, Fig. 7.13(b), to assess the impact of radiation on flame structure. At 0.5 atm, there is almost no difference between the predicted temperature fields at the two levels of gravity since the effects of radiation are small. However, radiation effects become

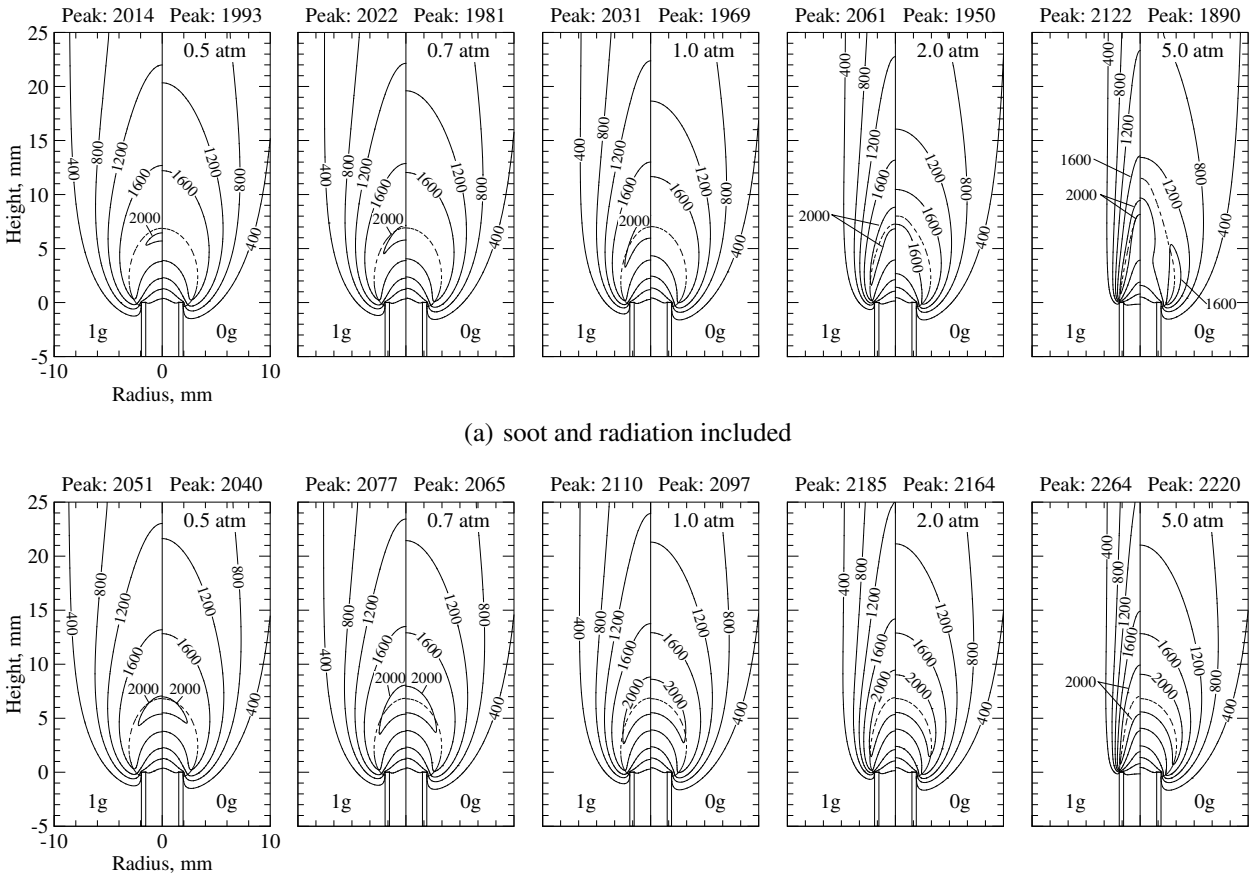

(a) soot and radiation included

(b) soot and radiation neglected

Figure 7.13: Predicted temperature contours for the normal-gravity (left) and zero-gravity (right) flames. Units in K. The dashed black lines correspond to the location where the mixture fraction is equal to the stoichiometric value.

large as pressure is increased to 5 atm which drastically alters the predicted temperature fields in both the normal- and zero-gravity flames. Residence times do not change much in the normal-gravity flames and, as such, radiation is primarily influenced only by the local soot concentrations. Increasing pressure has a much larger effect on radiation when gravity is absent as residence times are drastically increased and soot production is enhanced. This is evident by comparing the results computed with and without radiation, Figs. 7.13(a) and 7.13(b).

Considering the temperature predictions obtained without soot and radiation, Fig. 7.13(b), peak temperatures steadily increase with pressure. Temperatures are only marginally lower in zero-gravity since the transport of fresh reactants to the reaction zone is slower. When soot and radiation are included, Fig. 7.13(a), peak temperatures of the normal-gravity flames increase with pressure at a slower rate since any increases in heat-release is counter-acted by radiative heat losses. Radiation effects are much stronger at zero-gravity due to the increased residence time and, as a result, peak temperatures decrease with increasing pressure. Above 1 atm, the peak temperatures in the zero-gravity flames are significantly lower than those in the normal-gravity flames. There is also a considerable temperature drop along the centerline in zero-gravity. These low temperatures in the zero-gravity flames are one of the primary reasons for the decreased sensitivity of η_s to pressure observed above 1 atm.

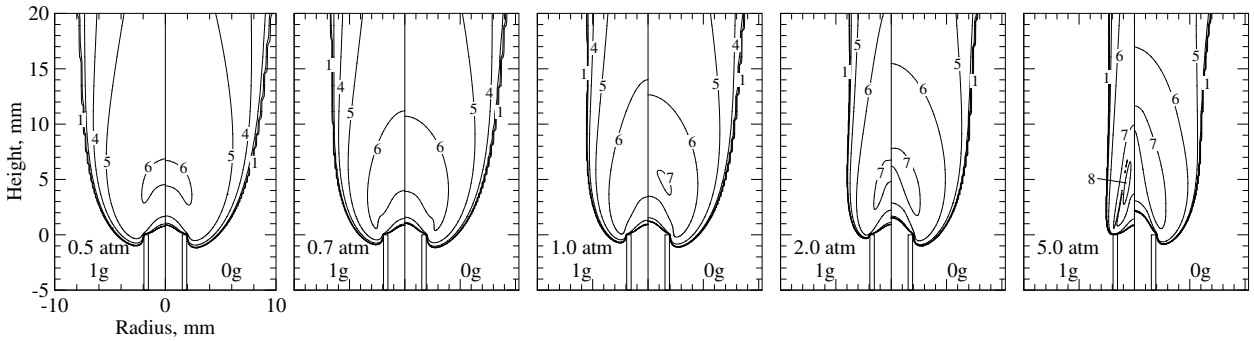

Figure 7.14: Predicted contours of the divergence of the radiative heat flux, $\nabla \cdot \vec{q}_{\text{rad}}$. Contours correspond to $\log_{10}\left[\max\left(-\nabla \cdot \vec{q}_{\text{rad}}\right), 1\right]$.

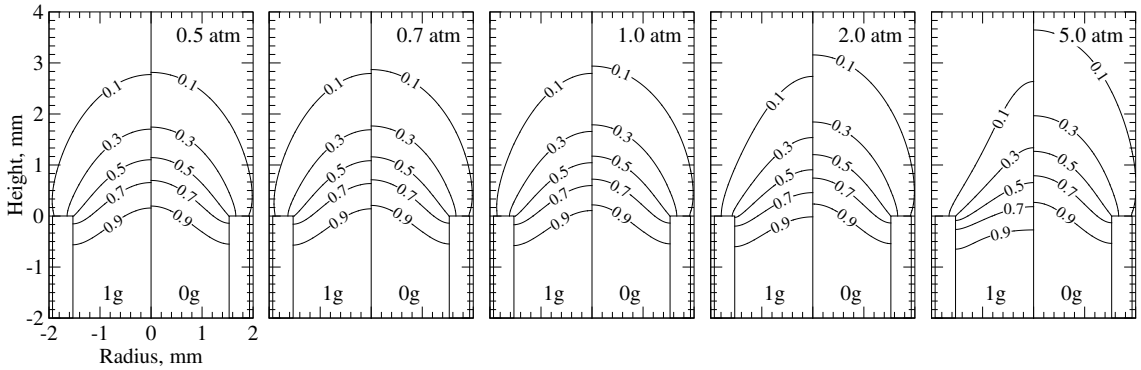

Figure 7.15: Predicted contours for ethylene mass fraction in the normal-gravity (left) and zero-gravity (right) flames.

The divergence of the radiative heat flux, $\nabla \cdot \vec{q}_{\text{rad}}$, is plotted in Fig. 7.14 for each flame. Since this quantity varies exponentially over the range of pressures studied, the logarithm of the negative component of $\nabla \cdot \vec{q}_{\text{rad}}$ is plotted in Fig. 7.14. At 0.5 atm, the predicted contours of $\nabla \cdot \vec{q}_{\text{rad}}$ at normal- and zero-gravity are very similar. However, the rapid increase in radiation transport with pressure produces significant differences between the predictions for $\nabla \cdot \vec{q}_{\text{rad}}$ in the two 5 atm flames. The magnitude of $\nabla \cdot \vec{q}_{\text{rad}}$ is larger in the zero-gravity flames below 2 atm but becomes larger in the normal-gravity flame at 5 atm. This is a direct result of the steeper temperature and soot concentration gradients in the normal-gravity flames at high pressures. There is also a significant amount of energy transported upstream into the coflow air supply tube. While this upstream energy transport vanishes under normal-gravity conditions when pressure is increased to 5 atm, it intensifies with pressure in the absence of gravity.

7.4.5 Species Mass Fractions

In the presence of gravity, buoyant forces rapidly accelerate the flow upward, entraining the surrounding co-flowing oxidizer stream and mixing the oxidizer with fresh fuel. Since buoyancy-induced acceleration scales with $p^2 g$, increasing pressure intensifies entrainment and speeds up oxidative pyrolysis. This phenomenon is observed in Fig. 7.15, which shows the predicted contours of ethylene mass fraction in the normal- and zero-gravity flames. For normal-gravity conditions, ethylene is consumed at a faster rate as pressure is increased from 0.5 to 5 atm. Early fuel pyrolysis is also observed inside the fuel tube at high pressures. When gravity is eliminated, increasing pressure while maintaining fixed mass flow rates has the opposite effect since flow

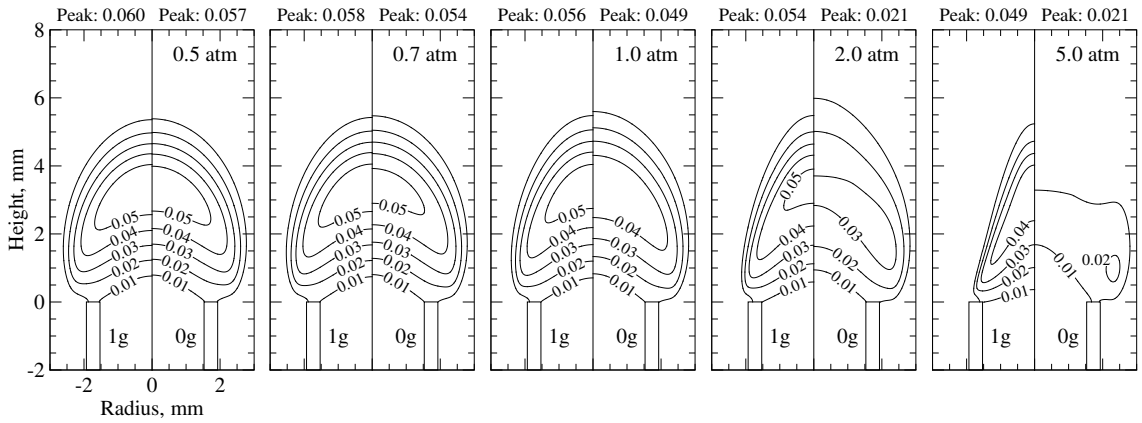

(a) soot and radiation included

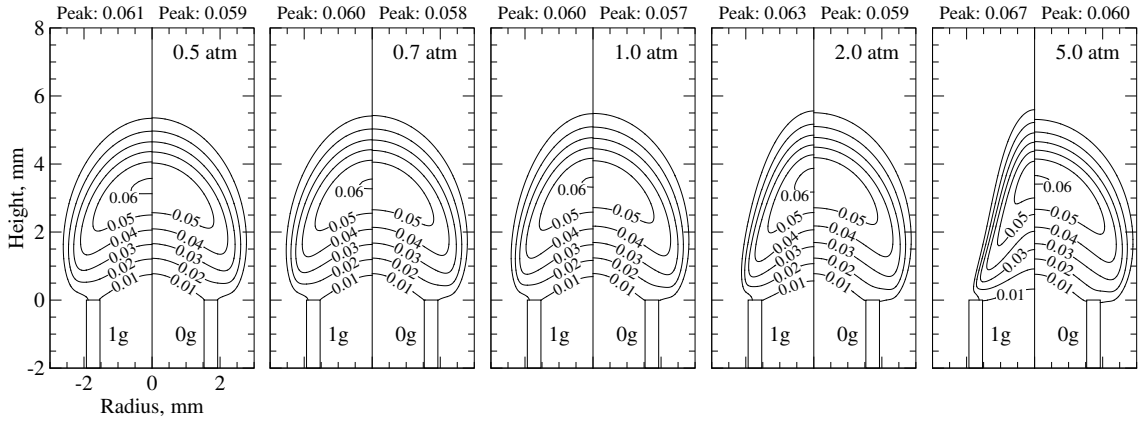

(b) soot and radiation neglected

Figure 7.16: Predicted contours for acetylene mass fraction in the normal-gravity (left) and zero-gravity (right) flames.

velocities are reduced. As such, convective transport slows and fuel consumption rates decrease. No early fuel pyrolysis is observed at zero-gravity due to the lower centerline temperatures which were observed in Fig. 7.13(a).

The predicted acetylene mass fractions for all of the flames studied are illustrated in Fig. 7.16(a). Acetylene concentrations steadily decrease as pressure is increased from 0.5 to 5 atm in both cases, normal- and zero-gravity, which is attributed to the consumption of acetylene to produce soot. This is confirmed by Fig. 7.16(b), which shows the predicted acetylene mass fractions computed when soot and radiation are neglected. The observed decrease in acetylene mass fraction with increasing pressure is substantially larger when gravity is neglected due to the long residence times and enhanced soot production. The low temperatures observed in Fig. 7.13(a) along the centerline at zero-gravity may also hinder the production of acetylene. These significantly lower acetylene concentrations above 1 atm in zero gravity contribute to the weaker η_s-pressure dependence observed when gravity is eliminated. Between 0.5 and 1 atm, acetylene concentrations and temperatures are similar at both levels of gravity, so the stronger η_s-pressure dependence in zero-gravity is caused by the effect of pressure on velocity and residence time.

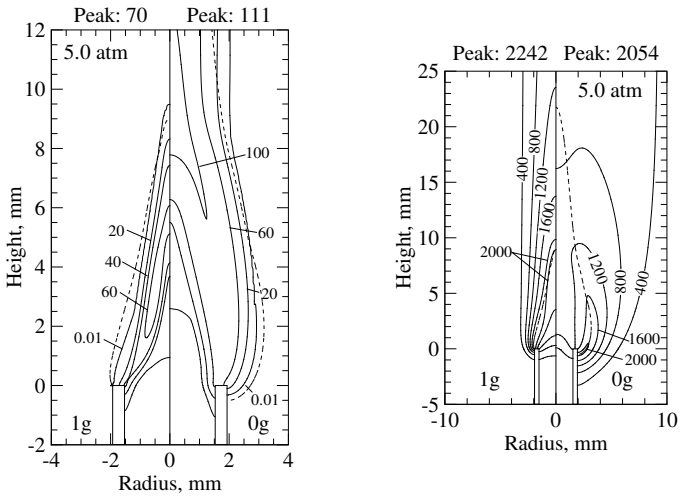

Figure 7.17: Soot volume fraction (left) and temperature (right) contours computed using an adiabatic wall boundary condition. Soot volume fraction in ppm and temperature in K. Dashed black lines denote the location where the mixture fraction is equal to the stoichiometric value.

7.5 Influence of Wall Boundary Condition

Panek and Gülder [93] observed a blue region at the base of the flame that vanished as pressure was increased to 5 atm. At this pressure, the yellow luminous portion of the flame extended from the flame tip all the way to the burner rim. Large gradients occur near the fuel tube rim, which were discussed in the previous sections, and significant heating of the fuel tube is expected as a result. The temperatures along the outer surface of the burner tube were measured by Gülder et al. [400] for laminar coflow diffusion flames of ethylene and propylene at atmospheric pressure. They reported fuel tube temperatures up to 100 K higher than the temperature of the fresh reactants. Based on the visual observations of Panek and Gülder [93] and the numerical results discussed in previous sections, this heating of the tube rim is expected to intensify as the flame base moves towards the burner rim with increasing pressure.

In order to assess the effect of gas-tube heat transfer on the numerical predictions, additional calculations were performed at 5 atm using an adiabatic boundary condition for the tube walls. Specifying adiabatic walls represents the opposite limit with respect to the effects of wall heating since the tube is allowed to heat up to the maximum possible temperature. The true boundary condition lies somewhere in between the two extremes.

The predicted soot volume fraction and temperature contours computed using the new boundary conditions are provided in Fig. 7.17 for the two flames. Changing the wall boundary condition significantly alters the numerical predictions; soot concentrations are larger and the visible flame heights of the two flames are longer in the absence of gas-tube heat transfer. Peak soot concentrations are 2.4 and 1.8 times larger using the adiabatic boundary conditions at normal and zero gravity, respectively. This increase in predicted soot volume fraction is attributed to the higher temperatures near the flame base which result when the walls are adiabatic. For adiabatic walls, temperatures exceed 2000 K near the tip of the tube in both cases. As such, soot production rates near the tube wall intensify and more soot is produced throughout the flame. For

the normal-gravity flame, the new calculations over-predicted the measured soot concentrations shown in Fig. 7.5 by about the same amount as they were under-predicted before. The newly predicted visible flame length is approximately 9.5 mm which is in better agreement with the experimental observations. When adiabatic walls are specified, the zero-gravity flame begins to emit smoke since soot is no longer fully oxidized before leaving the flame envelope. Changing the boundary condition also causes the peak soot volume fraction in zero-gravity flame to shift to the centerline.

Comparing the predictions for temperature in Fig. 7.13(a) and 7.17, the peak values are 120 and 164 K larger at normal- and zero-gravity, respectively, when adiabatic walls are specified as opposed to a fixed wall temperature. These peak values occur lower in the flame near the tip of the fuel tube. There is also a dramatic decrease in temperature along the centerline at zero-gravity since radiative heat losses are enhanced by the higher soot concentrations.

While there was some improvement in the predicted flame height, the overall agreement for temperature and soot volume fraction did not improve much when the adiabatic wall boundary condition was employed. A conjugate heat transfer analysis is required to obtain better agreement with the experimental results.

CHAPTER 8

EFFECTS OF PRESSURE AND GRAVITY IN METHANE DIFFUSION FLAMES

An analysis similar to the one described in Chapter 7 was also performed for the methane-air coflow diffusion flames of Joo and Gülder [44] between 10–60 atm. The details of the calculations and the numerical results are presented in the following sections.

8.1 Coflow Burner Configuration

Joo and Gülder [44] used the exact same experimental setup and burner as described in Chapter 7, although the fuel and flow rates were different. For all the flames, the mass flow rates of fuel and air were maintained at constant values of 0.55 mg/s and 0.4 g/s, respectively, which corresponds to an equivalent carbon flow rate of 0.412 mg/s. Note that both sets of flames, the ethylene-air ones studied in the previous chapter and the methane-air ones studied here, have equal carbon mass flow rates. This allows direct comparisons to be made between the sooting propensities of both fuels.

In the present study, calculations were performed at pressures between 1 to 60 atm both with and without gravity. Note that experimental data for the normal-gravity flames is only available between 10 to 60 atm because the SSE measurements were unreliable below 10 atm. The temperature of the fuel and air supplied to the burner was assumed to be equal to 300 K for all cases.

8.2 Numerical Model

The calculations described in this chapter were performed using the same numerical model as described in Chapter 7 with several modifications: finite-rate chemistry was modelled using the modified GRI-Mech 3.0 described in Section 6.1.1 and the three surfaces that lie along the tube wall were assumed adiabatic, not fixed-temperature. The reason for this last deviation and the implications are discussed in the following sections.

8.2.1 Boundary Conditions

All of the flames considered in this study are stabilized by the burner tube rim. As a result, significant heat transfer occurs between the flame and tube that causes the temperature of the tube surface to increase. This

heat transfer intensifies with increasing pressure as the flame base moves towards the burner rim and temperature gradients near the burner steepen [40]. As mentioned in Section 7.5, Gülder et al. [400] measured tube surface temperatures as much as 100 K higher than ambient conditions for similar laminar coflow diffusion flames at atmospheric pressure. They concluded that, based on SSE measurements, the heat transfer between the fuel tube and hot gases significantly affects local gas temperatures and soot volume fractions.

Most numerical studies involving burner-stabilized laminar coflow diffusion flames employ fixed-temperature boundary conditions and assume that the tube temperature is equal to that of the cold reactants [22, 52, 70]. These studies also neglect any increase in fuel or oxidizer temperature upstream of the burner exit plane. Specifying cold walls represents the limit in which absolutely no heating of the tube occurs whereas the adiabatic conditions used here represent the opposite limit for the effect of gas-tube heat transfer — that is, the tube is allowed to heat up to the maximum possible temperature. Based on prior experimental [400, 401] and numerical [64] findings, it is clear that accurate representation of laminar diffusion flames requires incorporating conjugate heat transfer between the gas and tube wall. However, such an analysis can be computationally demanding and is beyond the scope of this study.

Several investigators artificially increased the prescribed temperatures at the inlet (fuel, air, and tube surface) to improve the agreement between predictions and experimental measurements [50, 166]. However, this type of trial-and-error analysis is not ideal for large systematic studies with varying operating conditions. Guo et al. [64] found that predictions for temperature and soot volume fraction improved when the upstream portion of the tube was modelled with an experimentally-measured temperature distribution prescribed along the tube walls. However, experimental data for the tube temperature is not available for the flames studied here and the measurements obtained by Gülder et al. [400] are not applicable. Temperature increases in the tube wall are expected to be much larger in the present study, especially at higher pressures where the flame almost touches the burner rim [40, 44].

Preliminary calculations for the normal-gravity flames were first attempted using prescribed cold-wall boundary conditions. However, the predictions did not accurately represent the experimental results above 20 atm. For these cases at pressures above 20 atm, converged steady-state solutions could not be obtained and, in some cases, the flames descended into the fuel tube. Nor could a suitable temperature distribution along the tube wall be prescribed that mimicked the experimental results. As such, adiabatic wall conditions were chosen for the entire study as they provided the best agreement between numerical predictions and experimental measurements. The same adiabatic boundary conditions were prescribed for the zero-gravity flames.

8.3 Verification with Measurements

8.3.1 Numerical Convergence for High-Pressure Flames

In general, the proposed Newton-Krylov algorithm converged well and relatively quickly for all cases at low pressures, but unfortunately stalled at pressures of 30 atm and above when gravity was present. This convergence stall was attributed to the decreasing flow speeds and increasing ODE stiffness which occurred as pressure increased. The stiffness of the governing ODEs increased significantly with pressure as gas-

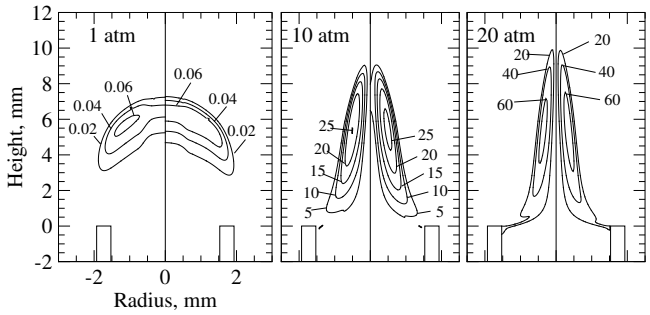

(a) Left: solving Eq. (3.2f); Right: assuming $N_s = 10^{18}$ kg^{-1}.

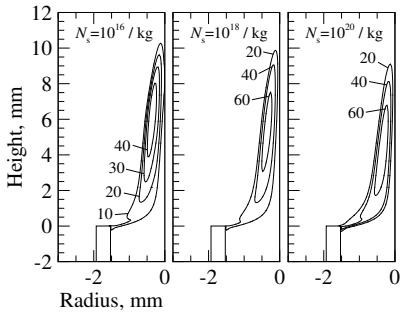

(b) Effect of constant number density.

Figure 8.1: Effect of number density on predicted contours for soot volume fraction in the normal-gravity flames. Units in ppm.

phase and soot-related reaction rates intensified. Several solutions were employed to avoid convergence stall. First, a relaxation factor of 0.1 was applied to the non-linear Newton update computed at each outer iteration. Second, the soot number density was taken to be constant and the corresponding transport equation (Eq. (3.2f)) was not solved, which further alleviated numerical stiffness. A similar approach was applied by Kennedy et al. [167] for the numerical prediction of soot in ethylene laminar diffusion flames. They found that the predicted soot volume fractions were relatively insensitive to the assumed number density provided that the production of soot mass was dominated by surface growth mechanisms. Based on their work, a constant number density of 10^{18} kg^{-1} was assumed for the 30, 40, 50, and 60 atm flames at normal-gravity. The maximum predicted values for the soot number density in the 1, 10, and 20 atm normal-gravity flames are 0.46×10^{18}, 1.33×10^{18}, and 1.47×10^{18} kg^{-1}, respectively. With these modifications, converged steady-state solutions were obtained in all cases. These modifications were not required for the zero-gravity flame calculations as no numerical difficulties were encountered. They were only employed for calculations of the normal-gravity flames between 30–60 atm.

8.3.2 The Implications of Assuming a Constant Number Density

Two separate tests were conducted to assess the implications of assuming a constant number density as described previously on soot volume fraction predictions. First, calculations for the normal-gravity flames were performed at 1, 10, and 20 atm assuming a constant number density of 10^{18} kg^{-1} and the results were compared to those obtained by solving Eq. (3.2f). Comparing the two sets of predictions, Fig. 8.1(a), the constant number density assumption has negligible effect on the predicted soot volume fraction. The largest differences between solutions occur at 1 atm where soot volume fractions are low. Based on these results, assuming a constant N_s is not expected to significantly affect the predictive accuracy of the soot model above 1 atm.

The second test consisted of comparing the results obtained for the 20 atm normal-gravity flame assuming different values for N_s. As illustrated in Fig. 8.1(b), which compares the predicted contours for soot volume fraction obtained using three different values of N_s, the solution is only sensitive to the assumed value of N_s when N_s is small. For example, increasing N_s by a factor of 100 from 10^{18} to 10^{20} kg^{-1} pro-

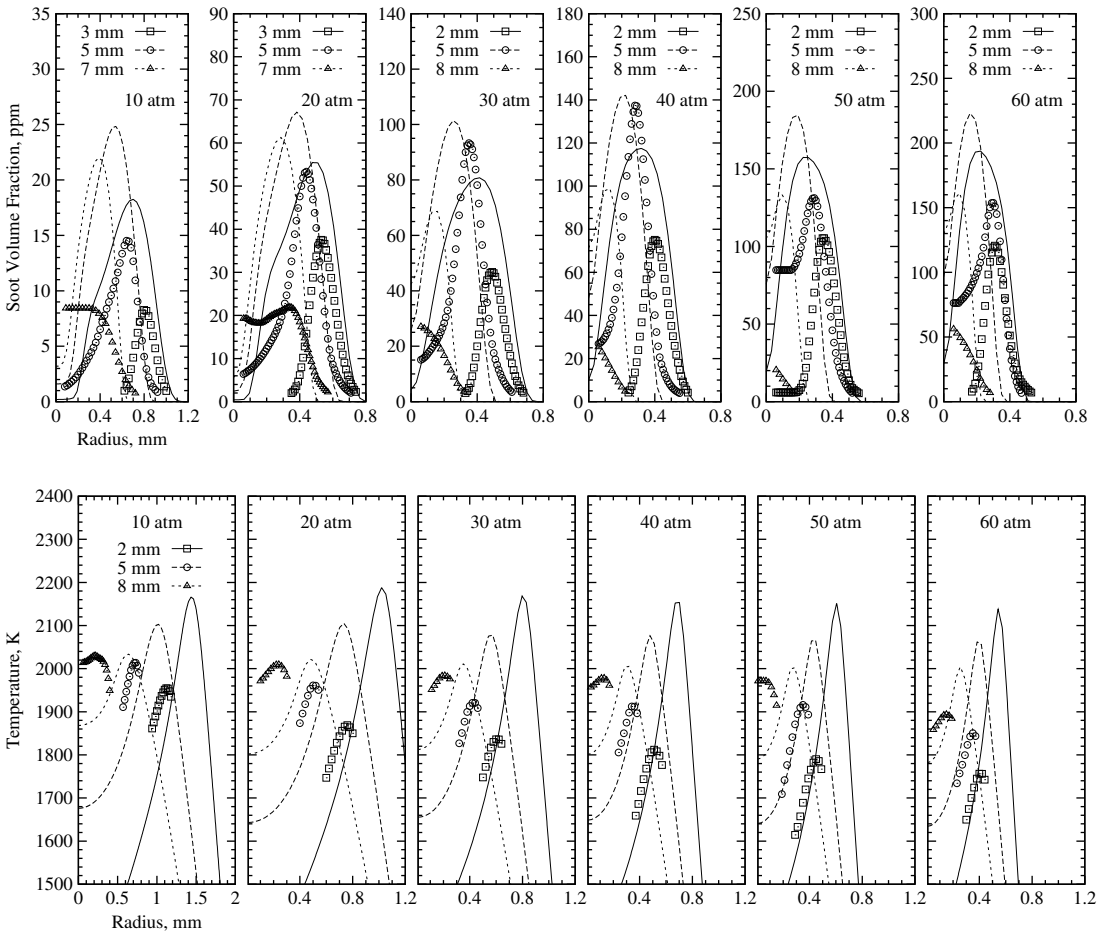

Figure 8.2: Measured (symbols) and predicted (lines) radial profiles for soot volume fraction and temperature. Measurements taken from Joo and Gülder [44].

duced a 5% increase in the peak soot volume fraction. However, a 33% decrease results from a 100-fold decrease in N_s from 10^{18} to 10^{16} kg^{-1}. These results indicate the soot model is fairly insensitive to N_s as long as a reasonable estimate for N_s is provided.

For the remainder of this study, calculations for all flames except the normal-gravity flames between 30–60 atm included the solution of Eq. (3.2f). The modifications discussed in Section 8.3.1, which include the assumption of a constant number density for soot, were only applied to the 30–60 atm normal-gravity flames.

8.3.3 Radial Profiles

The predicted radial profiles of soot volume fraction at various heights above the burner are compared with the measurements of Joo and Gülder [44] in Fig. 8.2. Only the numerical results obtained for the normal-gravity flames are presented in the figure. The model predicts many of the experimentally observed trends but tends to over-predict the soot volume fraction throughout the flames. In both the experiments and calculations, soot is formed in an annulus downstream of the fuel tube rim and the soot volume fractions initially increase with height. The locations of the peaks within this annulus converge towards the centerline as the inner accelerating core flow entrains the soot particles inwards. Oxidative processes begin to convert

soot to gaseous species such as CO higher up in the flame, causing soot levels to drop. As pressure is increased, the peaks in the radial profiles for soot volume fraction become more pronounced and their locations contract radially-inwards. Soot production also increases with pressure since the higher pressures and contracting flame result in higher gaseous species concentrations, larger mixture densities and faster reaction rates. While these features are observed in the numerical results, the magnitudes of the predicted soot volume fraction is greatly over-predicted in most cases, especially in the annular region with high soot levels. For example, the peak soot concentrations for the 10 atm flame are over-predicted by factors of 2.2, 1.7 and 2.5 at axial heights of 3, 5 and 7 mm, respectively. This agreement does not improve much as pressure is increased to 60 atm where the peaks are over-predicted by factors of 1.6, 1.4 and 2.8 at the 2, 5 and 8 mm heights, respectively. Along the centerline, the concentration of soot is under-predicted for the 10 and 20 atm flames and is consistently over-predicted for the other flames.

The predicted annular regions of high soot concentration in Fig. 8.2 are much thicker than the measured values and the locations of the predicted peaks are shifted radially-inward. One possible cause of the thicker predicted annular soot-containing region is errors introduced by the simplified representation of the PSD, but these discrepancies could also be caused by errors in the soot chemistry sub-model. The shifted locations of the predicted peaks are attributed to the simplified geometrical representation of the burner rim.

While many of the trends with pressure and flame height can be observed in both the numerical and experimental results depicted in Fig. 8.2, some trends are incorrectly predicted. Temperature has an annular structure similar to the radial profiles for soot volume fraction except that the radial location where temperature peaks occurs at a slightly larger radius. With increasing height in the flames, the experimental results show an increase in the peak temperature which gradually shifts in position towards the centerline. This radially-inward shift of the peaks is correctly predicted, although the calculated peak temperatures decrease with downstream distance. This indicates that the predicted peak temperature occurs much lower in the flames than in the experiments. Higher temperatures low in flame where there is an abundance of fresh fuel would result in larger soot formation rates and cause the over-predicted soot volume fractions previously discussed.

As pressure is increased, the measured temperature profiles contract inwards and the peaks become more pronounced. Increasing pressure is also observed to result in a slight decrease in the peak temperatures at each height as more soot is produced and radiative heat losses to the surroundings intensify. While the predictions show these same trends with pressure, the decrease in peak temperature with increasing pressure is not as severe. This suggests that the relationship between soot yield and pressure is incorrect because soot volume fraction and temperature are tightly coupled through radiation. Since radiation from soot was observed to have a strong effect on flame temperature, Section 7.4.4, the disagreement in the relationship between the peak flame temperatures and pressure may be caused by errors introduced by the soot model.

Temperature predictions in the lower portion of the flame at 2 and 5 mm agree reasonably well with the measurements, except that the peaks are over-predicted. Higher in the flame at 8 mm, the peak values are in better agreement with the experimental data except shifted radially-outward, especially for pressures between 10 and 40 atm. Peak temperatures at the lowest axial height, where their agreement is poorest, are

greatly over-estimated by 210 K at 10 atm, 310 K at 20 atm, 325 K at 30 atm, 340 K at 40 atm, 387 K at 50 atm, and 370 K at 60 atm. The high temperatures near the burner are a result of the adiabatic boundary condition over-predicting wall temperatures. The shifted temperature profiles are most likely caused by the simplified geometry.

8.3.4 Soot Volume Fraction Contours

Predicted contours of soot volume fraction are presented alongside those constructed from the measurements of Joo and Gülder [44] in Fig. 8.3. Qualitatively, the predicted and measured flame geometries are similar and the narrowing of the flame with increasing pressure is clearly observed in both sets of results. The flame height based on soot volume fraction is over-predicted for each pressure, but remains constant at approximately 11 mm between 20 to 60 atm. Decreasing pressure below 20 atm caused the predicted flame height to decrease to 10 mm at 10 atm and 7.5 mm at 1 atm. These numerical predictions for flame height are based on the location where the soot volume fraction is equal to 0.01 ppm. In contrast, a constant visible flame height of 9 mm was observed in the experimental results. Similar numerical results for flame height were obtained by Liu et al. [22] for the same flames, although they predicted a more agreeable constant flame height of 9.5 mm.

The model correctly predicts the general vicinity of the peak soot volume fraction, however, some significant differences between predicted and measured soot concentrations are observed in Fig. 8.3 at lower flame heights. For instance, the model always predicts that soot production begins further upstream than in the experiments. With increasing pressure, both experiments and predictions show that the initial onset of soot formation begins earlier and that the annular structure becomes thinner and more pronounced. Beginning at 10 atm, the model predicts a small amount of soot inside the fuel tube near the wall that intensifies as pressure is increased further to 60 atm. Soot concentrations inside the tube begin to approach the maximum levels for the whole flame around 30 atm and exceed the values which occur higher up in the 50 and 60 atm flames. These results for the predicted soot volume fraction are different from those presented by Liu et al. [22], who predicted much lower soot concentrations in better agreement with the experimental results for the same flames between 10–40 atm. They did not predict such high soot concentrations near the burner rim.

The differences between the numerical results obtained in this study and those presented by Liu et al. [22] are mainly attributed to the different wall boundary conditions employed — fixed-temperature versus adiabatic. Both studies used a similar numerical model with only a few differences: (1) Liu et al. did not model upstream of the burner exit; and (2) in this study, the unmodified equations governing compressible gas mixtures were solved instead of the low-Mach-number equations. As a result, Liu et al. were able to obtain realistic steady-state solutions for the normal-gravity flames between 5–40 atm with cold-wall boundary conditions and without requiring the constant number density approximation. Based on the results discussed in Section 8.3.2, the constant number density approximation is not expected to significantly affect the predictions. Rather, the adiabatic boundary conditions are assumed responsible for high predicted temperatures near the burner which causes soot formation to occur lower in the flame. Higher overall soot concentrations

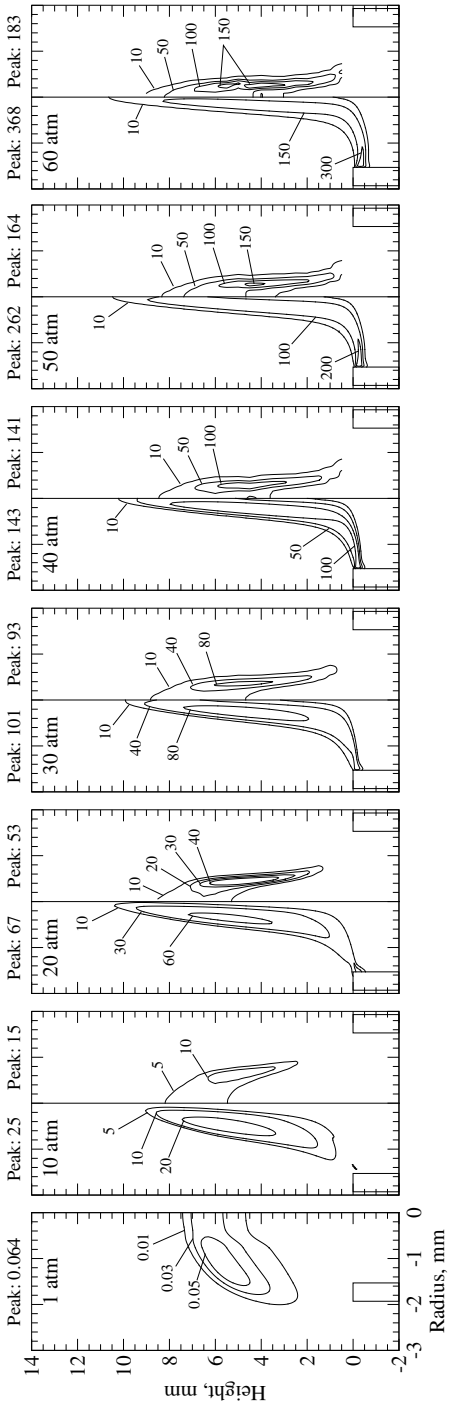

Figure 8.3: Predicted (left) and measured (right) contours for soot volume fraction in ppm. Measurements taken from Joo and Gülder [44].

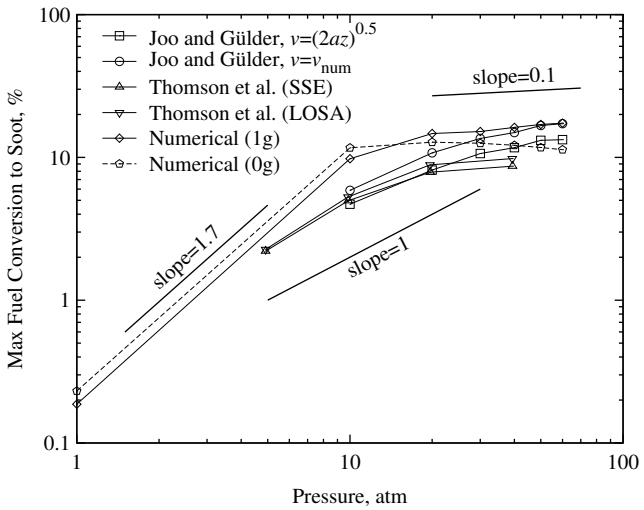

Figure 8.4: Maximum fuel carbon converted to soot as a function of pressure.

and longer flame heights occur as a result. While the adiabatic wall boundary condition may be somewhat inaccurate, it is felt that the resulting solutions better represent the physical behaviour of the flames when compared to solutions obtained assuming a fixed, low-temperature wall. There is some experimental support for high soot concentrations predicted within the fuel tube near the exit [402]. Using the same set-up, Mandatori and Gülder [402] observed the complete blockage of the fuel tube by soot at about 35 atm with an ethane diffusion flame.

8.3.5 Soot Yield

The results for the maximum carbon conversion factor based on the experimental measurements are compared with the numerical predictions in Fig. 8.4. The numerical results obtained for the zero-gravity flames are discussed in detail in the following section. Experimental results based on measurements obtained by Thomson et al. [40] using both line-of-sight attenuation (LOSA) and SSE are also displayed in the figure. Note that the results reported by Thomson et al. were derived using the $v = \sqrt{2az}$ approximation. Differences between the measurements reported by Thomson et al. and Joo and Gülder above 20 atm were attributed to systematic calibration errors in fuel flow rate introduced by Thomson et al. at high pressures [44].

As observed in Fig. 8.4, there is a significant difference between the two lines corresponding to the experimental results of Joo and Gülder based on the different velocity approximations (see Section 7.3.3). The values computed using the predicted velocity field are assumed to be more accurate.

The predictions for the normal-gravity flames mimic the experimentally observed trends reasonably well, although the model consistently over-predicts the maximum η_s in each flame. The degree of this over-prediction diminishes as pressure is increased to 60 atm. For example, the peak carbon conversion is over-predicted by a factor of 1.7 at 10 atm, a factor of 1.1 at 40 atm, and correctly predicted at 50 and 60 atm. Both the experimentally-based and predicted maximum values for η_s display a dependence on pressure that weakens as pressure is increased from 10 to 60 atm. However, the numerical predictions over-predict the slope at pressures below 10 atm and under-predict the slope above 10 atm. A slight discontinuity occurs

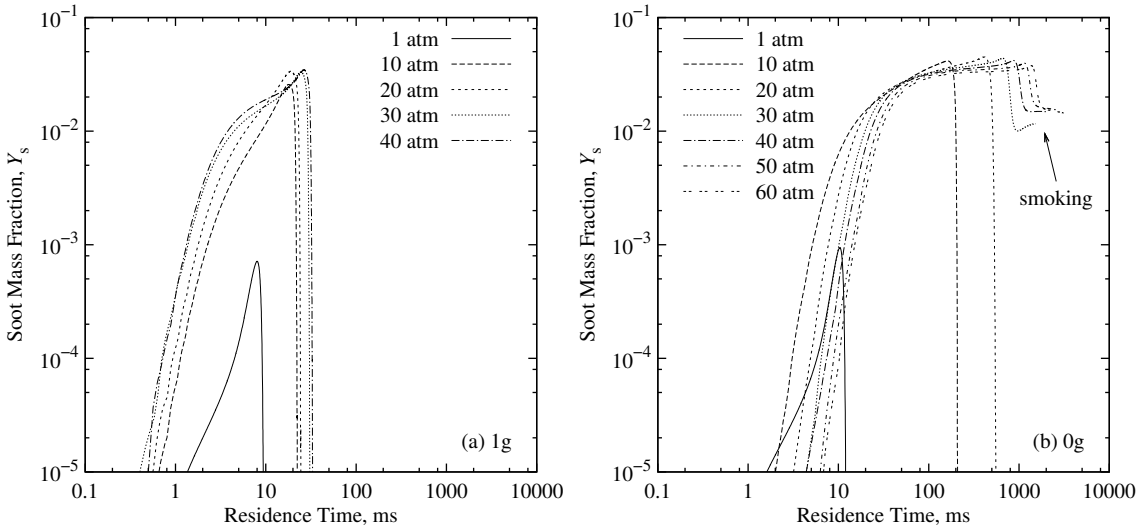

Figure 8.5: Soot mass fraction along a particle streamline originating from the reaction zone and passing through the maximum soot volume fraction.

in the predicted relationship between η_s and pressure at 30 atm where the soot model modifications for improved convergence were applied. Despite the modelling changes, the numerical results still predict the correct trends which would suggest that the majority of the total soot mass is produced through surface reactions.

8.4 Effects of Gravity and Pressure

8.4.1 Soot Yield

Eliminating gravity has a large effect on the predicted maximum η_s, Fig. 8.4. In the low-pressure flames at 1 and 10 atm, removing gravity enhances the maximum η_s by about a factor of 1.2 but does not alter the relationship between η_s and pressure within this range. However, the predictions for the two gravity levels begin to deviate significantly above 10 atm since increasing pressure further causes η_s to decrease for zero gravity and increase for normal gravity. As a result, η_s is lower in the zero-gravity flames for high pressures.

A similar analysis to the one described in Section 7.3.3 was performed to determine the cause of the differences observed in Fig. 8.4 at the two levels of gravity. The normal-gravity flames at 50 and 60 atm could not be analyzed in this manner due to difficulties defining a particle trajectory. Difficulties arose because the maximum soot volume fractions for these two flames occurred inside the tube instead of further downstream above the burner rim. The local variation of Y_s along a soot particle's path for each flame is shown in Fig. 8.5. The most noticeable difference between the results for the two gravity levels is that particle residence time in the normal-gravity methane flames initially increases with pressure from 1 to 10 atm, but then remains approximately fixed for further increases in pressure beyond 10 atm. This means that the flames above 10 atm are fully developed and that the residence times for these flames are independent of pressure, which corresponds with the theory described in Section 1.4. The pressure beyond which residence times stop increasing, 10 atm, corresponds with the drastic change in the pressure-η_s relationship observed in

Fig. 8.4 for the normal-gravity flames. Similar behaviour to the ethylene flames is observed at zero gravity, except that the peak soot mass fractions begin to decrease above 20 atm even though particle residence times continue to increase.

As can be seen in Fig. 8.6, pressure has differing effects on the predicted contours of soot mass fraction at the two levels of gravity. At 1 atm, the structure of the predicted contours are similar because the effects of buoyancy in the normal-gravity flame are relatively small. Soot concentrations are higher and the onset of soot occurs lower in the zero-gravity flame since residence times are longer. As pressure is increased, buoyant forces distort the flow, pulling streamlines towards the centerline and causing the normal-gravity flames to narrow. This narrowing increases temperatures along the centerline and enhances the production of soot. Since both radial velocities and reaction rates increase as pressure is increased in the presence of gravity, the reaction zone narrows and the annular soot zone becomes thinner in the normal-gravity flames.

When gravity is neglected, velocities decrease linearly with pressure while the streamlines remain unaffected. Therefore, soot production increases with pressure in the zero-gravity cases primarily because the residence times are longer and the entrainment of fresh oxidizer into the flame is slower. However, longer residence times and higher soot concentrations promote radiation losses and, as a result, temperatures in the zero-gravity flames decrease with pressure, Fig. 8.8(a). In addition to this, the amount of available acetylene for further soot production declines as pressure is increased and more soot is produced. At some critical pressure, around 30 atm in this study, the combined effects of low temperatures and reduced acetylene concentrations in the zero-gravity flames begin to negatively affect soot formation rates. This results in the declining soot mass fractions observed in Figs. 8.5 and 8.6 for the zero-gravity flames as pressure is increased above 30 atm.

Once pressure is increased to 20 atm, the zero-gravity flames begin smoking. Soot concentrations increase significantly with pressure between 1 and 20 atm regardless of gravity level, but the convective transport of oxygen to the flame is much lower in zero gravity. In addition, temperatures in the zero-gravity flames are drastically lowered by radiation at high pressures. Both contribute to slow oxidation rates in zero gravity.

There is a noticeable difference in the effect of pressure on flame structure at the two gravity levels. Under normal gravity, the annular soot-containing region becomes thinner and more pronounced as pressure is increased to 60 atm. However, thermophoretic forces become important in zero-gravity, especially at high pressures where flow velocities are low, driving particles off flow streamlines and thickening the annular soot-containing region. The increased effects of molecular diffusion, which also become more important as pressures are increased in the absence of gravity, contribute to the thickening of the soot-containing region by widening the reaction zone.

8.4.2 Residence Time and Velocity

The axial velocity profiles along the centerline for all methane-air flames are shown in Fig. 8.7(a). Consistent with the results in Fig. 7.12(a) for the ethylene-air flames, the axial velocity steadily decreases with increasing pressure under zero-gravity conditions. While there is a small decrease in axial velocity between

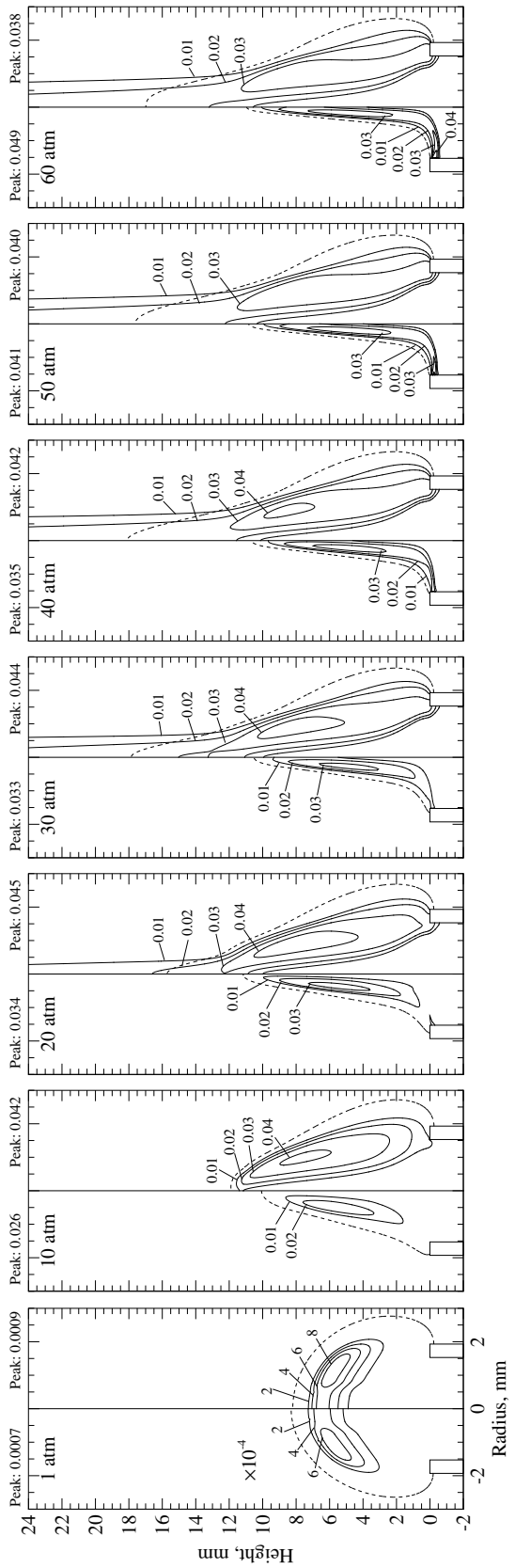

Figure 8.6: Predicted contours for soot mass fraction in the normal-gravity (left) and zero-gravity (right) flames. Dashed black lines denote the location where the mixture fraction is equal to the stoichiometric value.

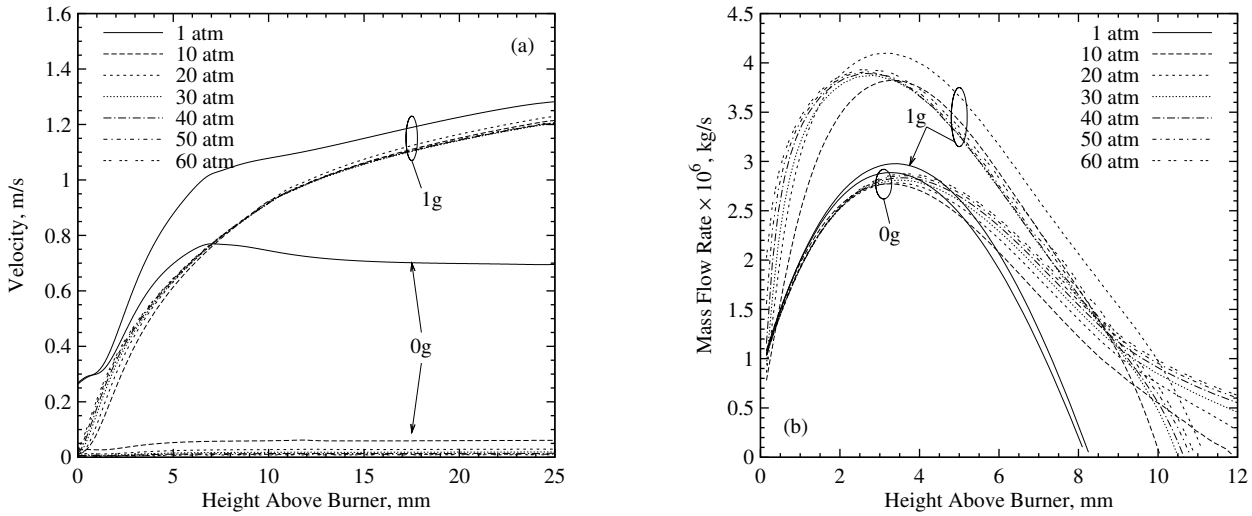

Figure 8.7: Distributions of the predicted axial velocity along the flame centerline and the mass flow rate through the stoichiometric flame envelope.

the 1 and 10 atm normal-gravity flames, there is almost no change above 10 atm. This pressure corresponds to the pressure above which the particle residence time stops increasing.

The mass flow rate through the stoichiometric flame envelope is shown in Fig. 8.7(b) for all flames. The mass flow rate through the normal-gravity flames first increases from 1 to 10 atm, but then remains roughly constant for all pressures above this. This means that the amount of air entrained into the flame does not increase above 10 atm. However, the rate of entrainment does appear to increase with pressure at normal gravity since the initial slopes of the lines in Fig. 8.7(b) become steeper. The mass flow through the zero-gravity flames is much lower, except at 1 atm, and doesn't change much as pressure is increased. This is one of the causes for the higher smoking propensity observed in zero gravity as there is less oxygen entrained into the flame even though soot production is enhanced.

8.4.3 Temperature and Radiation Heat Transfer

While there is almost no difference between the predicted temperature contours of the zero- and normal-gravity flames at 1 atm, Fig. 8.8(a), the significant changes that occur as pressure is increased cause large deviations at high pressure. In zero gravity, enhanced radiation losses resulting from the long residence times and high soot volume fractions reduce local gas temperatures steadily as pressure is increased. This observed decrease in temperature is especially pronounced along the centerline, causing a shift in the location of the peak temperature from the tip of the flame to the base. This shift does not occur in the normal-gravity flames and, in general, different behavior is observed when gravity is turned on. Instead, buoyant forces contract the flame while enhanced convective transport and high pressures promote fast reaction rates and thin reaction zones.

A considerable degree of preheating is observed along the centerline at high pressures and normal gravity levels while fuel preheating is negligible in zero gravity. Instead, the air stream is preheated near the tube wall in the zero-gravity flames. Both of these observed preheating effects are assumed to be somewhat

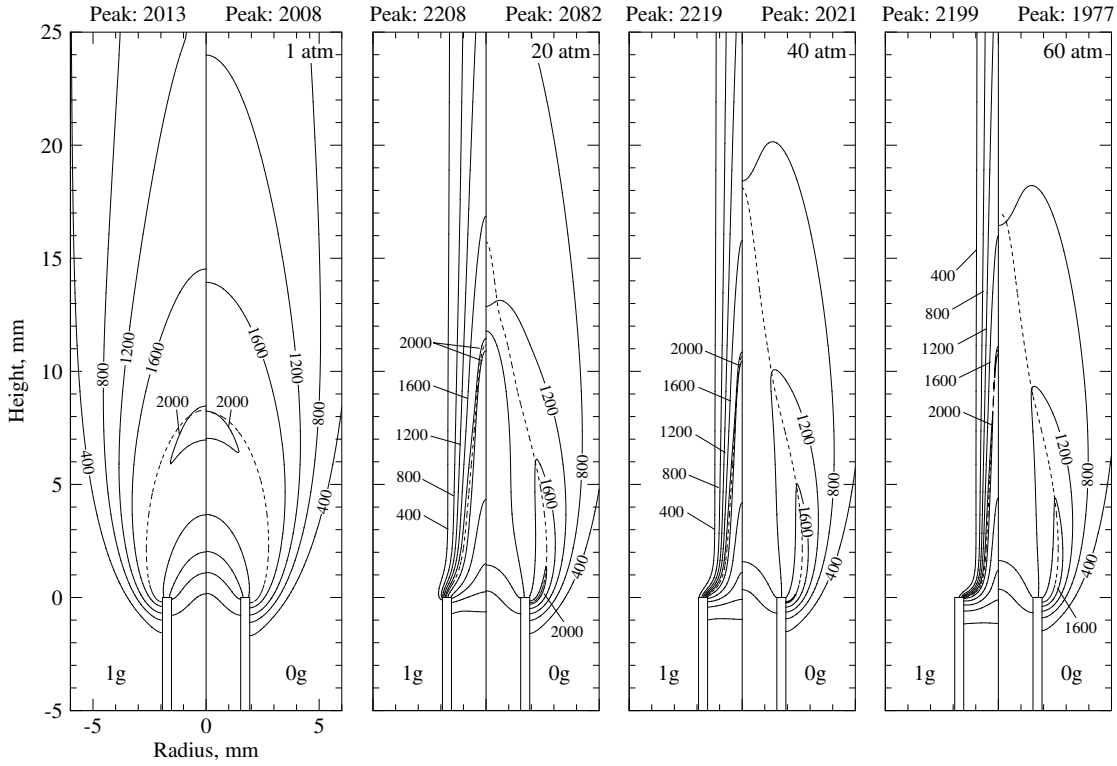

(a) soot and radiation included

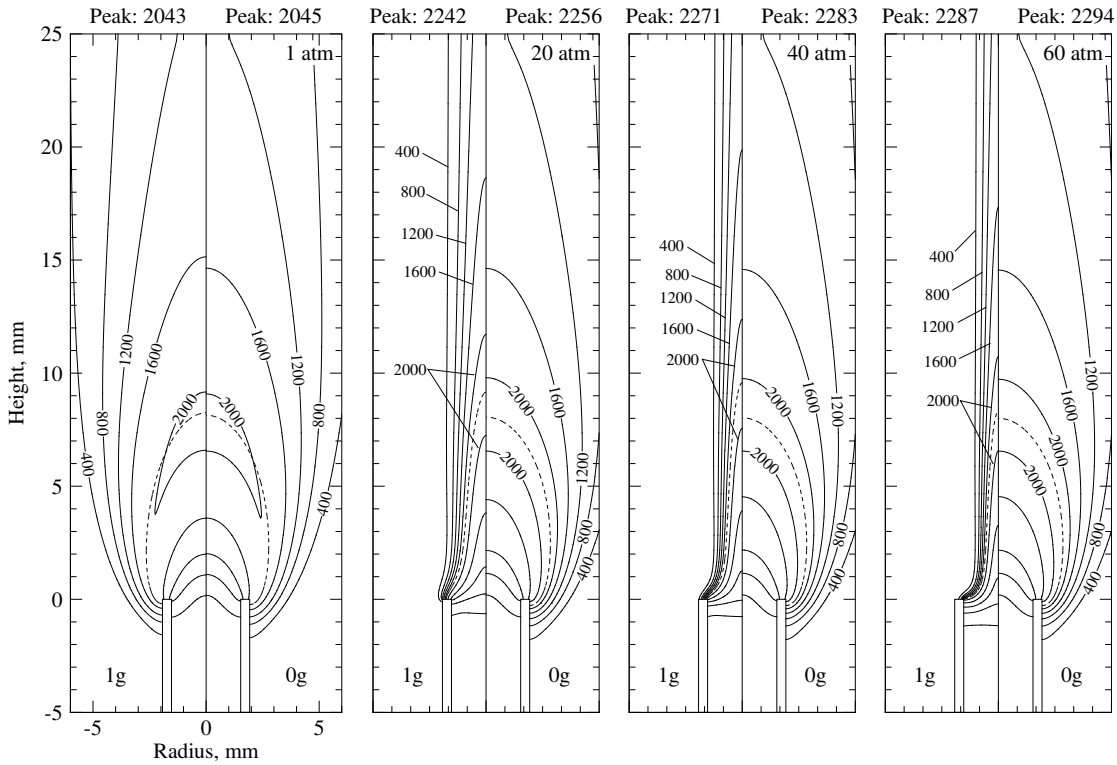

(b) soot and radiation neglected

Figure 8.8: Predicted temperature contours for the normal-gravity (left) and zero-gravity (right) flames. Units in K. The dashed black lines correspond to the location where the mixture fraction is equal to the stoichiometric value.

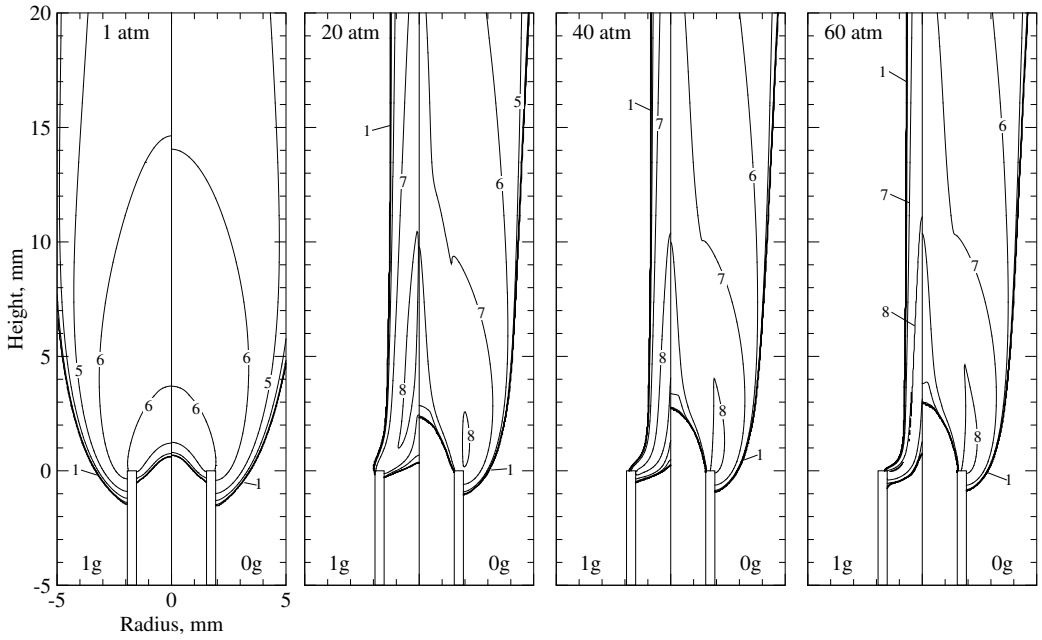

Figure 8.9: Predicted contours of the divergence of the radiative heat flux, $\nabla \cdot \vec{q}_{\text{rad}}$. Contours correspond to $\log_{10}\left[\max\left(-\nabla \cdot \vec{q}_{\text{rad}}\right), 1\right]$.

artificially enhanced by the adiabatic wall conditions.

The impact of radiation on temperature is confirmed by comparing predictions obtained without soot and radiation, Fig. 8.8(b), to predictions obtained when they are both included, Fig. 8.8(a). Considering the temperature predictions obtained without soot and radiation, peak temperatures steadily increase with pressure, regardless of gravity level. Temperatures are marginally higher in zero gravity, possibly because preheating the air stream has a larger impact than preheating the fuel stream. They may also be higher in zero gravity because the slower velocities provides reactions more time to complete and progress towards equilibrium. When soot and radiation are included, Fig. 8.8(a), peak temperatures of the normal-gravity flames increase with pressure at a slower rate than when they were neglected since any increase in heat-release is counter-acted by radiative heat losses. Radiation effects are much stronger at zero gravity and, as a result, peak temperatures decrease with increasing pressure when soot and radiation are included. Above 1 atm, the peak temperatures in the zero-gravity flames are significantly lower than those in the normal-gravity flames. These low temperatures in the zero-gravity flames are one of the primary reasons for the decreased sensitivity of η_{s} to pressure observed above 20 atm.

The divergence of the radiative heat flux, $\nabla \cdot \vec{q}_{\text{rad}}$, is plotted in Fig. 8.9 for each flame. Since this quantity varies exponentially over the range of pressures studied, the logarithm of the negative component of $\nabla \cdot \vec{q}_{\text{rad}}$ is plotted in Fig. 8.9. At 1 atm, the predicted contours of $\nabla \cdot \vec{q}_{\text{rad}}$ at normal and zero gravity are similar. However, the drastic increase in radiation transport with pressure produces significant differences between the predictions for $\nabla \cdot \vec{q}_{\text{rad}}$ in the two 60 atm flames. The magnitude of $\nabla \cdot \vec{q}_{\text{rad}}$ is always slightly larger in the normal-gravity flames, which is a direct result of the steeper temperature and soot concentration gradients in the normal-gravity flames at high pressures. However, radiation has a stronger impact in zero gravity since velocities are lower. There is also a significant amount of energy transported upstream into the coflow air

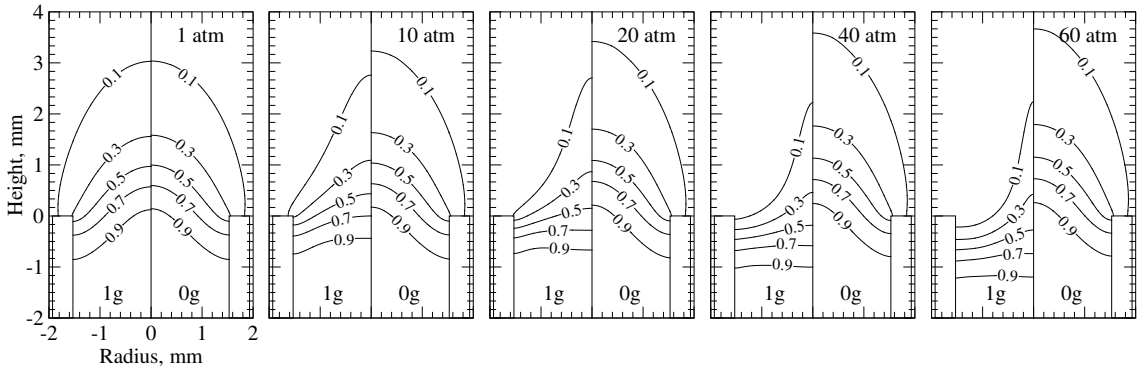

(a) soot and radiation included

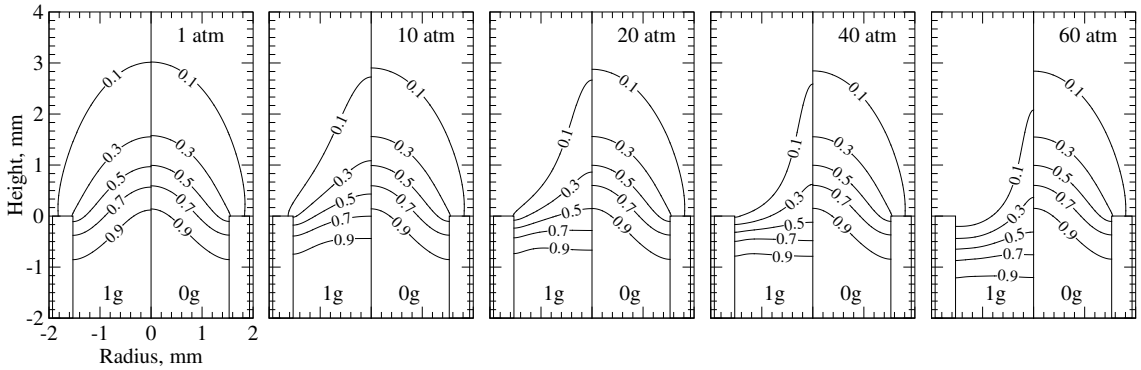

(b) soot and radiation neglected

Figure 8.10: Predicted contours for methane mass fraction in the normal-gravity (left) and zero-gravity (right) flames.

supply tube. While this upstream energy transport vanishes under normal-gravity conditions when pressure is increased to 60 atm, it intensifies with pressure in the absence of gravity.

8.4.4 Species Mass Fractions

In the presence of gravity, buoyant forces rapidly accelerate the flow upward. The accelerating flow entrains the surrounding co-flowing oxidizer stream and mixes the oxidizer with fresh fuel. Since buoyancy-induced acceleration scales with $p^2 g$, increasing pressure intensifies entrainment and speeds up oxidative pyrolysis. This phenomenon is observed in Fig. 8.10(a), which shows the predicted contours of methane mass fraction in the normal- and zero-gravity flames. At normal gravity, methane is consumed at a faster rate as pressure is increased from 1 to 60 atm. Early fuel pyrolysis is also observed inside the fuel tube at high pressures. This is possibly a result of high temperatures near the tube wall which result from the adiabatic boundary conditions. When gravity is eliminated, increasing pressure while maintaining fixed mass flow rates has the opposite effect since flow velocities are reduced. As such, convective transport slows and fuel consumption rates decrease. The lower temperatures at high pressure also contribute to the observed delay in fuel consumption. Additionally, longer residence times as pressure is increased in zero-gravity may allow axial diffusion to drive fuel downstream. Some early fuel pyrolysis is observed at zero-gravity due to the high temperatures near the wall, which is depicted in Fig. 8.8(a).

When soot and radiation are neglected, there is not much change in the normal-gravity results for

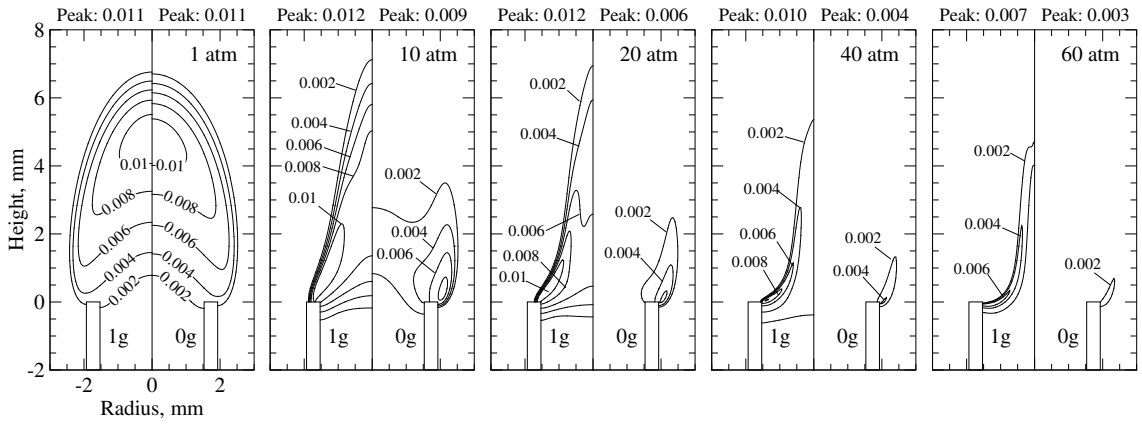

(a) soot and radiation included

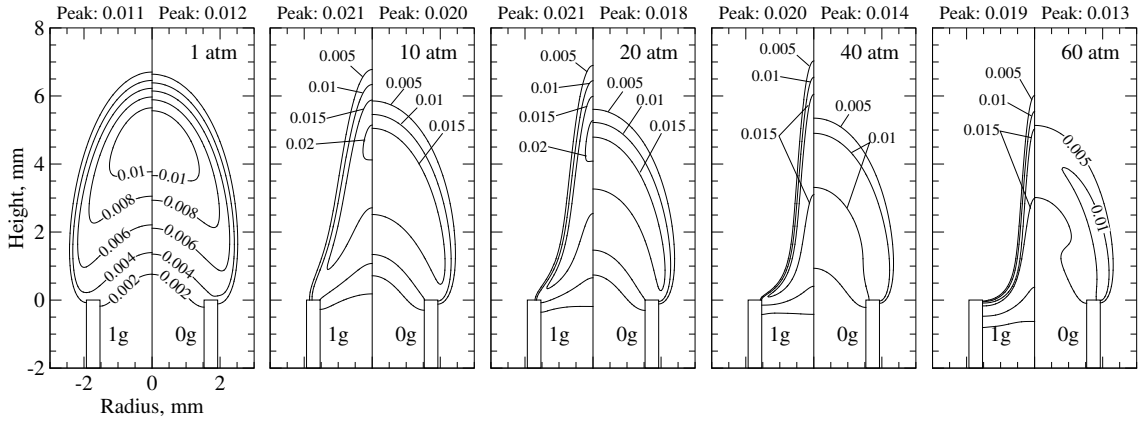

(b) soot and radiation neglected

Figure 8.11: Predicted contours for acetylene mass fraction in the normal-gravity (left) and zero-gravity (right) flames.

methane mass fraction, Fig. 8.10(b). However, the delayed fuel consumption with increasing pressure in zero gravity, observed in Fig. 8.10(a), does not occur. This is because temperatures are much higher when soot and radiation are neglected.

Regardless of gravity level, acetylene mass fractions decrease with increasing pressure, Fig. 8.11(a). This decrease is partially attributed to the consumption of acetylene through Reactions (2.2.2) and (2.2.2) to produce soot. In both cases, normal- and zero-gravity, acetylene is formed downstream of the fuel tube and peaks along the centerline at 1 atm. However, the peak in all flames above 1 atm occurs further upstream in an annular region near the fuel tube wall where temperatures are high (see Fig. 8.8(a)). It is at these higher pressures where the main differences occur between flames at the two gravity levels. For instance, acetylene completely disappears along the centerline of the zero-gravity flames above 10 atm. This is attributed to the decrease in temperature along the centerline which results as pressure is increased in the absence of gravity. In the normal-gravity flames, a considerable amount of acetylene is observed inside the fuel tube. Acetylene first appears inside the tube at 10 atm and concentrations increase when pressure is raised to 20 atm. However, acetylene concentrations begin to decrease with further increases in pressure. This behavior results from the competition between several processes which intensify at higher pressures:

(1) acetylene production inside the tube due to fuel preheating, and (2) consumption of acetylene to produce soot. This competition is confirmed by comparing the predictions obtained with and without soot and radiation, Figs. 8.11(a) and 8.11(b). When soot and radiation are neglected, acetylene concentrations inside the fuel tube of the normal-gravity flames increase steadily with pressure. Here, the effects of fuel preheating are still present but there is no gas-to-soot conversion to consume acetylene.

Several factors contribute to the higher acetylene concentrations observed under normal-gravity conditions:

1. The longer residence times in the zero-gravity flames promote the conversion of acetylene to soot.
2. Temperatures inside the fuel tube and near the wall are higher at normal gravity because radiation has less impact and buoyant forces contract the flame towards the centerline. These higher temperatures promote the breakdown of fuel and the production of acetylene.
3. Entrainment of air into the flame base, which also promotes fuel pyrolysis, intensifies with pressure at normal gravity while it does not change much with pressure at zero gravity.

These last two items are confirmed by comparing predictions obtained with and without soot and radiation, Figs. 8.11(a) and 8.11(b). Neglecting soot and radiation, peak acetylene concentrations are almost constant between 10 and 60 atm at normal gravity. However, they decrease significantly with pressure for zero gravity. The large initial increase in acetylene production between 1–10 atm for both normal- and zero-gravity flames occurs because of the ten-fold increase in pressure.

8.4.5 Flame Geometry

Since the zero-gravity flames begin smoking at relatively low pressures, 20 atm, it is difficult to compare the visible flame geometry. Typically, the predicted visible flame shape would be defined as the location where the soot volume fraction is equal to a certain value. Instead, we focus on the flame shape defined by the stoichiometric mixture fraction. A definition similar to Eq. (7.2) was used, but modified for methane-air flames [398] as follows:

$$Z = \frac{2Y_C/M_C + \frac{1}{2}Y_H/M_H + (Y_{O,2} - Y_O)/M_O}{2Y_{C,1}/M_C + \frac{1}{2}Y_{H,1}/M_H + Y_{O,2}/M_O} \tag{8.1}$$

From Eq. (8.1), the stoichiometric value of Z is equal to

$$Z_{st} = \frac{Y_{O,2}/M_O}{2Y_{C,1}/M_C + \frac{1}{2}Y_{H,1}/M_H + Y_{O,2}/M_O} \tag{8.2}$$

where Y_j and M_j are the mass fractions and atomic masses for the elements carbon, hydrogen, and oxygen. Subscripts 1 and 2 refer to values in the fuel and air streams, respectively.

The shapes of the normal- and zero-gravity flames are similar at 1 atm where the effects of buoyancy are small, Fig. 8.12(a). However, above this pressure, the zero-gravity flames become significantly longer and wider than the normal-gravity flames. Flame width decreases with increasing pressure at normal-gravity, in accordance with previous findings [22, 40, 42–44], but remains roughly unchanged with pressure at zero-gravity. This narrowing of the normal-gravity flames occurs because, as pressure is increased, buoyant forces

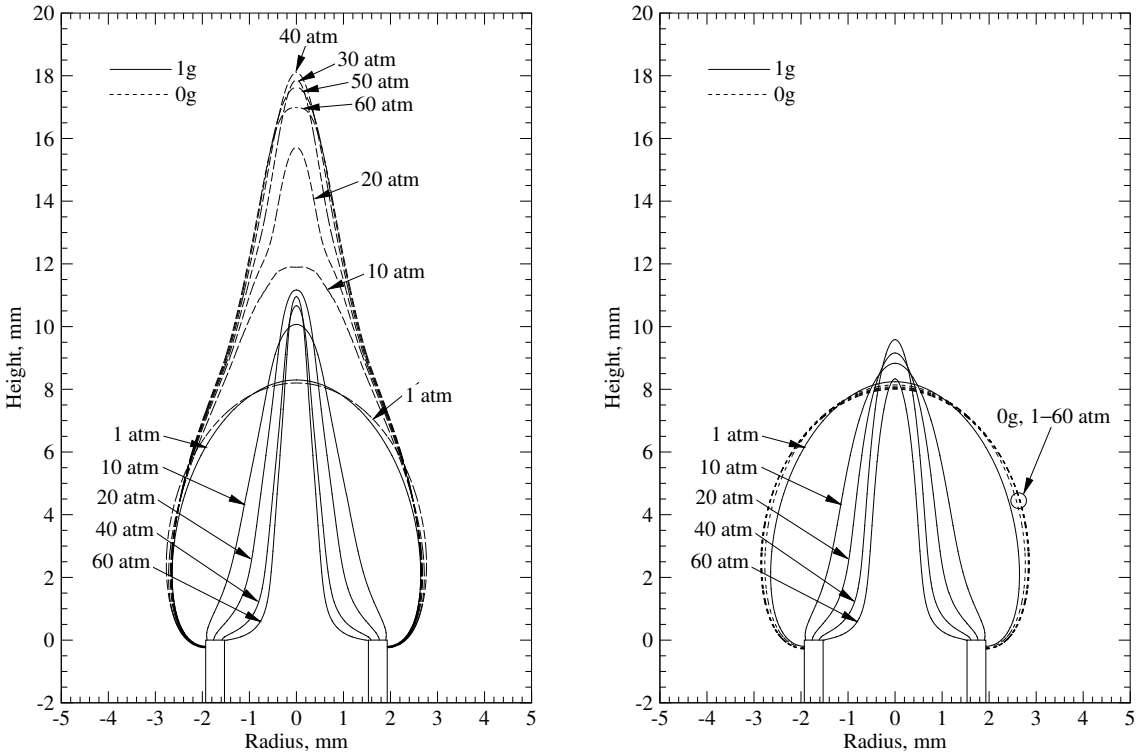

(a) soot and radiation included

(b) soot and radiation neglected

Figure 8.12: The effect of pressure and gravity on the stoichiometric mixture fraction surface.

contract streamlines inwards. Pressure has virtually no effect on the path of the streamlines in zero-gravity; it only effects the magnitudes of velocities throughout the flame.

The height of the normal-gravity flames increases significantly from 1 to 20 atm, but remains roughly constant with any further increases in pressure. It is not clear what causes this increase in height since the flames are all buoyancy-controlled (Froude number $\ll 1$) within the range of pressures studied. A much larger increase in height is observed as pressure is increased in zero-gravity due to the higher soot concentrations and large decrease in temperature. This is confirmed by comparing the results obtained with and without the inclusion of soot and radiation effects, Figs. 8.12(a) and 8.12(b). Without soot and radiation, the zero-gravity flames are much shorter and their shape is completely independent of pressure. The length of the non-sooting flames is also shorter when gravity is absent. This suggests that diffusion times are large enough that combustion is not hindered by slowing velocities and reduced convective transport.

CHAPTER 9

CONCLUSIONS

There were three main goals for this research: (1) to develop an efficient, scalable solver capable of modelling reacting gas flows with detailed chemical kinetics, radiation transport, and soot formation/oxidation; (2) to asses the predictive capability of current soot models applied to high pressure flames; and (3) to study the effects of gravity and pressure on the sooting behavior and flame structure of laminar diffusion flames. The steps taken to achieve these objectives have been described in detail in the preceding chapters and all of the goals have been accomplished. A summary and conclusions now follow, along with recommendations for future research.

9.1 Summary and Conclusions

A new framework for the study of soot formation in complex reacting laminar flows was presented in Chapter 5 which solves the unmodified compressible-gas equations to maintain applicability at all speeds. The framework uses a parallel implicit solver for fast, efficient solution and a block-based AMR scheme to capture small-scale processes on computationally tractable grids. Validation was performed by applying the framework to two different laminar coflow diffusion flames at atmospheric pressure and evaluating the algorithm's predictive accuracy. The effectiveness of the AMR procedure at providing grid-independent results in an efficient manner was shown. Although some small changes in the radial soot volume fraction profiles were still observed after the final level of refinement, grid-converged results were obtained for the most part for both the atmospheric-pressure flames investigated. This was achieved with a substantial reduction in mesh size compared to meshes with uniform spacing. Good agreement with published experimental data for temperature and soot volume fraction was achieved in both cases. The algorithm demonstrated excellent strong scaling performance by achieving a parallel efficiency greater than 70% up to 384 processors. Outstanding weak scaling performance (92% parallel efficiency on 1167 processors) was observed when the OTA was used to model radiation. However, the weak scaling performance degraded somewhat when the DOM was employed. The algorithm proved to be a robust, accurate, and highly-scalable solution method for sooting laminar flames. It successfully tackled large problems using domain decomposition and effectively minimized the sizes of computational meshes using AMR.

To examine the ability of the combustion framework and current two-equation soot model to capture the effects of pressure, the framework was applied to two sets of laminar coflow diffusion flames — the

ethylene-air flames of Panek and Gülder [93] between 0.5–5 atm and the methane-air flames of Joo and Gülder [44] between 10–60 atm. Overall, predictions for soot volume fraction and temperature differed significantly from the measurements, but the soot model was still able to capture the effects of pressure and predict the correct trends with reasonably good accuracy. Discrepancies were mainly attributed to errors introduced by the acetylene-based soot model and uncertainties in the boundary conditions. For the ethylene-air flames, the soot model captured the increase in maximum η_s with pressure and the decreased sensitivity of η_s to pressure above 1 atm, although this η_s-pressure dependence was under-estimated over the entire range of pressures investigated. Predicted flame heights based on soot were shorter, especially at higher pressures, mainly because the cold-wall boundary condition under-predicted temperatures near the wall. In contrast, the flame heights of the methane-air flames were over-predicted at all pressures because of the high temperatures near the wall predicted by the adiabatic boundary conditions. This also caused the predicted onset of soot formation to occur much lower in the flame. At high-pressures, fuel pyrolysis actually began inside the tube and caused high soot concentrations inside the tube and near wall. However, it is unclear whether the formation of soot inside the tube is an artifact of the over-predicted wall temperatures and uncertainties in the prescribed wall boundary condition at the burner rim. There is some experimental evidence to support these high soot concentrations predicted within the fuel tube near the exit [402].

Based on the numerical results, pressure and gravity were observed to significantly influence the sooting behavior and flame structure of laminar diffusion flames. Zero-gravity flames produced more soot, had lower temperatures, and thicker soot-containing regions than normal-gravity flames at the same pressure. These differences were negligible at low pressures, below about 10 atm, but became larger as pressure was increased. Flames at both levels of gravity displayed a similar power-law relationship between the η_s and pressure that weakened as pressure was increased, although the sensitivity of η_s to pressure decayed at a faster rate in zero gravity above 1 atm. For the methane-air flames, an inverse relationship between pressure and η_s was predicted above 20 atm at zero gravity. An investigation of the numerical results has revealed that these differences in the soot-pressure dependence is a result of several factors. At low pressures, the predicted temperatures and acetylene mass fractions for flames at the two gravity levels are similar because soot volume fractions are low and the effects of buoyancy are minimized. However, residence times become long and soot volume fractions high as pressure is increased above 1–10 atm in zero gravity, promoting large radiation losses and reducing temperatures. This decreases soot formation rates in the zero-gravity flames and results in the decaying carbon conversion factor as pressure is increased. Low acetylene concentrations at high pressures also contribute to this behavior. For the ethylene flames, the η_s-pressure dependence was actually strengthened below 1 atm in zero gravity by the effect of pressure on residence time.

Flame shape was observed to change when gravity and pressure were varied. The zero-gravity flames become longer while flames under normal-gravity conditions narrowed when pressure was increased. This lengthening of the zero-gravity flames was attributed to the low temperatures and slow oxidation of soot which results at high pressures. This suspicion was confirmed as it was also shown that all of the flames became shorter when soot and radiation were neglected. In fact, the shape of zero-gravity flames is only affected by soot and radiation.

9.2 Summary of Contributions

The following contributions were made as a result of this research:

- A new highly-scalable finite-volume scheme for reacting flows with detailed radiation and soot was proposed. The proposed algorithm represents the current state of the art in combustion modelling, making use of a second-order accurate finite-volume scheme and a parallel AMR algorithm on body-fitted, multi-block meshes. The framework is applicable to flows at all speeds via the application of low-mach number preconditioning. AMR allows grid-independent results to be achieved using substantially smaller meshes than equivalent uniform meshes with the same resolution.

- A highly scalable solution algorithm for the DOM/FVM was developed that made use of a similar finite-volume time-marching algorithm as the flow solver (see Appendix C). The proposed scheme is highly scalable, easily handles complex geometry, and captures large solution discontinuities with smaller meshes using AMR and limited high-order reconstruction. The implicit solution algorithm efficiently handles non-linearities introduced by scattering media and the employed high-order discretization.

- The first numerical solutions of laminar diffusion flames up to 60 atm were obtained. These results were validated in detail with experimental data to assess modelling errors associated with existing soot models.

- This is the first and only known detailed numerical study on the combined effects of gravity and pressure on laminar diffusion flames. While others have studied zero-gravity flames with detailed models that include soot and radiation [26, 27], none have specifically addressed the effects of pressure in zero gravity. This helped confirm why flames lengthen in zero gravity even though Roper's correlations [46] predict that flame heights are independent of gravitational acceleration.

- A modification to the existing acetylene-based soot models of Leung et al. [96] and Fairweather et al. [97] was made that improved their stability characteristics and aided convergence (Section 2.2.2.1). It damped the on/off switching caused by small oscillations in the solution and eliminated singularities.

9.3 Recommendations for Future Research

In Section 7.5, the wall boundary conditions were observed to have a fairly significant effect on the predicted temperatures and soot volume fractions for the 5 atm ethylene-air flame. In addition, it was concluded in Chapter 8 that the applied adiabatic boundary conditions — which provided the best agreement with the experimental measurements — over-predicted temperatures near the tube wall and resulted in high soot concentrations low in the flame. Since wall heating is expected to increase with pressure, a conjugate heat transfer analysis is required and recommended in future studies to accurately predict soot in high-pressure laminar coflow diffusion flames. Note that some researchers have chosen to study lifted flames [52], but lifted flames become increasingly unstable at high pressures.

The current implementation should be improved to solve Eq. (2.5b) for the soot number density over the entire range of pressures studied (i.e., for flames above 20 atm). This is expected to improve the predictions for soot in the high-pressure flames. Other means of improving quantitative predictions include the use of more detailed physical models for soot, real-gas effects, and diffusion. Detailed gas-phase kinetic mechanisms that describe the formation of large molecular weight soot precursors coupled with advanced descriptions for soot kinetics and aerosol dynamics were found to offer excellent quantitative predictions [17, 18, 71]. More physical models for soot particle nucleation, such as those based on PAH condensation reactions [31, 107], may improve the soot predictions low in the flame and near the centerline. However, none of these models have been verified or validated for high-pressure flames. The enhanced computational efficiency offered by the proposed numerical scheme should allow tractable and reliable computations using these more advanced and complex models.

Future developments of the proposed finite-volume scheme and framework for combustion should focus on improving the refinement efficiency and scalability of the algorithm. The currently employed gradient-based AMR criteria incorrectly flagged blocks for refinement in some cases where the solution was already adequately resolved. Refinement efficiency can be improved in these cases using more advanced a posteriori error estimates which do not rely solely on gradients of solution quantities [390, 391]. Anisotropic refinement would also improve the refinement efficiency [367, 403, 404]. Since the main parallel inefficiencies were attributed to the space-marching DOM, advanced DOM solution techniques specifically designed for use on large, parallel architectures would significantly improve the proposed algorithm's scalability. A new implicit solution algorithm for the DOM/FVM was developed to specifically address this issue, but the large computational storage requirements associated with implicit methods and non-gray radiation has thus far prohibited its use in multi-dimensional flame calculations. These storage requirements can be reduced by using methods for solving linear systems that require less storage than GMRES, such as Bi-CGStab [405] BiCGStab(l) [406]. The parallel performance of the proposed framework can also be improved through the use of more effective global preconditioners. Multi-level preconditioning methods are attractive because they outperform standard one-level preconditioners (like the one used here) in terms of scalability and convergence [407–409].

REFERENCES

[1] B. Dellinger, A. D'Alessio, A. D'Anna, A. Ciajolo, B. Gullett, H. Henry, M. Keener, J. Lighty, S. Lomnicki, D. Lucas, G. OberdoÌĹrster, D. Pitea, W. Suk, A. Sarofim, K.R. Smith, T. Stoeger, P. Tolbert, R. Wyzga, and R. Zimmermann. Combustion byproducts and their health effects: Summary of the 10th international congress. *Environmental Engineering Science*, 25(8):1107–1114, 2008.

[2] C.A. Pope III, R.T. Burnett, M.J. Thun, E.E. Calle, D. Krewski, K. Ito, and G.D. Thurston. Lung cancer, cardiopulmonary mortality, and long-term exposure to fine particulate air pollution. *Journal of the American Medical Society*, 287(9):1132–1141, 2002.

[3] J. Schwartz. Air pollution and daily mortality: A review and meta analysis. *Environmental Research*, 64(1):36–52, 1994.

[4] A. Peters, H.E. Wichmann, T. Tuch, J. Heinrich, and J. Heyder. Respiratory effects are associated with the number of ultrafine particles. *American Journal of Respiratory and Critical Care Medicine*, 155(4):1376–1383, 1997.

[5] L. Forti, N. Jeuland, S. Raux, and M. Pasquereau. Analysis of the particulates emitted by internal combustion engines. *Oil and Gas Science and Technology*, 60(6):995–1011, 2005.

[6] R.A. Dobbins. Hydrocarbon nanoparticles formed in flames and diesel engines. *Aerosol Science and Technology*, 41(5):485–496, 2007.

[7] C.K. Law and G.M. Faeth. Opportunities and challenges of combustion in microgravity. *Progress in Energy and Combustion Science*, 20(1):65–113, 1994.

[8] I.M. Miller and H.G. Maahs. High-pressure flame systems for pollution studies with results for methane-air diffusion flames. TN D-8407, NASA, 1977.

[9] W.L. Flower and C.T. Bowman. Soot production in axisymmetric laminar diffusion flames at pressures from one to ten atmospheres. *Proceedings of the Combustion Institute*, 21(1):1115–1124, 1988.

[10] P.S. Greenberg. Laser doppler velocimetry and full-field soot volume fraction measurements in microgravity. In *Proceedings of the 3rd International Microgravity Combustion Workshop*, pages 247–252, Cleveland, OH, April 10–13 1995. NASA.

[11] I. Glassman and P. Yaccarino. The temperature effect in sooting diffusion flames. *Proceedings of the Combustion Institute*, 18:1175–1183, 1981.

[12] J.H. Kent and H.G. Wagner. Temperature and fuel effects in sooting diffusion flames. *Proceedings of the Combustion Institute*, 20:1007–1015, 1984.

[13] R.J. Santoro, T.T. Yeh, J.J. Horvath, and H.G. Semerjian. The transport and growth of soot particles in laminar diffusion flames. *Combustion Science and Technology*, 53:89–115, 1987.

[14] C.M. Megaridis and R.A. Dobbins. Comparison of soot growth and oxidation in smoking and nonsmoking ethylene diffusion flames. *Combustion Science and Technology*, 66:1–16, 1989.

[15] K.T. Walsh, J. Fielding, M.D. Smooke, M.B. Long, A. Linan, K. Annamalai, V.R. Katta, J. Jeffries, and B. Dally. A comparison of computational and experimental lift-off heights of coflow laminar diffusion flames. *Proceedings of the Combustion Institute*, 30:357–365, 2005.

[16] B.M. Kumfer, S.A. Skeen, R. Chen, and R.L. Axelbaum. Measurement and analysis of soot inception limits of oxygen-enriched coflow flames. *Combustion and Flame*, 147(3):233–242, 2006.

[17] A. D'Anna and J.H. Kent. A model of particulate and species formation applied to laminar, non-premixed flames for three aliphatic-hydrocarbon fuels. *Combustion and Flame*, 152(4):573–587, 2008.

[18] S.B. Dworkin, M.D. Smooke, and V. Giovangigli. The impact of detailed multicomponent transport and thermal diffusion effects on soot formation in ethylene/air flames. *Proceedings of the Combustion Institute*, 32(1):1165–1172, 2009.

[19] Q. Zhang, M.J. Thomson, H. Guo, F. Liu, and G.J. Smallwood. A numerical study of soot aggregate formation in a laminar coflow diffusion flame. *Combustion and Flame*, 156(3):697–705, 2009.

[20] H. Guo, K.A. Thomson, and G.J. Smallwood. On the effect of carbon monoxide addition on soot formation in a laminar ethylene/air coflow diffusion flame. *Combustion and Flame*, 156(6):1135–1142, 2009.

[21] R.S. Mehta, D.C. Haworth, and M.F. Modest. An assessment of gas-phase reaction mechanisms and soot models for laminar atmospheric-pressure ethylene-air flames. *Proceedings of the Combustion Institute*, 32:1327–1334, 2009.

[22] F. Liu, K. Thomson, H. Guo, and G.J. Smallwood. Numerical and experimental study of an axisymmetric coflow laminar methane-air diffusion flame at pressures between 5 and 40 atmospheres. *Combustion and Flame*, 146:456–471, 2006.

[23] C.R. Kaplan, E.S. Oran, K. Kailasanath, and H.D. Ross. Gravitational effects on sooting diffusion flames. *Proceedings of the Combustion Institute*, 26(1):1301–1309, 1996.

[24] O.A. Ezekoye and Z. Zhang. Soot oxidation and agglomeration modeling in a microgravity diffusion flame. *Combustion and Flame*, 110:127–139, 1997.

[25] G. Legros, A. Fuentes, S. Rouvreau, P. Joulain, B. Porterie, and J.L. Torero. Transport mechanisms controlling soot production inside a non-buoyant laminar diffusion flame. *Proceedings of the Combustion Institute*, 32(2):2461–2470, 2009.

[26] W. Kong and F. Liu. Numerical study of the effects of gravity on soot formation in laminar coflow methane/air diffusion flames under different air stream velocities. *Combustion Theory and Modelling*, 13(6):993–1023, 2009.

[27] W. Kong and F. Liu. Effects of gravity on soot formation in a coflow laminar methane/air diffusion flame. *Microgravity Science and Technology*, 22(2):205–214, 2010.

[28] Z. Zhang and O.A. Ezekoye. Soot production rate calculations at elevated pressure in a methane-air jet jet diffusion flame. *Combustion Science and Technology*, 137:323–346, 1998.

[29] I.M. Kennedy. Models of soot formation and oxidation. *Progress in Energy and Combustion Science*, 23(2):95–132, 1997.

[30] B.S. Haynes and H.G. Wagner. Soot formation. *Progress in Energy and Combustion Science*, 7: 229–273, 1981.

[31] J. Appel, H. Bockhorn, and M. Frenklach. Kinetic modeling of soot formation with detailed chemistry and physics: Laminar premixed flames of C2 hydrocarbons. *Combustion and Flame*, 121(1-2):122–136, 2000.

[32] H. Richter, S. Granata, W.H. Green, and J.B. Howard. Detailed modeling of pah and soot formation in a laminar premixed benzene/oxygen/argon low-pressure flame. *Proceedings of the Combustion Institute*, 30:1397–1405, 2004.

[33] I. Glassman. Soot formation in combustion processes. *Proceedings of the Combustion Institute*, 22: 295–311, 1988.

[34] P.A. Libby and F.A. Williams, editors. *Turbulent Reacting Flows*. Springer-Verlag, Berlin, 1980.

[35] C.K. Law. *Combustion Physics*. Cambridge University Press, New York, 2006.

[36] S. Ghosal and L. Vervisch. Stability diagram for lift-off and blowout of a round jet laminar diffusion flame. *Combustion and Flame*, 124(4):646–655, 2001.

[37] J. Boulanger, L. Vervisch, J. Reveillon, and S. Ghosal. Effects of heat release in laminar diffusion flames lifted on round jets. *Combustion and Flame*, 134(4):355–368, 2003.

[38] F. Takahashi, W.J. Schmoll, and V.R. Katta. Attachment mechanisms of diffusion flames. *Proceedings of the Combustion Institute*, 1:675–684, 1998.

[39] F. Takahashi and V.R. Katta. Reaction kernel structure and stabilizing mechanisms of jet diffusion flames in microgravity. *Proceedings of the Combustion Institute*, 29(2):2509–2517, 2002.

[40] K.A. Thomson, Ö.L. Gülder, E.J. Weckman, R.A. Fraser, G.J. Smallwood, and D.R. Snelling. Soot concentration and temperature measurements in co-annular, nonpremixed CH_4/air laminar flames at pressures up to 4 MPa. *Combustion and Flame*, 140:222–232, 2005.

[41] I. Glassman. Sooting laminar diffusion flames: effect of dilution, additives, pressure, and microgravity. *Proceedings of the Combustion Institute*, 27:1589–1596, 1998.

[42] L.L. McCrain and W.L. Roberts. Measurements of the soot volume field in laminar diffusion flames at elevated pressures. *Combustion and Flame*, 140:60–69, 2005.

[43] D.S. Bento, K.A. Thomson, and Ö.L. Gülder. Soot formation and temperature field structure in laminar propane-air diffusion flames at elevated pressures. *Combustion and Flame*, 145:765–778, 2006.

[44] H.I. Joo and Ö.L. Gülder. Soot formation and temperature field structure in co-flow laminar methane-air diffusion flames at pressures from 10 to 60 atm. *Proceedings of the Combustion Institute*, 32(1): 769–775, 2009.

[45] F.G. Roper. The prediction of laminar jet diffusion flame sizes: Part I. theoretical model. *Combustion and Flame*, 29:219–226, 1977.

[46] F.G. Roper, C. Smith, and A.C. Cunningham. The prediction of laminar jet diffusion flame sizes: Part II. experimental verification. *Combustion and Flame*, 29:227–234, 1977.

[47] W. Lee and Y.D. Na. Soot study in laminar diffusion flames at elevated pressures using two-color pyrometry and Abel inversion. *JSME International Journal Series B*, 43(4):550–555, 2000.

[48] I.M. Kennedy, C. Yam, D.C. Rapp, and R.J. Santoro. Modelling and measurements of soot and species in a laminar diffusion flame. *Combustion and Flame*, 107:368–382, 1996.

[49] C.S. McEnally, A.M. Schaffer, M.B. Long, L.D. Pfefferle, M.D. Smooke, and M.B. Colket. Computational and experimental study of soot formation in a coflow, laminar ethylene diffusion flame. *Proceedings of the Combustion Institute*, 27:1497–1505, 1998.

[50] M.D. Smooke, C.S. McEnally, L.D. Pfefferle, R.J. Hall, and M.B. Colket. Computational and experimental study of soot formation in a coflow, laminar diffusion flame. *Combustion and Flame*, 117: 117–139, 1999.

[51] M.D. Smooke, R.J. Hall, M.B. Colket, J. Fielding, and M.B. Long. Investigation of the transition from lightly sooting towards heavily sooting co-flow ethylene diffusion flames. *Combustion Theory and Modelling*, 8:593–606, 2004.

[52] M.D. Smooke, M.B. Long, B.C. Connelly, M.B. Colket, and R.J. Hall. Soot formation in laminar diffusion flames. *Combustion and Flame*, 143:613–628, 2005.

[53] S.B. Dworkin, B.C. Connelly, A.M. Schaffer, B.A.V. Bennett, M.B. Long, M.D. Smooke, M.P. Puccio, B. McAndrews, and J.H. Miller. Computational and experimental study of a forced, time-dependent, methane-air coflow diffusion flame. *Proceedings of the Combustion Institute*, 31(1): 971–978, 2007.

[54] A. D'Anna, A. D'Alessio, and J.H. Kent. A computational study of hydrocarbon growth and the formation of aromatics in coflowing laminar diffusion flames. *Combustion and Flame*, 125:1196–1206, 2001.

[55] A. D'Anna, A. D'Alessio, and J. Kent. Reaction path analysis of the formation of aromatics and soot in a coflowing laminar diffusion flame of ethylene. *Combustion Science and Technology*, 174(11-12): 279–294, 2002.

[56] A. D'Anna and J.H. Kent. Aromatic formation pathways in non-premixed methane flames. *Combustion and Flame*, 132(4):715–722, 2003.

[57] A. D'Anna, G. Mazzotti, and J. Kent. Modeling of particulate formation in a coflowing diffusion flame. *Combustion Science and Technology*, 176(5-6):753–767, 2004.

[58] A. D'Anna and J.H. Kent. Modeling of particulate carbon and species formation in coflowing diffusion flames of ethylene. *Combustion and Flame*, 144(1-2):249–260, 2006.

[59] A. D'Anna, J.H. Kent, and R.J. Santoro. Investigation of species concentration and soot formation in a co-flowing diffusion flame of ethylene. *Combustion Science and Technology*, 179(1-2):355–369, 2007.

[60] F. Liu, H. Guo, G.J. Smallwood, and Ö.L. Gülder. Effects of gas and soot radiation on soot formation in a coflow laminar ethylene diffusion flame. *Journal of Quantitative Spectroscopy & Radiative Transfer*, 73:409–421, 2002.

[61] F. Liu, H. Guo, G.J. Smallwood, and Ö.L. Gülder. Numerical modelling of soot formation and oxidation in laminar coflow non-smoking and smoking ethylene diffusion flames. *Combustion Theory and Modelling*, 7:301–315, 2003.

[62] F. Liu, G.J. Smallwood, F. Migliorini, and G. Zizak. Effects of hydrogen and helium addition to fuel on soot formation in an axisymmetric coflow laminar methane-air diffusion flame. In *Proceedings of the Combustion Institute Canadian Section Spring Technical Meeting*, pages 90–95, Toronto, Canada, May 12-14 2008.

[63] H. Guo, F. Liu, G.J. Smallwood, and Ö.L. Gülder. A numerical study of the influence of transport properties of inert diluents on soot formation in a coflow laminar ethylene/air diffusion flame. *Proceedings of the Combustion Institute*, 29:2359–2365, 2002.

[64] H. Guo, F. Liu, G.J. Smallwood, and Ö.L. Gülder. The flame preheating effect on numerical modelling of soot formation in a two-dimensional laminar ethylene-air diffusion flame. *Combustion Theory and Modelling*, 6:173–187, 2002.

[65] H. Guo, F. Liu, G.J. Smallwood, and O.L. Gülder. A numerical investigation of thermal diffusion influence on soot formation in ethylene/air diffusion flames. *International Journal of Computational Fluid Dynamics*, 18(2):139–151, 2004.

[66] H. Guo, F. Liu, G.J. Smallwood, and Ö.L. Gülder. Numerical study on the influence of hydrogen addition on soot formation in a laminar ethylene-air diffusion flame. *Combustion and Flame*, 145 (1-2):324–338, 2006.

[67] H. Guo and G.J. Smallwood. The interaction between soot and NO formation in a laminar axisymmetric cofow ethylene/air diffusion flame. *Combustion and Flame*, 149(1-2):225–233, 2007.

[68] H. Guo and G.J. Smallwood. A numerical study on the influence of CO2 addition on soot formation in an ethylene/air diffusion flame. *Combustion and Flame*, 2007. in press.

[69] H. Guo, K.A. Thomson, and G.J. Smallwood. The effect of CO addition on soot formation in a laminar ethylene/air coflow diffusion flame. In *Proceedings of the Combustion Institute Canadian Section Spring Technical Meeting*, pages 96–101, Toronto, Canada, May 12-14 2008.

[70] Q. Zhang, H. Guo, F. Liu, G.J. Smallwood, and M.J. Thomson. Implementation of an advanced fixed sectional aerosol dynamics model with soot aggregate formation in a laminar methane/air coflow diffusion flame. *Combustion Theory and Modelling*, 12(4):621–641, 2008.

[71] Q. Zhang, H. Guo, F. Liu, G.J. Smallwood, and M.J. Thomson. Modeling of soot aggregate formation and size distribution in a laminar ethylene/air coflow diffusion flame with detailed pah chemistry and an advanced sectional aerosol dynamics model. *Proceedings of the Combustion Institute*, 32(1):761–768, 2009.

[72] V.R. Katta, W.M. Roquemore, A. Menon, S.Y. Lee, R.J. Santoro, and T.A. Litzinger. Impact of soot on flame flicker. *Proceedings of the Combustion Institute*, 32(1):1343–1350, 2009.

[73] P.B. Sunderland, B.J. Mendelson, Z.G. Yuan, and D.L. Urban. Shapes of buoyant and nonbuoyant laminar jet diffusion flames. *Combustion and Flame*, 116(3):376–386, 1999.

[74] T.H. Cochran. Experimental investigation of laminar gas jet diffusion flames in zero gravity. Technical report, NASA-TN-D-6523, 1972.

[75] S.H. Chung and C.K. Law. Burke-schumann flame with streamwise and preferential diffusion. *Combustion Science and Technology*, 37(1-2):21–46, 1984.

[76] M.Y. Bahadori, R.B. Edelman, D.P. Stocker, and S.L. Olson. Ignition and behavior of laminar gas-jet diffusion flames in microgravity. *AIAA Journal*, 28(2):236–244, 1990.

[77] E. Villermaux and D. Durox. On the physics of diffusion flames. *Combustion Science and Technology*, 84:279–294, 1992.

[78] S.S. Krishnan, J.M. Abshire, P.B. Sunderland, Z.. Yuan, and J.P. Gore. Analytical predictions of shapes of laminar diffusion flames in microgravity and earth gravity. *Combustion Theory and Modelling*, 12(4):605–620, 2008.

[79] A. Gomez and D.E. Rosner. Thermophoretic effects on particles in counterflow laminar diffusion flames. *Combustion Science and Technology*, 89(5-6):335–362, 1993.

[80] P.B. Sunderland, S. Mortazavi, G.M. Faeth, and D.L. Urban. Laminar smoke points of nonbuoyant jet diffusion flames. *Combustion and Flame*, 96(1-2):97–103, 1994.

[81] J.C. Ku, D.W. Griffin, P.S. Greenberg, and J. Roma. Buoyancy-induced differences in soot morphology. *Combustion and Flame*, 102(1-2):216–218, 1995.

[82] J. Reimann and S. Will. Optical diagnostics on sooting laminar diffusion flames in microgravity. *Microgravity Science and Technology*, 15(1):333–337, 2005.

[83] D.L. Urban, Z.G. Yuan, P.B. Sunderland, K.C. Lin, Z. Dai, and G.M. Faeth. Smoke-point properties of non-buoyant round laminar jet diffusion flames. *Proceedings of the Combustion Institute*, 28(2): 1965–1971, 2000.

[84] P.B. Sunderland, Ü.Ö. Köylü, and G.M. Faeth. Soot formation in weakly buoyant acetylene-fueled laminar jet diffusion flames burning in air. *Combustion and Flame*, 100(1-2):310–322, 1995.

[85] P.B. Sunderland and G.M. Faeth. Soot nucleation and growth in weakly-bouyant hydrocarbon diffusion flames. Technical report, AIAA-1995-149, 1995.

[86] P.B. Sunderland and G.M. Faeth. Soot formation in hydrocarbon/air laminar jet diffusion flames. *Combustion and Flame*, 105(1-2):132–146, 1996.

[87] P.S. Greenberg and J.C. Ku. Soot volume fraction maps for normal and reduced gravity laminar acetylene jet diffusion flames. *Combustion and Flame*, 108(1-2):227–230, 1997.

[88] R.L. Vander Wal. Laser-induced incandescence measurements in low-gravity. *Microgravity Science and Technology*, 10(2):66–74, 1997.

[89] K.T. Walsh, J. Fielding, M.D. Smooke, and M.B. Long. Experimental and computational study of temperature, species, and soot in buoyant and non-buoyant coflow laminar diffusion flames. *Proceedings of the Combustion Institute*, 28(2):1973–1979, 2000.

[90] D.L. Urban, Z.G. Yuan, P.B. Sunderland, G.T. Linteris, J.E. Voss, K.C. Lin, Z. Dai, K. Sun, and G.M. Faeth. Structure and soot properties of nonbuoyant ethylene/air laminar jet diffusion flames. *AIAA Journal*, 36(8):1346–1360, 1998.

[91] K.C. Lin, Z. Dai, and G.M. Faeth. Laminar soot processes. In *Fifth International Microgravity Combustion Workshop*, pages 147–150, Cleveland, OH, May 18–20 1999. NASA.

[92] F.J. Diez, C. Aalburg, P.B. Sunderland, D.L. Urban, Z.G. Yuan, and G.M. Faeth. Soot properties of laminar jet diffusion flames in microgravity. *Combustion and Flame*, 156(8):1514–1524, 2009.

[93] N. Panek and Ö.L. Gülder. Simulation of microgravity diffusion flames using sub-atmospheric pressures. In *48th AIAA Aerospace Sciences Meeting*, Orlando, Florida, 4–7 January 2010. AIAA 2010-1477.

[94] H. Richter and J.B. Howard. Formation of polycyclic aromatic hydrocarbons and their growth to soot-a review of chemical reaction pathways. *Progress in Energy and Combustion Science*, 26(4): 565–608, 2000.

[95] A. Thomas. Carbon formation in flames. *Combustion and Flame*, 6(C):46–62, 1962.

[96] K.M. Leung, R.P. Lindstedt, and W.P. Jones. A simplified reaction mechanism for soot formation in nonpremixed flames. *Combustion and Flame*, 87:289–305, 1991.

[97] M. Fairweather, W.P. Jones, and R.P. Lindstedt. Predictions of radiative transfer from a turbulent reacting jet in a cross-wind. *Combustion and Flame*, 89:45–63, 1992.

[98] K.H. Homann and H.G. Wagner. Some new aspects of the mechanism of carbon formation in premixed flames. *Proceedings of the Combustion Institute*, 11(1):371–379, 1967.

[99] A.V. Krestinin. Polyyne model of soot formation process. *Proceedings of the Combustion Institute*, 1:1557–1563, 1998.

[100] A.V. Krestinin. Detailed modeling of soot formation in hydrocarbon pyrolysis. *Combustion and Flame*, 121(3):513–524, 2000.

[101] H.F. Calcote. Mechanisms of soot nucleation in flames - a critical review. *Combustion and Flame*, 42(3):215–242, 1981.

[102] P. Weilmünster, A. Keller, and K.H. Homann. Large molecules, radicals, ions, and small soot particles in fuel-rich hydrocarbon flames: Part I: positive ions of polycyclic aromatic hydrocarbons (PAH) in low-pressure premixed flames of acetylene and oxygen. *Combustion and Flame*, 116(1-2):62–83, 1999.

[103] M. Frenklach and H. Wang. Detailed modeling of soot particle nucleation and growth. *Proceedings of the Combustion Institute*, 23:1559–1566, 1991.

[104] H. Richter and J.B. Howard. Formation and consumption of single-ring aromatic hydrocarbons and their precursors in premixed acetylene, ethylene and benzene flames. *Physical Chemistry Chemical Physics*, 4(11):2038–2055, 2002.

[105] H. Bockhorn, F. Fetting, and H.W. Wenz. Investigation of the formation of high molecular hydrocarbons and soot in premixed hydrocarbon-oxygen flames. *Berichte der Bunsengesellschaft*, 87(11): 1067–1073, 1983.

[106] J.A. Miller, M.J. Pilling, and J. Troe. Unravelling combustion mechanisms through a quantitative understanding of elementary reactions. *Proceedings of the Combustion Institute*, 30(1):43–88, 2005.

[107] M. Frenklach and H. Wang. Detailed mechanism and modeling of soot particle formation. *Springer Series in Chemical Physics*, 59:165–192, 1994.

[108] M.B. Colket and R.J. Hall. Successes and uncertainties in modeling soot formation in laminar, premixed flames. *Springer Series in Chemical Physics*, 59:442–470, 1994.

[109] M.J. Castaldi, N.M. Marinov, C.F. Melius, J. Huang, S.M. Senkan, W.J. Pitz, and C.K. Westbrook. Experimental and modeling investigation of aromatic and polycyclic aromatic hydrocarbon formation in a premixed ethylene flame. *Proceedings of the Combustion Institute*, 26:693–702, 1996.

[110] A. D'Anna and A. Violi. A kinetic model for the formation of aromatic hydrocarbons in premixed laminar flames. *Proceedings of the Combustion Institute*, 27(1):425–433, 1998.

[111] C.S. McEnally and L.D. Pfefferle. The use of carbon-13-labeled fuel dopants for identifying naphthalene formation pathways in non-premixed flames. *Proceedings of the Combustion Institute*, 28: 2569–2576, 2000.

[112] J.A. Mulholland, M. Lu, and D.H. Kim. Pyrolytic growth of polycyclic aromatic hydrocarbons by cyclopentadienyl moieties. *Proceedings of the Combustion Institute*, 28:2593–2599, 2000.

[113] M. Frenklach, N.W. Moriarty, and N.J. Brown. Hydrogen migration in polyaromatic growth. *Proceedings of the Combustion Institute*, 27(2):1655–1661, 1998.

[114] N.W. Moriarty, N.J. Brown, and M. Frenklach. Hydrogen migration in the phenylethen-2-yl radical. *Journal of Physical Chemistry A*, 103(35):7127–7135, 1999.

[115] M. Frenklach. Reaction mechanism of soot formation in flames. *Physical Chemistry Chemical Physics*, 4(11):2028–2037, 2002.

[116] M. Frenklach, C.A. Schuetz, and J. Ping. Migration mechanism of aromatic-edge growth. *Proceedings of the Combustion Institute*, 30(1):1389–1396, 2005.

[117] J.B. Howard. Carbon addition and oxidation reactions in heterogeneous combustion and soot formation. *Proceedings of the Combustion Institute*, 23(1):1107–1127, 1991.

[118] H. Bockhorn, editor. *Soot Formation in Combustion: Mechanisms and Models*. Springer-Verlag, New York, 1994.

[119] A. D'Anna, A. Violi, A. D'Alessio, and A.F. Sarofim. A reaction pathway for nanoparticle formation in rich premixed flames. *Combustion and Flame*, 127(1-2):1995–2003, 2001.

[120] J. Warnatz, U. Mass, and R.W. Dibble. *Combustion: Physical and Chemical Fundamentals, Modelling and Simulation, Experiments, Pollutant Formulation*. Springer-Verlag, New York, 2nd edition, 2002.

[121] S.J. Harris and A.M. Weiner. Surface growth of soot particles in premixed ethylene/air flames. *Combustion Science and Technology*, 31(3):155–167, 1983.

[122] S.J. Harris. Surface growth and soot particle reactivity. *Combustion Science and Technology*, 72(1-3): 67–77, 1990.

[123] T.G. Benish, A.L. Lafeur, K. Taghiadeh, and J.B. Howard. C2H2 and PAH as soot growth reactants in premixed C2H4-air flames. *Proceedings of the Combustion Institute*, 26(2):2319–2326, 1996.

[124] A. Kazakov and M. Frenklach. Dynamic modeling of soot particle coagulation and aggregation: Implementation with the method of moments and application to high-pressure laminar premixed flames. *Combustion and Flame*, 114(3-4):484–501, 1998.

[125] K.G. Neoh, J.B. Howard, and A.F. Sarofim. Soot oxidation in flames. *Particulate Carbon: Formation During Combustion*, pages 261–282, 1981.

[126] F. Liu, H. Guo, G.J. Smallwood, and Ö.L. Gülder. The chemical effects of carbon dioxide as an additive in an ethylene diffusion flame: Implications for soot and NOx formation. *Combustion and Flame*, 125(1-2):778–787, 2001.

[127] H. Guo and G.J. Smallwood. A numerical study on the influence of CO2 addition on soot formation in an ethylene/air diffusion flame. *Combustion Science and Technology*, 180(10-11):1695–1708, 2008.

[128] K.G. Neoh, J.B. Howard, and A.F. Sarofim. Effect of oxidation on the physical structure of soot. *Proceedings of the Combustion Institute*, 20(1):951–957, 1985.

[129] M. Frenklach, D.W. Clary, T. Yuan, W.C. Gardiner, and S.E. Stein. Mechanism of soot formation in acetylene-oxygen mixtures. *Combustion Science and Technology*, 50:79–115, 1986.

[130] M. Frenklach and J. Warnatz. Detailed modeling of PAH profiles in a sooting low-pressure acetylene flame. *Combustion Science and Technology*, 51:265–283, 1987.

[131] C. Pels Leusden and N. Peters. Experimental and numerical analysis of the influence of oxygen on soot formation in laminar counterflow flames of acetylene. *Proceedings of the Combustion Institute*, 28(2):2619–2624, 2000.

[132] S.K. Freidlander. *Smoke, Dust, and Haze: Fundamentals of Aerosol Dynamics*. Oxford University Press, New York, 2nd edition, 2000.

[133] J.D. Landgrebe and S.E. Pratsinis. Discrete-sectional model for particulate production by gas-phase chemical reaction and aerosol coagulation in the free-molecular regime. *Journal of Colloid and Interface Science*, 139(1):63–86, 1990.

[134] B. Sportisse. A review of current issues in air pollution modeling and simulation. *Computational Geosciences*, 11(2):159–181, 2007.

[135] M. Frenklach and S.J. Harris. Aerosol dynamics modeling using the method of moments. *Journal of Colloid and Interface Science*, 118(1):252–261, 1987.

[136] J.C. Barrett and J.S. Jheeta. Improving the accuracy of the moments method for solving the aerosol general dynamic equation. *Journal of Aerosol Science*, 27(8):1135–1142, 1996.

[137] R. McGraw. Description of aerosol dynamics by the quadrature method of moments. *Aerosol Science and Technology*, 27(2):255–265, 1997.

[138] F. Gelbard, Y. Tambour, and J.H. Seinfeld. Sectional representations for simulating aerosol dynamics. *Journal of Colloid and Interface Science*, 76(2):541–556, 1980.

[139] F. Gelbard and J.H. Seinfeld. Simulation of multicomponent aerosol dynamics. *Journal of Colloid and Interface Science*, 78(2):485–501, 1980.

[140] J.J. Wu and R.C. Flagan. A discrete-sectional solution to the aerosol dynamic equation. *Journal of Colloid and Interface Science*, 123(2):339–352, 1988.

[141] S.H. Park, S.N. Rogak, W.K. Bushe, J.Z. Wen, and M.J. Thomson. An aerosol model to predict size and structure of soot particles. *Combustion Theory and Modelling*, 9(3):499–513, 2005.

[142] J.Z. Wen. *Chemical and Physcial Aspects of Soot/Nano-Particle Formation in Combustion*. PhD thesis, University of Toronto, 2005.

[143] J.Z. Wen, M.J. Thomson, M.F. Lightstone, S.H. Park, and S.N. Rogak. An improved moving sectional aerosol model of soot formation in a plug flow reactor. *Combustion Science and Technology*, 178(5): 921–951, 2006.

[144] J.Z. Wen, M.J. Thomson, M.F. Lightstone, and S.N. Rogak. Detailed kinetic modeling of carbonaceous nanoparticle inception and surface growth during the pyrolysis of c6h6 behind shock waves. *Energy and Fuels*, 20(2):547–559, 2006.

[145] R.J. Hall and M.B. Colket. Predictions of soot particle growth based on aerosol dynamics modelling. *Journal of Aerosol Science*, 23(SUPPL 1):S129–S132, 1992.

[146] R.J. Hall, M.D. Smooke, and M.B. Colket. Prediction of soot dynamics in opposed jet diffusion flames. In F.L. Dryer and R.F. Sawyer, editors, *Physical and Chemical Aspects of Combustion: A Tribute to Irvin Glassman*, pages 189–230. Gordon & Breach, Amsterdam, 1997.

[147] M. Di Domenico, P. Gerlinger, and M. Aigner. Modeling soot formation in methane diffusion flames. *AIAA paper 2006-1163*, 2006.

[148] S.B. Dworkin, J.A. Cooke, B.A.V. Bennett, B.C. Connelly, M.B. Long, M.D. Smooke, R.J. Hall, and M.B. Colket. Distributed-memory parallel computation of a forced, time-dependent, sooting, ethylene/air coflow diffusion flame. *Combustion Theory and Modelling*, 13(5):795–822, 2009.

[149] B.C. Connelly, M.B. Long, M.D. Smooke, R.J. Hall, and M.B. Colket. Computational and experimental investigation of the interaction of soot and NO in coflow diffusion flames. *Proceedings of the Combustion Institute*, 32:777–784, 2009.

[150] K. Netzell, H. Lehtiniemi, and F. Mauss. Calculating the soot particle size distribution function in turbulent diffusion flames using a sectional method. *Proceedings of the Combustion Institute*, 31(1): 667–674, 2007.

[151] N.J. Brown, K.L. Revzan, and M. Frenklach. Detailed kinetic modeling of soot formation in ethylene/air mixtures reacting in a perfectly stirred reactor. *Proceedings of the Combustion Institute*, 27 (1):1573–1580, 1998.

[152] A. Kazakov, H. Wang, and M. Frenklach. Detailed modeling of soot formation in laminar premixed ethylene flames at a pressure of 10 bar. *Combustion and Flame*, 100(1-2):111–120, 1995.

[153] J. Appel, H. Bockhorn, and M. Wulkow. A detailed numerical study of the evolution of soot particle size distributions in laminar premixed flames. *Chemosphere*, 42(5-7):635–645, 2001.

[154] H. Wang, D.X. Du, C.J. Sung, and C.K. Law. Experiments and numerical simulation on soot formation in opposed-jet ethylene diffusion flames. *Proceedings of the Combustion Institute*, 26(2): 2359–2368, 1996.

[155] A. Kronenburg, R.W. Bilger, and J.H. Kent. Modeling soot formation in turbulent methane-air jet diffusion flames. *Combustion and Flame*, 121:24–40, 2000.

[156] M. Balthasar, F. Mauss, A. Knobel, and M. Kraft. Detailed modeling of soot formation in a partially stirred plug flow reactor. *Combustion and Flame*, 128(4):395–409, 2002.

[157] L. Wang, D.C. Haworth, S.R. Turns, and M.F. Modest. Interactions among soot, thermal radiation, and nox emissions in oxygen-enriched turbulent nonpremixed flames: A computational fluid dynamics modeling study. *Combustion and Flame*, 141(1-2):170–179, 2005.

[158] L. Wang, M.F. Modest, D.C. Haworth, and S.R. Turns. Modeling nongray gas-phase and soot radiation in luminous turbulent nonpremixed jet flames. *Combustion Theory and Modelling*, 9(4):673–691, 2005.

[159] R.P. Lindstedt, S.A. Louloudi, H. Pitsch, and J.P. Gore. Joint-scalar transported PDF modeling of soot formation and oxidation. *Proceedings of the Combustion Institute*, 30(1):775–783, 2005.

[160] A. Zucca, D.L. Marchisio, A.A. Barresi, and R.O. Fox. Implementation of the population balance equation in cfd codes for modelling soot formation in turbulent flames. *Chemical Engineering Science*, 61(1):87–95, 2006.

[161] H. El-Asrag, T. Lu, C.K. Law, and S. Menon. Simulation of soot formation in turbulent premixed flames. *Combustion and Flame*, 150(1-2):108–126, 2007.

[162] D.L. Marchisio and A.A. Barresi. Investigation of soot formation in turbulent flames with a pseudo-bivariate population balance model. *Chemical Engineering Science*, 64(2):294–303, 2009.

[163] F. Liu, H. Guo, G.J. Smallwood, and M. El Hafi. Effects of gas and soot radiation on soot formation in counterflow ethylene diffusion flames. *Journal of Quantitative Spectroscopy & Radiative Transfer*, 84(4):501–511, 2004.

[164] X. Zhu and J.P. Gore. Study of flame structure and soot formation on heptane/air diffusion flame. *AIAA Journal*, 42(7):1491–1495, 2004.

[165] X.L. Zhu and J.P. Gore. Radiation effects on combustion and pollutant emissions of high-pressure opposed flow methane/air diffusion flames. *Combustion and Flame*, 141(1-2):118–130, 2005.

[166] F. Liu, H. Guo, and G.J. Smallwood. Effects of radiation model on the modeling of a laminar coflow methane/air diffusion flame. *Combustion and Flame*, 138(1-2):136–154, 2004.

[167] I.M. Kennedy, W. Kollmann, and J.Y. Chen. A model for the soot formation in a laminar diffusion flame. *Combustion and Flame*, 81:73–85, 1990.

[168] C.R. Kaplan, S.W. Baek, E.S. Oran, and J.L. Ellzey. Dynamics of a strongly radiating unsteady ethylene jet diffusion flame. *Combustion and Flame*, 96:1–21, 1994.

[169] C.R. Kaplan, C.R. Shaddix, and K.C. Smyth. Computations of enhanced soot production in time-varying CH4/air diffusion flames. *Combustion and Flame*, 106(4):392–405, 1996.

[170] C.B. Saji, C. Balaji, and T. Sundararajan. Investigation of soot transport and radiative heat transfer in an ethylene jet diffusion flame. *International Journal of Heat and Mass Transfer*, 51(17-18):4287–4299, 2008.

[171] D. Carbonell, A. Oliva, and C.D. Perez-Segarra. Implementation of two-equation soot flamelet models for laminar diffusion flames. *Combustion and Flame*, 156(3):621–632, 2009.

[172] V.V. Barve, O.A. Ezekoye, and N.T. Clemens. Soot reduction in strongly forced lifted CH4-air laminar flames. *Combustion Theory and Modelling*, 13(4):671–703, 2009.

[173] D. Morvan, B. Porterie, M. Larini, and J.C. Loraud. Numerical simulation of turbulent diffusion flame in cross flow. *Combustion Science and Technology*, 140(1-6):93–122, 1998.

[174] P.E. Desjardin and S.H. Frankel. Two-dimensional large eddy simulation of soot formation in the near-field of a strongly radiating nonpremixed acetylene-air turbulent jet flame. *Combustion and Flame*, 119(1-2):121–132, 1999.

[175] D. Morvan, B. Porterie, J.C. Loraud, and M. Larini. A numerical investigation of cross wind effects on a turbulent buoyant diffusion flame. *Combustion Science and Technology*, 164(1-6):1–35, 2001.

[176] H.J. Kim and Y.M. Kim. Numerical modeling for combustion and soot formation processes in turbulent diffusion flames. *KSME International Journal*, 16(1):116–124, 2002.

[177] F. Tao, V.I. Golovitchev, and J. Chomiak. A phenomenological model for the prediction of soot formation in diesel spray combustion. *Combustion and Flame*, 136(3):270–282, 2004.

[178] G. Ma, J.Z. Wen, M.F. Lightstone, and M.J. Thomson. Optimization of soot modeling in turbulent nonpremixed ethylene/air jet flames. *Combustion Science and Technology*, 177(8):1567–1602, 2005.

[179] P.S. Cumber and M. Spearpoint. A computational flame length methodology for propane jet fires. *Fire Safety Journal*, 41(3):215–228, 2006.

[180] M. Frenklach, D.W. Clary, W.C. Gardiner, Jr., and S.E. Stein. Detailed kinetic modeling of soot formation in shock-tube pyrolysis of acetylene. *Proceedings of the Combustion Institute*, 20(1):887–901, 1985.

[181] P.A. Tesner, T.D. Smegiriova, and V.G. Knorre. Kinetics of dispersed carbon formation. *Combustion and Flame*, 17(2):253–260, 1971.

[182] P.A. Tesner, E.I. Tsygankova, L.P. Guilazetdinov, V.P. Zuyev, and G.V. Loshakova. The formation of soot from aromatic hydrocarbons in diffusion flames of hydrocarbon-hydrogen mixtures. *Combustion and Flame*, 17(3):279–285, 1971.

[183] H. Hiroyasu, T. Kadota, and M. Arai. Development and use of a spray combustion modeling to predict diesel engine efficiency and pollutant emissions (part 1 combustion modeling). *Bulletin of the JSME*, 26(214):569–575, 1983.

[184] H. Hiroyasu, T. Kadota, and M. Arai. Development and use of a spray combustion modeling to predict diesel engine efficiency and pollutant emissions (part 2 computational procedure and parametric study). *Bulletin of the JSME*, 26(214):576–583, 1983.

[185] S.C. Graham. Modelling of the growth of soot particles during the pyrolysis and partial oxidation of aromatic hydrocarbons. *Proceedings of the Royal Society of London A*, 377(1769):119–145, 1981.

[186] G.W. Mulholland. Global soot growth model. *Fire Safety Science*, 1:709–718, 1986.

[187] J.B. Moss, C.D. Stewart, and K.J. Syed. Flowfield modelling of soot formation at elevated pressure. *Proceedings of the Combustion Institute*, 22:413–423, 1988.

[188] K.J. Syed, C.D. Stewart, and J.B. Moss. Modelling soot formation and thermal radiation in buoyant turbulent diffusion flames. *Proceedings of the Combustion Institute*, 23:1533–1541, 1990.

[189] K.J. Young and J.B. Moss. Modelling sooting turbulent jet flames using an extended flamelet technique. *Combustion Science and Technology*, 105(1-3):33–53, 1995.

[190] D.R. Honnery and J.H. Kent. Soot mass growth modelling in laminar diffusion flames. *Proceedings of the Combustion Institute*, 24:1041–1047, 1992.

[191] J.H. Kent and D. Honnery. Soot and mixture fraction in turbulent diffusion flames. *Combustion Science and Technology*, 54:383–397, 1987.

[192] J.H. Kent and D.R. Honnery. Soot mass growth in laminar diffusion flames - parametric modelling. *Springer Series in Chemical Physics*, 59:199–220, 1994.

[193] J.H. Miller, D.R. Honnery, and J.H. Kent. Modeling the growth of polynuclear aromatic hydrocarbons in diffusion flames. *Twenty-Fourth Symposium (International) on Combustion*, 24:1031–1039, 1992.

[194] R. Said, A. Garo, and R. Borghi. Soot formation modeling for turbulent flames. *Combustion and Flame*, 108(1-2):71–86, 1997.

[195] M. Fairweather, W.P. Jones, H.S. Ledin, and R.P. Lindstedt. Predictions of soot formation in turbulent, non-premixed propane flames. *Proceedings of the Combustion Institute*, 24:1067–1074, 1992.

[196] R.P. Lindstedt. A simplified mechanism for soot formation in non-premixed flames. *Aerothermodynamics in Combustors*, pages 145–156, 1992.

[197] P.R. Lindstedt. Simplified soot nucleation and surface growth steps for non-premixed flames. *Springer Series in Chemical Physics*, 59:417–441, 1994.

[198] J. Nagle and R.F. Strickland-Constable. Oxidation of carbon between 1000-2000°C. In *Proceedings of the Fifth Conference on Carbon*, pages 154–164, London, 1962. Pergamon Press.

[199] C.S. Yoo and H.G. Im. Transient soot dynamics in turbulent nonpremixed ethylene-air counterflow flames. *Proceedings of the Combustion Institute*, 31(1):701–708, 2007.

[200] D.O. Lignell, J.H. Chen, P.J. Smith, T. Lu, and C.K. Law. The effect of flame structure on soot formation and transport in turbulent nonpremixed flames using direct numerical simulation. *Combustion and Flame*, 151(1-2):2–28, 2007.

[201] D.O. Lignell, J.H. Chen, and P.J. Smith. Three-dimensional direct numerical simulation of soot formation and transport in a temporally evolving nonpremixed ethylene jet flame. *Combustion and Flame*, 155(1-2):316–333, 2008.

[202] H. El-Asrag and S. Menon. Large eddy simulation of soot formation in a turbulent non-premixed jet flame. *Combustion and Flame*, 156(2):385–395, 2009.

[203] D. Ramkrishna. *Population Balances: Theory and Applications to Particulate Systems in Engineering*. Academic Press, 2000.

[204] G. Rudinger. *Fundamentals of Gas-Particle Flow*. Elsevier Scientific, 1980.

[205] S.N. Rogak. Modeling small cluster deposition on the primary particles of aerosol agglomerates. *Aerosol Science and Technology*, 26(2):127–140, 1997.

[206] C.N. Davies. Definitive equations for the fluid resistance of spheres. *Proceedings of the Physical Society*, 57(4):259–270, 1945.

[207] Z. Li and H. Wang. Drag force, diffusion coefficient, and electric mobility of small particles. i. theory applicable to the free-molecule regime. *Physical Review E*, 68(6):612061–612069, 2003.

[208] Z. Li and H. Wang. Drag force, diffusion coefficient, and electric mobility of small particles. ii. application. *Physical Review E*, 68(6):612071–6120713, 2003.

[209] C.M. Megaridis and R.A. Dobbins. Soot aerosol dynamics in a laminar ethylene diffusion flame. *Proceedings of the Combustion Institute*, 22(1):353–362, 1989.

[210] B. Zhao, Z. Yang, M.V. Johnston, H. Wang, A.S. Wexler, M. Balthasar, and M. Kraft. Measurement and numerical simulation of soot particle size distribution functions in a laminar premixed ethylene-oxygen-argon flame. *Combustion and Flame*, 133(1-2):173–188, 2003.

[211] A. Boiarciuc, F. Foucher, and C. MounaÃŕm-Rousselle. Soot volume fractions and primary particle size estimate by means of the simultaneous two-color-time-resolved and 2d laser-induced incandescence. *Applied Physics B*, 83(3):413–421, 2006.

[212] C.M. Sorensen and G.M. Wang. Note on the correction for diffusion and drag in the slip regime. *Aerosol Science and Technology*, 33(4):353–356, 2000.

[213] L. Waldmann and K.H. Schmitt. Thermophoresis and diffusiophoresis of aerosols. In C.N. Davies, editor, *Aerosol Science*. Academic Press, New York, 1966.

[214] E.H. Kennard. *Kinetic Theory of Gases*. McGraw-Hill, New York, 1938.

[215] J.R. Brock. On the theory of thermal forces acting on aerosol particles. *Journal of Colloid Science*, 17(8):768–780, 1962.

[216] L. Talbot, R.K. Cheng, R.W. Schefer, and D.R. Willis. Thermophoresis of particles in a heated boundary layer. *Journal of Fluid Mechanics*, 101(4):737–758, 1980.

[217] Z. Li and H. Wang. Thermophoretic force and velocity of nanoparticles in the free molecule regime. *Physical Review E*, 70(2):0212051–02120511, 2004.

[218] J.B. Moss, C.D. Stewart, and K.J. Young. Modeling soot formation and burnout in a high temperature laminar diffusion flame burning under oxygen-enriched conditions. *Combustion and Flame*, 101: 491–500, 1995.

[219] D. Bradley, G. Dixon-Lewis, S.E. Habik, and E.M.J. Mushi. The oxidation of graphite powder in flame reaction zones. *Proceedings of the Combustion Institute*, 20:931–940, 1984.

[220] R.J. Santoro and J.H. Miller. Soot particle formation in laminar diffusion flames. *Langmuir*, 3(2): 244–254, 1987.

[221] S.J. Harris, A.M. Weiner, and C. Cleveland Ashcraft. Soot particle inception kinetics in a premixed ethylene flame. *Combustion and Flame*, 64(1):65–81, 1986.

[222] K.K. Kuo. *Principles of Combustion*. John Wiley & Sons, Inc., New Jersey, 2nd edition, 2005.

[223] R.J. Hall. Radiative dissipation in planar gas-soot mixtures. *Journal of Quantitative Spectroscopy & Radiative Transfer*, 51(4):635–644, 1994.

[224] P. Colonna and P. Silva. Dense gas thermodynamic properties of single and multicomponent fluids for fluid dynamics simulations. *Journal of Fluids Engineering*, 125(3):414–427, 2003.

[225] S. Palle, C. Nolan, and R.S. Miller. On molecular transport effects in real gas laminar diffusion flames at large pressure. *Physics of Fluids*, 17(10), 2005.

[226] R.C. Reid, J.M. Prausnitz, and B.E. Poling. *The Properties of Gases and Liquids*. McGraw-Hill, New York, 4th edition, 1987.

[227] B.I. Lee and M.G. Kesler. Generalized thermodynamic correlation based on three-parameter corresponding states. *AIChE Journal*, 21(3):510–527, 1975.

[228] K.S. Pitzer, D.Z. Lippmann, R.F. Curl, Jr., C.M. Huggins, and D.E. Petersen. The volumetric and thermodynamic properties of fluids. ii. compressibility factor, vapor pressure and entropy of vaporization. *Journal of the American Chemical Society*, 77(13):3433–3440, 1955.

[229] O. Redlich and J.N.S. Kwong. On the thermodynamics of solutions. v: An equation of state. fugacities of gaseous solutions. *Chemical Reviews*, 44(1):233–244, 1949.

[230] G. Soave. Equilibrium constants from a modified redlich-kwong equation of state. *Chemical Engineering Science*, 27(6):1197–1203, 1972.

[231] D.Y. Peng and D.B. Robinson. A new two-constant equation of state. *Industrial and Engineering Chemistry Research*, 15(1):59–64, 1976.

[232] R.S. Miller, K.G. Harstad, and J. Bellan. Direct numerical simulations of supercritical fluid mixing layers applied to heptane-nitrogen. *Journal of Fluid Mechanics*, 436:1–39, 2001.

[233] N. Okong'o and J. Bellan. Real-gas effects on mean flow and temporal stability of binary-species mixing layers. *AIAA Journal*, 41(12):2429–2443, 2003.

[234] H. Lou and R.S. Miller. On ternary species mixing and combustion in isotropic turbulence at high pressure. *Physics of Fluids*, 16(5):1423–1438, 2004.

[235] A. Evlampiev, L.M.T. Somers, R.S.G. Baert, and L.P.H. De Goey. On the impact of the ideal gas assumption to high-pressure combustion phenomena in engines. *Combustion Science and Technology*, 180(2):371–390, 2008.

[236] C.H. Sohn, S.H. Chung, S.R. Lee, and J.S. Kim. Structure and acoustic-pressure response of hydrogen-oxygen diffusion flames at high pressure. *Combustion and Flame*, 115(3):299–312, 1998.

[237] S. Palle and R.S. Miller. Analysis of high-pressure hydrogen, methane, and heptane laminar diffusion flames: Thermal diffusion factor modeling. *Combustion and Flame*, 151(4):581–600, 2007.

[238] G. Ribert, N. Zong, V. Yang, L. Pons, N. Darabiha, and S. Candel. Counterflow diffusion flames of general fluids: Oxygen/hydrogen mixtures. *Combustion and Flame*, 154(3):319–330, 2008.

[239] S.R. Groot and P. Mazur. *Non-Equilibrium Thermodynamics*. Courier Dover Publications, 1984.

[240] A. Ern and V. Giovangigli. Thermal diffusion effects in hydrogen-air and methane-air flames. *Combustion Theory and Modelling*, 2(4):349–372, 1998.

[241] A. Ern and V. Giovangigli. Impact of detailed multicomponent transport on planar and counterflow hydrogen/air and methane/air flames. *Combustion Science and Technology*, 149(1):157–181, 1999.

[242] D.E. Rosner, R.S. Israel, and B. La Mantia. Heavy species ludwig-soret transport effects in air-breathing combustion. *Combustion and Flame*, 123(4):547–560, 2000.

[243] R.B. Dakhlia, V. Giovangigli, and D.E. Rosner. Soret effects in laminar counterflow spray diffusion flames. *Combustion Theory and Modelling*, 6(1):1–17, 2002.

[244] V. Gopalakrishnan and J. Abraham. Effects of multicomponent diffusion on predicted ignition characteristics of an n-heptane diffusion flame. *Combustion and Flame*, 136(4):557–566, 2004.

[245] D.E. Rosner and M. Arias-Zugasti. Soret-modified hydrocarbon mass transport across compressed nonisothermal gases. *AIChE Journal*, 53(7):1879–1890, 2007.

[246] J. Bellan. Supercritical (and subcritical) fluid behavior and modeling: drops, streams, shear and mixing layers, jets and sprays. *Progress in Energy and Combustion Science*, 26(4):329–366, 2000.

[247] C.P. Leusden, C. Hasse, and N. Peters. Aggregate formation in sooting counterflow diffusion flames. *Proceedings of the Combustion Institute*, 29(2):2383–2390, 2002.

[248] R. Hilbert, F. Tap, H. El-Rabii, and D. Thevénin. Impact of detailed chemistry and transport models on turbulent combustion simulations. *Progress in Energy and Combustion Science*, 30(1):61–117, 2004.

[249] P. Papas, I. Glassman, and C.K. Law. Effects of pressure and dilution on the extinction of counterflow nonpremixed hydrogen-air flames. *Proceedings of the Combustion Institute*, 25:1333–1339, 1994.

[250] C.H. Sohn and S.H. Chung. Effect of pressure on the extinction, acoustic pressure response, and no formation in diluted hydrogen-air diffusion flames. *Combustion and Flame*, 121(1-2):288–300, 2000.

[251] S.D. Tse, D.L. Zhu, and C.K. Law. Morphology and burning rates of expanding spherical flames in H2/O2/inert mixtures up to 60 atmospheres. *Proceedings of the Combustion Institute*, 28(2):1793–1799, 2000.

[252] O.C. Kwon, G. Rozenchan, and C.K. Law. Cellular instabilities and self-acceleration of outwardly propagating spherical flames. *Proceedings of the Combustion Institute*, 29(2):1775–1783, 2002.

[253] C.K. Law. Propagation, structure, and limit phenomena of laminar flames at elevated pressures. *Combustion Science and Technology*, 178(1-3):335–360, 2006.

[254] F.A. Lindemann. Discussion on the radiation theory of chemical action. *Transactions of the Faraday Society*, 17:598–606, 1921.

[255] R.G. Gilbert, K. Luther, and J. Troe. Theory of unimolecular reactions in the fall-off range. *Physical Chemistry Chemical Physics*, 87(2):169–177, 1983.

[256] M. Frenklach, H. Wang, C.L. Yu, M. Goldenberg, C.T. Bowman, R.K. Hanson, D.F. Davidson, E.J. Chang, G.P. Smith, D.M. Golden, W.C. Gardiner, and V. Lissianski. Gri-mech 1.2, 1995. http://www.me.berkeley.edu/gri_mech/.

[257] C.T. Bowman, R.K. Hanson, D.F. Davidson, W.C. Gardiner, Jr., V. Lissianski, G.P. Smith, D.M. Golden, M. Frenklach, and M. Goldenberg. Gri-mech 2.11, 1995. http://www.me.berkeley.edu/gri_mech/.

[258] G.P. Smith, D.M. Golden, M. Frenklach, N.W. Moriarty, B. Eiteneer, M. Goldenberg, C.T. Bowman, R.K. Hanson, S. Song, W.C. Gardiner, Jr., V.V. Lissianski, and Z. Qin. Gri-mech 3.0, 2002. http://www.me.berkeley.edu/gri_mech/.

[259] Y. Tan, P. Dagaut, M. Cathonnet, J. Claude Boettner, J. Sylvain Bachman, and P. Carlier. Natural gas and blends oxidation and ignition: Experiments and modeling. *Proceedings of the Combustion Institute*, 25(1):1563–1569, 1994.

[260] Y. Tan, P. Dagaut, M. Cathonnet, and J.C. Boettner. Oxidation and ignition of methane-propane and methane-ethane-propane mixtures: experiments and modeling. *Combustion Science and Technology*, 103(1):133–151, 1994.

[261] T. Le Cong and P. Dagaut. Experimental and detailed kinetic modeling of the oxidation of methane and methane/syngas mixtures and effect of carbon dioxide addition. *Combustion Science and Technology*, 180(10-11):2046–2091, 2008.

[262] T. Le Cong, P. Dagaut, and G. Dayma. Oxidation of natural gas, natural gas/syngas mixtures, and effect of burnt gas recirculation: Experimental and detailed kinetic modeling. *Journal of Engineering for Gas Turbines and Power*, 130(4), 2008.

[263] E.L. Petersen, D.F. Davidson, and R.K. Hanson. Kinetics modeling of shock-induced ignition in low-dilution CH4/O2 mixtures at high pressures and intermediate temperatures. *Combustion and Flame*, 117(1-2):272–290, 1999.

[264] J. Huang, P.G. Hill, W.K. Bushe, and S.R. Munshi. Shock-tube study of methane ignition under engine-relevant conditions: Experiments and modeling. *Combustion and Flame*, 136(1-2):25–42, 2004.

[265] J. Huang, W.K. Bushe, P.G. Hill, and S.R. Munshi. Experimental and kinetic study of shock initiated ignition in homogeneous methane-hydrogen-air mixtures at engine-relevant conditions. *International Journal of Chemical Kinetics*, 38(4):221–233, 2006.

[266] J. Huang and W.K. Bushe. Experimental and kinetic study of autoignition in methane/ethane/air and methane/propane/air mixtures under engine-relevant conditions. *Combustion and Flame*, 144(1-2): 74–88, 2006.

[267] V.P. Zhukov, V.A. Sechenov, and A.Y. Starikovskii. Spontaneous ignition of methane - air mixtures in a wide range of pressures. *Combustion, Explosion and Shock Waves*, 39(5):487–495, 2003.

[268] V.P. Zhukov. Kinetic model of alkane oxidation at high pressure from methane to n-heptane. *Combustion Theory and Modelling*, 13(13):427–442, 2009.

[269] Douté, J.L. Delfau, R. Akrich, and C. Vovelle. Experimental study of the chemical structure of low-pressure premixed n-heptane-O2-Ar and iso-octane-O2-Ar flames. *Combustion Science and Technology*, 124(1-6):249–276, 1997.

[270] B. Varatharajan and F.A. Williams. Ethylene ignition and detonation chemistry, part 1: Detailed modeling and experimental comparison. *Journal of Propulsion and Power*, 18(2):344–351, 2002.

[271] P. Dagaut, J.C. Boettner, and M. Cathonnet. Ethylene pyrolysis and oxidation. a kinetic modeling study. *International Journal of Chemical Kinetics*, 22(6):641–664, 1990.

[272] F.N. Egolfopoulos, D.L. Zhu, and C.K. Law. Experimental and numerical determination of laminar flame speeds: Mixtures of c2-hydrocarbons with oxygen and nitrogen. *Proceedings of the Combustion Institute*, 23(1):471–478, 1991.

[273] Y. Hidaka, T. Nishimori, K. Sato, Y. Henmi, R. Okuda, K. Inami, and T. Higashihara. Shock-tube and modeling study of ethylene pyrolysis and oxidation. *Combustion and Flame*, 117(4):755–776, 1999.

[274] Z. Qin, V.V. Lissianski, H. Yang, W.C. Gardiner, S.G. Davis, and H. Wang. Combustion chemistry of propane: A case study of detailed reaction mechanism optimization. *Proceedings of the Combustion Institute*, 28(2):1663–1669, 2000.

[275] H. Wang, X. You, A.V. Joshi, S.G. Davis, A. Laskin, F. Egolfopoulos, and C.K. Law. Usc mech version ii. high-temperature combustion reaction model of h2/co/c1-c4 compounds, 2007. http://ignis.usc.edu/USC_Mech_II.htm.

[276] F.A. Williams. Chemical-kinetic mechanisms for combustion applications, 2005. University of California at San Diego, http://maeweb.ucsd.edu/ combustion/cermech/.

[277] F.N. Egolfopoulos and P.E. Dimotakis. A comparative numerical study of premixed and non-premixed ethylene flames. *Combustion Science and Technology*, 162(1-6):19–35, 2001.

[278] K. Kumar, G. Mittal, C.J. Sung, and C.K. Law. An experimental investigation of ethylene/O2/diluent mixtures: Laminar flame speeds with preheat and ignition delays at high pressures. *Combustion and Flame*, 153(3):343–354, 2008.

[279] O.G. Penyazkov, K.L. Sevrouk, V. Tangirala, and N. Joshi. High-pressure ethylene oxidation behind reflected shock waves. *Proceedings of the Combustion Institute*, 32(2):2421–2428, 2009.

[280] K. Saito, F.A. Williams, and A.S. Gordon. A study of the two-color soot zone for small hydrocarbon diffusion flames. *Combustion Science and Technology*, 51:285–305, 1987.

[281] F.A. Williams. *Combustion Theory*. Benjamin Cummings, Menlo Park, CA, 1985.

[282] T. Poinsot and D. Veynante. *Theoretical and Numerical Combustion*. Edwards, Philadelphia, PA, 2nd edition, 2005.

[283] J.O. Hirschfelder, C.F. Curtiss, and R.B. Byrd. *Molecular Theory of Gases and Liquids*. John Wiley & Sons, New York, 1969.

[284] E.S. Oran and J.P. Boris. Detailed modelling of combustion systems. *Progress in Energy and Combustion Science*, 7(1):1–72, 1981.

[285] A. Ern and V. Giovangigli. Fast and accurate multicomponent transport property evaluation. *Journal of Computational Physics*, 120(1):105–116, 1995.

[286] D.N. Pope and G. Gogos. A new multicomponent diffusion formulation for the finite-volume method: Application to convective droplet combustion. *Numerical Heat Transfer Part B*, 48(3):213–233, 2005.

[287] D.G. Goodwin. An open-source, extensible software suite for CVD process simulation. *Chemical Vapor Deposition XVI and EUROCVD 14*, pages 155–162, 2003.

[288] S. Gordon and B.J. McBride. Computer program for calculation of complex chemical equilibrium composition, rocket performance, incident and reflected shocks and chapman-jouguet detonations. Report no. SP-273, NASA, 1971.

[289] S. Gordon and B.J. McBride. Computer program for calculation of complex chemical equilibrium compositions and applications i. analysis. Reference publication 1311, NASA, 1994.

[290] B.J. McBride and S. Gordon. Computer program for calculation of complex chemical equilibrium compositions and applications ii. users manual and program description. Reference publication 1311, NASA, 1996.

[291] C.R. Wilke. A viscosity equation for gas mixtures. *Journal of Chemical Physics*, 18:517–519, 1950.

[292] C.R. Mathur, P.K. Tondon, and S.C. Saxena. Thermal conductivity of binary, ternary and quaternary mixtures of rare gases. *Molecular Physics*, 12:569–579, 1967.

[293] M.F. Modest. *Radiative Heat Transfer*. Academic Press, New York, 2nd edition, 2003.

[294] J. de Ris. Fire radiation–a review. *Proceedings of the Combustion Institute*, 17(1):1003–1016, 1979.

[295] B.L. Drolen and C.L. Tien. Absorption and scattering of agglomerated soot particulate. *Journal of Quantitative Spectroscopy & Radiative Transfer*, 37(5):433–448, 1987.

[296] R. Viskanta and M.P. Mengüç. Radiation heat transfer in combustion systems. *Progress in Energy and Combustion Science*, 13:97–160, 1987.

[297] B.G. Carlson and K.D. Lathrop. Transport theory - the method of discrete ordinates. In H. Greenspan, C.N. Kelber, and D. Okrent, editors, *Computing Methods in Reactor Physics*, pages 171–266. Gordon and Breach, London, 1968.

[298] G.D. Raithby and E.H. Chui. A finite-volume method for predicting radiant heat transfer in enclosures with participating media. *Journal of Heat Transfer*, 112(2):415–423, 1990.

[299] J.C. Chai, H.S. Lee, and S.V. Patankar. Finite volume method for radiation heat transfer. *Journal of Thermophysics and Heat Transfer*, 8(3):419–425, 1994.

[300] A.A. Lacis and V. Oinas. A description of the correlated k distribution method for modeling nongray gaseous absorption, thermal emission, and multiple scattering in vertically inhomogeneous atmospheres. *Journal of Geophysical Research*, 96(D5):9027–9063, 1991.

[301] J.R. Howell. Application of monte carlo to heat transfer problems. *Advances in Heat Transfer*, 5: 1–54, 1968.

[302] H.C. Hottel and E.S. Cohen. Radiant heat exchange in a gas-filled enclosure: Allowance for nonuniformity of gas temperature. *AIChE Journal*, 4(1):3–14, 1958.

[303] H.C. Hottel and A.F. Sarofim. *Radiative Transfer*. McGraw-Hill, New York, 1967.

[304] V. Kourganoff. *Basic Methods in Transfer Problems*. Dover Publications, New York, 1963.

[305] F.C. Lockwood and N.G. Shah. A new radiation solution method for incorporation in general combustion prediction procedures. *Proceedings of the Combustion Institute*, pages 1405–1414, 1981.

[306] S.B. Dworkin, B.A.V. Bennett, and M.D. Smooke. A mass-conserving vorticity-velocity formulation with application to nonreacting and reacting flows. *Journal of Computational Physics*, 215(2):430–447, 2006.

[307] A. Soufiani and J. Taine. High temperature gas radiative property parameters of statistical narrow-band model for H_2O, CO_2 and CO, and correlated-k model for H_2O and CO_2. *International Journal of Heat and Mass Transfer*, 40(4):987–991, 1997.

[308] L. Pierrot, A. Soufiani, and J. Taine. Accuracy of narrow-band and global models for radiative transfer in H_2O, CO_2, and H_2O-CO_2 mixtures at high temperature. *Journal of Quantitative Spectroscopy & Radiative Transfer*, 62(5):523–548, 1999.

[309] V. Goutiere, F. Liu, and A. Charette. An assessment of real-gas modelling in 2D enclosures. *Journal of Quantitative Spectroscopy & Radiative Transfer*, 64(3):299–326, 2000.

[310] W.L. Godson. The evaluation of infrared radiation fluxes due to atmospheric water vapor. *Quarterly Journal of Royal Meteorological Society*, 79:367–379, 1953.

[311] S.J. Young. Nonisothermal band model theory. *Journal of Quantitative Spectroscopy & Radiative Transfer*, 18(1):1–28, 1977.

[312] R.M. Goody and Y.L. Yung. *Atmospheric Radiation: Theoretical Basis*. Oxford University Press, 2nd edition, 1989.

[313] R. Goody, R. West, L. Chen, and D. Crisp. The correlated-k method for radiation calculations in nonhomogeneous atmospheres. *Journal of Quantitative Spectroscopy & Radiative Transfer*, 42(6): 539–550, 1989.

[314] L.S. Rothman, I.E. Gordon, A. Barbe, D.C. Benner, P.F. Bernath, M. Birk, V. Boudon, L.R. Brown, A. Campargue, J.P. Champion, K. Chance, L.H. Coudert, V. Dana, V.M. Devi, S. Fally, J.M. Flaud, R.R. Gamache, A. Goldman, D. Jacquemart, I. Kleiner, N. Lacome, W.J. Lafferty, J.Y. Mandin, S.T. Massie, S.N. Mikhailenko, C.E. Miller, N. Moazzen-Ahmadi, O.V. Naumenko, A.V. Nikitin, J. Orphal, V.I. Perevalov, A. Perrin, A. Predoi-Cross, C.P. Rinsland, M. Rotger, M. ÅăimeÄĎkovÃą, M.A.H. Smith, K. Sung, S.A. Tashkun, J. Tennyson, R.A. Toth, A.C. Vandaele, and J. Vander Auwera. The HITRAN 2008 molecular spectroscopic database. *Journal of Quantitative Spectroscopy & Radiative Transfer*, 2009.

[315] W. Malkmus. Random Lorentz band model with exponential-tailed s^{-1} line-intensity distribution function. *Journal of the Optical Society of America*, 57(3):323–329, 1967.

[316] J. Taine. A line-by-line calculation of low-resolution radiative properties of CO_2-CO-transparent nonisothermal gases mixtures up to 3000 K. *Journal of Quantitative Spectroscopy & Radiative Transfer*, 30(4):371–379, 1983.

[317] J.M. Hartmann, R. Levi Di Leon, and J. Taine. Line-by-line and narrow-band statistical model calculations for H_2O. *Journal of Quantitative Spectroscopy & Radiative Transfer*, 32(2):119–127, 1984.

[318] A. Soufiani, J.M. Hartmann, and J. Taine. Validity of band-model calculations for CO_2 and H_2O applied to radiative properties and conductive-radiative transfer. *Journal of Quantitative Spectroscopy & Radiative Transfer*, 33(3):243–257, 1985.

[319] L.S. Rothman, R.R. Gamache, R.H. Tipping, C.P. Rinsland, M.A.H. Smith, D.C. Benner, V.M. Devi, J.M. Flaud, C. Camy-Peyret, A. Perrin, A. Goldman, S.T. Massie, L.R. Brown, and R.A. Toth. The HITRAN molecular database: Editions of 1991 and 1992. *Journal of Quantitative Spectroscopy & Radiative Transfer*, 48(5-6):469–507, 1992.

[320] M.Y. Perrin and A. Soufiani. Approximate radiative properties of methane at high temperature. *Journal of Quantitative Spectroscopy & Radiative Transfer*, 103(1):3–13, 2007.

[321] Q. Fu and K.N. Liou. On the correlated k-distribution method for radiative transfer in nonhomogeneous atmospheres. *Journal of Atmospheric Sciences*, 49(22):2139–2156, 1992.

[322] F. Liu, G.J. Smallwood, and Ö.L. Gülder. Application of the statistical narrow-band correlated-k method to low-resolution spectral intensity and radiative heat transfer calculations - effects of the quadrature scheme. *International Journal of Heat and Mass Transfer*, 43(17):3119–3135, 2000.

[323] F. Liu, G.J. Smallwood, and Ö.L. Gülder. Application of the statistical narrow-band correlated-k method to non-grey gas radiation in CO_2-H_2O mixtures: Approximate treatments of overlapping bands. *Journal of Quantitative Spectroscopy & Radiative Transfer*, 68(4):401–417, 2001.

[324] F. Liu, G.J. Smallwood, and Ö.L. Gülder. Radiation heat transfer calculations using the SNBCK method. *AIAA Paper 99-3679*, 1999.

[325] F. Liu, G.J. Smallwood, and Ö.L. Gülder. Band lumping strategy for radiation heat transfer calculations using a narrowband model. *Journal of Thermophysics and Heat Transfer*, 14(2):278–281, 2000.

[326] V. Goutiere, A. Charette, and L. Kiss. Comparative performance of nongray gas modeling techniques. *Numerical Heat Transfer Part B*, 41(3-4):361–381, 2002.

[327] F. Liu and G.J. Smallwood. An efficient approach for the implementation of the snb based correlated-k method and its evaluation. *Journal of Quantitative Spectroscopy & Radiative Transfer*, 84(4):465–75, 2004.

[328] S.C. Lee and C.L. Tien. Effect of soot shape on soot radiation. *Journal of Quantitative Spectroscopy & Radiative Transfer*, 29(3):259–265, 1983.

[329] J.H. Kent and D.R. Honnery. A soot formation rate map for a laminar ethylene diffusion flame. *Combustion and Flame*, 79:287–298, 1990.

[330] J.D. Felske and C.L. Tien. Use of the Milne-Eddington absorption coefficient for radiative heat transfer in combustion systems. *Journal of Heat Transfer*, 99(3):458–465, 1977.

[331] K.D. Lathrop and B.G. Carlson. Discrete ordinates angular quadrature of the neutron transport equation. Report LA-3186, Los Alamos Scientific Laboratory, 1965.

[332] C.P. Thurgood, A. Pollard, and H.A. Becker. TN quadrature set for the discrete ordinates method. *Journal of Heat Transfer*, 117(4):1068–1070, 1995.

[333] A. Ern, C.C. Douglas, and M.D. Smooke. Detailed chemistry modeling of laminar diffusion flames on parallel computers. *International Journal of Supercomputer Applications and High Performance Computing*, 9(3):167–186, Fall 1995.

[334] P. Deuflhard. A modified newton method for the solution of ill-conditioned systems of nonlinear equations with application to multiple shooting. *Numerische Mathematik*, 22(4):289–315, 1974.

[335] M.S. Day and J.B. Bell. Numerical simulation of laminar reacting flows with complex chemistry. *Combustion Theory and Modelling*, 4(4):535–556, 2000.

[336] J.B. Bell, A.J. Aspden, M.S. Day, and M.J. Lijewski. Numerical simulation of low mach number reacting flows. *Journal of Physics: Conference Series*, 78(1), 2007.

[337] S.A. Northrup and C.P.T. Groth. Solution of laminar diffusion flames using a parallel adaptive mesh refinement algorithm. In *43rd AIAA Aerospace Sciences Meeting and Exhibit*, Reno, Nevada, 10-13 January 2005. AIAA paper 2005-0547.

[338] S.A. Northrup and C.P.T. Groth. Solution of laminar combusting flows using a parallel implicit adaptive mesh refinement algorithm. In *Proceedings of the Fourth International Conference on Computational Fluid Dynamics, ICCFD4*, pages 341–346, Ghent, Belgium, July 10-14 2006.

[339] X. Gao and C.P.T. Groth. Parallel adaptive mesh refinement scheme for turbulent non-premixed combusting flow prediction. In *44th AIAA Aerospace Sciences Meeting and Exhibit*, volume 23, pages 17450–17463, Reno, Nevada, 9-12 January 2006. AIAA paper 2006-1448.

[340] X. Gao and C.P.T. Groth. Parallel adaptive mesh refinement scheme for three-dimensional turbulent non-premixed combustion. In *46th AIAA Aerospace Sciences Meeting and Exhibit*, Reno, Nevada, 7–10 January 2008. AIAA paper 2008-1017.

[341] S.A. Northrup and C.P.T. Groth. Parallel implicit adaptive mesh refinement algorithm for solution of laminar combusting flows. In *Proceedings of the 14th Annual Conference of the CFD Society of Canada*, pages 221–228, Kingston, Ontario, Canada, July 16-18 2006. paper 1106.

[342] S. Venkateswaran and C.L. Merkle. Analysis of preconditioning methods for the Euler and Navier-Stokes equations. *Von Karman Institute Lecture Series*, 1999.

[343] M.S. Liou. A sequel to AUSM, part ii: AUSM+-up for all speeds. *Journal of Computational Physics*, 214(1):137–170, 2006.

[344] Y.H. Choi and C.L. Merkle. The application of preconditioning in viscous flows. *Journal of Computational Physics*, 105(2):207–223, 1993.

[345] E. Turkel. Review of preconditioning methods for fluid dynamics. *Applied Numerical Mathematics*, 12(1-3):257–284, 1993.

[346] E. Turkel, R. Radespiel, and N. Kroll. Assessment of preconditioning methods for multidimensional aerodynamics. *Computers & Fluids*, 26(6):613–634, 1997.

[347] J.S. Shuen. A coupled implicit method for chemical non-equilibrium flows at all speeds. *Journal of Computational Physics*, 106(2):306–318, 1993.

[348] J.M. Weiss and W.A. Smith. Preconditioning applied to variable and constant density flows. *AIAA Journal*, 33(11):2050–2057, 1995.

[349] S. Venkateswaran, M. Deshpande, and C.L. Merkle. The application of preconditioning to reacting flow computations. In *12th AIAA Computational Fluid Dynamics Conference*, San Diego, CA, Jun. 19-22 1995. AIAA paper 1995-1673.

[350] S.Y. Hsieh and V. Yang. A preconditioned flux-differencing scheme for chemically reacting flows at all Mach numbers. *International Journal of Computational Fluid Dynamics*, 8(1):31–49, 1997.

[351] S. Venkateswaran, J.W. Lindau, R.F. Kunz, and C.L. Merkle. Computation of multiphase mixture flows with compressibility effects. *Journal of Computational Physics*, 180(1):54–77, 2002.

[352] H. Meng and V. Yang. A unified treatment of general fluid thermodynamics and its application to a preconditioning scheme. *Journal of Computational Physics*, 189(1):277–304, 2003.

[353] D. Li, V. Sankaran, J.W. Lindau, and C.L. Merkle. A unified computational formulation for multi-component and multi-phase flows. *AIAA paper 2005-1391*, 2005.

[354] V. Sankaran and J.C. Oefeleint. Advanced preconditioning strategies for chemically reacting flows. *AIAA paper 2007-1432*, 2007.

[355] J.M. Weiss, J.P. Maruszewski, and W.A. Smith. Implicit solution of preconditioned Navier-Stokes equations using algebraic multigrid. *AIAA Journal*, 37(1):29–36, 1999.

[356] S.K. Godunov. Fintite-difference method for numerical computations of discontinuous solutions of the equations of fluid dynamics. *Matematicheskii Sbornik*, 47:271–306, 1959.

[357] P.L. Roe. Approximate Riemann solvers, parameter vectors, and difference schemes. *Journal of Computational Physics*, 43:357–372, 1981.

[358] P.L. Roe and J. Pike. Efficient construction and utilisation of approximate Riemann solutions. In R. Glowinski and J.L. Lions, editors, *Computing Methods in Applied Science and Engineering*, volume VI, pages 499–518, Amsterdam, 1984. North-Holland.

[359] A. Harten. High resolution schemes for hyperbolic conservation laws. *Journal of Computational Physics*, 49:357–393, 1983.

[360] J.S. Shuen. Inviscid flux-splitting algorithms for real gases with non-equilibrium chemistry. *Journal of Computational Physics*, 90(2):371–395, 1990.

[361] R. Walters, P. Cinnella, D. Slack, and D. Halt. Characteristic-based algorithms for flows in thermochemical nonequilibrium. *AIAA Journal*, 30(5):1304–1313, 1992.

[362] B. Engquist and S. Osher. One-sided difference approximations for nonlinear conservation laws. *Mathematics of Computation*, 36:321–352, 1981.

[363] B. Van Leer. Towards the ultimate conservative difference scheme. V. A second-order sequel to Godunov's method. *Journal of Computational Physics*, 32:101–136, 1979.

[364] V. Venkatakrishnan. Convergence to steady state solutions of the euler equations on unstructured grids with limiters. *Journal of Computational Physics*, 118(1):120–130, 1995.

[365] T.J. Barth and D.C. Jespersen. The design and application of upwind schemes on unstructured meshes, 1989. AIAA Paper 89-0366.

[366] W.J. Coirier. *An Adaptively-Refined, Cartesian, Cell-Based Scheme for the Euler and Navier-Stokes Equations*. PhD thesis, University of Michigan, 1994.

[367] W.J. Coirier and K.G. Powell. Solution-adaptive Cartesian cell approach for viscous and inviscid flows. *AIAA Journal*, 34(5):938–945, May 1996.

[368] D.W. Zingg and M. Yarrow. A method of smooth bivariate interpolation for data given on a generalized curvilinear grid. *SIAM Journal for Scientific and Statistical Computing*, 13:687–693, 1992.

[369] C.P.T. Groth and S.A. Northrup. Parallel implicit adaptive mesh refinement scheme for body-fitted multi-block mesh. In *17th AIAA Computational Fluid Dynamics Conference*, Toronto, Ontario, Canada, 6-9 June 2005. AIAA paper 2005-5333.

[370] Y. Saad and M.H. Schultz. GMRES: A generalized minimal residual algorithm for solving nonsymmetric linear systems. *SIAM Journal for Scientific and Statistical Computing*, 7(3):856–869, 1986.

[371] Y. Saad. Krylov subspace methods on supercomputers. *SIAM Journal for Scientific and Statistical Computing*, 10(6):1200–1232, 1989.

[372] P.N. Brown and Y. Saad. Hybrid Krylov methods for nonlinear systems of equations. *SIAM Journal for Scientific and Statistical Computing*, 11(3):450–481, 1990.

[373] Y. Saad. *Iterative Methods for Sparse Linear Systems*. PWS Publishing Company, Boston, 1996.

[374] R.S. Dembo, S.C. Eisenstat, and T. Steihaug. Inexact newton methods. *SIAM Journal on Numerical Analysis*, 19(2):400–408, 1982.

[375] W.A. Mulder and B. Van Leer. Experiments with implicit upwind methods for the Euler equations. *Journal of Computational Physics*, 59:232–246, 1985.

[376] J.S. Sachdev, C.P.T. Groth, and J.J. Gottlieb. A parallel solution-adaptive scheme for multi-phase core flows in solid propellant rocket motors. *International Journal of Computational Fluid Dynamics*, 19 (2):159–177, 2005.

[377] J.S. Sachdev and C.P.T. Groth. A mesh adjustment scheme for embedded boundaries. *Communications in Computational Physics*, 2(6):1095–1124, 2007.

[378] M.J. Berger. Adaptive mesh refinement for hyperbolic partial differential equations. *Journal of Computational Physics*, 53:484–512, 1984.

[379] M.J. Berger and P. Colella. Local adaptive mesh refinement for shock hydrodynamics. *Journal of Computational Physics*, 82:67–84, 1989.

[380] M.J. Berger and J.S. Saltzman. AMR on the CM-2. *Applied Numerical Mathematics*, 14:239–253, 1994.

[381] M.J. Aftomis, M.J. Berger, and J.E. Melton. Robust and efficient Cartesian mesh generation for component-base geometry. *AIAA Journal*, 36(6):952–960, 1998.

[382] J.J. Quirk. *An Adaptive Grid Algorithm for Computational Shock Hydrodynamics*. PhD thesis, Cranfield Institute of Technology, January 1991.

[383] D. De Zeeuw and K.G. Powell. An adaptively refined Cartesian mesh solver for the Euler equations. *Journal of Computational Physics*, 104:56–68, 1993.

[384] J.J. Quirk and U.R. Hanebutte. A parallel adaptive mesh refinement algorithm. *ICASE Report 93-63*, 1993.

[385] W. Gropp, E. Lusk, and A. Skjellum. *Using MPI*. MIT Press, Cambridge, Massachussets, 1999.

[386] J. Gonçalves and P.J. Coelho. Parallelization of the discrete ordinates method. *Numerical Heat Transfer Part B*, 32(2):151–173, 1997.

[387] L.H. Howell. A parallel AMR implementation of the discrete ordinates method for radiation transport. In T. Plewa, T. Linde, and V.G. Weirs, editors, *Adaptive Mesh Refinement - Theory and Applications*, volume 41 of *Lecture Notes in Computational Science and Engineering*, pages 255–270. Springer Berlin Heidelberg, 2005.

[388] D.R. Snelling, K.A. Thomson, G.J. Smallwood, and Ö.L. Gülder. Two-dimensional imaging of soot volume fraction in laminar diffusion flames. *Applied Optics*, 38(12):2478–2485, 1999.

[389] C.K. Law. Comprehensive description of chemistry in combustion modeling. *Combustion Science and Technology*, 177(5-6):845–870, 2005.

[390] R. Bustinza, G.N. Gatica, and B. Cockburn. An a posteriori error estimate for the local discontinuous Galerkin method applied to linear and nonlinear diffusion problems. *Journal of Scientific Computing*, 22-23:147–185, 2005.

[391] M. Nemec, M.J. Aftosmis, and M. Wintzer. Adjoint-based adaptive mesh refinement for complex geometries. *AIAA Paper 2008-0725*, 2008.

[392] A. Kazakov and M. Frenklach. Reduced reaction sets based on GRI-Mech 1.2, 1994. http://www.me.berkeley.edu/drm/.

[393] G. Amdahl. Validity of the single processor approach to achieving large-scale computing capabilities. *AFIPS '67 (Spring): Proceedings of the April 18-20, 1967, spring joint computer conference*, pages 483–485, 1967.

[394] N. Panek. An investigation of ethylene laminar diffusion flames at sub-atmospheric pressures to simulate microgravity. Master's thesis, University of Toronto, 2009.

[395] D.R. Snelling, K.A. Thomson, G.J. Smallwood, Ö.L. Gülder, E.J. Weckman, and R.A. Fraser. Spectrally resolved measurement of flame radiation to determine soot temperature and concentration. *AIAA Journal*, 40(9):1789–1795, September 2002.

[396] D.R. Honnery and J.H. Kent. Soot formation in long ethylene diffusion flames. *Combustion and Flame*, 82(3-4):426–434, 1990.

[397] J.H. Kent and D.R. Honnery. Soot formation rates in diffusion flamesâĂŤa unifying trend. *Combustion Science and Technology*, 75(4):167âĂŞ177, 1991.

[398] R.W. Bilger. The structure of turbulent nonpremixed flames. *Proceedings of the Combustion Institute*, 22(1):475–488, 1989.

[399] C.M. Megaridis, D.W. Griffin, and B. Konsur. Soot-field structure in laminar soot-emitting microgravity nonpremixed flames. *Proceedings of the Combustion Institute*, 26(1):1291–1299, 1996.

[400] Ö.L. Gülder, K.A. Thomson, and D.R. Snelling. Effect of fuel nozzle material properties on soot formation and temperature field in coflow laminar diffusion flames. *Combustion and Flame*, 144: 426–433, 2006.

[401] J.H. Kent and H.G. Wagner. Why do diffusion flames emit smoke. *Combustion Science and Technology*, 41(5-6):245–269, 1984.

[402] P.M. Mandatori and Ö.L. Gülder. Complete conversion of ethane to soot in a coflow laminar diffusion flame at 3.65 MPa. *Combustion and Flame*, 150(4):400–403, 2007.

[403] F.E. Ham, F.S. Lien, and A.B. Strong. A Cartesian grid method with transient anisotropic adaptation. *Journal of Computational Physics*, 179(2):469–494, 2002.

[404] W.A. Keats and F.S. Lien. Two-dimensional anisotropic Cartesian mesh adaptation for the compressible Euler equations. *International Journal for Numerical Methods in Fluids*, 46(11):1099–1125, 2004.

[405] H.A. van der Vorst. Bi-CGSTAB: A fast and smoothly converging variant of Bi-CG for the solution of nonsymmetric linear systems. *SIAM Journal for Scientific and Statistical Computing*, 13(2):631–644, 1992.

[406] G.L. Sleijpen and D.R. Fokkema. BiCGStab(*l*) for linear equations involving unsymmetric matrices with complex spectrum. *Electronic Transactions on Numerical Analysis*, pages 11–32, 1993.

[407] X.C. Cai, W.D. Gropp, D.E. Keyes, R.G. Melvin, and D.P. Young. Parallel Newton-Krylov-Schwarz algorithms for the transonic full potential equations. *SIAM Journal on Scientific Computing*, 19(1): 246–265, 1998.

[408] K. Germaschewski, A. Bhattacharjee, R. Grauer, D. Keyes, and B. Smith. Using Krylov-Schwarz methods in an adaptive mesh refinement environment. In T. Plewa, T. Linde, and V. Gregory Weirs, editors, *Adaptive Mesh Refinement - Theory and Applications*, volume 41 of *Lecture Notes in Computational Science and Engineering*, pages 115–124. Springer Berlin Heidelberg, 2005.

[409] E.E. Prudencio and X.C. Cai. Parallel multilevel restricted Schwarz preconditioners with pollution removing for PDE-constrained optimization. *SIAM Journal on Scientific Computing*, 29(3):964–985, 2007.

[410] F. Liu, H.A. Becker, and A. Pollard. Spatial differencing schemes of the discrete-ordinates method. *Numerical Heat Transfer Part B*, 30(1):23–43, 1996.

[411] J.P. Jessee and W.A. Fiveland. Bounded, high-resolution differencing schemes applied to the discrete ordinates method. *Journal of Thermophysics and Heat Transfer*, 11(4):540–548, 1997.

[412] P.H. Gaskell and A.K.C. Lau. Curvature-compensated convective transport: SMART a new boundedness- preserving transport algorithm. *International Journal for Numerical Methods in Fluids*, 8(6):617–641, 1988.

[413] B. Van Leer. Towards the ultimate conservative difference scheme. II. Monotonicity and conservation combined in a second order scheme. *Journal of Computational Physics*, 14:361–370, 1974.

[414] P.J. Coelho. Bounded skew high-order resolution schemes for the discrete ordinates method. *Journal of Computational Physics*, 175(2):412–437, 2002.

[415] S.R. Mathur and J.Y. Murthy. Acceleration of anisotropic scattering computations using coupled ordinates method (COMET). *Journal of Heat Transfer*, 123(3):607–612, 2001.

[416] A. Fiterman, R. Ben-Zvi, and A. Kribus. DOTS: Pseudo-time-stepping solution of the discrete ordinate equations. *Numerical Heat Transfer Part B*, 35(2):163–183, 1999.

[417] N. Selçuk and G. Kirbaş. The method of lines solution of the discrete ordinates method for radiative heat transfer in enclosures. *Numerical Heat Transfer Part B*, 37(3):379–392, 2000.

[418] I. Ayranci and N. Selçuk. MOL solution of DOM for transient radiative transfer in 3-D scattering media. *Journal of Quantitative Spectroscopy & Radiative Transfer*, 84(4):409–422, 2004.

[419] A.U. Bilge, T. Tarhan, and N. Selçuk. Transient simulation of reacting radiating flows. *International Journal of Thermal Sciences*, 45(10):969–976, 2006.

[420] A.C. Hindmarsh. LSODE and LSODI, two new initial value ordinary differential equation solvers. *ACM-SIGNUM Newsletter*, 15(4):10–11, 1980.

[421] E. Fehlberg. Classical fourth- and lower order Runge-Kutta formulas with stepsize control and their application to heat transfer problems. *Computing*, 6(1-2):61–71, 1970.

[422] G.S. Jiang and C.W. Shu. Efficient implementation of weighted ENO schemes. *Journal of Computational Physics*, 126(1):202–228, 1996.

[423] D.S. Balsara and C.W. Shu. Monotonicity preserving weighted essentially non-oscillatory schemes with increasingly high order of accuracy. *Journal of Computational Physics*, 160(2):405–452, 2000.

[424] D. Balsara. Fast and accurate discrete ordinates methods for multidimensional radiative transfer - Part I, basic methods. *Journal of Quantitative Spectroscopy & Radiative Transfer*, 69:671–707, 2001.

[425] P.L. Roe. Optimum upwind advection on a triangular mesh. *ICASE Report 90-75*, 1990.

[426] D. Sidilkover and P.L. Roe. Unification of some advection schemes in two dimensions. *ICASE Report 95-10*, 2000.

[427] A. Brandt. Guide to multigrid development. In W. Hackbusch and U. Trottenberg, editors, *Multigrid Methods*, volume 960 of *Lecture Notes in Mathematics*, pages 220–312. Springer Berlin, 1982.

[428] J.C. Chai. Transient radiative transfer in irregular two-dimensional geometries. *Journal of Quantitative Spectroscopy & Radiative Transfer*, 84:281–294, 2004.

[429] P.J. Coelho and J. Gonçalves. Parallelization of the finite volume method for radiation heat transfer. *International Journal of Numerical Methods for Heat and Fluid Flow*, 9(4):388–404, 1999.

[430] J. Liu, H.M. Shang, and Y.S. Chen. Parallel simulation of radiative heat transfer using an unstructured finite-volume method. *Numerical Heat Transfer Part B*, 36:115–137, 1999.

[431] G. Krishnamoorthy, R. Rawat, and P.J. Smith. Parallel computations of radiative heat transfer using the discrete ordinates method. *Numerical Heat Transfer Part B*, 46:19–38, 2005.

[432] Ö. Yıldız and H. Bedir. A parallel solution to the radiative transport in three-dimensional participating media. *Numerical Heat Transfer Part B*, 50(1):79–95, 2006.

[433] T.J. Barth and P.O. Fredrickson. Higher order solution of the Euler equations on unstructured grids using quadratic reconstruction, 1990. AIAA Paper 90-0013.

[434] P.J. Coelho. A comparison of spatial discretization schemes for differential solution methods of the radiative transfer equation. *Journal of Quantitative Spectroscopy & Radiative Transfer*, 109(2):189–200, 2008.

[435] V. Venkatakrishnan. On the accuracy of limiters and convergence to steady state solutions. *AIAA Paper 93-0880*, 1993.

[436] G.D. Van Albada, B. Van Leer, and W.W. Roberts. A comparative study of computational methods in cosmic gas dynamics. *Astronomy and Astrophysics*, 108:76–84, 1982.

[437] P. Cheng. Exact solutions for multi-dimensional radiative transfer in cartesian coordinate configurations. Paper 1972-21, AIAA, 1972.

[438] J.P. Jessee, W.A. Fiveland, L.H. Howell, P. Colella, and R.B. Pember. An adaptive mesh refinement algorithm for the radiative transport equation. *Journal of Computational Physics*, 139(2):380–398, 1998.

[439] T.K. Kim and H. Lee. Effect of anisotropic scattering on radiative heat transfer in two-dimensional rectangular enclosures. *International Journal of Heat and Mass Transfer*, 31(8):1711–1721, 1988.

[440] P.K. Khosla and S.G. Rubin. A diagonally dominant second-order accurate implicit scheme. *Computers & Fluids*, 2(2):207–209, 1974.

[441] B. Van Leer, C. Tai, and K.G. Powell. Design of optimally smoothing multi-stage schemes for the euler equations. *AIAA Paper 89-1933*, 1989.

Appendix A

GOVERNING EQUATIONS

For a two-dimensional axisymmetric coordinate system, Eqs. (3.2a)–(3.2f) can be reformulated as

$$\frac{\partial}{\partial t}\mathbf{U} + \frac{\partial}{\partial r}\mathbf{F} + \frac{\partial}{\partial z}\mathbf{G} = \frac{\partial}{\partial r}\mathbf{F}_{\mathrm{v}} + \frac{\partial}{\partial z}\mathbf{G}_{\mathrm{v}} + \frac{\mathbf{S}_{\mathrm{axis}}}{r} + \mathbf{S}_{\mathrm{p}} \tag{A.1}$$

where $\mathbf{U}$ is the vector of conserved variables,

$$\mathbf{U} = \left[\rho, \quad \rho u, \quad \rho v, \quad \rho e, \quad \rho Y_1, \quad \ldots, \quad \rho Y_N, \quad \rho Y_{\mathrm{s}}, \quad \rho N_{\mathrm{s}}\right]^T,$$

$\mathbf{S}_{\mathrm{axis}}$ and $\mathbf{S}_{\mathrm{p}}$ are the axisymmetric and non-axisymmetric source terms,

$$\mathbf{S}_{\mathrm{axis}} = \begin{bmatrix} -\rho u \\ -\rho u^2 + \tau_{rr} - \tau_{\theta\theta} \\ -\rho u v + \tau_{rz} \\ -\rho u\left(e + \dfrac{p}{\rho}\right) - \mathrm{q}_r + u\tau_{rr} + v\tau_{rz} \\ -\rho Y_1 u + \rho D_1 \frac{\partial Y_1}{\partial r} \\ \vdots \\ -\rho Y_N u + \rho D_N \frac{\partial Y_N}{\partial r} \\ -\rho Y_{\mathrm{s}} u + \rho D_{\mathrm{s}} \frac{\partial Y_{\mathrm{s}}}{\partial r} \\ -\rho N_{\mathrm{s}} u + \rho D_{\mathrm{s}} \frac{\partial N_{\mathrm{s}}}{\partial r} \end{bmatrix} \quad \text{and} \quad \mathbf{S}_{\mathrm{p}} = \begin{bmatrix} 0 \\ 0 \\ \rho \mathrm{g}_z \\ \rho \mathrm{g}_z v \\ \rho \dot{\omega}_1 \\ \vdots \\ \rho \dot{\omega}_N \\ S_Y \\ S_N \end{bmatrix},$$

F and **G** are the inviscid solution flux vectors,

$$\mathbf{F} = \begin{bmatrix} \rho u \\ \rho u^2 + p \\ \rho v u \\ \rho u \left(e + \dfrac{p}{\rho} \right) \\ \rho Y_1 u \\ \vdots \\ \rho Y_N u \\ \rho Y_\mathrm{s} u \\ \rho N_\mathrm{s} u \end{bmatrix} \quad \text{and} \quad \mathbf{G} = \begin{bmatrix} \rho v \\ \rho u v \\ \rho v^2 + p \\ \rho v \left(e + \dfrac{p}{\rho} \right) \\ \rho Y_1 v \\ \vdots \\ \rho Y_N v \\ \rho Y_\mathrm{s} v \\ \rho N_\mathrm{s} v \end{bmatrix}$$

and $\mathbf{F}_\mathrm{v}$ and $\mathbf{G}_\mathrm{v}$ are the viscous solution flux vectors,

$$\mathbf{F}_\mathrm{v} = \begin{bmatrix} 0 \\ \tau_{rr} \\ \tau_{zr} \\ -\mathrm{q}_r + u\tau_{rr} + v\tau_{rz} \\ \rho D_1 \frac{\partial Y_1}{\partial r} \\ \vdots \\ \rho D_N \frac{\partial Y_N}{\partial r} \\ \rho D_\mathrm{s} \frac{\partial Y_\mathrm{s}}{\partial r} \\ \rho D_\mathrm{s} \frac{\partial N_\mathrm{s}}{\partial r} \end{bmatrix} \quad \text{and} \quad \mathbf{G}_\mathrm{v} = \begin{bmatrix} 0 \\ \tau_{rz} \\ \tau_{zz} \\ -\mathrm{q}_z + u\tau_{rz} + v\tau_{zz} \\ \rho D_1 \frac{\partial Y_1}{\partial z} \\ \vdots \\ \rho D_N \frac{\partial Y_N}{\partial z} \\ \rho D_\mathrm{s} \frac{\partial Y_\mathrm{s}}{\partial z} \\ \rho D_\mathrm{s} \frac{\partial N_\mathrm{s}}{\partial z} \end{bmatrix}$$

Here, u and v are the radial and axial components of velocity, g_z is the component of gravity in the axial direction, q_r and q_z are the radial and axial components of the energy flux, and τ_{rr}, τ_{rz}, τ_{zr}, τ_{zz} and $\tau_{\theta\theta}$ are the elements of the fluid stress tensor.

The viscous stress tensor, $\vec{\boldsymbol{\tau}}$, of a Newtonian fluid is expressed in terms of the viscosity and strain rates. For an axisymmetric coordinate system, the individual components of $\vec{\boldsymbol{\tau}}$ are

$$\tau_{rr} = 2\mu \left[\frac{\partial u}{\partial r} - \frac{1}{3} \left(\frac{\partial u}{\partial r} + \frac{\partial v}{\partial z} + \frac{u}{r} \right) \right] \tag{A.2a}$$

$$\tau_{rz} = \tau_{zr} = \mu \left(\frac{\partial u}{\partial r} + \frac{\partial v}{\partial z} \right) \tag{A.2b}$$

$$\tau_{zz} = 2\mu \left[\frac{\partial v}{\partial z} - \frac{1}{3} \left(\frac{\partial u}{\partial r} + \frac{\partial v}{\partial z} + \frac{u}{r} \right) \right] \tag{A.2c}$$

$$\tau_{\theta\theta} = 2\mu \left[\frac{u}{r} - \frac{1}{3} \left(\frac{\partial u}{\partial r} + \frac{\partial v}{\partial z} + \frac{u}{r} \right) \right] \tag{A.2d}$$

Appendix B

THE OPTICALLY-THIN APPROXIMATION FOR RADIATION HEAT TRANSFER

As the media becomes optically-thin, $\kappa_\nu / L \ll 1$ where L is some length scale, the intensity leaving the surfaces travels through the domain without any attenuation. Every point within the medium has the same incident radiation and attenuation rate, so the intensity field is known and $\nabla \cdot \vec{q}_{\text{rad}}$ can be directly evaluated without solving the RTE. Integrating the spectral heat flux, Eq. (4.7), over the entire wavelength spectrum gives

$$\nabla \cdot \vec{q}_{\text{rad}} = \nabla \cdot \int_0^\infty \vec{q}_\nu \, \mathrm{d}\nu = \int_0^\infty \kappa_\nu \left(4\pi I_{\text{b}\nu} - G_\nu\right) \, \mathrm{d}\nu \tag{B.1}$$

The total incident intensity at a point inside the domain is equal to the unattenuated intensity emitted from the surrounding domain boundaries. Thus, Eq. (B.1) can be written as

$$\nabla \cdot \vec{q}_{\text{rad}} = 4\pi \int_0^\infty \kappa_\nu \left(I_{\text{b}\nu} - I_{\text{b}\nu,\infty}\right) \, \mathrm{d}\nu \tag{B.2}$$

where $I_{\text{b}\nu,\infty}$ is the spectral blackbody intensity evaluated at the domain boundary. For a gray media with $\kappa = \kappa_\nu =$ constant, Eq. (B.2) becomes

$$\nabla \cdot \vec{q}_{\text{rad}} = 4\sigma\kappa \left(T^4 - T_\infty^4\right) \tag{B.3}$$

where $\sigma = 5.67 \times 10^{-8} \, \text{W m}^{-2} \, \text{K}^{-4}$ is the Stefan-Boltzmann constant, T is the gas temperature, and T_∞ is the temperature of the ambient surroundings.

It is convenient for non-gray media to rearrange Eq. (B.2) in terms of the medium blackbody intensity as follows:

$$\nabla \cdot \vec{q}_{\text{rad}} = 4\pi \left[\frac{\int_0^\infty \kappa_\nu I_{\text{b}\nu} \, \mathrm{d}\nu}{\int_0^\infty I_{\text{b}\nu} \, \mathrm{d}\nu} I_\text{b} - \frac{\int_0^\infty \kappa_\nu I_{\text{b}\nu,\infty} \, \mathrm{d}\nu}{\int_0^\infty I_{\text{b}\nu,\infty} \, \mathrm{d}\nu} I_\text{b}, \infty \right] \tag{B.4a}$$

$$= 4\pi \left(\kappa_\text{P} I_\text{b} - \kappa_\text{m} I_\text{b}, \infty\right) \tag{B.4b}$$

where κ_P is the Planck-mean and κ_m the modified-Planck-mean absorption coefficient. Equation (B.4) can be simplified since the surroundings of a laminar flame are cold in comparison to the hot combustion gases ($\kappa_P I_b \gg \kappa_m I_b, \infty$):

$$\nabla \cdot \vec{q}_{rad} \approx 4\pi\sigma\kappa_P \left(T^4 - T_\infty^4\right) \tag{B.5}$$

The Planck-mean absorption coefficient is defined as

$$\kappa_P \equiv \frac{\int_0^\infty I_{b\nu}\kappa_\nu \, d\nu}{\int_0^\infty I_{b\nu} \, d\nu} = \frac{\pi}{\sigma T^4} \int_0^\infty I_{b\nu}\kappa_\nu \, d\nu \tag{B.6}$$

Making the narrow band approximation (see Section 4.2.1), Eq. (B.6) is restated as [293]

$$\kappa_P = \sum_{j=1}^{N_b} \left(\frac{\pi I_{b\nu 0}}{\sigma T^4}\right)_j \int_{\Delta\nu_j} \left(\frac{S}{d}\right)_\nu d\nu \tag{B.7}$$

where $I_{b\nu 0}$ is the Planck function evaluated at the center of each band, S is the line strength and d is the average line spacing. The integral in Eq. (B.7) represents the intensity of the jth narrow band and can be related to the band averaged absorption coefficient as follows:

$$\int_{\Delta\nu} \left(\frac{s}{d}\right)_\nu d\nu = \overline{\kappa_{\Delta\nu}}\Delta\nu \quad \text{where} \quad \overline{\kappa_{\Delta\nu}} = \frac{1}{\Delta\nu} \int_{\nu-\Delta\nu/2}^{\nu+\Delta\nu/2} \kappa_{\nu'} \, d\nu' \tag{B.8}$$

Thus, Eq. (B.7) can be rewritten as

$$\kappa_P = \sum_{j=1}^{N_b} \left(\frac{\pi I_{b\nu 0}}{\sigma T^4} \overline{\kappa_{\Delta\nu_j}} \Delta\nu\right)_j \tag{B.9}$$

For a gas described by the Malkmus model, $\overline{\kappa_{\Delta\nu_j}} = S_j$, where S_j is the effective line strength for band j. Note that the S_j is one of the band model parameters mentioned in Section 4.2.1.

APPENDIX C

SOLUTION OF THE RTE USING A NEWTON-KRYLOV APPROACH

Detailed treatment of radiation heat transfer is essential to the development of mathematical models that accurately describe combusting flows. Unfortunately, as discussed in Chapter 4, modelling radiative heat transfer can be an arduous task requiring the solution of complex integro-differential equations with many degrees of freedom and widely varying properties. Since detailed combustion models must also incorporate complex chemistry, turbulence, and multi-species transport, the remaining computational resources available for radiation transport can be limited. As such, there is a need for scalable, efficient radiation solvers that can be easily integrated into today's CFD solution methods and take advantage of growing trends towards large-scale parallel computing. This appendix presents a new parallel-implicit framework for solving the RTE on adaptively-refined multi-block body-fitted mesh for the treatment of both emitting-absorbing and anisotropically scattering media on geometrically complex computational domains.

C.1 Introduction

Chapter 4 described the dependence of the spectral intensity on location in space, direction of photon and wavenumber. This large number of degrees of freedom coupled with the dependence of radiative properties on temperature, pressure and composition makes solving the RTE a formidable task. Additional difficulties for numerical solution techniques are created by the tight coupling that arises between intensities in each direction for scattering media.

Due to the linear upwind nature of the RTE, space-marching techniques are commonly applied to solve both the DOM [297] and FVM [298, 299] equations. For non-scattering media and constant coefficient spatial discretization schemes, a converged solution can be obtained in one full sweep of the domain as the intensity at the downstream boundaries is related directly to upstream quantities. However, constant coefficient schemes are either overly dissipative or unstable as only first-order upwind schemes guarantee positivity [410]. Liu et al. [410] and Jessee and Fiveland [411] have applied bounded high-resolution schemes developed for CFD to the DOM. Applied schemes include the SMART [412], MUSCL [363], CLAM [413] and minmod [359] which avoid spurious oscillations near discontinuities that would otherwise occur with

high-order spatial discretizations by limiting. Both investigators were able to achieve bounded solutions with a dramatic increase in accuracy at the expense of computational efficiency. Coelho [414] reformulated the SMART, MUSCL and CLAM schemes such that interpolation was performed in the ordinate directions. These skew high-order schemes yielded further improvements in accuracy yet required more iterations than their non-skew counterparts. It is obvious that there exists a need for improved solution techniques that readily handle the local non-linearities introduced by high-resolution schemes without significant increase in solution time.

Space-marching algorithms perform poorly when applied to scattering media with high optical thickness where strong coupling exists between the intensities in different directions. Such computations can require a large number of iterations to converge, are prone to unphysical oscillations, and can fail to converge. While standard techniques for solving linear equations may be used to cope with this coupling, large storage requirements can be prohibitive even for coarse angular and spatial discretizations. Mathur and Murthy [415] devised a point-implicit coupled solution procedure that accelerates convergence in optically-thick scattering media by updating the intensities in all directions for a particular cell simultaneously. The procedure was most effective for moderate to high optical thicknesses and relatively simple scattering phase functions. This coupled procedure does not address issues related to complex geometry and non-orthogonal meshes, which further complicate standard space-marching techniques.

Several researchers have applied time-evolution solution techniques to cope with arbitrary meshes and scattering media. Fiterman et al. [416] developed a finite-volume pseudo-time stepping solution procedure specifically for the DOM. They employed an explicit Euler temporal discretization with multigrid acceleration and an artificial viscosity-based spatial discretization. Selçuk and co-workers [417–419] have applied the method of lines (MOL) to solve the DOM equations in a variety of applications. A three-dimensional DOM solver based on the MOL was presented by Selçuk and Kirbaş [417] and applied to a rectangular enclosure with black walls, a gray absorbing-emitting medium, and steep temperature gradients. Spatial gradients were evaluated using linear upwind and biased-upwind finite-differences and the equations were relaxed to a steady-state using both the LSODE [420] and RKF45 [421] ODE solvers. Ayranci and Selçuk [418] later compared these differencing procedures with more advanced second-order upwind total-variation-diminishing (TVD) schemes using the Van Leer and Superbee limiter functions on uniform grids. Third- and fifth-order biased WENO [422] and MPWENO [423] finite-difference schemes were also assessed by the authors. They found that the Van Leer limiter provided the best results based on accuracy and efficiency when coupled with the RKF45 solver. High-order schemes were found to have stability problems and require extremely small time-step sizes for stable integration.

Others have looked at the use of implicit time-marching methods in conjunction with high-resolution discretizations since these methods offer improved stability and convergence characteristics. Balsara [424] solved the DOM for emitting-absorbing and scattering media using a multidimensional fluctuation-splitting scheme [425, 426]. In Balsara's work, the discretized equations were relaxed to a steady-state with full-approximation storage (FAS) multigrid [427] and a restarted Newton-Krylov method [372] as a nonlinear smoother. While good convergence properties were observed in both optically thick and thin media, the per-

formance and memory requirements compared to standard space-marching techniques were not discussed. The large amount of memory required for the implicit smoother on each multigrid level would probably prohibit the application of this approach to large-scale CFD problems. Another implicit approach is that of Chai [428] who solved the transient FVM equations for radiative transfer with scattering media in irregular geometries. This approach made use of a tri-diagonal matrix solver and the CLAM scheme. Neither of the two implicit approaches discussed here is directly compatible with standard parallel solution techniques.

Aside from the challenges associated with the treatment of complex geometries and scattering media, parallel implementations of conventional space-marching techniques are also problematic due to their inherently serial nature. This serial nature makes space-marching techniques unattractive for large-scale parallel CFD solution algorithms. Gonçalves and Coelho [386, 429] have studied parallel space-marching implementations of the DOM and FVM using both angular and spatial decomposition strategies. The authors found that while angular decomposition strategies yielded high efficiencies and speedups, their scalability is limited by the size of the angular discretization which is typically much coarser than the spatial discretization. Additionally, these methods require excessive communication when evaluating integrals over the solid angle and do not integrate with commonly used parallel CFD solution techniques based on domain decomposition. Gonçalves and Coelho's work also showed that domain decomposition strategies applied to standard space-marching solvers yield only modest parallel efficiencies despite their attempt to devise an optimized sweeping procedure. Liu et al. [430] developed a spatial-domain-based parallel algorithm for the FVM, solving the equations semi-implicitly with a conjugate gradients method and Dupont-Kendall-Rachford incomplete factorization. Modest performance was achieved on up to 18 processors. An AMR algorithm with a similar parallel sweeping strategy as the one proposed by Gonçalves and Coelho [386, 429] was developed by Howell [387]. Krishnamoorthy et al. [431] applied several iterative matrix solvers to a spatially decomposed DOM but sequentially solved the intensity for each direction. Using both block and point Jacobi preconditioners, the parallel performance deteriorated when more than 8 processors were employed. Yıldız and Bedir [432] applied a pipeline parallelization strategy to improve processor utilization over standard parallel sweeping algorithms. Parallel efficiencies of 70% were observed with 20 processors.

Of particular importance to this work is the parallel framework for solving transient reacting laminar diffusion flames proposed by Bilge et al. [419]. Their framework uses domain decomposition combined with the same MOL scheme for the DOM developed by Selçuk and co-workers that was previously mentioned. The work clearly illustrates the applicability of spatial decomposition and time-marching methods to the parallel solution of the RTE.

C.2 Numerical Method

Both of the DOM and FVM produce a set of PDEs with only spatial and temporal gradients. These PDEs are linear hyperbolic and thus many of the techniques developed for solving the Euler equations of compressible gas dynamics can be applied. Since the two techniques differ only slightly from each other, a general formulation applicable for both is derived.

Applying the DOM to the RTE yields

$$\frac{1}{c}\frac{\partial I_m}{\partial t} + \hat{s}_m \cdot \nabla I_m = \kappa I_b - (\kappa + \sigma_s)\, I_m + \frac{\sigma_s}{4\pi}\sum_{n=1}^{M} w_n I_n \Phi(\hat{s}_n, \hat{s}_m) \tag{C.1}$$

where the subscript m denotes the discrete ordinate direction, M is the total number of ordinate directions, I_m is the intensity in the mth direction, and $\hat{s}_m$ and w_m are the ordinate direction vector and associated quadrature weight. The FVM equations are obtained by discretizing the solid angle into M control-angle elements and integrating the RTE over each element to give

$$\frac{1}{c}\frac{\partial I_m}{\partial t} + \vec{s}_m \cdot \nabla I_m = \kappa I_b - (\kappa + \sigma_s) I_m + \frac{\sigma_s}{4\pi}\sum_{n=1}^{M} I_n \Phi_{mn} \Delta\Omega_n \tag{C.2}$$

where the control-angle-averaged direction cosine vector, $\vec{s}_m$, and phase function, Φ_{mn}, are defined as

$$\Phi_{mn} = \frac{1}{\Delta\Omega_m \Delta\Omega_n}\int_{\Delta\Omega_m}\int_{\Delta\Omega_n} \Phi(\hat{s}', \hat{s})\, \mathrm{d}\Omega'\, \mathrm{d}\Omega \tag{C.3}$$

$$\vec{s}_m = \frac{1}{\Delta\Omega_m}\int_{\Delta\Omega_m} \hat{s}\, \mathrm{d}\Omega \tag{C.4}$$

Equation (C.2) was derived assuming piecewise-constant intensity over each control angle and therefore I_m represents the average intensity in mth control angle. This first-order approximation limits the overall order of the solution regardless of spatial (or temporal for transient analyses) discretization practices. This accuracy limitation will be addressed further in the following sections.

Let us now consider a two-dimensional Cartesian coordinate system. The proposed algorithm extends readily to three-dimensions but such extensions are not the focus here. Both Eqs. (C.1) and (C.2) can be reformulated into a weak-conservation form since $\hat{s}_m$ and $\vec{s}_m$ are independent of spatial location. The resulting equation is given by

$$\frac{\partial I_m}{\partial t} + \frac{\partial}{\partial x}(c\mu_m I_m) + \frac{\partial}{\partial y}(c\eta_m I_m) = S_m \tag{C.5}$$

where the source term S_m is defined as the right-hand side (RHS) of either Eq. (C.1) or (C.2) for the DOM or FVM, respectively, multiplied by the speed of light. The directional coefficients μ_m and η_m are either the direction cosines defined by the numerical quadrature scheme or the x and y components of $\vec{s}_m$. Equation (C.5) can be re-expressed in vector form as

$$\frac{\partial \mathbf{U}}{\partial t} + \frac{\partial \mathbf{F}}{\partial x} + \frac{\partial \mathbf{G}}{\partial y} = \mathbf{S} \tag{C.6}$$

where the solution vector, $\mathbf{U}$, x-direction flux, $\mathbf{F}$, y-direction flux, $\mathbf{G}$, and source vector, $\mathbf{S}$, are defined by

$$\left.\begin{aligned} \mathbf{U} &= I_m \\ \mathbf{F} &= c\mu_m I_m \\ \mathbf{G} &= c\eta_m I_m \\ \mathbf{S} &= S_m \end{aligned}\right\} \quad \text{for } m = 1, \ldots, M \tag{C.7}$$

C.2.1 Solution Procedure

The proposed scheme for the RTE uses the same upwind finite-volume spatial discretization procedure described in Section 5.1 to solve Eq. (C.6). It is applied on a multi-bock mesh composed of arbitrary quadrilateral cells, which is illustrated in Fig. 5.1. Integrating Eq. (C.6) over a control volume and applying to cell (i, j) yields a system of coupled semi-discrete ODEs given by

$$\frac{\mathrm{d}\mathbf{U}_{ij}}{\mathrm{d}t} = -\frac{1}{A_{ij}} \sum_{k} \left(\vec{\mathbf{F}}_k \cdot \hat{n}_k \Delta l_k \right)_{ij} + \mathbf{S}(\mathbf{U}_{ij}) = \mathbf{R}_{ij}(\mathbf{U}) \tag{C.8}$$

In two-dimensions, the numerical flux at the cell interface is

$$\vec{\mathbf{F}} \cdot \hat{n} = \mathcal{F} \left(\mathbf{U}_{\mathbf{L}}, \mathbf{U}_{\mathbf{R}}, \hat{n} \right) \tag{C.9}$$

where $\mathcal{F}$ is the upwind solution flux in a direction aligned along the face normal $\hat{n}$. The linear least-squares reconstruction error minimization technique of Barth and Fredrickson [433] is used to evaluate the cell solution gradients and interpolate the solution at the cell faces. Slope limiting is performed with a slope limiter specifically designed for use in multiple dimensions [364].

For cases involving scattering, the equations for radiative transport in each direction become coupled through the source terms and this coupling increases with optical thickness. This angular coupling combined with the non-linearities introduced by the TVD spatial discretization scheme can be problematic for space-marching techniques. In many cases, these solution techniques may require excessive iterations or even fail to converge. The Newton algorithm developed by Groth and Northrup [369] (described in Section 5.1.6) was applied in this work to overcome these difficulties and relax the semi-discrete form of the governing equations to steady-state.

C.3 Numerical Results

A variety of test cases were examined as part of this study to analyze the performance of the algorithm in terms of discontinuity-capturing ability, spatial and angular accuracy, adaptive mesh refinement, parallel efficiency, and serial performance compared to other standard solution algorithms. All computations were performed on a high performance parallel cluster consisting of 104 IBM P6-575 nodes with 128 GB RAM per node and a high-speed interconnect. The nodes each have 32 IBM POWER6 cores (4.7GHz) and are connected to a non-blocking switch with four 4x-DDR InfiniBand links.

C.3.1 Transparent Medium

The first test problem considered was a two-dimensional unit square enclosure defined on $-0.5 \leq x \leq 0.5$ and $-0.5 \leq y \leq 0.5$ with a transparent medium. For this case, all walls are black and cold ($I_{\mathrm{b_w}} = 0$) except the bottom wall where $I_{\mathrm{b_w}} = 1$. This case is similar to the one previously studied by Coelho [414, 434] who employed a variety of high-resolution schemes and compared the resulting solution errors. The problem is re-considered here only to verify that the current implementation properly captures solution discontinuities. In this test case, radiation propagating along a single direction with direction cosines corresponding

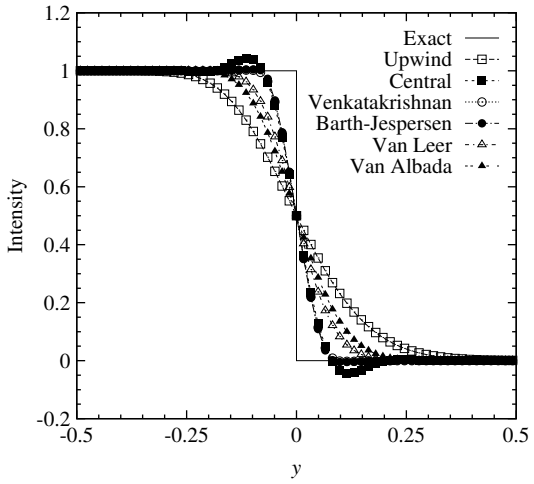

Figure C.1: Radiation intensity profiles along the vertical symmetry plane of a two-dimensional square enclosure with transparent medium.

to $\mu = \eta = \sqrt{2}/2$ is computed. Numerical diffusion is expected to be large in this direction since the propagating ray makes a 45 degree angle with both the vertical and horizontal cell boundaries. The domain is discretized into 61 by 61 uniform cells and the solution computed using various schemes. The discretization schemes tested include the first-order upwind and second-order unlimited approximations, and the TVD schemes of Venkatakrishnan [435], Barth and Jespersen [365], Van Albada et al. [436], and Van Leer [413]. The computed intensity along the y-direction at $x = 0$ is compared with the exact solution in Fig. C.1. As expected, the upwind scheme is overly dissipative while unphysical oscillations are obtained using the second-order unlimited scheme. Limiting the second-order solution offers considerable improvement, with the Venkatakrishnan and Barth-Jespersen limiters outperforming the Van Albada and Van Leer limiters. The latter two limiters yield much smoother solutions which can be expected since they were primarily designed for one-dimension. The limiter of Venkatakrishnan was selected for all remaining test cases for its superior performance characteristics.

C.3.2 Discretization Accuracy

The proposed scheme was analyzed in terms of spatial and angular accuracy through comparison with exact solutions for the RTE in rectangular enclosures. Similar to the previous test case, the enclosure for this study was taken to consist of a unit square except with all walls cold and black and containing a hot, absorbing-emitting medium with $\kappa = 10\ \mathrm{m}^{-1}$. Exact solutions were previously derived by Cheng [437] for this particular problem. The overall error between numerical and exact solutions was defined by the change in the two-norm of the error in direction-integrated radiative intensity. It is defined as

$$\|\mathrm{Error}\|_2 = \left\{ \frac{\sum_{i=1}^{N_c} \left[G_{\mathrm{exact}}(x_i, y_i) - G_i \right]^2 A_i}{\sum_{i=1}^{N_c} A_i} \right\}^{1/2} \tag{C.10}$$

where N_c is the total number of cells, A_i is the cell area, $G_{\mathrm{exact}}(x_i, y_i)$ and G_i are the exact and numerical solution for the direction-integrated intensity evaluated at the center of the ith cell. The direction-integrated

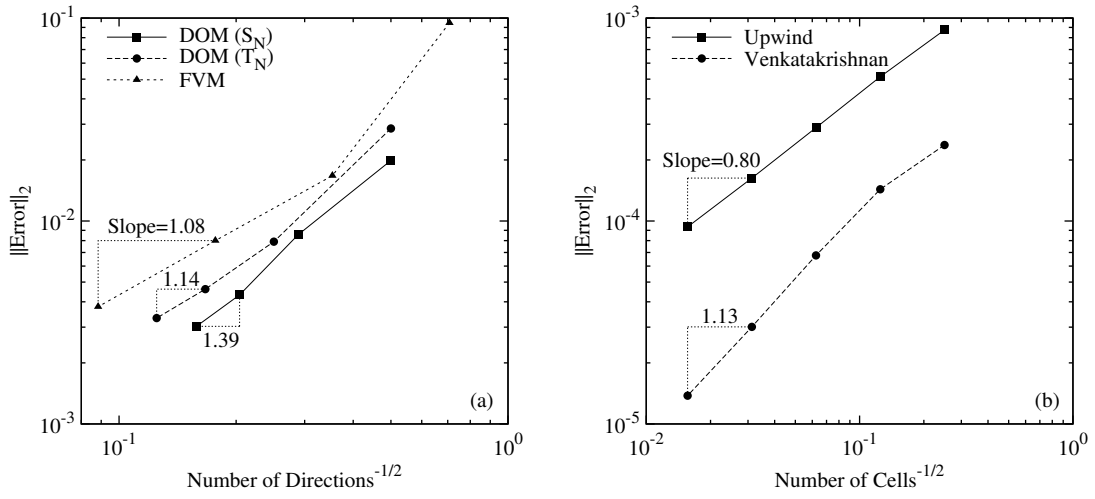

Figure C.2: Change in numerical error with (a) angular and (b) spatial discretization for the square enclosure.

intensity is given by

$$G = \int_{4\pi} I(\hat{s})\,\mathrm{d}\Omega \approx \sum_{m=1}^{M} \delta\Omega_m I_m \tag{C.11}$$

where $\delta\Omega_m = w_m$ for the DOM and $\delta\Omega_m = \Delta\Omega_m$ for the FVM, respectively.

The change in error between numerical and exact solutions of the RTE with increasing number of directions of propagation is illustrated in Fig. C.2(a). Here, solutions were obtained on a fixed spatial grid of 64 by 64 uniform cells with either the DOM or FVM and varying levels of angular resolution. Quadrature rules used for the DOM include the S_2, S_4, S_6, and S_8 schemes of Lathrop and Carlson [331] as well as the T_1, T_2, T_3, and T_4 schemes of Thurgood et al. [332]. For the FVM, uniform angular meshes were employed over the hemisphere ($0 \le \theta \le \pi/2, 0 \le \psi \le 2\pi$) with 1×2, 2×4, 4×8, and 8×16 control angles in the polar and azimuthal directions, respectively. The figure confirms that reductions in error are achieved by increasing the angular resolution and that both DOM quadrature rules provide larger rates of decrease with number of directions than the FVM. The estimated slopes in regimes for asymptotic convergence are 1.39, 1.14, and 1.08 for the DOM with S_N, DOM with T_N, and FVM, respectively. It is interesting to note that the S_N scheme performs slightly better than the T_N scheme with consistently lower errors for the same number of propagation directions.

The accuracy of the spatial discretization was also assessed using a procedure similar to the one used for the angular discretization analysis. However, numerical solutions were compared to exact solutions for the DOM equations themselves instead of exact solutions of the RTE. These are spatially exact solutions to the angular approximation introduced by the DOM and therefore errors in the numerical solution are attributed to the spatial discretization only. Exact solutions for the DOM in rectangular enclosures were previously presented by Jessee et al. [438]. A unit square enclosure with cold and black walls that contains a hot, absorbing-emitting medium with $\kappa = 0.01$ m^{-1} was modelled. Results for the effect of grid resolution on the error defined by Eq. (C.10) are presented in Fig. C.2(b) for both the upwind and TVD spatial discretizations of the S_6 DOM equations. The figure indicates that only first order-accuracy is achieved for both schemes as

Table C.1: AMR statistics for square enclosure test case.

	Uniform Refinement		Refinement Based on ∇G			Refinement Based on Max $\lvert\nabla I_m\rvert$		
Level	Cells	$\lVert\text{Error}\rVert_2$	Blocks	Cells	$\lVert\text{Error}\rVert_2$	Blocks	Cells	$\lVert\text{Error}\rVert_2$
0	16	2.4×10^{-4}	16	256	6.8×10^{-5}	16	256	6.8×10^{-5}
1	64	1.4×10^{-4}	52	832	4.4×10^{-5}	52	832	4.4×10^{-5}
2	256	6.8×10^{-5}	136	2 176	4.0×10^{-5}	64	1 024	3.0×10^{-5}
3	1 024	3.0×10^{-5}	268	4 288	2.1×10^{-5}	148	2 368	2.5×10^{-5}
4	4 096	1.4×10^{-5}	556	8 896	1.9×10^{-5}	256	4 096	1.4×10^{-5}
5			1444	23 104	1.4×10^{-5}	520	8 320	1.1×10^{-5}
6						1024	16 384	6.5×10^{-6}

the slopes in the asymptotic regime are 0.80 and 1.13 for the upwind and TVD schemes, respectively. This first-order convergence observed by the TVD scheme is attributed to the large discontinuities that exist in the intensity of rays originating from the corners in all directions. Despite this lack of improvement in the order of accuracy over the upwind scheme as the mesh is refined, the TVD scheme still provides a far more accurate solution with fewer grid points. The absolute error obtained using the TVD scheme is nearly one order of magnitude lower than the first-order scheme.

C.3.3 Adaptive Mesh Refinement

C.3.3.1 Square Enclosure

The previous case for assessing the spatial discretization scheme was solved once again using the proposed AMR algorithm. The initial mesh consisted of 16 by 16 cells uniformly-spaced and divided into four equally-sized blocks. Using the DOM and the S_6 quadrature scheme, solutions were obtained on subsequently refined meshes using various refinement criteria. Both the gradient of the direction-integrated intensity and the maximum gradient of the individual directional intensities were employed as a measure of the local truncation error. The two refinement criteria are defined by

$$\epsilon_1 \propto \nabla G \tag{C.12}$$

$$\epsilon_2 \propto \max\left(|\nabla I_1|, |\nabla I_2|, \ldots, |\nabla I_M|\right) \tag{C.13}$$

where M is the total number of directions. Based on either of these criteria, the mesh is refined and blocks are added wherever the measures ϵ_1 or ϵ_2 are large.

The mesh statistics and resulting errors obtained using uniform refinement and AMR are tabulated in Table C.1 and the effect of mesh resolution on grid convergence is plotted in Fig. C.3(a). The convergence characteristics obtained using the maximum ∇I_m criterion (ϵ_2) are almost identical to those obtained using uniform refinement. This is due to large discontinuities in the individual intensities that occur in all directions. The maximum gradient criterion flags all blocks for refinement and the resulting mesh is almost uniform. A slight degradation in convergence performance is observed when using the gradient of

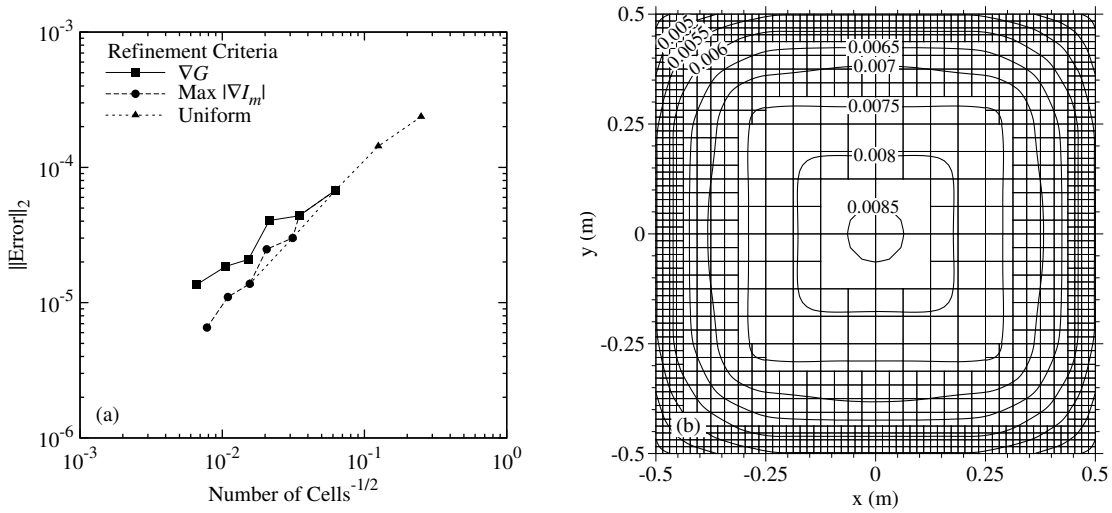

Figure C.3: Numerical solution for the square enclosure with cold and black walls containing a hot, absorbing-emitting medium with $\kappa = 0.01$ m^{-1}. (a) Change in numerical error with mesh refinement; (b) computational mesh block boundaries and contours of normalized direction-integrated radiative intensity, $G/(4\pi I_b)$, after 5 levels of refinement using ∇G refinement criterion (1 444 blocks and 23 104 cells).

the direction-integrated intensity criterion (ϵ_1). This is explained by examining the solution contours for $G/4\pi I_b$, which are illustrated in Fig. C.3(b) along with the block boundaries for the refined computational grid. These contours were obtained using the ϵ_1 criterion on the finest mesh. The direction-integrated intensity appears smooth when in fact large discontinuities in I_m are present. This results in only blocks near the wall being refined which do not help reduce the error along rays originating from the corners. Since the mesh is refined in incorrect locations when using the ϵ_1 criterion, the two-norm of the solution error decreases with decreasing average mesh spacing at a slower rate compared to using uniform refinement.

Due to the lack of disparate length scales in this particular test problem, AMR does not offer any significant improvements in terms of numerical efficiency over uniform refinement. Jessee et al. [438] obtained similar results for this test case when using a different AMR algorithm with similar physics-based refinement criterion. This emphasizes the need for refinement techniques that rely on improved estimates of the local error instead of physics-based criteria. More favourable results are expected for realistic test cases that do indeed contain a wider range of length scales.

C.3.3.2 Circular Enclosure

To demonstrate the advantages of mesh refinement and the ability of the proposed method to deal with more complex geometry, the AMR scheme was applied to an additional, more realistic test case which possessed both steep gradients and curved boundaries. The test case consisted of a discontinuous absorbing-emitting medium confined between two concentric circular enclosures, shown schematically in Fig. C.4(a). Both walls are black with an emissivity of $\epsilon_{w1} = \epsilon_{w2} = 1$, inner wall temperature of $T_{w1} = 100$ K, and outer wall temperature of $T_{w2} = 0$ K. The walls are located at $r_{w1} = 0.1$ m and $r_{w2} = 2.0$ m while the medium inside the enclosure is discontinuous at $r_3 = 0.59$ m. The temperature and absorption coefficient for the inner gas are $T_{g1} = 100$ K and $\kappa_{g1} = 10$ m^{-1} while they are $T_{g2} = 0$ K and $\kappa_{g2} = 100$ m^{-1} for the outer surrounding

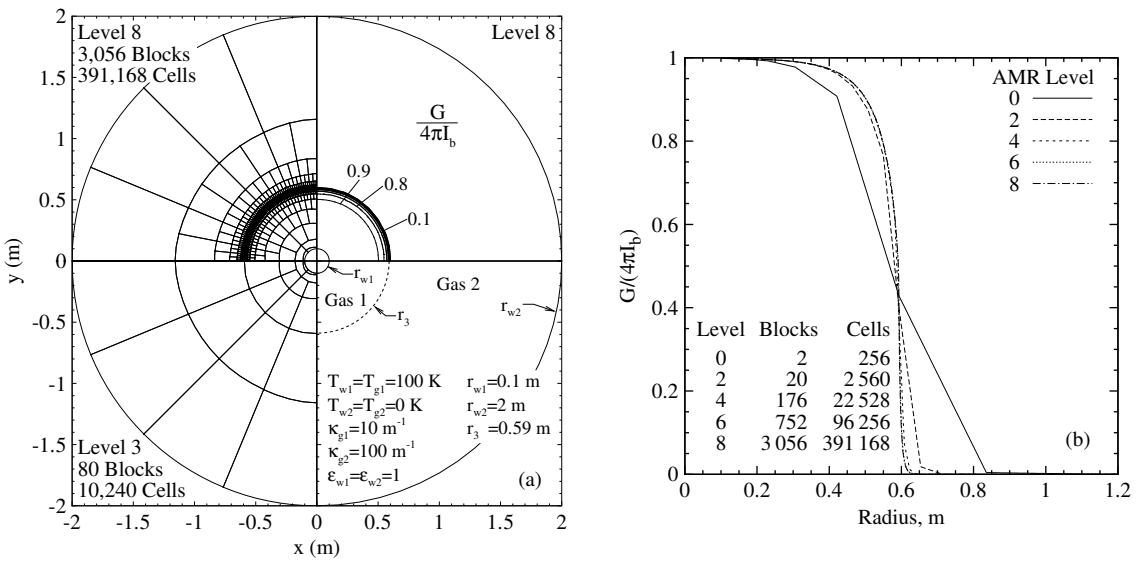

Figure C.4: Numerical solution for the circular enclosure with a discontinuous absorbing-emitting medium. (a) Problem description, computational mesh block boundaries, and contours of normalized direction-integrated radiative intensity after 8 levels of refinement; (b) direction-integrated intensity as a function of radius and AMR level.

gas, respectively.

Radiative heat transfer between the two concentric cylinders was studied numerically by solving the RTE using the proposed Newton-Krylov-Schwarz (NKS) algorithm and the Venkatakrishnan TVD spatial discretization scheme. The FVM was used to discretize the angular coordinate and divide the hemisphere into 4 control angles in the polar- and 24 in the azimuthal-direction. The circular computational domain was sub-divided into an initial non-uniform, body-fitted mesh with two equally-sized blocks and 256 total cells. The maximum ∇I_m AMR criterion (ϵ_2) was employed here as it provided the most favourable results in Section C.3.3.1.

Computed contours for G along with the mesh block boundaries after 8 levels of refinement are provided in Fig. C.4(a). Block boundaries for an intermediate mesh refinement level, level 3, are also provided in the figure to illustrate the AMR process. The AMR algorithm correctly identified the large gradient in G at $r = 0.59$ m produced by the discontinuity and refined the mesh in the corresponding location. A large improvement in the solution accuracy as the mesh is initially refined is observed in Fig. C.4(b), which depicts the effect of mesh resolution on the radial profile for G. The figure also provides mesh statistics for each level including number of blocks and computational cells. Refining the mesh beyond six levels yielded little change in the solution. At the finest level, level 8, the mesh consists of 3056 blocks and 391 168 cells which corresponds to a refinement efficiency of 97.7% or an equivalent uniform mesh with 16 777 216 total cells.

C.3.4 Parallel Performance

The parallel performance of the algorithm applied to the square enclosure case was assessed by examining both the strong and weak scaling properties. These two properties are a measure of the ability to demonstrate a proportionate increase in parallel speedup with more processors. For the strong scaling test, the problem

size is held fixed while the number of processors used to perform the computation is varied. Weak scaling is measured by holding the work load per processor fixed and varying the problem size with the number of processors. These two scaling properties are measured by the parallel speedup S_p and efficiency η_p which are defined as

$$S_p = \frac{t_1}{t_p} \tag{C.14}$$

$$\eta_p = \frac{S_p}{p} \tag{C.15}$$

where t_1 and t_p are the total wall times required to solve the problem with 1 and p processors, respectively.

C.3.4.1 Strong Scaling

Strong scaling was measured by dividing a uniform mesh of 512 by 512 cells amongst a number of equally sized blocks and solving the problem in parallel. The test was first carried out using two different meshes divided into a fixed number of blocks with either 32 by 32 or 64 by 64 cells. This allowed the work load per processor to be varied by changing the number of blocks assigned to each processor without affecting the partitioning of the mesh. As a result, only the effect of inter-processor communication on efficiency is observed since the number of residual evaluations to achieve converged solutions does not change. Each solution was said to have converged when the two-norm of the residual was reduced by 10 orders of magnitude from the original. Spatial discretization was performed using the Venkatakrishnan TVD scheme, angular discretization was performed with the S_6 quadrature scheme, and ILU(0) was used as the block preconditioner. GMRES was restarted every 20 inner iterations and terminated after 80 iterations or when the residual for the linear problem was reduced by one order of magnitude. The resulting relationship between parallel speedup, efficiency, and number of processors is shown in Fig. C.5(a) for the two meshes with different fixed block sizes. Excellent parallel performance is achieved with an efficiency greater than 85% on 256 processors. A slight deviation from ideal speedup begins to occur as the number of processors is increased beyond 16 which is magnified as more processors are used. This degradation in parallel performance is attributed to the increase in the communication-to-work ratio for each processor as they are assigned less work and the amount of communication for each block remains the same. The observed effect of block size is minimal as almost no change in performance is observed when the block size is reduced by a factor of two from 64 by 64 cells to 32 by 32.

The strong scaling test was performed a third time with the same uniform mesh of 512 by 512 cells as the one used previously except the mesh partitioning was varied such that only one block was assigned to each processor. As a result, the mesh was divided into smaller blocks as more processors were used. This test not only measures the scalability of the particular implementation as the previous test did, but also the scalability of the overall algorithm. It includes the negative effect of partitioning on convergence which results from global Schwarz preconditioning in addition to the effect of communication. The results from this test are illustrated in Fig. C.5(a) along with those obtained using the fixed block sizes. The results indicate similar performance to the fixed block size cases with a slight improvement observed when using

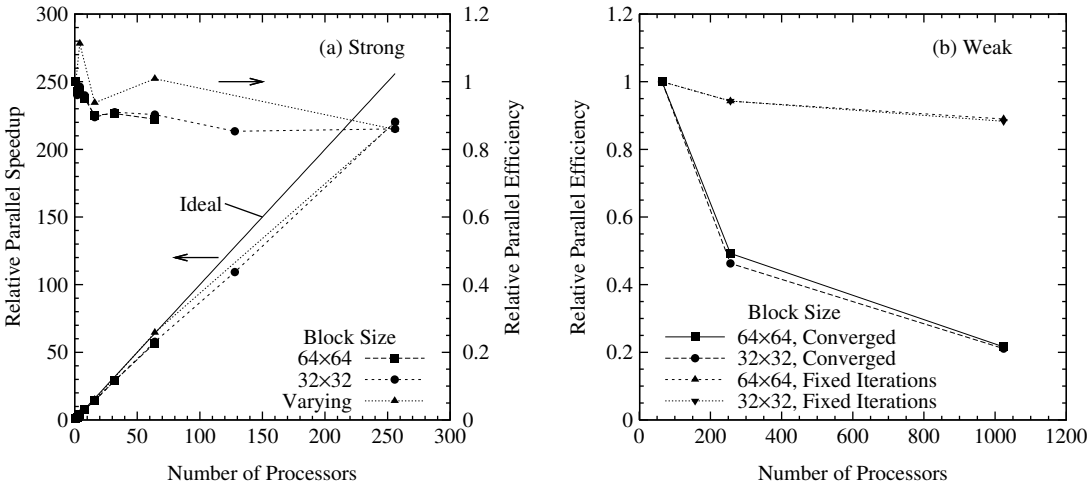

Figure C.5: Algorithm (a) strong and (b) weak scaling parallel performance.

fewer than 256 processors. This is due to the fact that the largest possible block sizes are used in the third case and the effect of the global preconditioner is minimized.

The effect of block size on the convergence characteristics of the Newton solver was assessed in more detail by plotting the convergence history against equivalent residual evaluations for the third strong scaling test, Fig. C.6(a). The performance of the Newton method degrades as the block size is reduced and the total number of blocks increases. This is due to the reduced effectiveness of additive Schwarz preconditioning with increased partitioning. As a result, a slight increase in equivalent residual evaluations is observed every time the total number of blocks is increased. An unexpected decrease in the required number of residual evaluations is observed when the problem is solved using four processors (blocks) as compared to using no partitioning at all. A super-linear speedup is also observed in Fig. C.5(a) between one and four processors. This super-linear speedup occurs as a result of the increasing accumulated cache size as processors are added on the IBM POWER6 platform.

C.3.4.2 Weak Scaling

Weak scaling performance of the proposed RTE solution algorithm is observed in Fig. C.5(b) for two different block sizes of 32 by 32 and 64 by 64 cells. It was obtained by assigning each processor a single block and either iterating for a fixed number of Newton steps or until the solutions were fully converged. Solutions were deemed fully converged when the residual was reduced by ten orders of magnitude. Excellent performance for the fixed iteration case is observed up to 1024 processors (blocks) with a parallel efficiency greater than 90% relative to 64 processors. This indicates that the parallel implementation effectively minimizes the necessary inter-processor communication. However, efficiencies of only 50% and 20% were achieved on 256 and 1024 processors, respectively, when the solutions were fully converged. This drastic loss of performance is largely attributed to the effect of mesh partitioning and size on convergence history, which is illustrated in Fig. C.6(b) for a block size of 64 by 64 cells. The number of residual evaluations increases drastically as the problem is discretized using a larger mesh with more blocks. For example, a

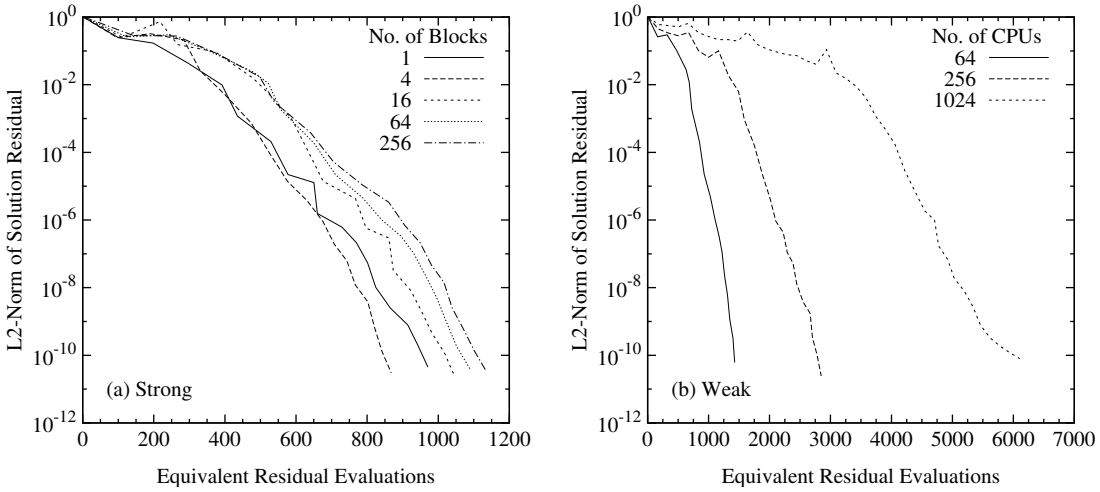

Figure C.6: Convergence histories for (a) strong scaling test using a varying block size and (b) weak scaling test with a fixed block size of 64 by 64 cells.

factor of 16 increase in mesh size resulted in a four-fold increase in the number of residual evaluations to obtain a converged solution. This occurred since more GMRES iterations were required to solve the linear system (Eq. (5.20)) at each Newton iteration as the condition number of the Jacobian matrix, $\mathbf{J}$, increased significantly with problem size. This degradation of the GMRES performance is the main cause of the poor weak scaling obtained for the fully converged computations. It was less severe in the strong scaling test (Section C.3.4.1) since the problem size remained fixed and was generally smaller than for the larger weak scaling cases. Only the partitioning was altered for the strong scaling test. Despite these weak scaling results, a substantial benefit is achieved through parallel solution of the radiation transport problem.

C.3.5 Serial Performance

A final test was carried out to compare the serial performance of the proposed solver with other standard space-marching solution techniques discussed in this work. Two unit square enclosures were studied. The first enclosure was the same one studied in Section C.3.2 containing a purely absorbing medium while the second enclosure contained a purely scattering medium. For the second enclosure, all walls are cold ($T = 0$ K) and black except the bottom wall which is hot and black. The emissivity of all walls was set to one. The medium is also cold but scatters photons according to the high back-scattering B2 phase function described by Kim and Lee [439]. The effect of optical thickness, spatial discretization, and mesh resolution on overall performance for each solver is discussed for both test cases.

All of the solution methods considered in the serial performance assessment made use of the S_6 DOM quadrature and solutions were obtained for three single-block mesh sizes: 32 by 32, 64 by 64, and 128 by 128 uniformly spaced cells. The proposed NKS scheme with a GMRES tolerance of 0.1 was used in combination with the upwind and Venkatakrishnan TVD discretizations. In addition to this, the standard space-marching solution technique outlined by Carlson and Lathrop [297] was employed with a variety of finite-volume schemes. Solutions were obtained using the space-marching technique with the upwind, central, CLAM, and the genuinely multidimensional (GM) [424] schemes. The high-resolution CLAM and

Table C.2: CPU times (s) for square enclosure with absorbing-emitting medium.

	$\kappa = 0.01$ m^{-1}			$\kappa = 10.0$ m^{-1}		
Scheme	32×32	64×64	128×128	32×32	64×64	128×128
NKS (Upwind)	1.6	11.2	78.1	1.0	5.8	38.2
NKS (Limited)	1.9	12.8	90.7	2.5	8.4	52.1
Space-March (Upwind)	0.0	0.1	0.5	0.0	0.1	0.5
Space-March (Central)	0.0	0.1	0.5	0.0	0.1	0.5
Space-March (CLAM)	0.6	3.5	31.3	0.4	2.6	19.5
Space-March (GM)	0.3	1.7	14.5	0.3	1.5	11.4
FAS Multigrid (Upwind)	12.9	69.7	495.5	3.3	14.5	88.6
FAS Multigrid (Limited)	48.7	272.8	1612.2	25.4	58.3	313.5

Table C.3: CPU times (s) for square enclosure with scattering medium.

	$\sigma_s = 0.01$ m^{-1}			$\sigma_s = 10.0$ m^{-1}		
Scheme	32×32	64×64	128×128	32×32	64×64	128×128
NKS (Upwind)	2.6	17.4	105.4	2.1	12.0	82.6
NKS (Limited)	4.8	30.8	252.5	3.2	24.0	155.0
Space-March (Upwind)	0.0	0.3	1.2	1.8	8.5	40.0
Space-March (Central)	0.1	0.3	1.2	2.2	9.4	42.3
Space-March (CLAM)	0.7	6.0	52.5	6.6	47.2	439.2
Space-March (GM)	1.0	6.2	51.2	5.1	27.9	176.4
FAS Multigrid (Upwind)	14.7	79.0	516.5	19.8	71.7	334.8
FAS Multigrid (Limited)	55.8	301.1	1672.0	32.6	100.1	576.1

GM schemes were implemented using the deferred correction procedure of Khosla and Rubin [440]. An explicit time-marching algorithm was also tested in this study for comparison purposes despite the poor performance characteristics of these types of solvers. The explicit solver makes use of FAS multigrid with a regular V-cycle and the five-stage optimally smoothing relaxation scheme of Van Leer et al. [441]. The iterations with the multigrid and Newton-Krylov solvers were stopped when residuals were reduced by 10 orders of magnitude while the space-marching solver used a convergence criterion of

$$\max\left(|\Delta I_m|\right) < 10^{-5} \tag{C.16}$$

where $\max\left(|\Delta I_m|\right)$ is the maximum absolute change in spectral intensity between iterations. It should be noted that the tight convergence tolerances that are used for the time-stepping algorithms could not be met by the space-marching solver in most cases.

The resulting CPU times required to solve each case using the various methods are provided in Tables C.2 and C.3 for the purely absorbing and purely scattering media, respectively. For the absorbing case,

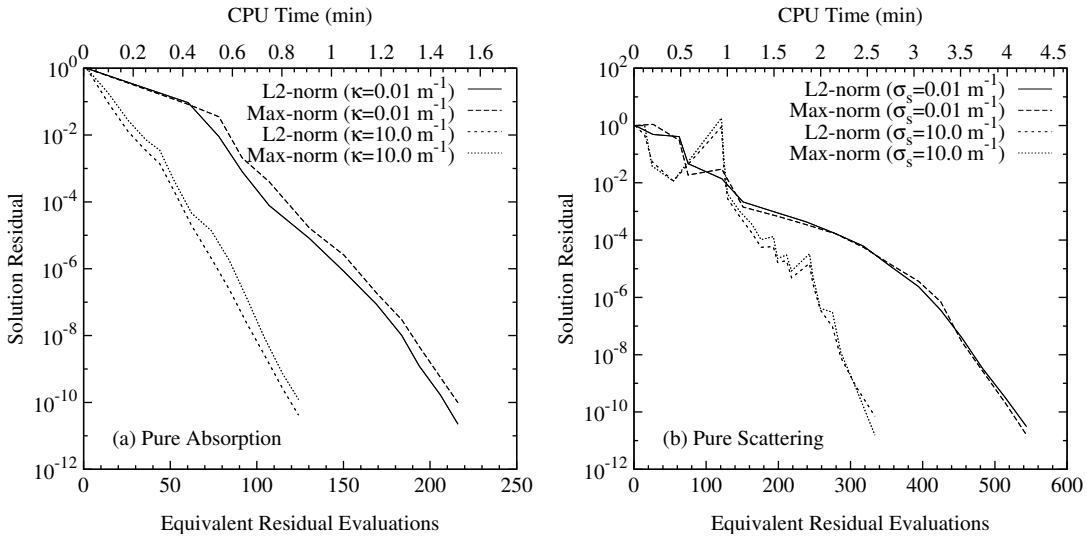

Figure C.7: Norms of solution residuals for square enclosure with (a) absorbing-emitting and (b) scattering media obtained using the proposed solution algorithm and the Venkatakrishnan TVD scheme on a mesh with 128 by 128 uniform cells.

the resulting upwind nature of the governing equations is easily handled by the space-marching technique. Both upwind and central schemes require only one iteration in each direction to reduce the residual below the specified convergence criterion. Despite the added iterations required by the space-marching solver when using either of the two high-resolution schemes, they still outperform the proposed solution algorithm. The combined NKS and TVD scheme is a factor of 3.2 and 4.7 times slower on average than the CLAM scheme for the optically thin ($\kappa = 0.01$ m^{-1}) and thick ($\kappa = 10$ m^{-1}) cases, respectively. The GM scheme performs slightly better than the CLAM scheme. Multigrid performs the poorest, requiring excessively long solution times. The solution time required for all schemes is observed to decrease with optical thickness. This is confirmed in Fig. C.7(a) which shows the convergence histories for the implicit TVD scheme obtained on the finest mesh. As shown in the figure, the optically thick case converges much more rapidly.

The Newton-Krylov algorithm compared more favourably to the space-marching method when scattering was introduced. Comparing the high-resolution schemes, the Newton algorithm is at least twice as fast as the CLAM scheme and 1.3 times faster on average than the GM scheme for the optically thick case ($\sigma_s = 10$ m^{-1}). However, similar results to those obtained for the purely absorbing case are observed near the optically thin limit ($\sigma_s = 0.01$ m^{-1}). It is interesting to note that the convergence characteristics of both time-marching solvers improve as the optical thickness is increased while they decrease for the space-marching solvers. This loss of performance for the space-marching solver is due to the high back-scattering nature of the medium, which requires additional passes to propagate scattered rays in all directions. As the optical thickness increases, the coupling between intensities strengthens and is easily taken into account by the proposed scheme. Convergence histories are provided in Fig. C.7(b) for the finest mesh. As for the purely absorbing case, convergence is much more rapid for large optical thickness ($\sigma_s = 10.0$ m^{-1}). For completeness, contours of the total radiative intensity are provided in Fig. C.8. Increasing the optical thickness raises the total intensity near the hot wall as energy emitted from this wall is scattered back.

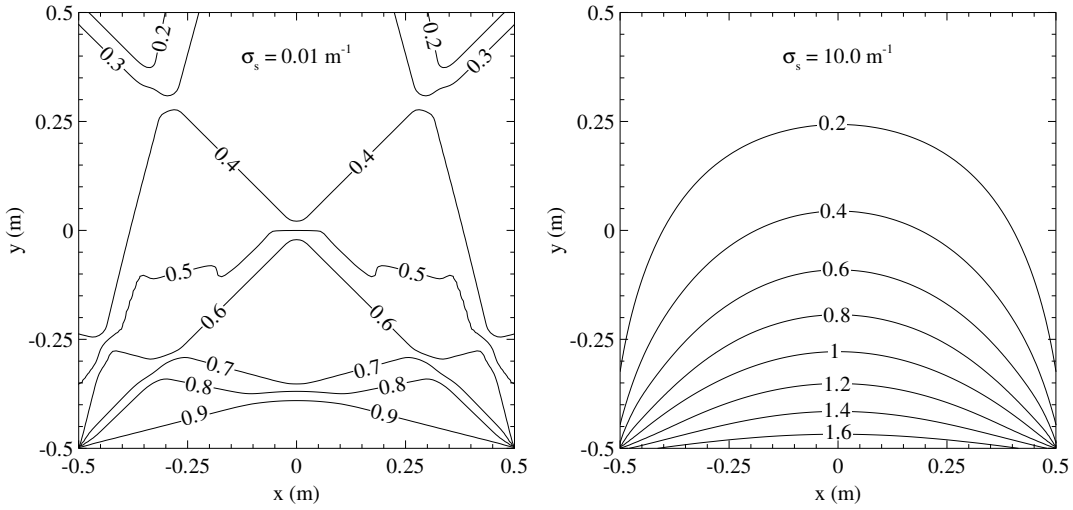

Figure C.8: Contours of normalized direction-integrated intensity, $G/(2\pi I_b)$, for square enclosure with scattering medium obtained using Venkatakrishnan TVD scheme on a mesh with 128 by 128 uniform cells.

C.4 Conclusion

A parallel implicit algorithm and TVD finite-volume scheme was successfully applied to the solution of the DOM and FVM discretizations of the RTE. The algorithm uses an implicit Newton-Krylov solution technique to handle non-linearities introduced by the discretization scheme and the strong omnidirectional coupling in scattering media. Block ILU(p) and additive Schwarz preconditioning were used to improve the effectiveness of the iterative linear solver. An AMR algorithm was also applied to reduce the size of the computational mesh and the required computational resources. The overall performance of the algorithm was assessed by studying both purely absorbing and scattering media in various two-dimensional enclosures.

The proposed algorithm displayed excellent scaling characteristics with greater than 85% parallel efficiency up to 256 processors. Decreasing the block size had a small negative effect on convergence due to the additional partitioning used in the Schwarz preconditioner. However, the number of residual evaluations required to obtain a converged solution can increase significantly with problem size and condition number of the system. Comparing the CPU times required for several different solution techniques and high-resolution schemes, the proposed algorithm outperformed standard TVD space-marching methods by at least a factor of two for strongly scattering media. This favorable performance was not observed for weakly scattering and purely absorbing media. Nonetheless, the algorithm proves promising for large-scale computations of more realistic cases having complex geometry that must be solved in parallel. One of the main limitations of this algorithm is the large memory requirements well in excess of those for explicit or space-marching methods. Recommendations for future work include the implementation of low-memory iterative linear solvers, the use of more effective global preconditioners such as multi-level preconditioning methods, and the application of the algorithm to more realistic test cases. Additionally, error-based refinement criteria should be explored with specific application to test cases that include disparate scales.